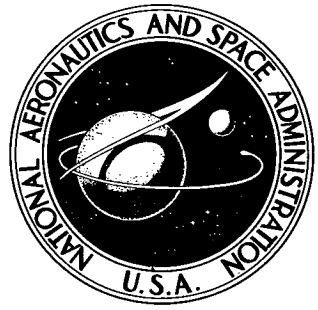
N74-10640

NASA CONTRACTOR REPORT



NASA CR-2306

NASA CR-2306

CASE FILE COPY

SOUND PROPAGATION IN AND RADIATION FROM ACOUSTICALLY LINED FLOW DUCTS: A COMPARISON OF EXPERIMENT AND THEORY

by Harry E. Plumblee, Jr., Peter D. Dean, George A. Wynne, and Robert H. Burrin

Prepared by
LOCKHEED-GEORGIA COMPANY
Marietta, Ga. 30063
for Langley Research Center

NATIONAL AERONAUTICS AND SPACE ADMINISTRATION • WASHINGTON, D. C. • OCTOBER 1973

1. Report No.	2. Government Accession No.	3. Recipient's Catalog No.
NASA CR-2306		

4. Title and Subtitle	5. Report Date
SOUND PROPAGATION IN AND RADIATION FROM ACOUSTICALLY LINED FLOW DUCTS : A COMPARISON OF EXPERIMENT AND THEORY	October 1973
	6. Performing Organization Code
7. Author(s)	8. Performing Organization Report No.
Harry E. Plumblee, Jr., Peter D. Dean, George A. Wynne, and Robert H. Burrin	
	10. Work Unit No.
9. Performing Organization Name and Address	11. Contract or Grant No.
Lockheed-Georgia Company Marietta, GA	NAS1-10472
	13. Type of Report and Period Covered
12. Sponsoring Agency Name and Address	Contractor Report
National Aeronautics and Space Administration Washington, DC 20546	14. Sponsoring Agency Code

15. Supplementary Notes

This is a final report.

16. Abstract

The report presents the results of an experimental and theoretical study of many of the fundamental details of sound propagation in hard wall and soft wall annular flow ducts. The theory of sound propagation along such ducts and the theory for determining the complex radiation impedance of higher order modes of an annulus are outlined. The facility at the Lockheed-Georgia Company Research Laboratory for testing the predictions is described. Methods for generating acoustic duct modes are developed. The results of a detailed measurement program on propagation in rigid wall annular ducts with and without airflow through the duct are presented. Techniques are described for measuring cut-on frequencies, modal phase speed, and radial and annular mode shapes. The effects of flow velocity on cut-on frequencies and phase speed are measured. Comparisons are made with theoretical predictions for all of the effects studies. The theory of the two-microphone method of impedance measurement is outlined. The method is used to measure the effects of flow on acoustic liners. A numerical study of sound propagation in annular ducts with one or both walls acoustically lined is presented. An experimental program which presents the measured values of attenuation, phase speed, and mode shapes for five sets of liners is discussed. Comparisons are made with theory where possible. A method for measuring radiation impedance is described. A series of radiation patterns showing the effects of mode order, frequency and flow are presented.

17. Key Words (Suggested by Author(s))	18. Distribution Statement
Flow ducts Lined ducts Duct acoustics Aerodynamic noise	Unclassified

19. Security Classif. (of this report)	20. Security Classif. (of this page)	21. No. of Pages	22. Price*
Unclassified	Unclassified	228	Domestic, $5.75 Foreign, $8.25

*For sale by the National Technical Information Service, Springfield, Virginia 22151

TABLE OF CONTENTS

		Page
	SUMMARY	1
I.	INTRODUCTION	2
II.	THEORETICAL SUMMARY	3
	II.1 Sound Propagation in Ducts	4
	II.2 Energy Dissipation in Acoustically Lined Flow Ducts	11
	II.3 Modal Reflection Coefficients for Finite-Length Ducts	13
	II.3.1 Method of Analysis	13
III.	EXPERIMENTAL GOALS AND FACILITY DESCRIPTION AND OPERATION	18
	III.1 Major Objectives	18
	III.1.1 Rigid wall duct without flow	19
	III.1.2 Rigid wall duct with mean flow velocity	19
	III.1.3 Finite wall impedance without mean flow	19
	III.1.4 Finite wall impedance with mean flow velocity	19
	III.2 Facility Description	19
	III.3 Operational Details	29
	III.3.1 Instrumentation and controls	29
	III.3.2 Facility dimensions and characteristics	31
	III.3.3 Sound pressure spatial control: preliminary study	35
	III.3.4 Sound pressure spatial control: experimental results	41
IV.	SOUND PROPAGATION IN RIGID WALL ANNULAR DUCTS	49
	IV.1 Description of Experiments	51
	IV.1.1 Determination of cut-on frequency	51
	IV.1.2 Method for experimentally determining phase speed	57
	IV.1.3 Mode shape measurement	59
	IV.2 Analytical Predictions	59
	IV.2.1 Mode shape predictions	60
	IV.3 Comparison of Experiment with Theory	60
	IV.3.1 Cut-on frequency	60
	IV.3.2 Axial propagation constant	63
	IV.3.3 Mode shapes	64
	IV.3.4 Frequency response in hard wall duct	68
	IV.3.5 Flow effects on cut-on frequency and mode shape	76

TABLE OF CONTENTS - Continued

		Page
V.	WALL IMPEDANCE MEASUREMENTS	78
	V.1 Basic Theory of Local Impedance Measurement	81
	V.2 Measurement Error Effects	82
	V.2.1 General considerations	82
	V.2.2 Error effects on two-microphone method evaluations	83
	V.3 Experimental Configurations	86
	V.4 Results of Measurements	94
	V.4.1 General comments	94
	V.4.2 Effect of material property variations	97
	V.4.3 Mean values and related flow effects	105
	V.5 Conclusions	106
VI.	SOUND PROPAGATION IN LINED ANNULAR DUCTS	106
	VI.1 Description of Experiments	107
	VI.1.1 Liner description	107
	VI.1.2 Data requirements	108
	VI.1.3 Phenomena to be verified	108
	VI.2 Analytical Predictions	110
	VI.2.1 Features of computer analysis for sound pressure in ducts	110
	VI.2.2 Numerical studies	111
	VI.2.2.1 Effects of wall impedance without flow	111
	VI.2.2.2 Effects of frequency without flow	117
	VI.2.2.3 Effects of flow	120
	VI.2.2.4 Sound pressure distribution across the duct	122
	VI.3 Comparison of Theory with Experiment	127
	VI.3.1 Modal attenuation and propagation constant - no flow	128
	VI.3.1.1 Single lower-order radial mode	128
	VI.3.1.2 Radial characteristics of the 'plane' mode	133
	VI.3.1.3 Fourier-Bessel analysis technique for radial modes	135
	VI.3.1.4 Higher order radial modes	142
	VI.3.1.5 Complex propagation constant measurements for non-locally reacting liners	144
	VI.3.2 Mode shapes and pressure distribution	146
	VI.3.2.1 Liner 1 mode shapes	148
	VI.3.2.2 Mode shape and pressure distribution for liner 2	150
	VI.3.3 Effect of flow velocity in lined ducts	156

TABLE OF CONTENTS - Continued

		Page
VII.	THE MEASUREMENT OF HIGHER ORDER CIRCUMFERENTIAL MODE RADIATION IMPEDANCE FOR AN ANNULAR DUCT WITH FLOW	179
	VII.1 Introduction	179
	VII.2 Experimental Technique for Determining Modal Radiation Impedance	180
	VII.2.1 Sound field mapping	181
	VII.2.2 Duct sound field	181
	VII.2.3 Measurements in flow	182
	VII.3 Data Analysis Methods for Determining Radiation Impedance	182
	VII.3.1 Fourier analysis of angular pressure distribution	182
	VII.3.2 Spinning/standing mode decomposition	184
	VII.3.3 Axial standing wave calculation	185
	VII.3.4 Acoustic impedance calculation	187
	VII.3.5 Optimization of propagation constant	188
	VII.4 Experimental Values of Radiation Impedance and Comparison with Theory	189
VIII.	RADIATED FIELD	194
	VIII.1 Description of Experiment	196
	VIII.2 Experimental Results	196
	VIII.2.1 Effect of mode number and flow velocity at a fixed frequency	196
	VIII.2.2 Effect of frequency and multiple modes	202
IX.	CONCLUSIONS	209
	REFERENCES	211

LIST OF TABLES

Table	Title	Page
I	Comparison of Theoretical and Experimental Hard Wall Annular Duct Eigenvalues (HTR = 0.966)	63
II	Frequencies for Constructive and Destructive Interference	75
III	Sign Changes of Errors in Impedance	85
IV	Impedance Variations of Six Samples of 2" Thick Polyurethane Foam at 1000 Hz	105
V	Complex Propagation Constant for 40 Rayl, 1.5" Deep Liner for (3,0) Mode	130
VI	Comparison of Calculated and Measured Complex Propagation Constant (3,0 Mode)	131
VII	Angular Mode Distribution for Plane (0,0) Mode Simulation	135
VIII	Fourier Analysis of Angular Pressure Distribution at Nine Radial Stations for Four Axial Stations - (3,0) Mode Simulation at 1000 Hertz	137
IX	Radial Mode Analysis for 3rd Angular Mode Set	138
X	First Radial Mode For Four Equal Amplitude Angular Modes	141
XI	Comparison of Experimental and Theoretical Attenuation Rates for First Four Angular Modes	141
XII	Radial Mode Analysis for Combined (2,0) and (2,1) Modes	142
XIII	Two-Dimensional Analysis Showing Effect of Air Flow Velocity on (3,0) Mode	168
XIV	Effect of Air Flow Velocity on Complex Propagation Constant	179
XV	Radiation Impedance Calculated at Theoretical β By Least-Square Method	192

LIST OF ILLUSTRATIONS

Figure	Caption	Page
1	Plan View of Engine Noise Attenuation Analysis Facility	21
2	Side Elevation and Details of Source and Test Section of Engine Noise Attenuation Analysis Facility	21
3	Engine Noise Attenuation Analysis Facility	22
4	Microphone Drive Mechanism	25
5	Axial Probe Microphone Installation	25
6	Anechoic Room Interior	26
7	Exterior View of Exhaust Muffler	26
8	20 Rayl Felted Metal Liners	27
9	20 Rayl Outer Liner Installed in Test Duct	27
10	Welded Fibrous Metal Outer Liner	28
11	Welded Fibrous Metal Outer Liner Illustrating Holes for Probe Microphone	28
12	System Controls for Engine Noise Attenuation Analysis Facility	30
13	Schematic of Data Acquisition System	30
14	Annular Flow Duct Test Section	32
15	Variation of Mean Flow Velocity with Test Section Angle	33
16	Radial Velocity Profiles	33
17	Empirical Shear Profiles	36
18	Source Location Configurations Considered in Preliminary Design	37
19	Rectangular Test Duct Illustrating Wall Placement of Source Transducers	38
20	Illustration of Recording Technique for Driver "Signature"	42
21	Characteristic Function for Driver Number 8 at 876 Hertz	44
22	Characteristic Function for Driver Number 2 at 876 Hertz	44

LIST OF ILLUSTRATIONS - Continued

Figure	Caption	Page
54	Duct Acoustic Response for One Driver Excitation at an Axial Location of 5.3 Feet from Driver	72
55	Illustration of Modal Axial Wavelength	74
56	Comparison of Experimental and Theoretical Mach Number Effects on Cut-on Frequency	77
57	Effect of Flow Velocity on Angular Hard Wall (3,0) Mode Shape	79
58	Effect of Flow Velocity on Radial Hard Wall (5,1) Mode Shape	80
59	Classical Resonant Cavity Liner Element	81
60	Effect of 10% Variation in SPL, Phase Angle, Temperature and Cavity Depth on a Nominal 40 Rayl Liner with 1/2" Cavity Depth	84
61	Schematic and Photograph of Two-Microphone Test Arrangement	87
62	Overall View of Two-Microphone Test Installation	88
63	Analog Computer Circuit for Accurate Measurement of Two-Microphone Difference SPL	89
64	Traversing "One-Microphone" Modification of Two-Microphone Impedance Measuring Method	89
65	Effect of Frequency on SPL and Phase Angle Traverse Measurements for Welded Fibrous Metal Liner with 1-1/2 Inch Cavity Depth (300 - 2000 Hz)	91
66	Effect of Frequency on SPL and Phase Angle Traverse Measurements for Welded Fibrous Metal Liner with 1-1/2 Inch Cavity Depth (3000 and 4000 Hz)	92
67	Effect of Velocity on SPL and Phase Angle Traverse Measurements for Welded Fibrous Metal Liner with 1-1/2 Inch Cavity Depth	93
68	Effect of Material Non-Uniformities on SPL and Phase Angle Traverse Measurements for Welded Fibrous Metal Liner with 1-1/2 Inch Cavity Depth	95
69	Examples of Surface Non-Uniformities in Felted-Metal Acoustic Lining Material	96
70	Two-Microphone Wall Impedance Measurements for Liner 2 (20 Rayl - 1/2 Inch Cavity Depth) Without Flow	98

LIST OF ILLUSTRATIONS - Continued

Figure	Caption	Page
71	Two-Microphone Wall Impedance Measurements for Liner 2 (20 Rayl - 1/2 Inch Cavity Depth) at 50 fps Mean Flow Velocity	98
72	Two-Microphone Wall Impedance Measurements for Liner 2 (20 Rayl - 1/2 Inch Cavity Depth) at 150 fps Mean Flow Velocity	98
73	Two-Microphone Wall Impedance Measurements for Liner 3 (40 Rayl 1/2 Inch Cavity Depth) Without Flow	98
74	Two-Microphone Wall Impedance Measurements for Liner 3 (40 Rayl - 1/2 Inch Cavity Depth) at 50 fps Mean Flow Velocity	99
75	Two-Microphone Wall Impedance Measurements for Liner 3 (40 Rayl - 1/2 Inch Cavity Depth) at 150 fps Mean Flow Velocity	99
76	Two-Microphone Wall Impedance Measurements for Liner 3 (40 Rayl - 1/2 Inch Cavity Depth) at Hole Number 22, Illustrating a "Bad" Measurement	99
77	Two-Microphone Wall Impedance Measurement for Liner 3 (40 Rayl - 1/2 Inch Cavity Depth) at Hole Number 30, Illustrating a "Good" Measurement	99
78	Composite Plot of Two-Microphone Wall Impedance Measurements for Liner 2 (20 Rayl - 1/2 Inch Cavity Depth) Showing Effect of Velocity	100
79	Composite Plot of Two-Microphone Wall Impedance Measurements for Liner 3 (40 Rayl - 1/2 Inch Cavity Depth) Showing Effect of Velocity	100
80	Average of Standard Impedance Tube Measurements for Two Liner 2 (20 Rayl - 1/2 Inch Cavity Depth) Samples	100
81	Average of Standard Impedance Tube Measurement for Two Liner 3 (40 Rayl - 1/2 Inch Cavity Depth) Samples	100
82	Comparison of Impedance Tube and Two-Microphone Impedance Measurements for Liner 1 (Welded Fibrous Metal - 1-1/2 Inch Cavity Depth) Without Flow	101
83	Two-Microphone Wall Impedance Measurement for Liner 1 (Welded Fibrous Metal - 1-1/2 Inch Cavity Depth) at 50 fps Mean Flow Velocity	101

Figure	Caption	Page
84	Effect of Axial Measurement Position on Wall Impedance for Liner 1 (Welded Fibrous Metal - 1-1/2 Inch Cavity Depth) Without Flow, f = 1000 Hz	103
85	Average of Standard Impedance Tube Measurements for Five Liner 4 (Commercial Foam) Samples	104
86	Average of Standard Impedance Tube Measurements for Three Liner 5 (Acoustic Foam) Samples	104
87	Isocontours of Sound Power Level Attenuation One Diameter Downstream in Annular Duct, for Plane Radial - Third Angular Mode Set	113
88	Isocontours of (3,0) Modal Attenuation and Propagation Constant, β, in Annular Duct	114
89	Variation of (3,0) Modal Amplitude Along Trace of 8 dB Contour in Figure 88	115
90	Variation of (3,0) Modal Amplitude Along Trace of 16 dB Contour in Figure 88	115
91	Isocontours of (3,0) Mode Amplitude and Phase Angle Differences Between Inner and Outer Walls (re. Outer Wall) of Annular Duct	118
92	Isocontours of (0,0) Modal Attenuation and Propagation Constant, β, in Annular Duct	118
93	Isocontours of Sound Power Level Attenuation One Diameter Downstream in Annular Duct for Plane Radial - Plane Angular Mode Set	118
94	Isocontours of (2,0) Modal Attenuation in Annular Duct	119
95	Isocontours of (2,1) Modal Attenuation in Annular Duct	119
96	Modal and Power Level Attenuation Frequency Response for Liner 1 - Second Angular Mode Set	121
97	Modal and Power Level Attenuation Frequency Response for Liner 1 - Plane Angular Mode Set	121
98	Modal and Power Level Attenuation Frequency Response for Liner 1 - Fifth Angular Mode Set	121

LIST OF ILLUSTRATIONS - Continued

Figure	Caption	Page
99	Modal and Power Level Attenuation Frequency Response for Liner 1 - Sixth Angular Mode Set	121
100	Isocontours of (3,0) Modal Attenuation in Annular Duct with 50 fps Sheared Flow	123
101	Isocontours of Sound Power Attenuation One Diameter Downstream in Annular Duct for Plane Radial - Third Angular Mode Set with 50 fps Sheared Flow	123
102	Isocontours of Sound Power Attenuation Two Diameters Downstream in Annular Duct for Plane Radial - Third Angular Mode Set with 50 fps Sheared Flow	123
103	Isocontours of Sound Power Attenuation Three Diameters Downstream in Annular Duct for Plane Radial - Third Angular Mode Set with 50 fps Sheared Flow	123
104	Isocontours of (3,0) Modal Attenuation and Propagation Constant, β, in Annular Duct with 150 fps Sheared Flow	124
105	Isocontours of Sound Power Attenuation One Diameter Downstream in Annular Duct for Plane Radial - Third Angular Mode Set with 150 fps Sheared Flow	124
106	Downstream Sound Pressure Distribution in Annular Duct for $Z = 0.6 - 0.2i$	125
107	Downstream Sound Pressure Distribution in Annular Duct for $Z = 0.4 - 0.2i$	125
108	Downstream Sound Pressure Distribution in Annular Duct for $Z = 0.4 - 0.6i$	125
109	Downstream Sound Pressure Distribution in Annular Duct for $Z = 0.1 + 0.0i$	125
110	Effect of Outer Wall Impedance on Power Level Attenuation in Annular Duct	126
111	Sound Pressure Level Decay and Phase Change for Liner 1 for (3,0) Mode at Various Frequencies	129
112	Comparison of Experiment and Theory for Power Level Attenuation in Liner 1	132

Figure	Caption	Page
113	Comparison of Various Experimental Methods for Impedance Measurement	134
114	Sound Pressure Level Decay and Phase Change for Liner 1 for (0,0) Mode at 1000 Hz	136
115	Example of (0,0) Mode Angular Distribution in Hard Wall Section Upstream of Liner	136
116	Measurement Locations for Two-Dimensional Digital Data Recording	140
117	Comparison of Analog and Digitally Analyzed SPL Decay and Phase Change for Liner 1 (See figure 111(b))	140
118	Sound Pressure Level and Phase Angle for Second Angular Mode Set - Derived from Digital Analysis of Angular Sweep Data - Liner 1, 1808 Hz	143
119	Sound Pressure Level Decay for Liner 4 for (0,0) Mode at 1000 Hertz	145
120	Sound Pressure Level Decay and Phase Angle Change for Liner 5 for (3,0) Mode at Various Frequencies	147
121	Measured Sound Pressure and Phase Contours for (3,0) Mode in Liner 1 at 1000 Hertz	149
122	Comparison of Experiment and Theory for SPL and Phase Angle Contours for (3,0) Mode in Liner 1 at 1000 Hertz	151
123	Comparison of Experiment and Theory for SPL and Phase Angle Contours for (3,0) Mode in Liner 1 at 884 Hertz	151
124	Comparison of Experiment and Theory for SPL and Phase Angle Contours for (3,0) Mode in Liner 1 at 1430 Hertz	151
125	Comparison of Experiment and Theory for SPL and Phase Angle Contours for (0,0) Mode in Liner 1 at 1000 Hertz	151
126	Radial SPL and Phase Angle Contours in Hard Wall Section and Liner 2 Test Section for (2,1) Mode at 1800 Hertz	152
127	Radial SPL and Phase Angle Contours in Hard Wall Section and Liner 2 Test Section for (5,1) Mode at 2330 Hertz	153

LIST OF ILLUSTRATIONS - Continued

Figure	Caption	Page
128	Radial SPL and Phase Angle Contours in Hard Wall Section and Liner 2 Test Section for (6,2) Mode at 3778 Hertz	154
129	Calculated Mode Shapes In Liner 2 for Comparison with Experimental Data of Figures 126 and 128	155
130	Pressure Distribution Across Annulus for Sixth Angular Mode Set at 3750 Hertz	157
131	Angular SPL and Phase Angle Distribution in Liner 1 at 1000 Hertz Without Flow for Two-Dimensional 'Fourier-Bessel' Analysis	158
132	Comparison of Outer Wall Angular SPL Distribution for Four Axial Stations (see Figure 131)	162
133	Angular SPL and Phase Angle Distribution in Liner 1 at 1000 Hertz for Four-Mode Combination	163
134	Radial SPL and Phase Angle Contours for the Plane (0,0) Mode in Liner 4 (Two Sides Lined with Foam) at 1000 Hertz	164
135	Radial SPL and Phase Angle Contours for the (3,0) Mode in Liner 5 (Acoustic Foam on Outer Wall) at Various Frequencies	165
136	Sound Pressure Level Decay and Phase Angle Change for the (0,0) and (3,0) Modes in Liner 1 at 1000 Hertz with 50 fps Flow Velocity	166
137	Radial SPL and Phase Angle Contours for the (0,0) and (3,0) Modes in Liner 1 at 1000 Hertz with 50 fps Flow Velocity	167
138	Sound Pressure Level Decay and Phase Angle Change for the (3,0) Mode in Liner 1 for Various Frequencies at 150 fps Flow Velocity	169
139	Radial SPL and Phase Angle Contours for the (3,0) Mode in Liner 1 at 884 and 1430 Hertz with 150 fps Flow Velocity	170
140	Angular SPL and Phase Angle Distributions in Liner 1 at 1000 Hertz with 50 fps Flow Velocity for Two-Dimensional 'Fourier-Bessel' Analysis	171
141	Angular SPL and Phase Angle Distributions in Liner 1 at 1000 Hertz with 150 fps Flow Velocity for Two-Dimensional 'Fourier-Bessel' Analysis	175

Figure	Caption	Page
142	Examples of Angular SPL and Phase Distributions in Hard Wall Test Section	183
143	Examples of Axial Standing Waves in Annular Duct Showing Effects of Mode Number and Velocity	190
144	Comparison of Experimental and Theoretical Values of Radiation Impedance for a Flanged Annulus	193
145	Effects of Flow Velocity on Radiation Impedance of an Annulus for Various Modes	195
146	Schematic of Microphone Boom Arrangement for Measuring Radiated Sound Field	197
147	Duct Co-ordinates	197
148	Duct Exit and Radiated Field Patterns of (0,0) Mode, $kR_o = 4.485$	198
149	Duct Exit and Radiated Field Patterns of (1,0) Mode, $kR_o = 4.485$	199
150	Duct Exit and Radiated Field Patterns of (2,0) Mode, $kR_o = 4.485$	200
151	Duct Exit and Radiated Field Patterns of (3,0) Mode, $kR_o = 4.485$	201
152	Summary Plot of Radiated Field of Annular Duct Modes Showing the Effects of Flow and Angular Mode Order at 1000 Hz	203
153	Duct Exit and Radiated Field Patterns for (0,0) + (1,0) Equal Mode Combination, $kR_o = 1.538$	204
154	Duct Exit and Radiated Field Patterns for (0,0) + (1,0) Equal Mode Combination $kR_o = 2.518$	205
155	Duct Exit and Radiated Field Patterns for (0,0), (1,0) and (2,0) Equal Mode Combination, $kR_o = 3.755$	206
156	Duct Exit and Radiated Field Patterns for (0,0), (1,0), (2,0) and (3,0) Equal Mode Combinations, $kR_o = 4.410$	207
157	Duct Exit and Radiated Field Patterns for (0,0), (1,0), (2,0) and (3,0) Equal Mode Combinations, $kR_o = 6.021$	208

SOUND PROPAGATION IN AND RADIATION FROM ACOUSTICALLY LINED FLOW DUCTS: A COMPARISON OF EXPERIMENT AND THEORY

by Harry E. Plumblee, Jr., Peter D. Dean,
George A. Wynne and Robert H. Burrin
The Lockheed-Georgia Company

SUMMARY

An experimental and theoretical comparison of many of the fundamental details of sound propagation in acoustically lined flow ducts comprises the main body of this study.

A description of the theory used for comparison with the experimental results is included as the first section of this report. The theory of sound propagation in acoustically lined annular ducts is outlined and the method of solution is presented. Methods for calculating energy dissipation in lined flow ducts are discussed. Then, the theory for determining the complex radiation impedance of higher order modes of an annulus is outlined.

A facility at the Lockheed-Georgia Company Research Laboratory, designed for the explicit purpose of testing the predictions of the theory of sound propagation in flow ducts, is described. Methods of simulating acoustic duct modes and the fundamental characteristics of fan-tone noise are described.

A detailed measurement program on sound propagation in rigid wall annular ducts with and without air flow is discussed. Techniques are described for measuring cut-on frequency, modal phase speed and radial and angular mode shapes. Measured effects of flow velocity on cut-on frequency and phase speed are presented. Comparisons are made with theoretical predictions for all effects studied.

The theory of the two microphone method of impedance measurement is outlined. Measurement error effects are discussed. An experimental program and results are discussed which detail the effects of flow on the impedance of locally reacting acoustic liner materials. Acoustic impedance for five sets of liners is presented under various flow conditions.

A numerical study on sound propagation in annular ducts with one or both sides acoustically lined is presented. Following this, an experimental program which presents the measured values of attenuation, phase speed and mode shapes for all five liner sets is discussed in detail. Comparisons are made with theory where possible.

A method for measuring the modal radiation (or termination) impedance from a finite-length annular duct is described and experimental results are presented and compared with theory for the case without flow.

Finally, a series of radiation patterns from an annular duct, measured in an anechoic room, are presented. This experimental study shows the effect of mode order, frequency, jet flow and multiple mode pressure distribution on the radiated field patterns.

I. INTRODUCTION

Aircraft engine acoustic duct liners have been successfully designed for reducing the level of internally generated noise radiated to the community. Three large commercial passenger aircraft which incorporated community noise specifications into the design are now operational. These aircraft, the Lockheed L-1011, the Douglas DC-10 and the Boeing 747 have successfully passed the FAA certifications in force at the time of their initial deliveries. These aircraft are positive evidence that acoustic materials can, with reasonable assurance, be used to reduce radiation of internally generated engine noise. The question for the future is not, 'Can internally generated noise be effectively reduced to reasonable levels?', but instead, 'how efficiently can the acoustic materials be utilized in reducing internally generated noise?'.

The primary goal of this research program was to provide data which would imply answers to the second question above. The program was not a research study on optimization of acoustic liner materials, as the above stated goal could imply. It was instead, primarily an experimental program, designed around a unique flow duct facility, to provide data points for correlation with theoretical predictions. The rationale was, 'provided the experimental data could be used to verify the appropriate theory, then the theory could be used for design optimization studies'. This, in simplistic terms, is the basic motivation underlying the study to be described in what follows.

The subject of sound propagation in ducts holds great current interest. In the eight year period, 1964 - 1972, twenty-six papers on the subject were published in the Journal of Sound and Vibration. To show that the interest is not waning, fifteen of these were published in the year 1971. Of all the papers surveyed, only a few contained experimental data and very few had data suitable for detailed correlation with theory.

There were many aspects of the theory of duct acoustics involving assumptions which needed experimental verification. One aspect which required validation involved effects of parameters, such as geometry, flow velocity, temperature and liner impedance, on the wave properties in the duct. Another aspect involved validation of the mathematical representation of the physical problem as an eigenvalue problem. Still another aspect of the subject was the radiation of sound pressure from the termination of the duct through the jet flow to the surrounding ambient medium. In this case, there were no representative theoretical results with which to correlate, thus the experiment should be used as a guide for future theoretical studies.

In particular, a facility was needed to provide experimental data for determining the effects on sound propagation within a duct of realistic geometry (circular or circular annular), liner impedance (both outer and inner walls in the case of the annulus), source sound pressure distribution, finite-length, mean flow velocity and velocity profile and temperature. Since most of the theoretical efforts were concentrating on various eigenvalue approaches, the data was required to be comprehensive enough to show effects of the above listed parameters on both the complex propagation constant and mode shape. Additionally, information on radiated noise from the duct was very sparse, especially for correlation with in-duct conditions. Thus, another feature of the tests was to provide radiated noise data which showed the effect of some of the above parameters and which could be used in future correlations with theory.

The work reported on herein was conducted in the Lockheed-Georgia Company Research Laboratory in a facility specifically designed to satisfy the requirements of the stated goal. The work included the development of techniques for operating the facility as well as for obtaining the desired data.

The work presented involved detailed measurements of the sound transmission through and radiation from hard wall and acoustically lined annular ducts with and without mean air flow velocity. It was necessary to develop techniques for measuring the impedance of acoustic materials in the presence of high velocity air flow. Also, techniques were developed for measuring the modal radiation impedance in the presence of air flow. Additionally, the radiated acoustic field for a series of duct modes was measured in an anechoic room.

II. THEORETICAL SUMMARY

The theoretical study of excitation, transmission and radiation of sound from sources in ducts has elicited considerable interest in the published literature during the past few years. At first, there were numerous engineering studies which utilized the Morse theory for rectangular ducts (ref. 1). Other studies then presented numerical solutions for sound propagation in lined circular ducts, such as that of Rice (ref. 2). In an attempt to more adequately represent the physical situation usually encountered, Mungur and Gladwell (ref. 3) incorporated the ideas of Pridmore-Brown (ref. 4) and Tack and Lambert (ref. 5) in a study of the effects of shear flow on sound transmission through the duct. In a later study, Mungur and Plumblee (ref. 6) studied sound transmission through a lined annular duct carrying a sheared mean flow. Several recent studies have presented numerical variations on the reference 6 approach, but have incorporated the same basic assumptions.

All of the studies mentioned were concerned with sound propagation in an infinite length duct with uniform axial characteristics. In order to more closely represent the actual physical situation encountered in practice, that of a fan in a circular or annular duct, it is necessary to take into account source characteristics, the effect of finite duct length on the sound field, and finally, the radiated sound field from the duct termination. An approach

to the complete problem was given by Sofrin and Tyler (ref. 7) and Morfey (ref. 8), based on concepts introduced by Rayleigh (ref. 9). These studies, primarily analytical but also including some experimental work, were made for hard wall ducts. But the concept of considering the source, the duct and the radiation field as separate acoustic elements was outlined and justified in detail.

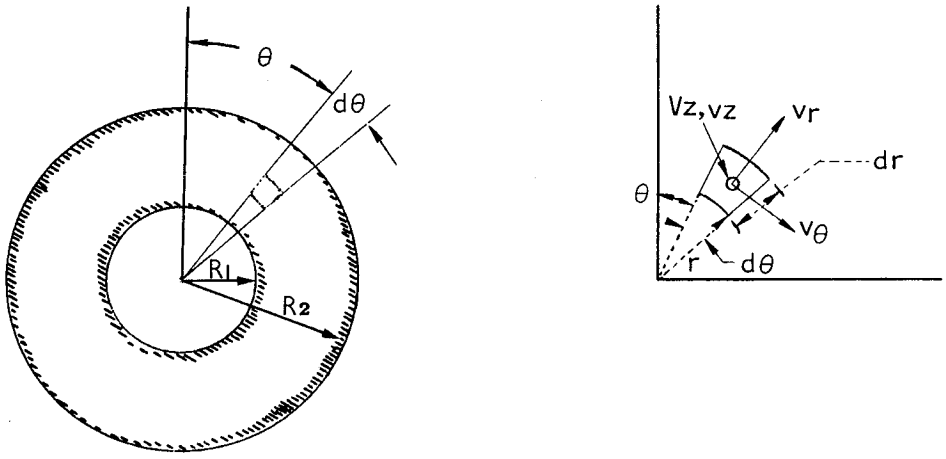
An entirely different approach for calculating the radiated sound field for a source distribution within the duct used a mathematical method based on the Weiner-Hopf technique for the solution of partial differential equations. Examples are outlined in a text by Noble (ref. 10) and problems concerned with sound radiation from unflanged circular pipes have been solved by Levine and Schwinger (ref. 11) and Carrier (ref. 12). These techniques have been extended by Lansing, Zorumski and their co-workers at NASA (ref. 13, 14, 15) to include effects of mean flow through the duct and axial discontinuities in the liner impedance, as well as computing exact radiation patterns for representative pressure distributions within the duct. In these calculations, the radiation field does not contain the very significant effects of refraction due to the jet flow, and it is questionable that the convection effects in the radiation field calculations are representative.

The first method, that of analyzing each effect in relative isolation, appeared to be most attractive in the early theoretical studies at Lockheed, because of the building block approach which could be adopted in preparing computer analyses. For this reason, and since the Weiner-Hopf method becomes intractable when realistic duct and jet flows are considered, the first approach was adopted.

The following sub-sections outline the theory which is to be evaluated for comparison with experimental results in the sections to follow. The theory is classified into sub-sections on sound propagation in lined ducts, energy flow in lined ducts and modal radiation impedance. This presentation gives only a brief outline of the derivations. Amplification of the details can be obtained from the relevant reference material.

II.1. Sound Propagation in Ducts

The following presentation begins with a summary of the derivation of the convected wave equation as presented by Mungur and Plumblee (ref. 6). The starting point for this analysis, as with most aeroacoustics problems, is with the Navier-Stokes momentum equations, the mass continuity equation and the energy equation. For the purposes of this study, a cylindrical coordinate system is appropriate. The variables are defined in the sketch at the top of the following page.



Cylindrical coordinate system used for wave equation

The basic assumption used in deriving the linearized acoustic equations are:

(1) viscous effects are negligible,

(2) products of fluctuating quantities are negligible,

(3) the mean flow is axial and is uniform in that direction,

$$V_r = V_\theta = 0 \quad \text{and} \quad \frac{\partial V_z}{\partial z} = 0$$

(4) there is no mean swirl, $\frac{\partial V_z}{\partial \theta} = 0$

(5) radial gradients of the axial mean flow are permitted. (i.e. $\frac{\partial V_z}{\partial r} \neq 0$).

If the density, pressure and velocity variables are perturbed and the equations resulting from time averaging the fully perturbed equations are subtracted, the following linearized equations describing acoustic motion for the specified physical situation result. The linearized momentum equations are,

$$\rho_o\left[\frac{\partial v_z}{\partial t} + \frac{\partial V_z}{\partial r} v_r + V_z \frac{\partial v_z}{\partial z}\right] = - \frac{\partial p'}{\partial z} , \tag{1}$$

$$\rho_o\left[\frac{\partial v_r}{\partial t} + V_z \frac{\partial v_r}{\partial z}\right] = - \frac{1}{r} \frac{\partial p'}{\partial r} \tag{2}$$

$$\rho_o\left[\frac{\partial v_\theta}{\partial t} + V_z \frac{\partial v_\theta}{\partial z}\right] = -\frac{1}{r}\frac{\partial p'}{\partial \theta} . \qquad (3)$$

where V_z is the mean axial velocity, v_r, v_z and v_θ are the acoustic velocity components, p' is the sound pressure and ρ_o is the mean density. The linearized mass continuity equation is,

$$\frac{\partial \rho'}{\partial t} + V_z \frac{\partial \rho'}{\partial z} + \rho_o\left\{\frac{\partial v_z}{\partial z} + \frac{\partial v_r}{\partial r} + \frac{1}{r}\frac{\partial v_\theta}{\partial \theta}\right\} + \rho_o \frac{v_r}{r} = 0, \qquad (4)$$

where ρ' is the acoustic density component.

From this point, the objective is to derive a wave-type equation by elimination of the acoustic velocity terms. If one differentiates equations (1), (2) and (3) with respect to z, r, and θ respectively and sums the resulting equations, the single equation which follows is

$$\rho_o\left[\frac{\partial}{\partial t}\left\{\frac{\partial v_z}{\partial z} + \frac{\partial v_r}{\partial r} + \frac{1}{r}\frac{\partial v_\theta}{\partial \theta}\right\} + 2\frac{\partial V_z}{\partial r}\frac{\partial v_r}{\partial z} + V_z \frac{\partial}{\partial z}\left\{\frac{\partial v_z}{\partial z} + \frac{\partial v_r}{\partial r} + \frac{1}{r}\frac{\partial v_\theta}{\partial \theta}\right\}\right]$$

$$= -\left(\frac{\partial^2 p'}{\partial z^2} + \frac{\partial^2 p'}{\partial r^2} + \frac{1}{r^2}\frac{\partial^2 p'}{\partial \theta^2}\right) \qquad (5)$$

If one observes that the term in curly brackets is the divergence in cylindrical coordinates less a v_r/r term and corresponds to the bracketed term in the continuity equation, a useful substitution can be made. The result of combining equation (4) with (5) is

$$-\frac{\partial^2 \rho'}{\partial t^2} - 2V_z \frac{\partial^2 \rho'}{\partial t \partial z} - \frac{\rho_o}{r}\frac{\partial v_r}{\partial t} + 2\rho_o \frac{\partial V_z}{\partial r}\frac{\partial v_r}{\partial z} - V_z^2 \frac{\partial^2 \rho}{\partial z^2} - \frac{\rho_o V_z}{r}\frac{\partial v_r}{\partial z}$$

$$= -\left(\frac{\partial^2 p'}{\partial z^2} + \frac{\partial^2 p'}{\partial r^2} + \frac{1}{r^2}\frac{\partial^2 p'}{\partial \theta^2}\right) \qquad (6)$$

The previous assumptions concerning neglect of viscous effects in conjunction with an assumption of negligible thermal conductivity allows the energy equation to reduce to

$$p' = \rho' c^2 , \qquad (7)$$

with c being the speed of sound in the fluid. For a particular frequency, ω, variables are assumed to have the following axial dependence

$$p', v_r, v_z, v_\theta, \propto e^{i\omega t - ikKz}. \tag{8}$$

The complex propagation constant, K, is represented as $K = \beta - i\alpha$ and $k = \omega/c$.

From equation (2), using the assumption in equation (8), it is determined that

$$v_r(r,\theta) = - \frac{1}{i\rho_o ck(1-MK)} \frac{\partial p'}{\partial r} \tag{9}$$

where $M = V_z(r)/c$. Substitution of equation (7), (8), and (9) into equation (6) results in the following 'convective-refractive' wave equation, as given in reference 6,

$$\frac{\partial^2 p'}{\partial r^2} + \left[\frac{1}{r} + \frac{2K}{1-MK}\frac{\partial M}{\partial r}\right] \frac{\partial p'}{\partial r} + k^2\left[(1-MK)^2 - K^2\right]p' + \frac{1}{r^2}\frac{\partial^2 p'}{\partial \theta^2} = 0. \tag{10}$$

The effect of convection is represented by the terms, $k^2(-2MK + M^2K^2)p'$ and the shear refraction is accounted for by the term

$$\frac{2K}{1-MK}\frac{\partial M}{\partial r}\frac{\partial p'}{\partial r}. \tag{11}$$

If the boundary conditions on the inner and outer radii are independent of angle, θ, then the equation is separable. Also, it is convenient to non-dimensionalize the radial variable, r, with respect to a convenient length. For the case of a cylinder, the radius is appropriate and in the case of an annular duct, the duct width is a desirable parameter. The new variable is

$$X = r/L.$$

The separation variables are $p'(X,\theta) = P(X)\,\Theta(\theta)$. The resulting angular differential equation is

$$\frac{d^2\Theta}{d\theta^2} + k_\theta^2\,\theta = 0, \tag{12}$$

from which it is determined that

$$\Theta = \begin{Bmatrix} \sin m\theta \\ \cos m\theta \end{Bmatrix} \tag{13}$$

and $k_\theta = 0,1,2,\ldots,m,\ldots,N$.

The resulting radial differential equation is

$$\frac{d^2p}{dx^2} + \left[\frac{1}{X} + \frac{2K}{1-MK}\frac{dM}{dX}\right]\frac{dP}{dX} + (kL)^2\left[(1-MK)^2 - K^2 - \frac{m^2}{(kL)^2X^2}\right]P = 0. \tag{14}$$

The solution of this equation yields the eigenvalue, $K = \beta - i\alpha$, for a particular set of boundary conditions, angular mode number, m, frequency, kL, and Mach number profile, M(X).

Several techniques are available for determining the solution. For the idealistic case of plug flow, an exact analytical eigen solution exists. This solution has been discussed in detail for a cylinder, with and without flow, by Rice (refs. 2, 16) (but with a flow boundary condition which assumes continuity of particle velocity rather than particle displacement (see Mungur (ref. 17) and Tester (ref. 22)).

For the case with shear flow, Mungur and Plumblee numerically integrated equation (14) and utilized an eigenvalue search procedure in the complex eigenvalue plane. The initial numerical program was relatively inefficient and in many cases, skipped modes. Mungur later improved this numerical routine by incorporating a steepest descent prediction for locating eigenvalues.

In a more recent study of equation (14), Wynne and Plumblee (ref. 18) arranged the finite-difference equations in the form of an eigenvalue problem. The difficulty in this approach resulted from the fact that the eigenvalue formulation was non-linear. The form of the eigenvalue equation, to which the finite difference was applied, is displayed in equation (15), which is a slight rearrangement of equation (14);

$$\frac{d^2P}{dX^2} + \left\{\frac{1}{X} + \frac{2K_n}{1-MK_n}\frac{dM}{dX}\right\}\frac{dP}{dX} + \left\{(kL)^2(-2MK_n + M^2K_n^2) - \lambda_n - \frac{m^2}{X^2}\right\}P = 0. \tag{15}$$

The eigenvalue, λ_n, is defined, from equation (14), as

$$\lambda_n = -(kL)^2(1 - K_n^2). \tag{16}$$

The finite-difference equation which results from a simple partitioning scheme is

$$A_j P_{j-1} + B_j P_j + C_j P_{j+1} - \lambda_n P_j = 0 \tag{17}$$

where

$$A_j = \frac{2}{(X_{j+1}-X_{j-1})\,(X_j-X_{j-1})} - \left(\frac{1}{X_j} + \frac{2K_n}{1-M_jK_n}\frac{dM_j}{dX_j}\right)\frac{1}{2(X_j-X_{j-1})}$$

$$B_j = -\frac{2}{(X_{j+1}-X_j)\,(X_j-X_{j-1})} - \left[\frac{1}{X_j} + \frac{2K_n}{1-M_jK_n}\frac{dM_j}{dX_j}\right]\left[\frac{1}{2(X_{j+1}-X_j)}\right.$$

$$\left. - \frac{1}{2(X_j-X_{j-1})}\right] - (kL)^2(-2M_jK_n + M_j^2K_n^2) - \frac{m^2}{X_j^2}$$

$$C_j = \frac{2}{(X_{j+1}-X_{j-1})\,(X_{j+1}-X_j)} + \left(\frac{1}{X_j} + \frac{2K_n}{1-M_jK_n}\frac{dM_j}{dX_j}\right)\frac{1}{2(X_{j+1}-X_j)} \tag{18}$$

The impedance boundary conditions are applied at station X_1 and X_N. In the finite-difference scheme utilized, all variables were defined at the central point of the finite-difference increment. The program was written for variable increments so that the step size could be optimized in regions of rapid change in the variables. The derivative is

$$\frac{dP_j}{dX_j} = \frac{P_{j+1}}{2(X_{j+1}-X_j)} - \frac{P_j}{2}\left(\frac{1}{X_{j+1}-X_j} - \frac{1}{X_j-X_{j-1}}\right) - \frac{P_{j-1}}{2(X_j-X_{j-1})} \tag{19}$$

and

$$\frac{d^2P_j}{dX_j^2} = \frac{2P_{j+1}}{(X_{j+1}-X_j)\,(X_{j+1}-X_{j-1})} - \frac{2P_j}{X_{j+1}-X_{j-1}}\left(\frac{1}{X_{j+1}-X_j} - \frac{1}{X_j-X_{j-1}}\right)$$

$$+ \frac{2P_{j-1}}{(X_{j+1}-X_{j-1})\,(X_j-X_{j-1})}\,. \tag{20}$$

The form of the eigenvalue matrix, from equation (17) is

$$\{[A] - \lambda_n [I]\}P = 0 \tag{21}$$

with the A matrix being tri-diagonal as observed in equation (17).

In order to determine the complex eigenvalues in the presence of a sheared flow, $M_j(X_j)$, an iterative procedure was established. First the no-flow eigenvalue is introduced into the [A] matrix as an initial guess and the eigenvalue problem is solved for the eigenvalue of smallest magnitude. This first solution incorporates some flow effects. This new eigenvalue or a suitable modification thereto by the Newton-Ralphson scheme, is then substituted into [A] matrix once again, after convergence tests have been performed. The iteration is continued until a converged value is obtained for the lowest eigenvalue. This procedure is repeated until the desired number of solutions is obtained.

Needless to say, convergence problems were encountered at many stages in the solution process. One of the more rudimentary techniques used for counteracting the slow convergence was a gradual introduction of the flow magnitude and shear gradients. The region where most convergence problems occurred was in the vicinity of a branch point. Most of these were cured, but there are still certain conditions where the numerical program allows the solution process to oscillate between two eigenvalues, across the branch line. When this occurs, the numerical solution is very slow and sometimes fails.

The solutions which result from the procedure described above also contain the mode shapes appropriate to the set of eigenvalues. It is noted that the concept of modes is very useful from the standpoint of a mathematical examination of sound transmission through ducts, however, the problem of physical concern is that of propagation of a source pressure or acoustic velocity distribution. Thus, while individual modes are, in many instances, physically meaningless they are required as a means of representing the behavior of a complex sound pressure distribution as it propagates through the duct.

Based on the above, the numerical analysis was written such that propagation of an arbitrary sound pressure distribution could be studied. In order to simulate the complex radial pressure distribution, a least square fit to that pressure distribution was accomplished, making use of the set of radial modes for a particular angular mode. The error function for the least square representation is

$$E_m(r_i) = P_m(r_i) - \sum_{n=0}^{N} A_n^m \phi_{mn}(r_i) \tag{22}$$

where $P_m(r_i)$ is the measured pressure distribution for the m^{th} angular mode at the i^{th} radial station and $\phi_{mn}(r_i)$ is the complex mode shape. The mode coefficients are determined by minimizing the total error magnitude with respect to the coefficients. Thus, if

$$G_m = \sum_{i=1}^{I} r_i E_m(r_i) E_m^*(r_i), \tag{23}$$

where * denotes the complex conjugate and where r_i has been included as the appropriate weighting function for the cylindrical coordinate system, then the conditions

$$\frac{\partial G_m}{\partial \mathrm{Re}(A_n^m)} = 0 \quad \text{and} \quad \frac{\partial G_m}{\partial \mathrm{Im}(A_n^m)} = 0, \tag{24}$$

gives a set of simultaneous equations from which A_n^m can be determined. A similar set of conditions could be used to match an acoustic velocity source distribution with the complex mode shapes.

This forms the basic analysis for sound propagation in circular or annular lined flow ducts. A number of similar analyses utilizing different numerical approaches have been done within the past three years. These have been different in the solution technique but have generally utilized the basic assumptions leading to equation (14). Thus, further discussion of the similar reference material is not felt to be necessary.

II.2. Energy Dissipation in Acoustically Lined Flow Ducts

The results from the previous analysis yield eigenvalues which define the attenuation rate of individual modes. However, as will be demonstrated in a subsequent numerical study, the modal attenuation rate can be very misleading when trying to predict the performance of a liner. The overall power attenuation can differ from the attenuation of the least damped mode for at least two reasons. The first results from reflections from the termination and the second is a result of interference between multiple propagating modes. Other causes of variations between energy attenuation and attenuation of the least damped mode are due to source sound pressure distribution, source impedance and refraction due to inlet or exhaust flows. Some of these have been introduced in the numerical procedures but termination and source impedance and inlet and exhaust flow effects were not included.

The subject of acoustic energy in non-uniform flows has been discussed extensively by Morfey (refs. 19 and 20), Möhring (ref. 21) and Tester (ref. 22). Cantrell and Hart (ref. 23) derived an expression for acoustic energy

which, Morfey (ref. 19) showed, is conserved in non-uniform but irrotational mean flows. Morfey also included in his studies a description of energy production terms due to interactions in rotational (sheared) mean flows. Tester used the work of Morfey and that of Möhring to examine certain "strange" modes (modes which have phase velocities in the direction opposite to the direction of decay), and showed that the Cantrell and Hart energy flow appears to be amplifying in the uniform flow region, whereas the Möhring energy flow in the thin shear layer is in a direction opposite to that in the uniform flow region and compensates for the apparent energy "amplification." Tester also showed that the energy of well cut-on modes could be determined with the Cantrell and Hart energy expression.

Although the work of Möhring results in a definition of energy which has no production terms in a parallel sheared flow, it is not valid for a match condition between a duct and the radiated field. The work would require reformulation to represent the energy in free-field with either an irrotational or a rotational flow. However, as long as the flow is irrotational, for instance an ideal inlet flow, Cantrell and Hart's energy will be conserved.

In the presentation which follows, the Cantrell and Hart energy expressions as given by Morfey are used for determining power level attenuation. The results are expected to be valid for modes which are cut-on, but could be questionable for non-cut-on modes.

The form of Morfey's energy is

$$I_i = \langle p' v_i \rangle + \frac{V_i}{\rho_o c^2} \langle p' p' \rangle + \frac{V_i V_j}{c^2} \langle p' v_j \rangle + \rho_o V_j \langle v_l v_j \rangle \quad . \tag{25}$$

For the axial flow of the present analysis, the axial intensity is

$$I_z(X,\theta) = \frac{Re}{2} \{ p' v_z^* (1 + M^2) + (\frac{p' p'^*}{\rho_o c} + \rho_o c v_z v_z^*) M \} \quad , \tag{26}$$

where * denotes the complex conjugate. It is necessary to derive an expression for the axial acoustic velocity, v_z. This is accomplished by substituting equation (9) and (8) into equation (1), with the result for the n^{th} mode being,

$$v_{zn} = \frac{1}{\rho_o c} \left[\frac{K_n p'_n}{1-MK_n} - \frac{\frac{dM}{dX} \frac{dp'_n}{dX}}{(kL)\ (1-MK_n)^2} \right] . \tag{27}$$

After substitution of equation (27) into (26), the total power at a particular cross section can be found with the following integral relationship,

$$E = \int_0^{2\pi} \int_{X_1}^{X_2} I(X,\theta) X dX d\theta, \tag{28}$$

where X_1 is the inner radius and X_2 is the outer radius. The ratio of the powers at two different cross-sections is taken to be the parameter which most closely represents the attenuation performance of a particular liner design in the radiated field from a lined duct if effects such as flow refraction, diffraction and reflections at the end are neglected.

II.3. Modal Reflection Coefficients for Finite-Length Ducts

A very elegant analysis for determining the modal reflection coefficient in an arbitrarily shaped duct of finite length was performed by Doak (ref. 24). The modal reflection coefficients, in this instance, can be used to completely specify the sound field within the duct and in the radiated field, based upon a specific source sound pressure or acoustic velocity distribution. Thus, for practical purposes the specific modal impedance coefficient, resulting from the modal reflection coefficient is equivalent to the radiation impedance for a piston of the same cross-section as that of the duct termination in a rigid baffle and with a velocity equal to the modal velocity distribution over the duct cross-section.

The analysis by Doak, which is a more general study than that to be summarized in the following subsection, leads to a derivation of the modal reflection coefficients for an arbitrarily shaped finite-length duct with radiation from the termination at either end. The analysis is only applicable to orthogonal duct modes, but as is pointed out in ref. 24 any set of non-orthogonal modes can be orthogonalized. Thus, in principle at least, the analysis can be applied to ducts of arbitrary geometry where the modes would not normally be orthogonal.

The method, as described in the following, was applied to a rigid-wall duct of annular cross section by Haddle (ref. 15). Calculations were performed by numerical evaluation of a triple-integral over the surface of the annulus. The results for the real part of the impedance were compared with calculations by Morfey (ref. 26) and shown to be identical, although the methods of analysis in the two cases were considerably different.

II.3.1. Method of analysis

It is shown in ref. 24 that the sound pressure, $p^-(X_j;\omega)$, inside a duct can be represented as (in the absence of mean flow, $V_z = 0$).

$$p^-(X_j;\omega) = \sum_{m,n} \psi_{mn}(X_1,X_2) \left[a_{mn} e^{-ik_{mn}X_3} + b_{mn} e^{ik_{mn}X_3} \right], \tag{29}$$

where ψ_{mn} satisfies the equation,

$$\frac{\partial^2 \psi_{mn}}{\partial X_1^2} + \frac{\partial^2 \psi_{mn}}{\partial X_2^2} + \kappa_{mn}^2 \psi_{mn} = 0, \tag{30}$$

and the boundary condition,

$$\frac{\partial \psi_{mn}}{\partial X_1} = \frac{\partial \psi_{mn}}{\partial X_2} = 0 \ , \tag{31}$$

on the duct boundaries (the (-) superscript refers to conditions within the duct). These boundary conditions permit determination of the wave numbers, κ_{mn}, from which the axial wave number k_{mn} can be determined as

$$k_{mn}^2 = k^2 - \kappa_{mn}^2 \ . \tag{32}$$

The axial acoustic particle velocity from equation (1) for the case of no mean flow is, after spectral transformation.

$$\bar{v}_{X_3} = - \frac{1}{i\omega\rho_o} \frac{\partial \bar{p}}{\partial X_3} \ . \tag{33}$$

Substitution of equation (29) yields the following relationship,

$$\bar{v}_{X_3} = \sum_{m,n} \psi_{mn} \left[\frac{a_{mn}}{\rho_o c_{mn}} e^{-ik_{mn}X_3} - \frac{b_{mn}}{\rho_o c_{mn}} e^{ik_{mn}X_3} \right] \tag{34}$$

where the complex phase velocity, c_{mn}, is related to the wave number, k_{mn}, by

$$c_{mn} = \frac{\omega}{k_{mn}} \ . \tag{35}$$

At this point, the modal reflection coefficient is defined as the amplitude of the reflected wave to the amplitude of the incident wave, (the possibility of reflection in several modes with only one mode incident occurs and in some cases is very important; see Lansing, et al., ref. 14)

$$R_{mnj} = \frac{b_{mj}}{a_{mn}} \quad . \tag{36}$$

The analysis which follows ignores the modal reflection coupling coefficients and considers only the self-modal reflection coefficients. Thus, for the mn^{th} mode, it can be shown that at the end $z = 0$, the inner solution can be used to define a modal impedance of the following form:

$$\frac{Z_{mn}}{\rho_o c} = \frac{\bar{p}_{mn}}{\rho_o c \bar{v}_{mn}} = \frac{1+R_{mn}}{1-R_{mn}} \quad , \tag{37}$$

Doak then proceeded to determine an acoustic solution appropriate to the region external to the duct, i.e., a solution which satisfies the boundary conditions in the exterior region, but utilizing the set of orthonormal characteristic functions of the duct termination cross-section. The pressure at an arbitrary point in the acoustic field of a piston in a rigid baffle is formulated in terms of the Green's function for a unit point source on the surface of a plane, rigid baffle of infinite extent.

The general Green's function solution, $p_\delta^+(X_j; X_j')$, is

$$p_\delta^+(X_j;X_j) = \sum_{mn} \alpha_{mn}(X_3;X_3') \; \Psi_{mn}(X_1,X_2) \; \Psi_{mn}(X_1',X_2') \tag{38}$$

where the (+) superscript refers to locations in the outer region, and the coefficients α_{mn} are,

$$\alpha_{mn}(X_3;X_3') = \frac{1}{A^2} \int_S \iint_S p_\delta^+(X_j;X_j')\Psi_{mn}^*(X_1,X_2)\Psi_{mn}^*(X_1',X_2')dX_1 dX_2 dX_1' dX_2' . \tag{39}$$

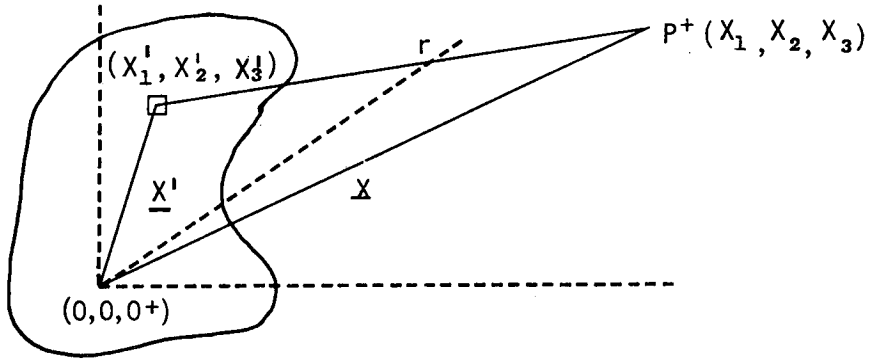
The Green's function appropriate to the case of interest is

$$p_\delta^+(X_1,X_2,\ell,X_1',X_2',\ell) = i\omega\rho_o \frac{e^{-i\frac{\omega}{c}\sqrt{(X_1-X_1')^2+(X_2-X_2')^2}}}{2\pi\sqrt{(X_1-X_1')^2+(X_2-X_2')^2}} \quad . \tag{40}$$

Thus, the acoustic pressure in terms of the Green's function and the acoustic velocity on the outer surface of the duct can be shown to be (Haddle, ref. 25)

$$p^+ = -i\rho_o ck \sum_{mn} \int_S\int \frac{e^{ik|\underline{X}-\underline{X}'|}}{2\pi|\underline{X}-\underline{X}'|} v_{mn}^+ \, dX_1' dX_2' \, , \tag{41}$$

with the nomenclature defined in the sketch below. This step is equivalent to that discussed in Morse and Ingard (ref. 27) for the circular piston.



The solution for the reflection coefficient, R_{mn}, can be accomplished with application of the condition of continuity of sound pressure and particle velocity across the interface between the duct and the radiated field, i.e.;

$$p_{mn}^+ = p_{mn}^- \tag{42}$$

$$v_{mn}^+ = v_{mn}^- \, .$$

Use of the orthogonality relationships for the duct modes is necessary to complete the evaluation. Also, the modes are normalized such that

$$\frac{1}{A}\int_S\int \Psi_{\mu\nu}(X_1,X_2)\Psi_{mn}(X_1,X_2)dX_1dX_2 = \begin{cases} 0, & (\mu,\nu) \neq (m,n) \\ 1, & (\mu,\nu) = (m,n) \end{cases} , \tag{43}$$

where $\Psi_{mn} = E_{mn}(k_{mn}\sigma)$. The E functions were defined by Sofrin and Tyler (ref. 7).

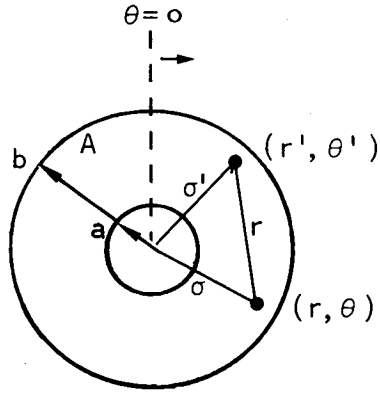
Upon performing the required manipulations, the modal termination impedance can be formulated as

$$Z_{mn} = -\frac{ik}{2\pi N_{mn}} \int_a^b \int_o^{2\pi} \int_a^b \int_o^{2\pi} e^{i[kr+m(\theta'-\theta)]} E_{mn}(k_{mn}\sigma) \times E_{mn}(k_{mn}\sigma')\frac{\sigma\sigma'}{r}\, d\sigma d\theta d\sigma' d\theta' \,. \qquad (44)$$

In this expression, N_{mn} is the normalizing constant defined by

$$N_{mn} = 2\pi \int_a^b E_{mn}^2(k_{mn}\sigma)\sigma\, d\sigma \,. \qquad (45)$$

The nomenclature for the annulus is defined in the sketch below.



It was possible to reduce the integral expression of equation (44) to a triple integral by changing variables such that

$$\theta - \theta' = \phi,$$

and performing the indicated integration with respect to θ'. The resulting integral, which was evaluated numerically is

$$Z_{mn} = -\frac{ik}{N_{mn}} \int_a^b \int_a^b \int_o^{2\pi} e^{i(kr-m\phi)} E_{mn}(k_{mn}\sigma) E_{mn}(k_{mn}\sigma')\frac{\sigma\sigma'}{r}\, d\sigma d\sigma' d\phi \qquad (46)$$

where $r = r(\sigma,\sigma',\phi)$.

Haddle's numerical results were compared with Morfey's (ref. 26) calculations for the radiation resistance for hub/tip ratios of 0.0, 0.3 and 0.5 and were found to be in agreement. Some of these results will be shown in a later section for the experimental configuration discussed in this report.

III. EXPERIMENTAL GOALS AND FACILITY DESCRIPTION AND OPERATION

As stated briefly in the introduction, and further indicated in the theoretical synopsis, the primary goal of this program was to provide experimental data in sufficient quantity and detail and with sufficient accuracy to verify the major predictions of the theory for sound propagation in a lined annular duct with mean flow. In the implementation of this goal, a facility built at the Lockheed-Georgia Company, with Lockheed fixed asset and IR and D funding, was used exclusively. The following subsections include a detailed explanation of the program goals and an explicit description of the facility and the techniques developed for operating the facility.

III.1. Major Objectives

There were several major areas for detailed research, as well as subsidiary research tasks necessary for calibration of the facility and complete definition of the test conditions, such as determination of wall impedance and radiation impedance. A basic aspect of the primary goal was to be able to measure the complete sound field, at a discrete frequency, within a finite-length acoustically lined annular duct sustaining a mean flow velocity, for comparison with theoretical predictions. However, the approach to implementation of this objective was considerably more basic than simply launching into a detailed measurement program.

It was shown in the previous section that solutions to the convected wave equation, which describes the duct sound field, are in the form of eigenvalues (the complex modal propagation constant which defines attenuation rate and phase speed) and eigenvectors (the complex mode shape or sound pressure distribution in the duct corresponding to a particular eigenvalue). It is a basic premise that these fundamental solutions or functions can be superimposed to represent any arbitrary pressure distribution at any point in the duct. Validation of these basic solutions provides proof sufficient for prediction of the complete sound field.

The experimental program was sub-divided into four major areas for research, with subsidiary research investigations into mode simulation, wall impedance measurements and radiation impedance measurements. The four basic investigations were measurement of sound pressure wave propagation

characteristics in (1) a rigid wall annular duct containing an ambient medium, (2) a rigid wall annular duct with an axial mean flow velocity, (3) an acoustically lined annular duct containing an ambient medium, and (4) an acoustically lined annular duct with an axial mean flow. A brief description of each of the listed investigations, as planned, follows,

III.1.1. Rigid wall duct without flow

This task, in addition to providing basic information for comparison with theory, was to serve as a calibration for the facility and as a test bed for developing operational and measurement techniques. First, methods for simulating (or exciting) angular standing modes (acoustically identical to spinning modes) were to be developed. Then a number of angular modes were to be excited individually and the mode shapes, phase speed, axial standing wave ratio and radiated field were to be determined. Excitation frequencies were to encompass the first three radial modes.

III.1.2. Rigid wall duct with mean flow velocity

The survey of mode characteristics initiated above was to continue in the presence of axial mean flow velocity. As designed, the facility could provide a sustained velocity of 200 fps with blow-down capability of 450 fps for short runs (on the order of one minute). The useful test range with flow was to be determined.

III.1.3. Finite wall impedance without mean flow

A minimum of two sets of acoustic duct liners were to be constructed for measurement of attenuation, phase speed and mode shape for a frequency range encompassing the first three radial modes. The tests were to include detailed studies of the characteristics of individual modes and of more complex sound pressure patterns at a discrete frequency.

III.1.4. Finite wall impedance with mean flow velocity

This series of tests was to be similar to the one above, but would include mean flow velocity up to the maximum possible as determined in the earlier series of hard wall tests.

III.2. Facility Description

The development of experimental techniques for evaluating acoustic liner design has followed a somewhat different course from that of the theoretical developments described in Section II. Experimental facilities have been primarily designed to give the average acoustic energy attenuation of Helmholtz type acoustic liner materials, developed over the past decade for

use in fan jet engine ducting. These facilities, termed flow duct facilities, have been built at the major airframe companies and extensive material evaluation tests have been conducted. Descriptions of some of these tests are given in NASA contractor summary reports (ref. 28, 29) and the proceedings of NASA Langley contractors conferences on Noise Alleviation of Large Subsonic Jet Aircraft (ref. 30, 31). Design considerations for the flow duct type of facility were discussed in detail by Melling and Doak (ref. 32). Melling also discusses the limitations and interpretations of test results from the double-reverberant chamber flow duct facilities.

The major points of concern in using data from this type of facility for detailed confirmation of the analytical predictions are:

- Sound pressure distribution at the duct entrance is uncontrolled but is generally diffuse.
- The sound pressure in the source chamber is broadband noise in most cases (narrow band or discrete frequency peaks may exist).
- The receiving chamber is reverberant.

As a result of these facility characteristics, it is very unlikely that many of the details of the theory can be verified using flow duct facility data.

As a result of the above considerations, a new type of facility was designed for verification of many of the theoretical trends and predictions. In particular, the facility was designed to overcome the above objections, thus permitting experimental determination of (1) the individual mode cut-on frequencies and shapes, (2) modal propagation constant, (3) duct termination impedance, and (4) the radiated sound field from the duct termination for single modes and complex pressure distributions. In addition, the facility was designed to permit evaluation of effects of mean flow and finite wall impedance on the above fundamental acoustic properties of the duct.

The facility to be described was designed and constructed at the Lockheed-Georgia Company's Research Laboratory in late 1969 and early 1970. Initial testing techniques were developed under Lockheed IR and D funding during 1970.

A basic plan view of the complete facility is shown in figure 1 and a side elevation of the flow duct is shown in figure 2. Figure 3 contains a sketch of the complete facility and a photograph of the source section. Basically, the facility consists of (with the numbered items corresponding to the circled numbers in figures 1 and 2): (1) a high-pressure air supply, (2) a control valve, (3) a wide-angle expansion, (4) a muffler section, (5) another wide-angle expansion, (6) an acoustically lined plenum, (7) a flow-straightening and turbulence-reducing honeycomb section, (8) a contraction, (9) a final muffler, (10) the acoustic source section, (11) the test section, (12) an anechoic room, and (13) an exhaust and muffler. A brief description of each of these components is given below.

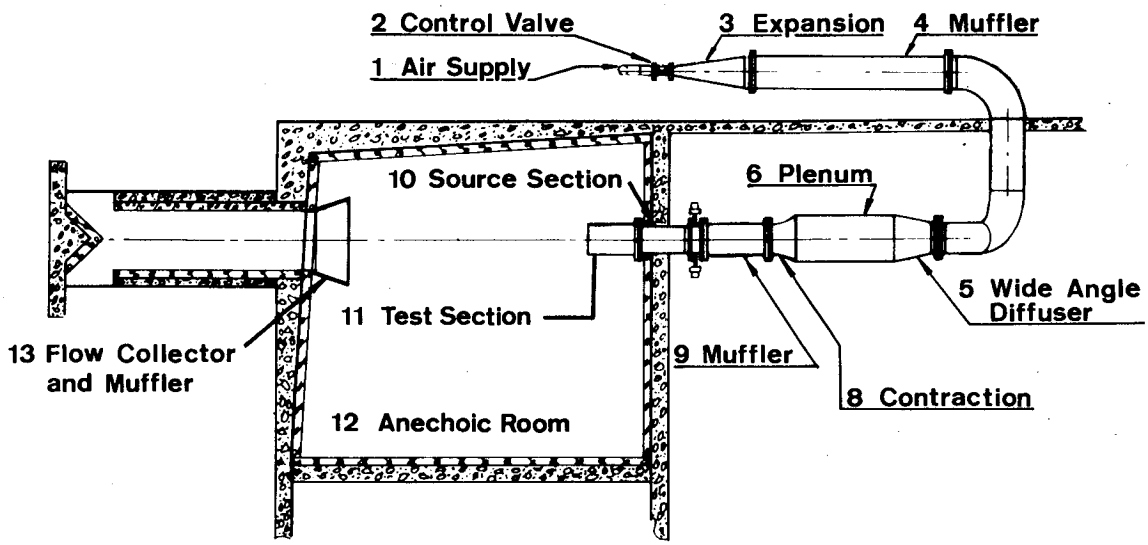


Figure 1. Plan View of Engine Noise Attenuation Analysis Facility

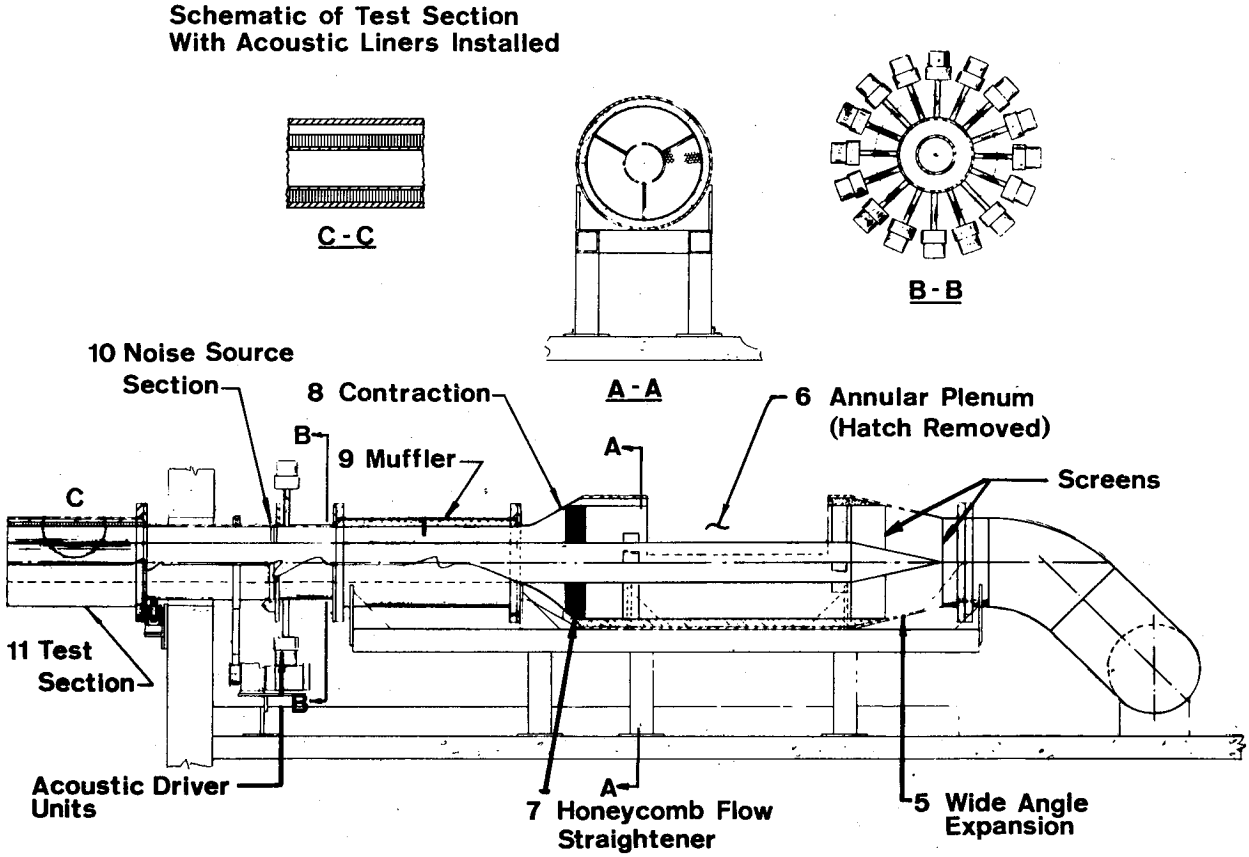


Figure 2. Side Elevation and Details of Source and Test Section of Engine Noise Attenuation Analysis Facility

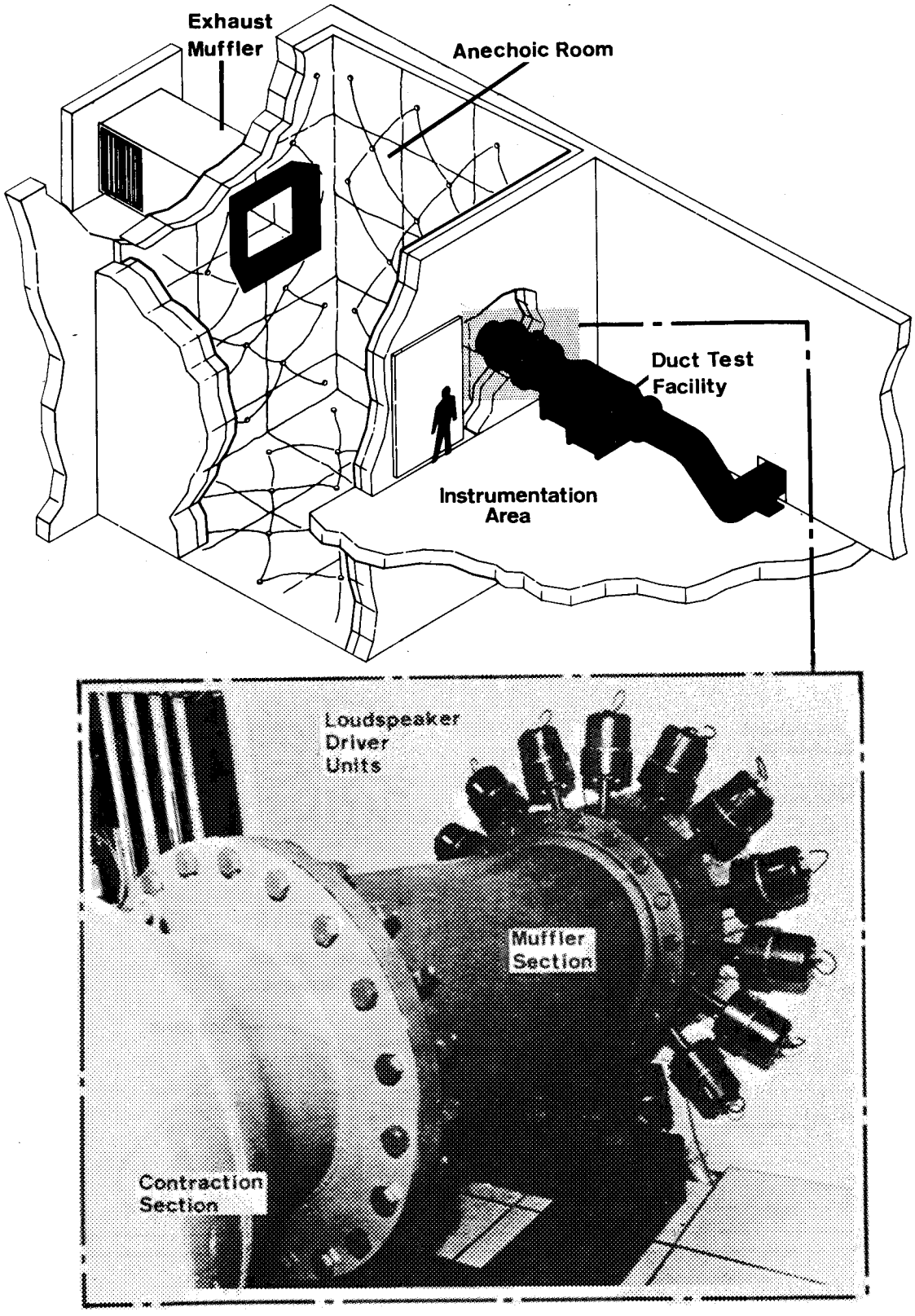


Figure 3. Engine Noise Attenuation Analysis Facility

(1) The air supply system (which is also used by the Lockheed wind tunnels) continuously delivers 20 lb/sec. of cleaned, dry air compressed to 300 psi. If required, a low-pressure pump can be added to the system for delivery of 30 lb/sec. at 100 psi. The air system also has blow-down capability of 12,000 cubic feet of air at 300 lb/in^2.

(2) The valve is a 6-inch throttling ball valve with a pressure servo-controller. It is designed to be most effective on pressure control for speed ranges of 50 to 450 ft/sec in the test section.

(3) The wide-angle conical expansion connects the 6-inch valve to a 20-inch muffler section.

(4) The muffler section is 13 feet long and is lined with 2 inches of polyurethane foam, retained with a perforated metal sheet. The muffler also contains a full-length, similarly treated, cruciform section.

(5) The wide-angle expansion section has strategically placed screens to effect a smooth flow transition from the 20-inch supply pipe to the 36-inch plenum.

(6) The plenum is made from a 36-inch pipe and is lined with polyurethane foam retained with perforated metal. The plenum contains a 10-3/4 inch pipe which forms an annular flow region.

(7) The delivery end of the plenum contains an 8-inch long section of a 1/8-inch cell honeycomb for reducing the turbulence level in the supply air.

(8) The contraction section connects the 36-inch plenum to a 19-inch inner diameter muffler section.

(9) The muffler section is 4 feet long with a lining similar to that in the other acoustically lined sections.

(10) The noise source section also shown in figure 3 is equipped with 16 loudspeaker driver units spaced at 22.5° intervals and connected to the outer wall of the source section. The ends of the driver tubes, at the juncture with the source section, are covered with 20-Rayl felted metal to minimize acoustic flow resonance and to prevent turbulence generation. The driver units are individually controlled, both with regard to amplitude and phase, and the useful range extends from 300 to 6000 Hz. Electrical power input to the driver units is up to 100 watts peak. The source section has a joint, pressure-sealed with Teflon, immediately downstream of the driver tubes. The downstream section is rotatable with respect to the driver units, permitting acoustic pressure or velocity to be mapped azimuthally, using transducers fixed in the downstream source section or in the test section, which is fixed to the rotatable part

of the source section. Radial traversing of transducers is also achieved. Two configurations of the microphone traversing units are shown in figures 4 and 5.

Figure 4 is a photograph of the basic radial traversing unit which was designed for automatic traversing and recording of microphones, hot-wire anemometer probes, pitot tubes and thermocouples. It contains a variable speed D.C. motor which drives the probe through a belt and a linear wire-wound potentiometer for generation of a D.C. voltage proportional to frequency. Figure 5 is a modification of the basic traversing mechanism for obtaining SPL measurements in the region upstream of the lined test section. It utilized two of the traversing mechanisms, one mounted at the duct termination and another mounted in the test section. A one-half inch microphone with a long probe tube attached was fixed to the ends of the radial traversing mechanisms. Axial locations were obtained by way of manual positioning of this device. An automatic axial traversing microphone would have been desirable for some of the tests, however, construction and installation was not practical considering cost and schedule commitments.

(11) The test section consists of a basic steel shell three feet in length with a 23 inch inner diameter. The center pipe has a 10-3/4 inch outer diameter. Liner materials are placed on the inner and outer walls of this section as desired. In all the tests reported herein, the i.d. of the outer liner remained at 19 inches (this provides for application of material up to 2 inches deep on the walls). The o.d. of the inner liner was 10-3/4 inches for all tests. Provision was made for inserting transducers with radial drive capability, as discussed, on a 1-inch axial spacing. Azimuthal mapping is accomplished by rotating the test section with respect to the driver units.

(12) The anechoic room illustrated in figure 3, was converted from a reverberant room by adding 6 inches of polyurethane foam to all interior surfaces. The room is anechoic for frequencies above 500 Hz.

(13) An exhaust port is provided in the wall of the anechoic room as shown in the photograph of figures 6 and 7. A 1/10 scale flow model of the room was constructed and tested to determine an optimum exhaust port configuration for minimizing the flow circulation in the anechoic room. It was finally determined that the collector shown, with a 20° angle from a normal to the wall, resulted in minimum circulation within the major acoustic measurement volume in the room.

Before the tests were completed, five sets of acoustic liners were tested. Two of these liner sets are shown in figures 8-11. The liner set illustrated in figures 8 and 9 was constructed of a felted metal acoustic material over a 1/2 inch plastic honeycomb with 3/8 inch cells. Two sets of inner and outer

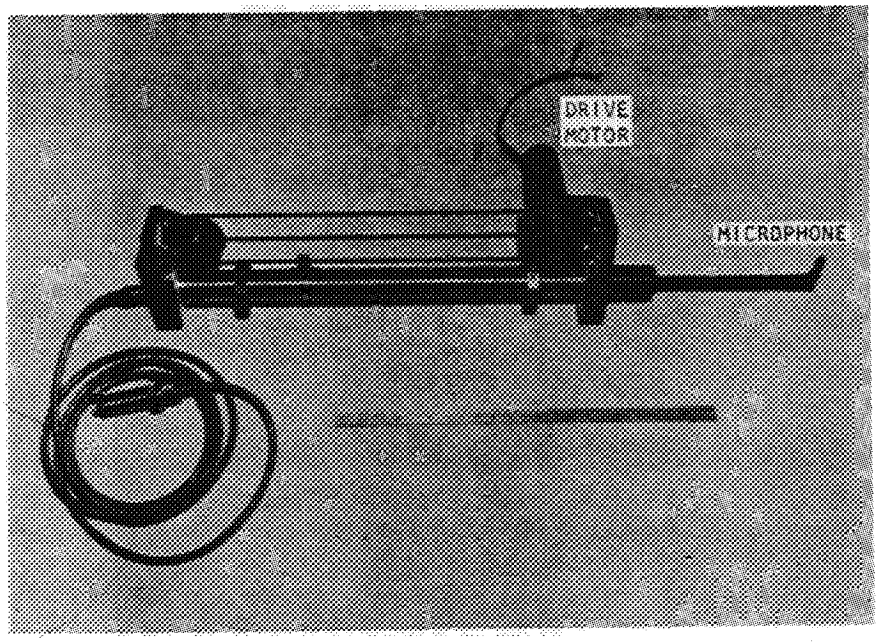


Figure 4. Microphone Drive Mechanism

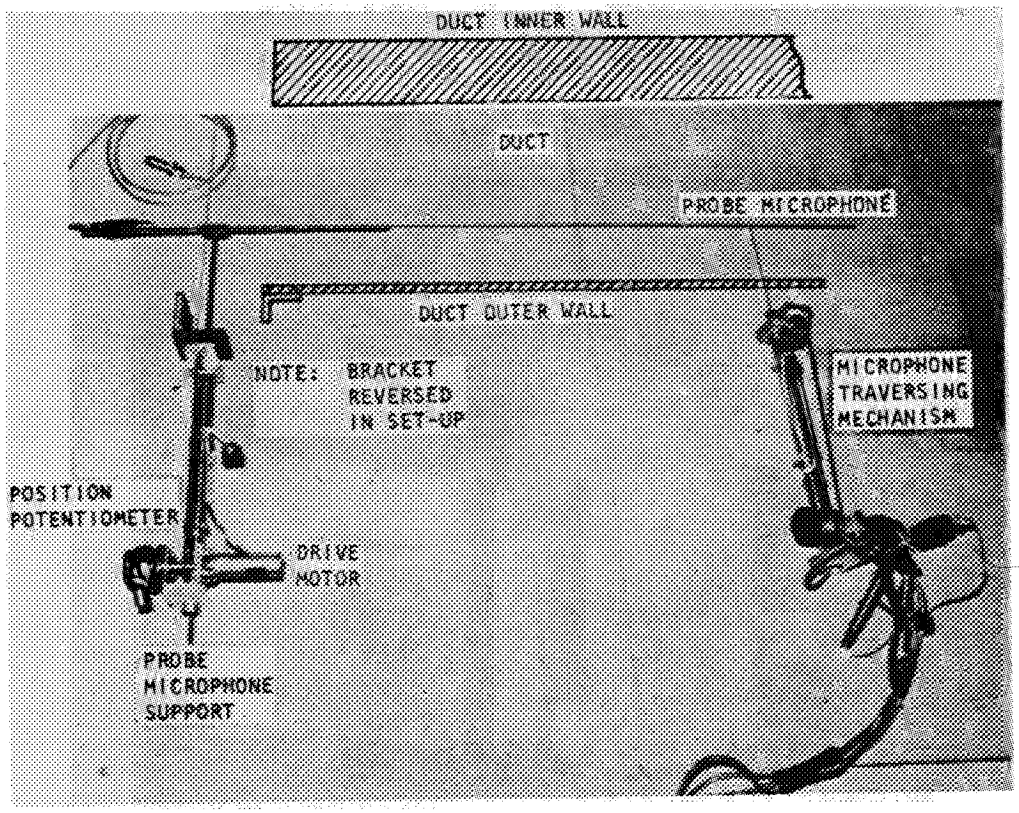


Figure 5. Axial Probe Microphone Installation

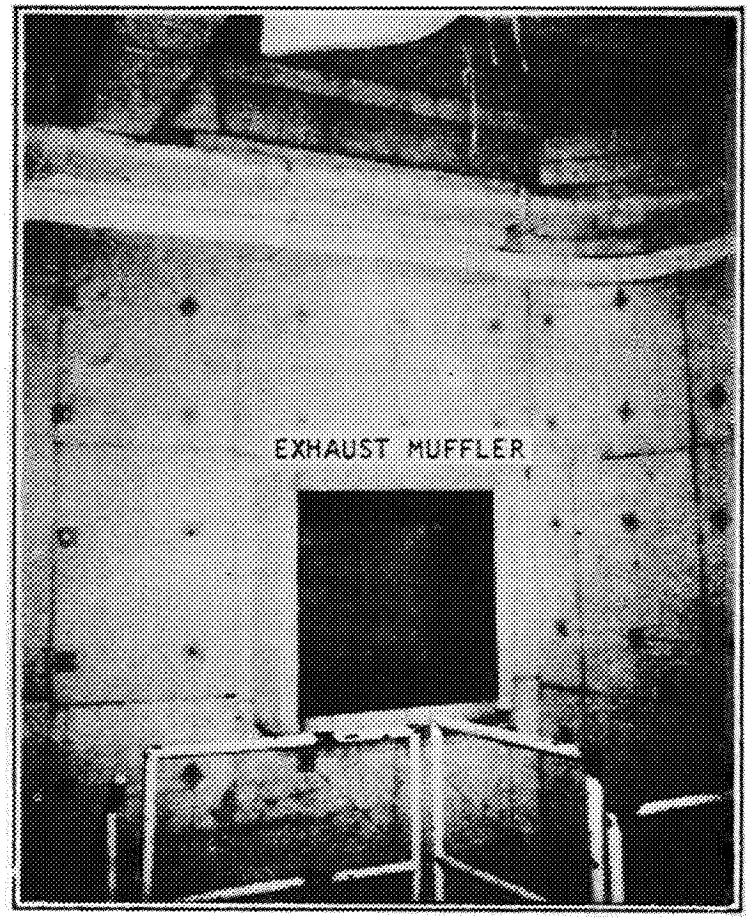


Figure 6. Anechoic Room Interior

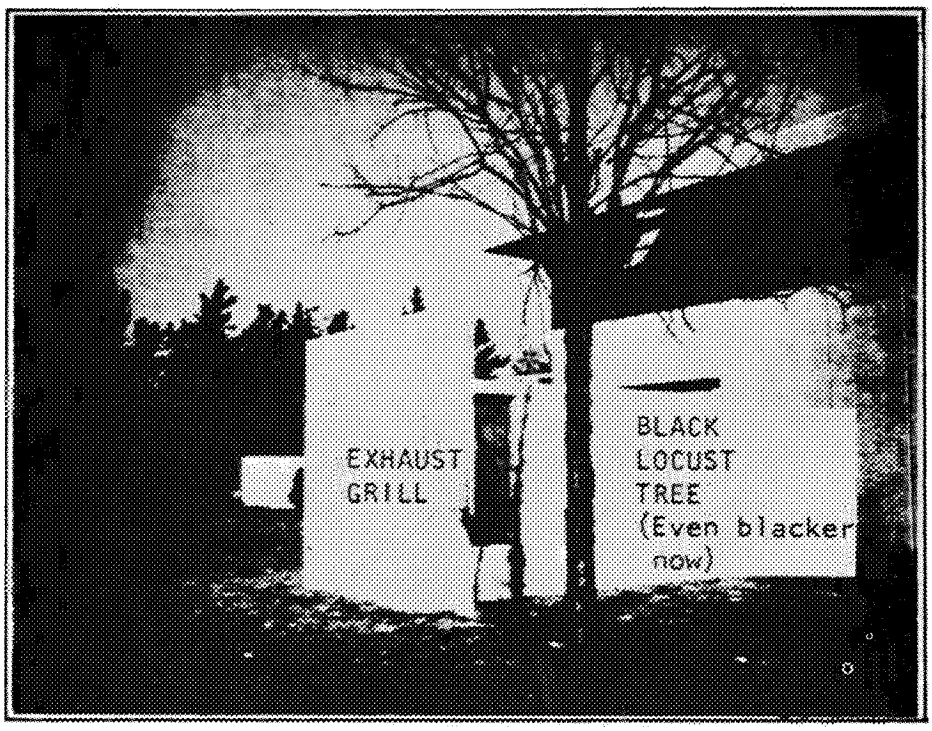


Figure 7. Exterior View of Exhaust Muffler

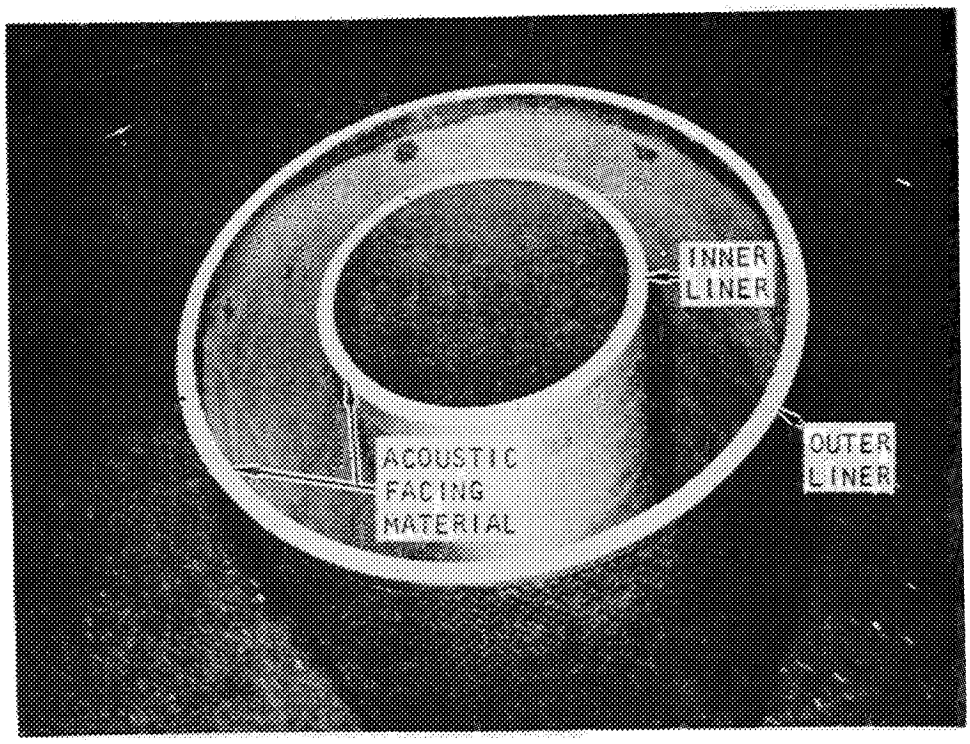


Figure 8. 20 Rayl Felted Metal Liners

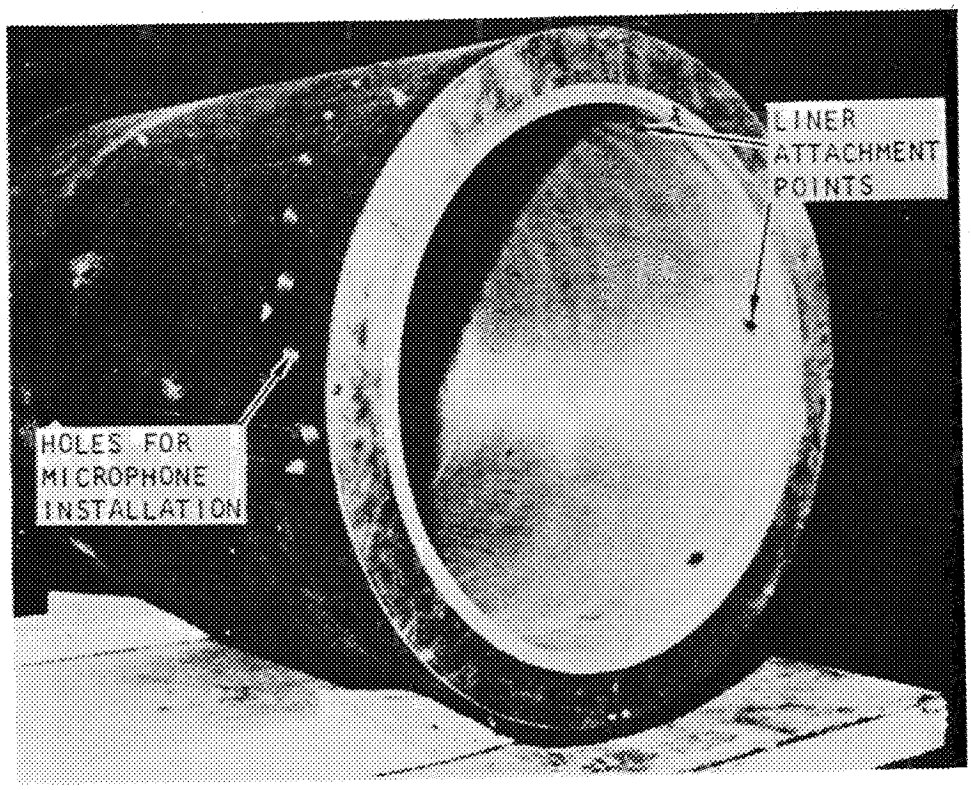


Figure 9. 20 Rayl Outer Liner Installed in Test Duct

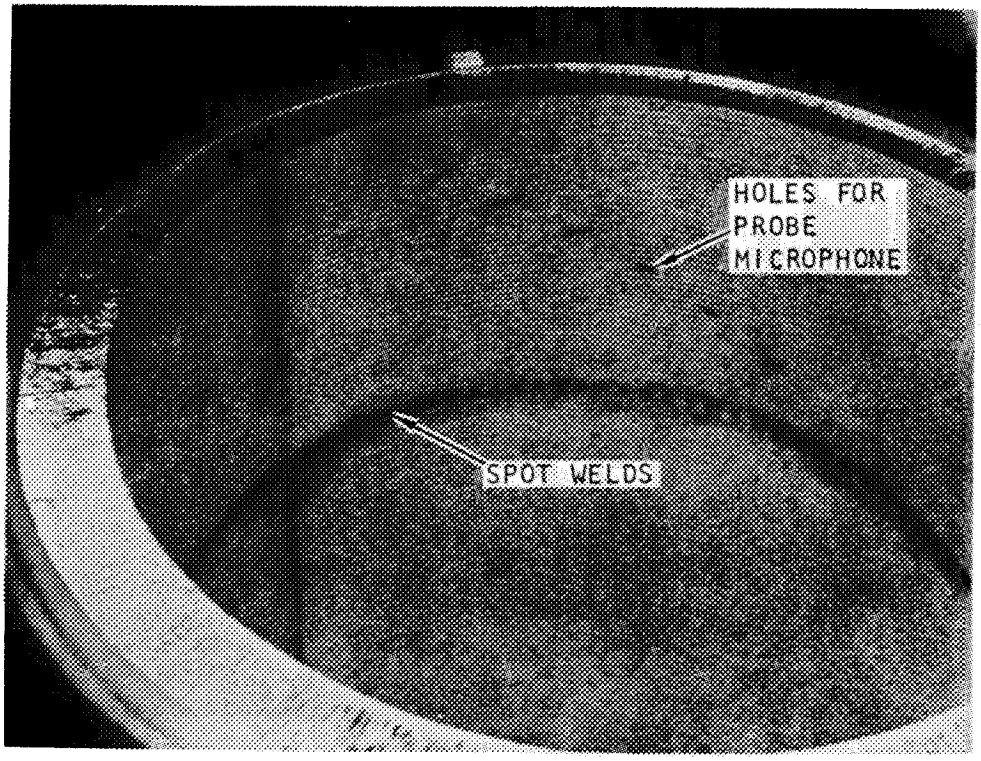


Figure 10. Welded Fibrous Metal Outer Liner

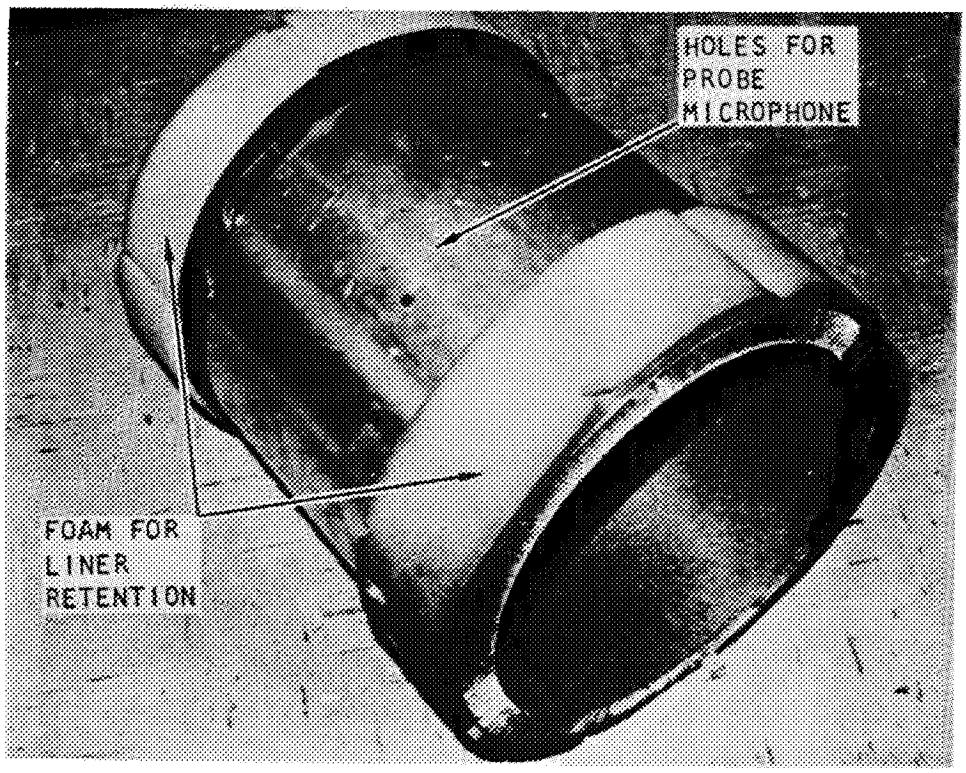


Figure 11. Welded Fibrous Metal Outer Liner Illustrating Holes for Probe Microphone

liners of this design were constructed, utilizing a nominal 20 Rayl acoustic material on one set and a nominal 40 Rayl acoustic material on the other. The liner illustrated in figures 10 and 11 consisted of a single unit for the outer wall of the test section and used a welded fibrous type acoustic material over a 1-1/2 inch honeycomb with a 1/8 inch diameter aluminum cellular core.

III.3. Operational Details

III.3.1. Instrumentation and Controls

The controls are divided into three sections, viz, air supply, microphone position, and acoustic excitation and are illustrated with a block diagram in Figure 12.

The air supply is automatically controlled by a 6-inch throttling ball valve and servo controller, with the velocity head monitored by a pitot probe upstream from the plenum, located in an area of low turbulence.

The duct probe microphone position is controlled angularly with respect to the drivers by a motor which rotates the duct test section, the angle being monitored by a cable deflection box. This signal is input to the X-Y plotter and computer interface via suitable signal conditioners. The radial probe is motor driven and its position is monitored by an interconnected potentiometer, which is also connected to the plotter and computer interface. The boom microphone's angular travel is also detected by a deflection box. All microphone position controllers have limit switches to eliminate the possibility of excess travel and consequent equipment damage.

The frequency control circuit for acoustic excitation utilizes a voltage controlled oscillator coupled to an analog computer which provides for automatic frequency compensation for temperature changes sensed by a thermocouple in the duct. The frequency controller has been designed to hold wavenumber, $k = 2\pi f/c$, constant, where c is the speed of sound in the duct and is, therefore, proportional to square root of duct temperature.

The data acquisition system has two functions; the first is to provide a visual instantaneous record on an X-Y plotter; the second is to store data in digitized form on the disc storage of a UNIVAC 418 computer. This data can then be manipulated as required, after being transferred to magnetic digital tape. The computer storage is controlled by a teletype and MAC 16 computer in the laboratory. A block diagram of the complete recording systems can be seen in figure 13.

The probe microphone in the duct (set normal to the flow) is a standard 2mm diameter B&K probe (suitably damped and modified to have sensing ports in the side instead of the end, as shown in figure 64), coupled to a standard 1/2" B&K microphone. The reference microphone is a 1/4 inch diameter B&K microphone mounted in the rotating section at an axial position such that it is projecting upstream and in the plane of the drivers. This microphone is used to set up the individual drivers for amplitude and phase such that their

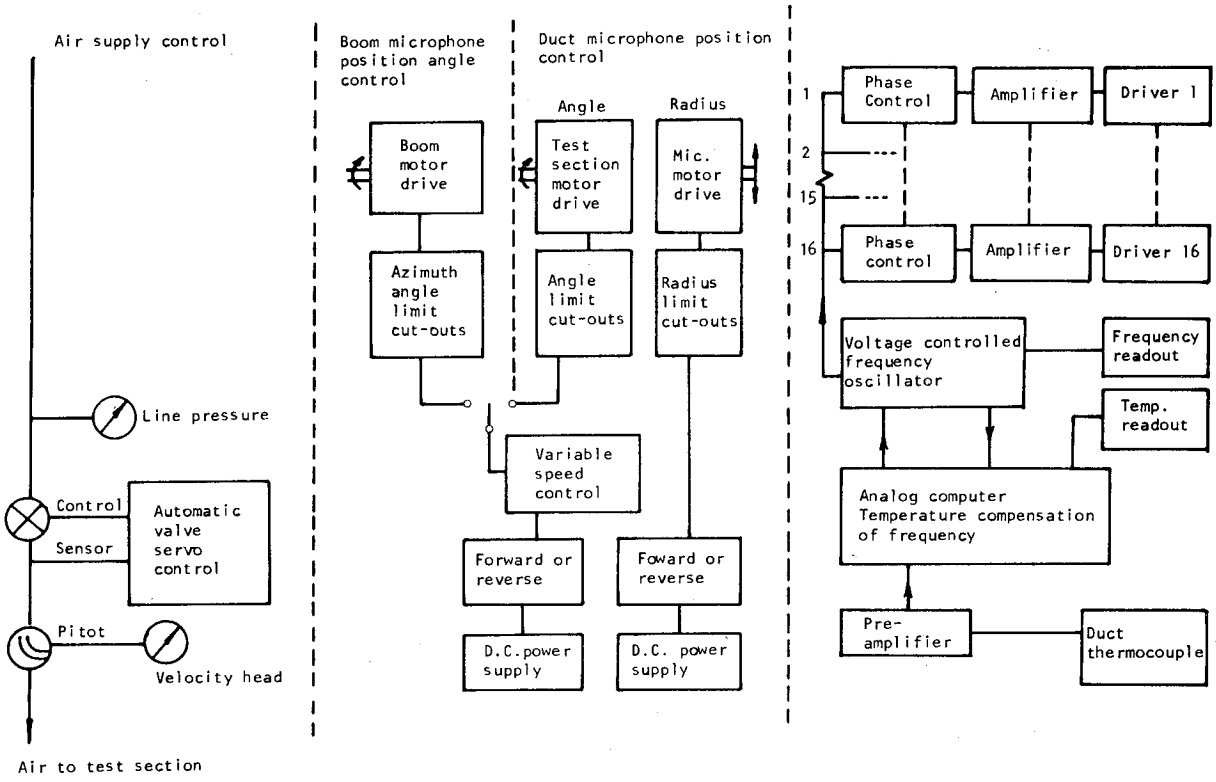


Figure 12. System Controls for Engine Noise Attenuation Analysis Facility

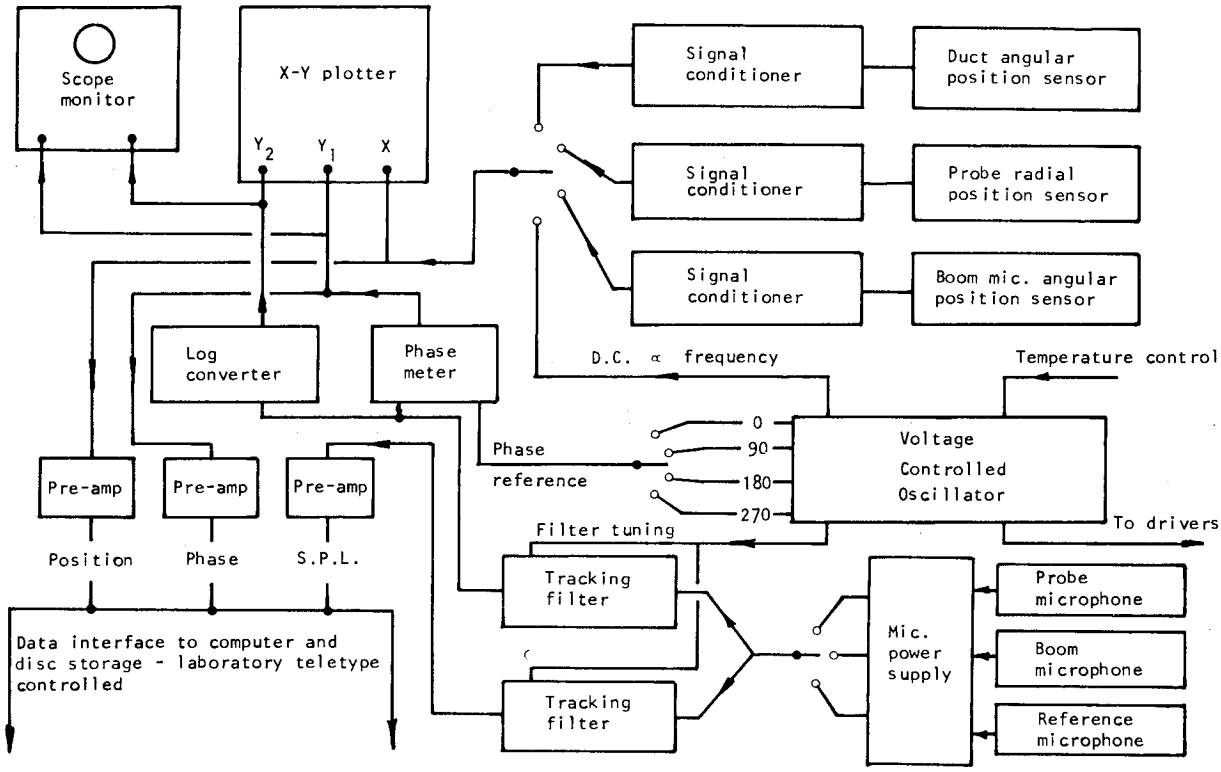


Figure 13. Schematic of Data Acquisition System

combination will produce the desired circumferential standing mode (as will be described later). The boom microphone is a 1/2 inch B&K with a 2mm diameter "static pressure" probe attached. This type of probe minimizes the pressure fluctuations due to probe aerodynamic interactions. All the microphone outputs are filtered through a 2 Hz tracking filter, which eliminates the broadband components of flow turbulence. The resultant signal to noise ratio of the excitation peaks is better than 60 dB for zero flow tests, reducing the order of 10 to 20 dB at 200 fps mean flow velocity. However, unless one reverted to signal averaging or signal recovery techniques, the random fluctuations introduced by the flow noise made exact comparisons with theory difficult. Thus, all acoustic comparison tests were restricted to 150 fps flow velocity.

III.3.2. Facility dimensions and characteristics

The test section geometry and dimensions are illustrated in figure 14 which also includes pertinent dimensions for the various acoustic liners which were tested. The test section is three feet long, the center pipe or liner is 10-3/4 inches in diameter and the outer rigid pipe or liner has a 19 inch inner diameter. This results in an annulus of 4-1/8 inches width and a hub-tip ratio of 0.566.

Air flow velocity can be maintained at 200 fps but all tests reported in this study were limited to 150 fps. Circumferential velocity profiles measured in the test section are shown in figure 15. This shows approximately 10% variations in mean flow velocity due to non-uniformities in the surface of the final muffler stage (figure 2, muffler (9)).

The radial velocity profiles shown in figure 16 were reconstructed from the velocity measurements as described in the following discussion.

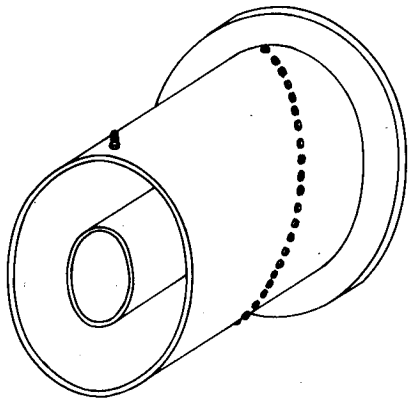
Measurements of velocity cannot be made very close to the duct walls, primarily because probe errors become large in the high velocity gradient region. As a result, useful measurements usually cease some distance from the surface and a layer of large shear remains which cannot be easily explored experimentally.

In order to provide reliable estimates of the velocity gradients in the wall layer, calculations were made using the universal law of the wall (ref. 38) for two-dimensional flow.

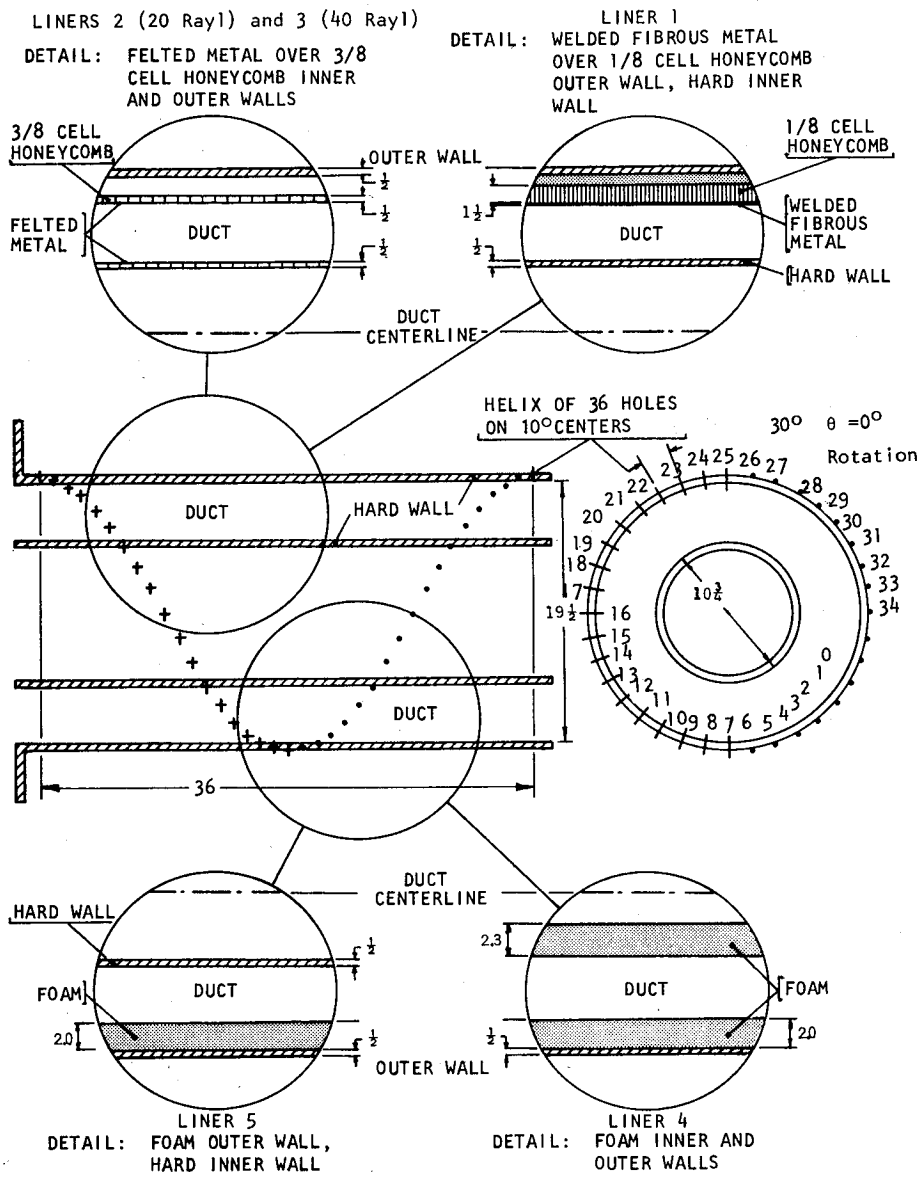
The wall layer is idealized into a viscous sublayer, in which viscosity is assumed to be the only source of shear stresses, and a fully-turbulent layer in which viscosity is neglected; no blending region is admitted between them.

In the viscous sublayer, the velocity, u, is proportional to the distance, y, from the surface:

$$u^+ = y^+ , \tag{47}$$



(a) Sketch of Annular Test Section



(b) Details of Liner Installations

Figure 14. Annular Flow Duct Test Section

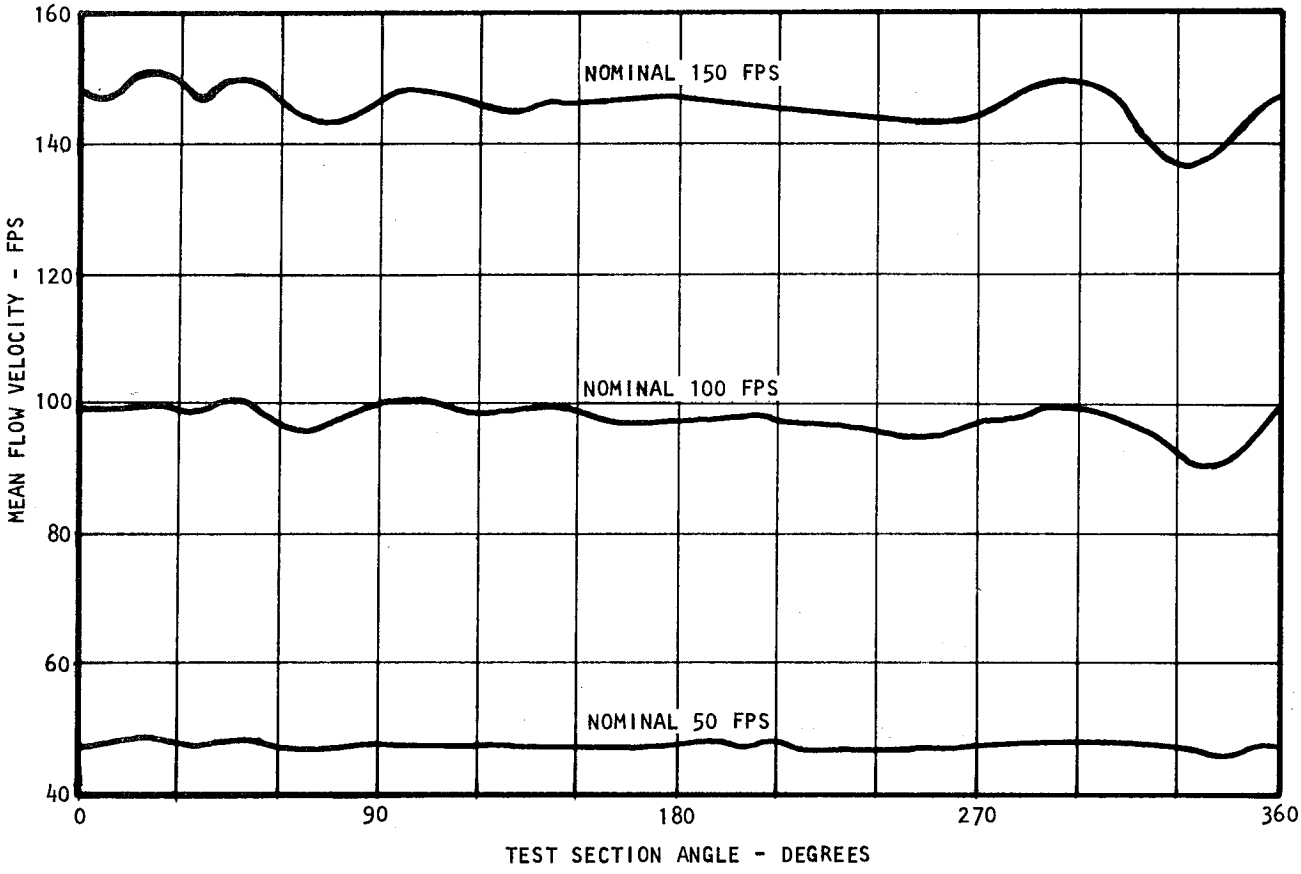
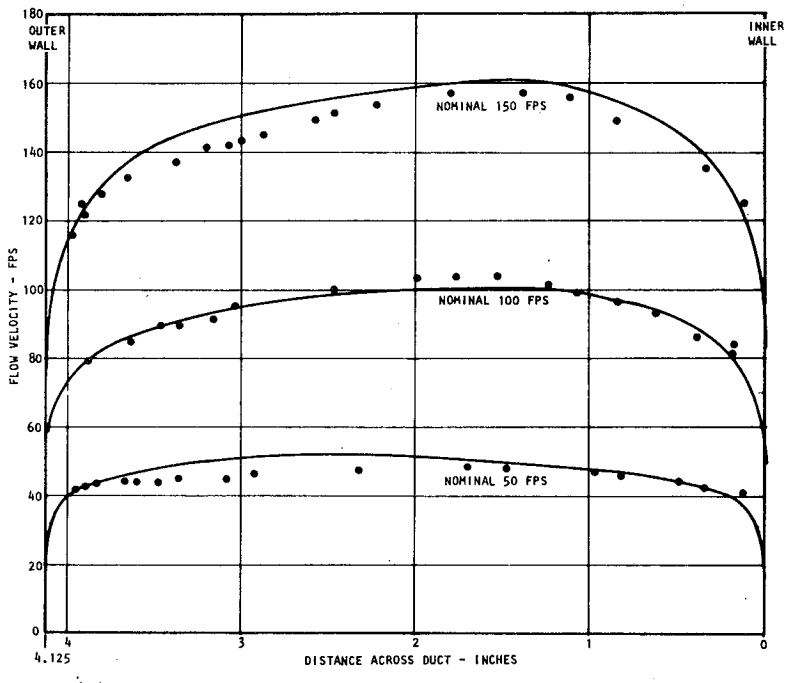
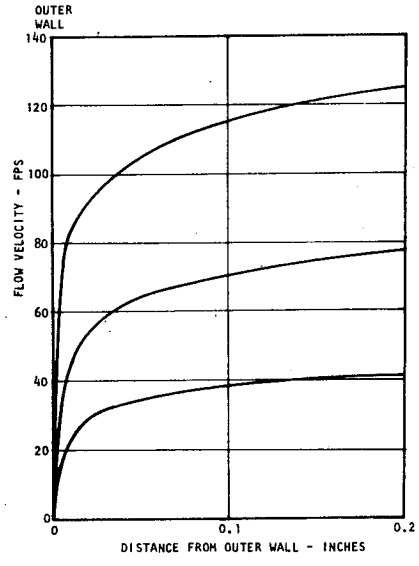


Figure 15. Variation of Mean Flow Velocity with Test Section Angle



(a) Experimental and Empirical Velocity Profiles



(b) Details of Empirical Velocity Profile in Wall Layer

Figure 16. Radial Velocity Profiles

where,

$$u^+ = u/\left(\frac{\tau_w}{\rho}\right)^{\frac{1}{2}}, \tag{48}$$

$$y^+ = \frac{y}{\nu}\left(\frac{\tau_w}{\rho}\right)^{\frac{1}{2}}, \tag{49}$$

and where τ_w is the wall shear stress, ρ the density of the fluid, and ν its kinematic viscosity.

In the fully turbulent region, the velocity varies logarithmically with y:

$$u^+ = \frac{1}{\kappa}\ (\ln y^+ + C), \tag{50}$$

where κ is von Karman's constant, equal to about 0.418, and C is a second empirical constant, equal to about 2.31 for smooth walls (ref. 34).

The "edge" of the viscous sublayer is given by the intersection of equations 47 and 50, and corresponds to a value of y^+, over an appreciable fraction (.1 or .2, perhaps) of the duct width. Its outer boundary of validity is ill-defined, but it certainly extends out into the region where reliable probe measurements can be made.

Both equations 47 and 50 contain τ_w as a parameter, and its value is unknown at the outset. The procedure adopted for finding it was based on the assumption that several reliable data points lay in the region of validity of equation 50. It was then only necessary to choose a value of τ_w which ensured that equation 50 merged smoothly into the measured velocity profile. This method is equivalent to the use of a Clauses plot for determining wall shear stress (ref. 35). The values of τ_w obtained were of the right order of magnitude for a duct of the appropriate Reynolds number.

Once τ_w is known, the complete velocity profile, in the region of interest, can be calculated. The velocity gradient can then be obtained by differentiation. In the viscous sublayer:

$$\frac{\partial u}{\partial y} = \frac{\tau_w}{\rho \upsilon}, \tag{50}$$

and in the logarithmic region:

$$\frac{\partial u}{\partial y} = \frac{1}{\kappa y}\left(\frac{\tau_w}{\rho}\right)^{\frac{1}{2}} \tag{51}$$

The velocity gradients calculated by this procedure are shown in figure 17.

III.3.3. Sound pressure spatial control: preliminary study

A primary requirement for the facility was the ability to set up a particular spatial pattern of sound pressure in the operating frequency range to simulate the sound pressure distribution in an angular mode. In the design study of the facility, it was decided that radial control of sound pressure in the source section would be impractical to achieve, thus the design focused on angular control in the source section.

A detailed study on source characteristics was conducted. Two source distribution schemes were considered in detail. One was a crude method for exciting one higher order radial mode as illustrated in figure 18a. This scheme would result in maximum sound pressure level in the test section, but would pose difficult problems in spatial control. However, construction difficulty and lack of confidence in the final control over the sound pressure eliminated this technique. It was finally determined that for the purpose of this facility the scheme shown in figure 18b would be most practical, both from a construction and a control standpoint. This scheme assumed 16 loudspeaker driver units with independent level and phase controls for each unit.

A simplified example, as derived by Doak (ref. 36) during a preliminary study of the facility design, can be used to illustrate the expected response in a hard wall duct from a phased array of transducers mounted in the duct walls, using rectangular geometry as being representative of a thin annulus. The purpose of the example is to show the expected enhancement of one mode relative to all other cut-on modes at a particular frequency ω.

For simplicity it is assumed that all transducers have the same dimensions (square, of edge length d), all have their centers on the intersection of the x = o and z = o planes, and all are driven at the single frequency, ω.

Let V_ℓ be the complex velocity amplitude of the ℓ^{th} transducer (see figure 19), with its center at $(o,y_\ell,0)$. Then the pressure field in the region $z>d/2$ is given by the following equation, as derived by Doak.

$$p(x,y,z,t) = \sum_{m,n=o}^{N} \rho_o \left| C_{mn} \right| e^{i\omega t} (2-\delta_{om}) (2-\delta_{on})$$

$$\times \cos \frac{m\pi x}{a} \cos \frac{n\pi y}{b} \sum_{\ell} V_\ell \cos(n\pi y_\ell / b)$$

$$\times \frac{A_p}{A} \frac{\sin(n\pi d/2b)}{n\pi d/2b} \frac{\sin(\omega d/2 \left| C_{mn} \right|)^{\frac{1}{2}}}{(\omega d/2 \left| C_{mn} \right|)} e^{-i\omega z/\left| C_{mn} \right|}$$

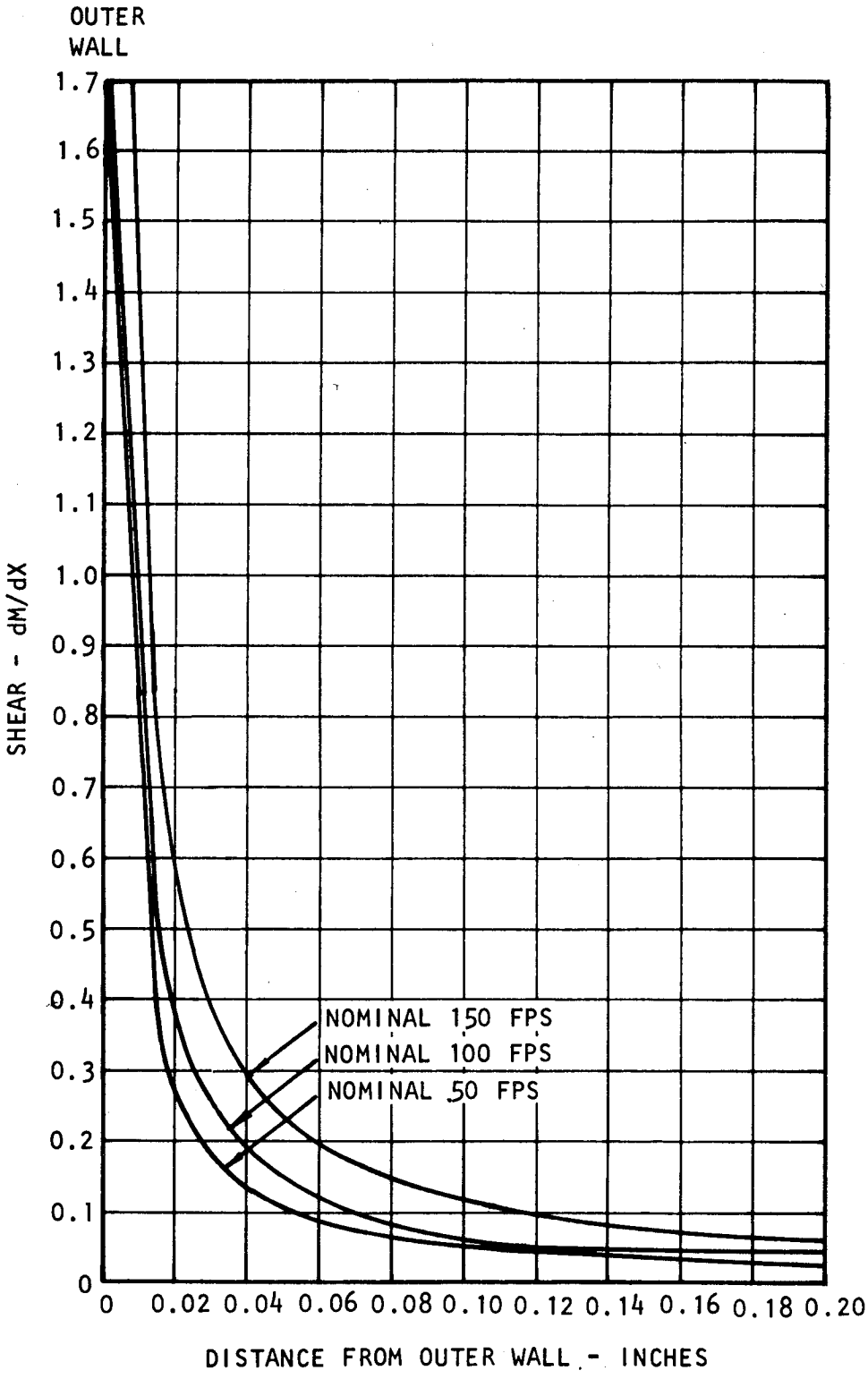
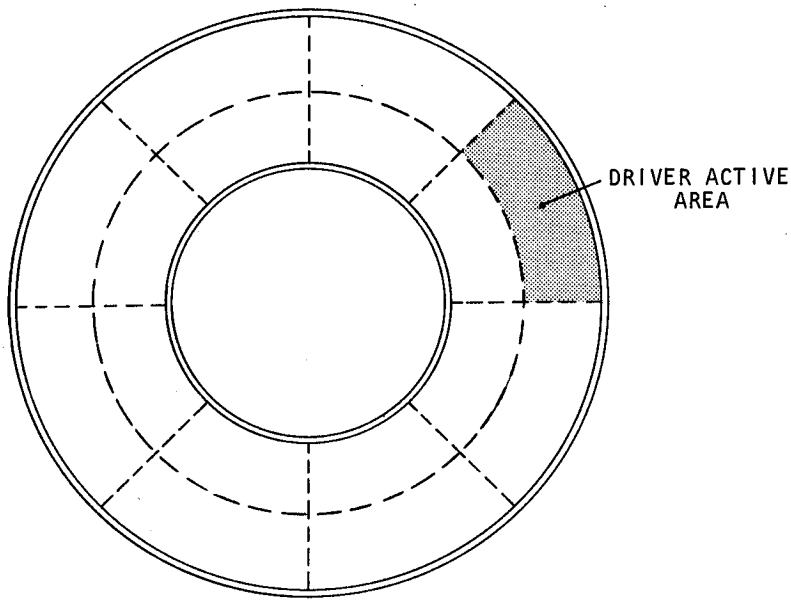
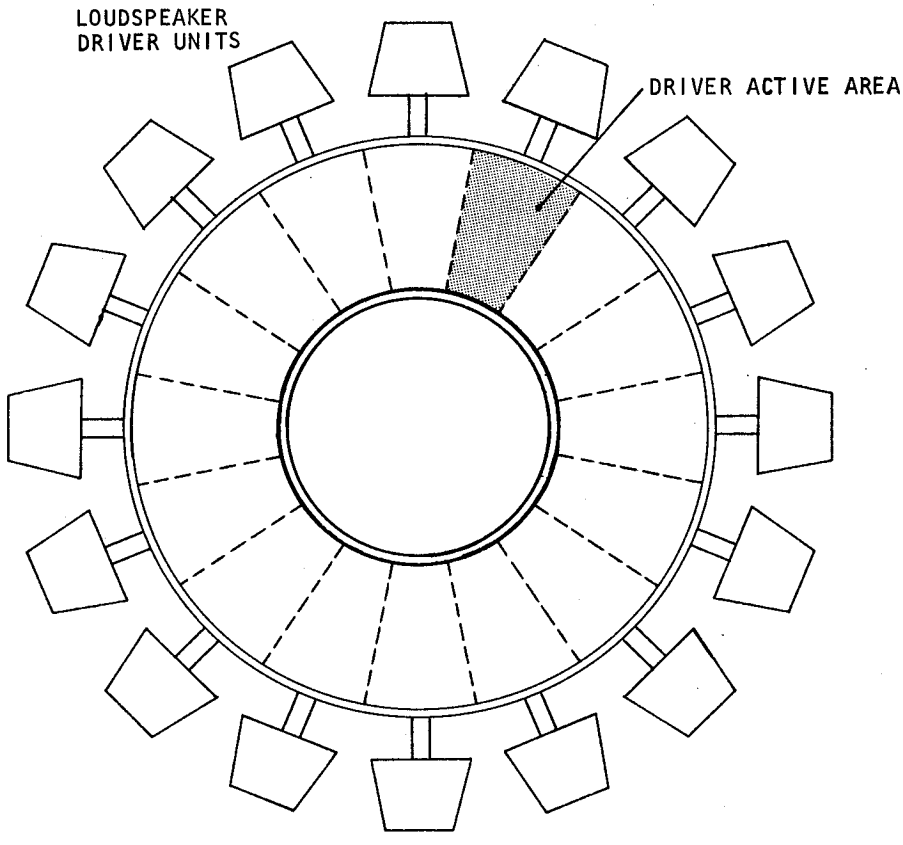


Figure 17. Empirical Shear Profiles



(a) driver axis parallel to duct axis



(b) driver axis normal to duct axis

Figure 18. Source Location Configurations Considered in Preliminary Design

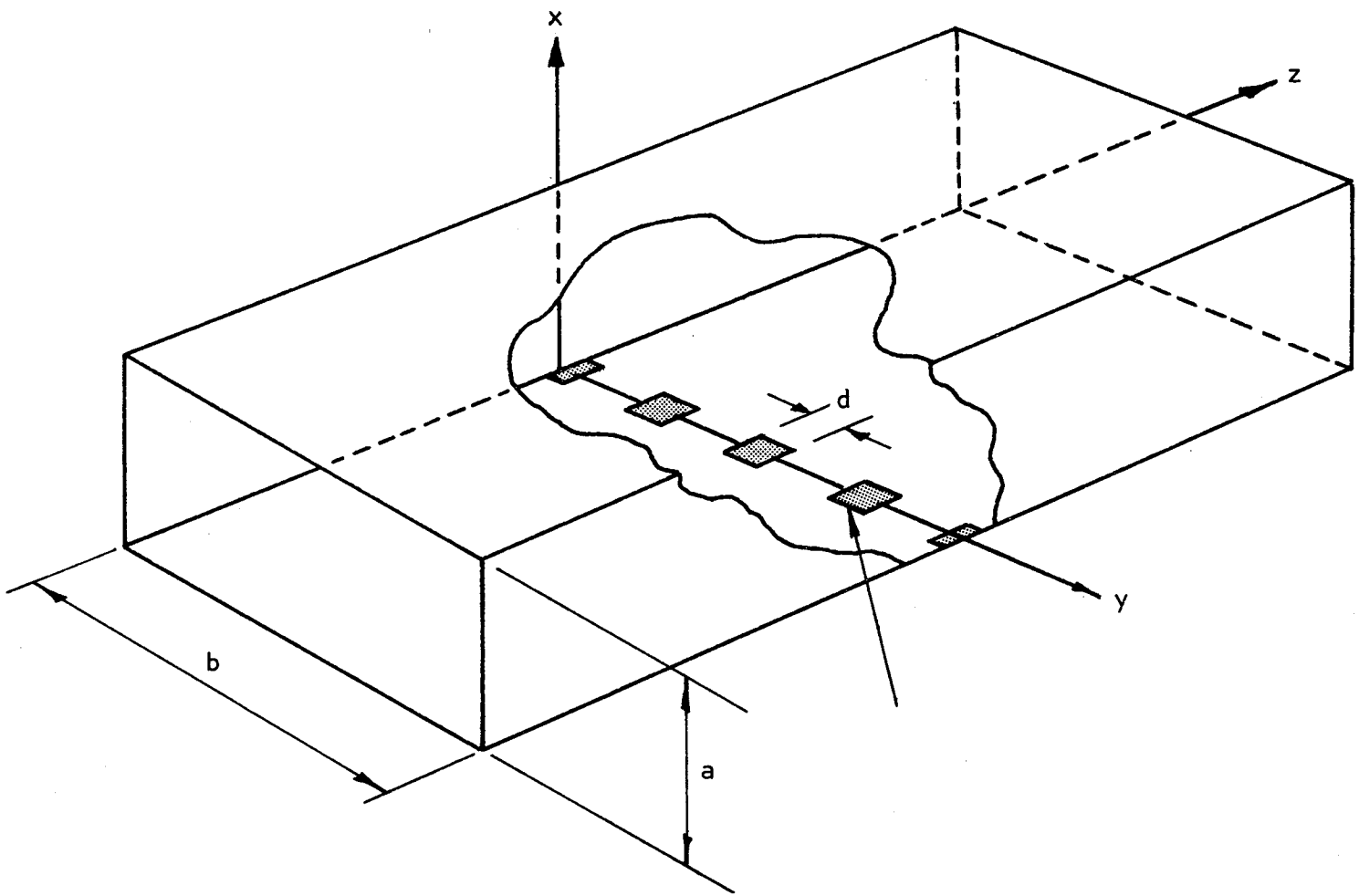


Figure 19. Rectangular Test Duct Illustrating Wall Placement of Source Transducers

$$+ i \sum_{m,n=N}^{\infty} \rho_o \left|C_{mn}\right| e^{i\omega t} (2-\delta_{om})(2-\delta_{on}) \cos\frac{m\pi x}{a}$$

$$\times \cos\frac{n\pi y}{b} \sum_{\ell} V_{\ell} \cos(n\pi y_{\ell}/b) \frac{A_p}{A} \frac{\sin(n\pi d/2b)}{(n\pi d/2b)}$$

$$\times \frac{1}{2} \frac{e^{-\left|\frac{\omega}{C_{mn}}\right|(z-d/2)} - e^{-\left|\frac{\omega}{C_{mn}}\right|(z+d/2)}}{(\omega d/2\left|C_{mn}\right|)} . \qquad (52)$$

Suppose, for example, that it was desired to enhance the response in the (0,4) mode. One might do this by using five (but in effect, only four) transducers, placed at (0,0,0), (0,b/4,0), (0,b/2,0), (0,3b/4,0), and (0,b,0), as shown in figure 19, with respective amplitudes ($v_o/2$, $-V_o$, V_o, $-V_o$&$V_o/2$). Strictly speaking, of course, a finite-sized transducer cannot have its center at (0,0,0), etc., in a rectangular duct. However, if the rectangular duct is considered as an analog of an annular duct, this difficulty does not arise. In other words, the idealized example being considered here is really that of a duct which is infinite in the y-direction, excited by an infinite number of transducers with centers at (0, $\pm\ell b/4$,0).

For this array of transducers $\sum_{\ell} V_{\ell} \cos(n\pi y_{\ell}/b)$ is zero for the modes (0,0), (0,1), (0,2) and (0,3), but for the mode (0,4), it is $4V_o$. The sum is similarly zero for all modes (m,n) for which n is less than 4. Hence only those modes (m,n) for which n is equal to or greater than four can be excited by this transducer array, whatever the frequency.

In general, for this array,

$$\sum_{\ell} V_{\ell} \cos\left(\frac{n\pi y_{\ell}}{b}\right) = Vo\left[\frac{1}{2}\cos(n\pi.0) - \cos\left(\frac{n\pi}{4}\right) + \cos\left(\frac{n\pi}{2}\right)\right.$$

$$\left. -\cos\left(\frac{3n\pi}{4}\right) + \frac{1}{2}\cos(n\pi)\right],$$

$$= Vo\left[\left(\frac{1}{2} - \cos\left(\frac{n\pi}{4}\right)\right)\left((1 + \cos(n\pi)\right) + \cos\left(\frac{n\pi}{2}\right)\right]. \qquad (53)$$

For all odd values of n the sum is zero. For even values of n (n = 2m), the sum can be written as

$$\sum_{\ell} V_{\ell} \cos\left(\frac{n\pi y_{\ell}}{b}\right) = Vo\left[\left(1 + \cos(m\pi)\right) - 2\cos\left(\frac{m\pi}{2}\right)\right]. \qquad (54)$$

If m is odd the sum is again zero. For m even, m=2k, the sum becomes

$$\sum_{\ell} V_{\ell} \cos\left(\frac{n\pi y_{\ell}}{b}\right) = 2\,Vo\left(1 - \cos(k\pi)\right) . \qquad (55)$$

This is zero for k=0, 2, 4, 6..., and equal to $4V_o$ when k=1, 3, 5....

Therefore, for this array of transducers, and independently of frequency, the amplitude of excitation of all (m,n) modes is zero except for the modes (m, 4k) where k=1, 3, 5, ... For these modes the array excitation factor is

$$\sum_{\ell} V_{\ell} \cos\left(\frac{n\pi y_{\ell}}{b}\right) = 4\,Vo. \qquad (56)$$

The implication of this result is clearly, that as far as the (0,n) modes are concerned, a phased arrangement of transducers can provide excitation of only, say, the (0,j) mode, over a frequency range from the cut-on frequency for that mode, $\omega_{o,j}$, up to a frequency of an octave or more higher than the cut-on frequency, the range depending on the mode number concerned and also perhaps on the array geometry. In a particular case, as considered above, the frequency range can easily be determined.

In practice, however, another factor is more likely to limit the range over which an isolated mode can be excited. If all (m,n) modes are considered, as well as just the (0,n) modes, then among the modes that can be excited by the above array, the (1,4) mode may well have a cut-on frequency lower than that of the (0,12) mode. In a rectangular duct of cross-section shape representative of an annular duct, one might have, say, a breadth equal to 1/8 the height (i.e., a = b/8). Then the ratios of the cut-on frequencies concerned, namely (0,4) (1,4) and (0,12) are 1:2:3. Thus, the frequency range over which the (0,4) mode could be excited in isolation in this case is limited to the octave beginning with its cut-on frequency. However, since for this cross-section shape the cut-on frequency ratio (relative to that of the (0,4) mode) for the (2,4) mode is even larger than for the (0,12) mode, it follows that in the frequency range from the (0,4) cut-on frequency to the (0,12) cut-on frequency (a range of a one-to-three ratio in frequency) only the (0,4) mode will be excited over the first octave of the range, and only the (0,4) and (1,4) modes will be excited over the remainder of the range. Furthermore, relative amplitudes and phases of excitation of the (0,4) and (1,4) modes over the whole range can readily be estimated from the appropriate theoretical expressions.

To suppress the (1,4) mode would require twice as many transducers, the additional transducers being placed on the wall at x = a.

It should be mentioned that the enhancement-suppression properties of the transducer array considered above are to a great extent insensitive to the sizes and shapes of the transducers, and of the velocity distributions over their faces. Also, it can be shown that variation of the transducer velocity

over the face could occur without substantially altering the mode response, as long as the average normal velocity times the transducer face area remained approximately constant. In such a case, of course, the "acoustic center" of the transducer might not correspond to its geometric center.

This brief consideration of duct excitation by an array of transducers shows that practical arrays can be designed and operated to give predictable, isolated generation of selected duct modes, for a relatively large range of modes in a given duct. The major limitation of this idealized modal excitation, in practice, is the variability of the acoustic velocity distribution of the individual transducers, over the degree of interaction isolation which can be maintained between individual units in the phased array and the local geometric variations in the duct at the mounting positions of the transducers. Each of these factors will cause variations from the idealized situation discussed above with the primary effect being excitation of modes other than the desired excitation pattern.

III.3.4. Sound pressure spatial control: experimental results

After initial operating experience with the facility, it was determined that interaction effects between individual transducers in the phased array were negligible, but that each transducer produced its own individual "signature" in the duct. The method of characterizing the output of each transducer is illustrated in figure 20. Each driver was excited individually and the microphone in the source plane, at the driver exit plane, was used to record the circumferential distribution of sound pressure and phase in that plane around the circumference of the source section as shown by the dashed line in figure 20. The method of recording the driver output was standardized. The microphone circumferential traverse was always initiated at the same angular position, i.e., $\theta=0$. The resulting sound pressure distribution is illustrated in figure 21 for driver number eight which is located at 157.5°. This driver characteristic curve was made at 876 Hertz (at 71°F), which is slightly above the angular mode cut-on frequency.

The most obvious freature of the SPL distribution in the source plane as shown in figure 21 is the near field pressure behavior at the transducer exit plane near the duct wall. This near field is characterized by a peak in both the amplitude and phase. In this near field dominated region, the wave is propagating outward, thus the phase change should be linear as the microphone traverses the circumferential contour. If the source is considered as a point source, then in the free field of that source the spherical wave generated will propagate outward, decaying at 6 dB per doubling of distance with a phase change of k per unit distance traversed. In this particular case, the phase change for the propagating wave is calculated to be 3.8 degrees phase/degree test section angle. The experimental behavior for the point source phase change and amplitude decay are compared with the theoretical point source behavior in figure 21. This illustration is particularly outstanding for demonstrating the point source influence.

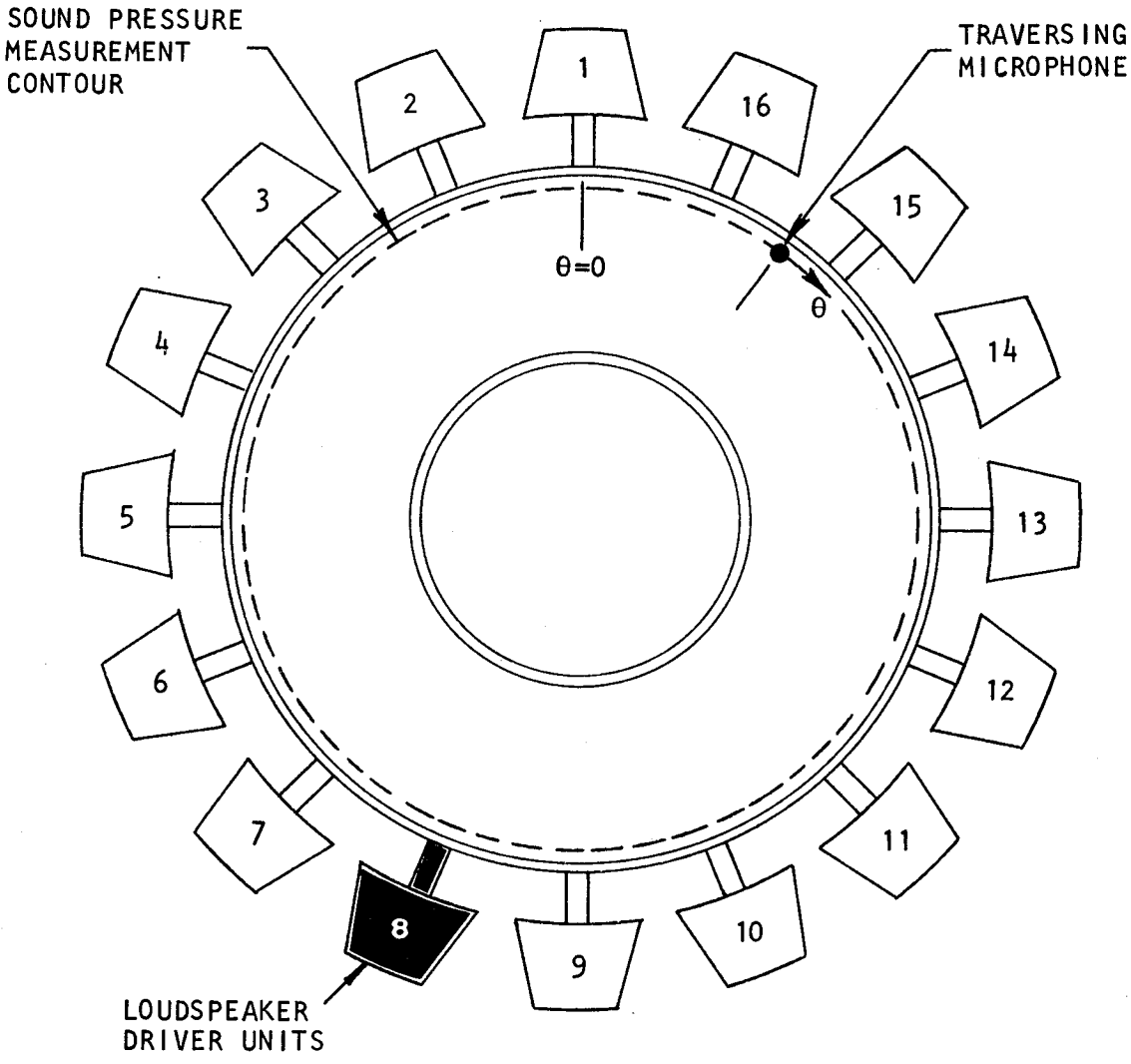


Figure 20. Illustration of Recording Technique for Driver "Signature"

At some point around the duct circumference, the propagating wave merges with the modal structure in the duct which was excited by that source. In this particular example, which is just above the calculated (3,0) mode cut-on frequency, the primary response is in the (3,0) mode as can be seen by examining the sound pressure amplitude and phase response in the duct. The shape of the amplitude should be that of log (cos (3θ)) and the phase, for a standing wave, should have 180 degree changes at the node lines. This pattern is not strictly attained, as the phase shows the characteristic of a propagating wave in some regions (i.e. a linear increase with distance). Figure 22 is included to show how closely matched the individual driver units are. Figure 22 shows that the characteristic for driver 2 is exceptionally similar to that of driver 8 shown in figure 21, with only very minor differences in amplitude and phase shape. Other drivers did have greater deviations, probably due to duct dimensional differences as much as anything. Differences of the order of 1 to 2 decibels and 5 to 15° phase were noted in the characteristic shapes at a particular frequency at points away from the peak amplitude. While these differences away from the peak sound pressure under the driver may appear minor, they can give rise to significant errors when attempting a modal simulation.

In the discussion in the preceding section, it was shown how, in the ideal situation, all modes other than the one desired, could be excluded by simple adjustment of the amplitude and phase of the piston type transducer as appropriate to the mode amplitude at the location of that transducer. For the example, which utilized four transducers (effectively), the amplitudes were Vo/2, -Vo, Vo, -Vo, Vo/2, where the end points were effectively 1/2 transducers. If the transducers were identical, then the amplitude of each driver unit, directly under the exit of that unit, could simply be computed from the modal amplitude and phase desired at that location. An example of this is shown in figures 23-25. In figure 23, the amplitude and phase of each driver is shown, with phase indicated by a plus or minus sign. Figure 24 shows the response in the source section at 1000 Hertz with the idealized setup and indicates the location of each driver. The near field sound pressure and phase of the individual drivers has a predominant influence on the spatial distribution. However, these higher order spatial variations would tend to excite the (8,0) mode and this mode does not propagate at 1000 Hertz, since its cut-on frequency is of the order of 2200 Hertz. Figure 25 shows the wave as it propagated into the test section. Although the waveform and phase are very similar to the required log (cosθ) and ±180 degrees shapes, there is significant deviation. Although not immediately obvious here, much of the deviation is caused by a spinning mode component of the same mode form. Other attempts at mode set-up were more effective, utilizing this simplified approach. However, in general, it was determined that the simple scheme was inadequate for satisfactory mode simulation over a broad frequency range.

In order to obtain a more accurate modal simulation a more rigorous approach was used. In this method, all the details of sound pressure in the source section were incorporated. The more exact, mathematical, method for mode simulation is described below.

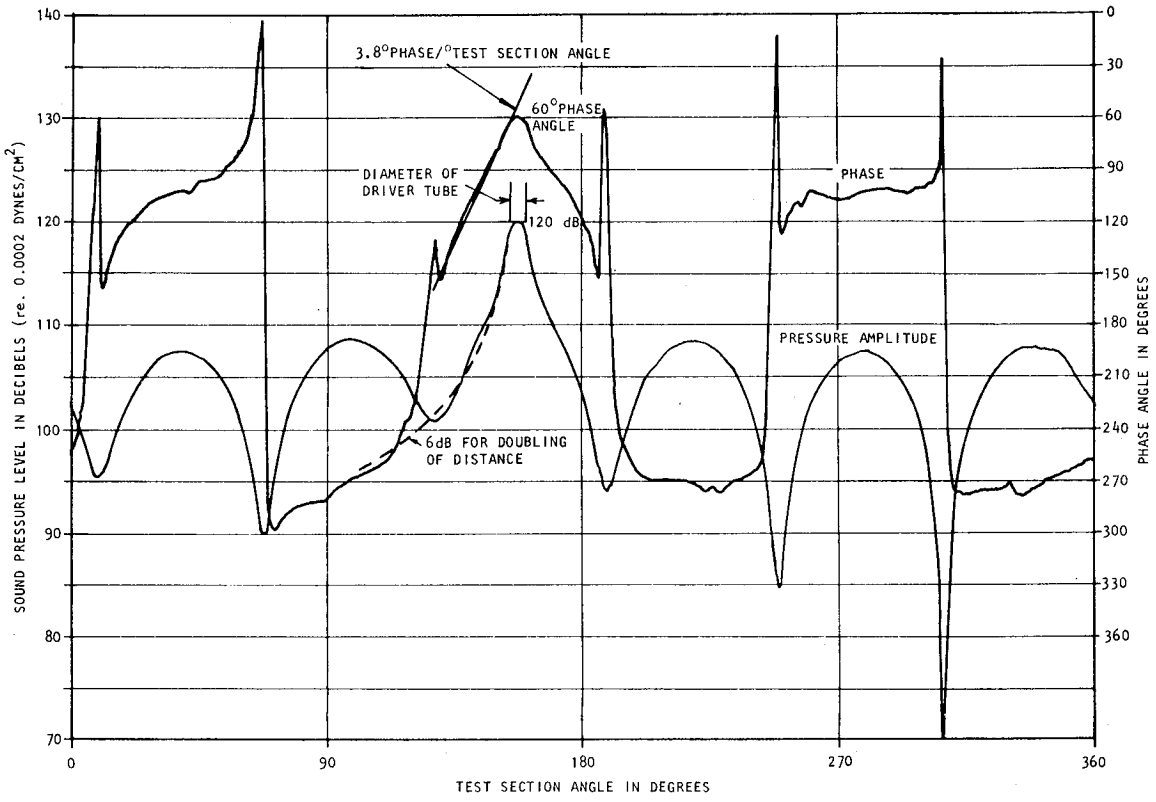


Figure 21. Characteristic Function for Driver Number 8 at 876 Hertz

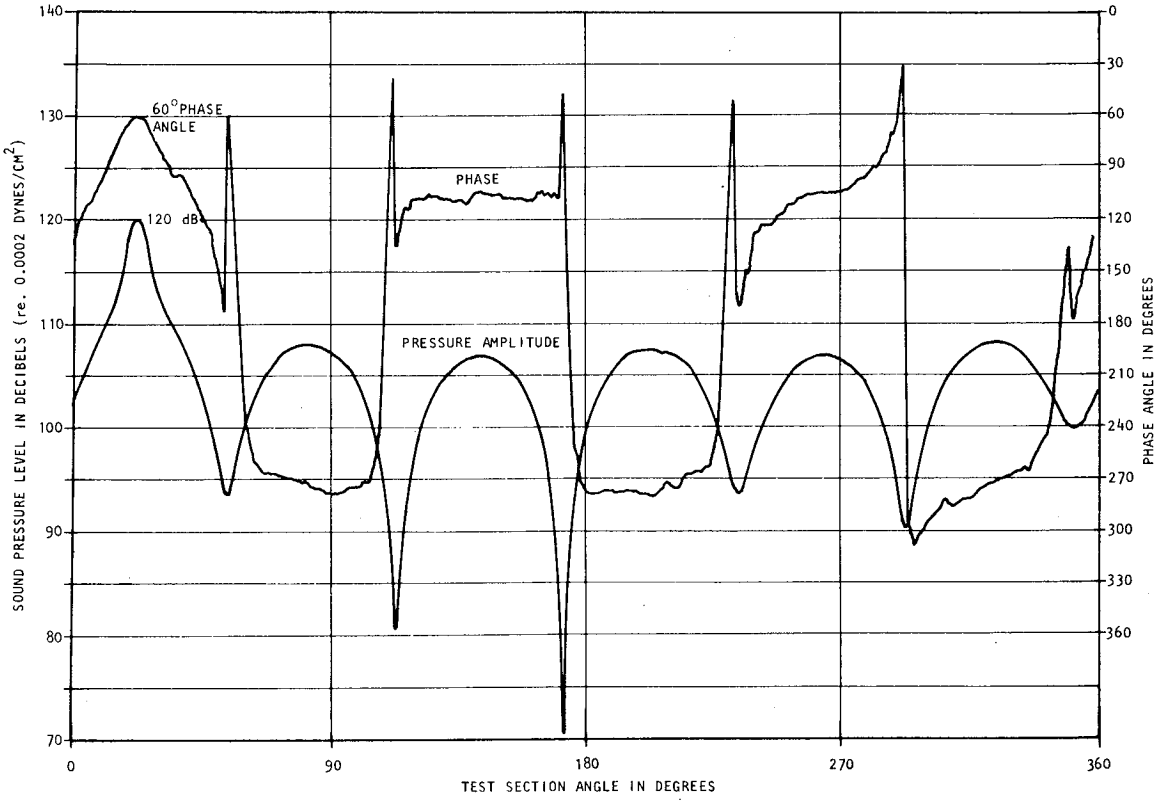


Figure 22. Characteristic Function for Driver Number 2 at 876 Hertz

(1,0) MODE SET-UP

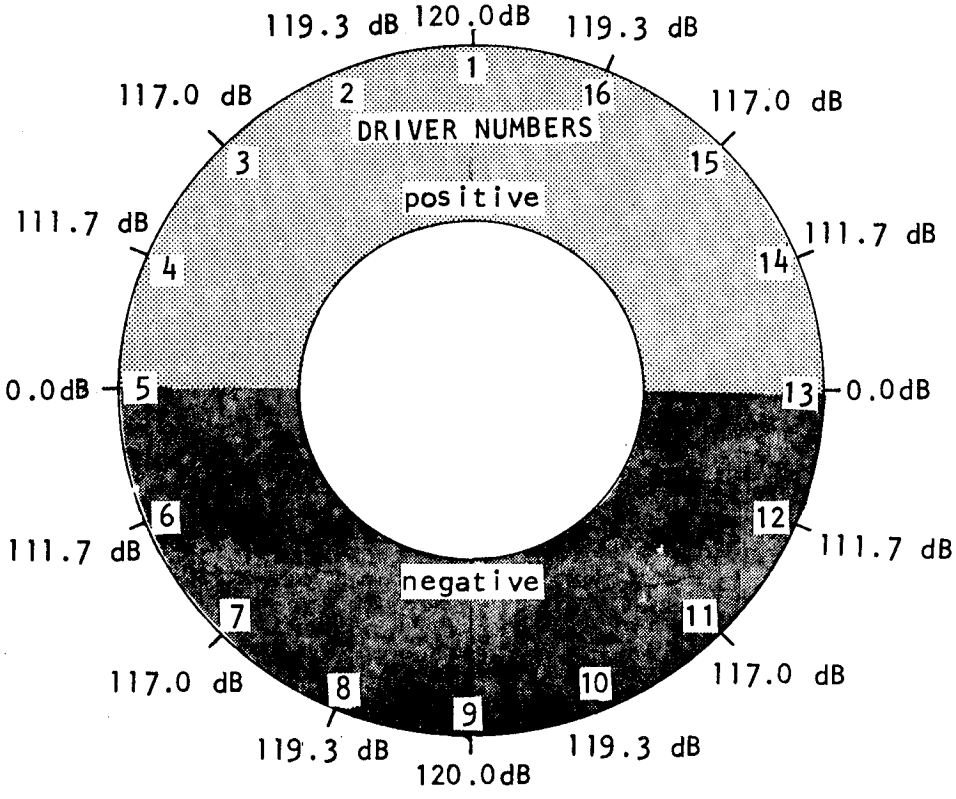


Figure 23. (1,0) Mode Set-up for Idealized Driver Output

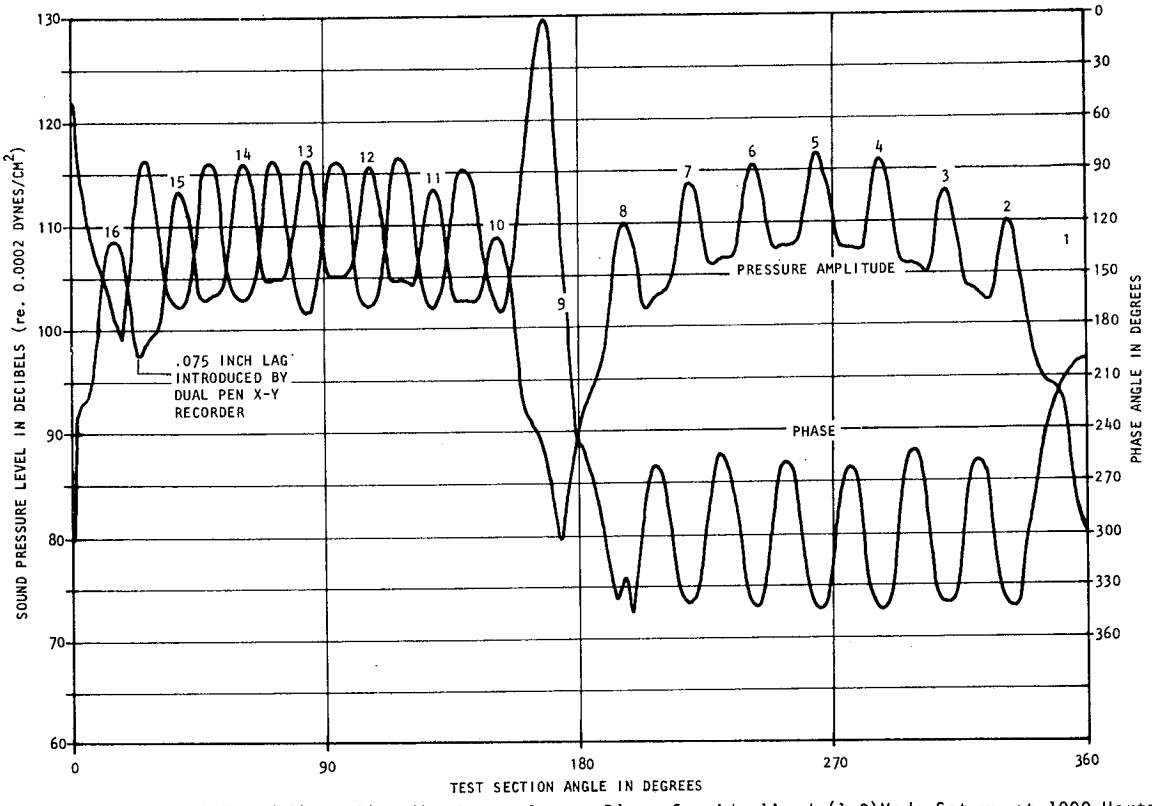


Figure 24. Angular SPL and Phase Distribution at Source Plane for Idealized (1,0) Mode Set-up at 1000 Hertz

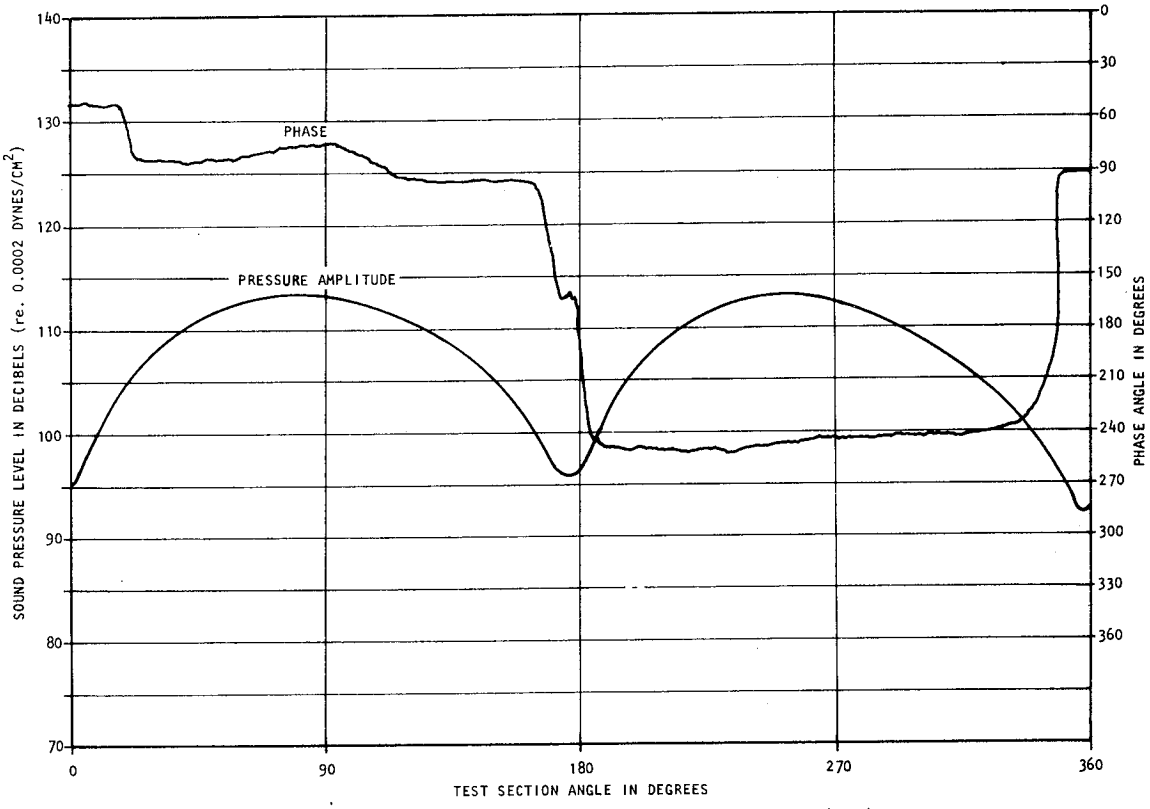


Figure 25. Angular SPL and Phase Distribution in Test Section for Idealized (1,0) Mode Set-up at 1000 Hertz

First, the individual driver response, as shown in figure 21, was characterized as an individual complex function. This function was digitally recorded during an angular sweep at 128 equally spaced locations around the circumference of the duct. Both dB amplitude and phase in degrees were recorded. This function was then converted to a complex pressure for each of the driver units. With this information available, the following expression can be written to show the simulation of the desired angular function, $f(\theta)$, by the complex driver response functions, $\phi(\theta)$,

$$\sum_{n=1}^{16} A_n \phi_n(\theta) = f(\theta) + E(\theta) \tag{57}$$

where A_n can be represented as the complex amplitude of each transducer directly in front of the transducer outlet. A least squares approach for simulating the function, $f(\theta)$, is ideally suited to this requirement. The function, $f(\theta)$ is transferred to the left hand side of the above equation and the resulting error, $E(\theta)$, is minimized with respect to the complex amplitude, A_n, after squaring. The operations are

$$\sum_{n=1}^{16} A_n \phi_n(\theta) - f(\theta) = E(\theta). \tag{58}$$

The modulus of the squared error function is

$$G(\theta) = E(\theta)\, E^*(\theta) = \left[\sum_{n=1}^{16} A_n \phi_n(\theta) - f(\theta)\right] \left[\sum_{n=1}^{16} A_n^* \phi_n^* - f^*(\phi)\right]. \tag{59}$$

The unknown coefficients, A_n, are determined by the minimization indicated below:

$$\frac{\partial G}{\partial \mathrm{Re}(A_n)} = 0, \quad \frac{\partial G}{\partial \mathrm{Im}(A_n)} = 0. \tag{60}$$

These operations were performed with a digital computer analysis and the resulting amplitude and phase at the exit plane of each driver was numerically determined.

The calculated sound pressure and phase for each driver unit for the case illustrated in figures 23-25 is shown in figure 26. These are the driver outputs determined as necessary to produce a wave of 120 decibels amplitude. Because of the differences in individual driver response, the amplitudes and

CALCULATED AMPLIFIER AND PHASE POT SETTINGS
FOR THE FOLLOWING TEST CONDITIONS

REQUIRED PRESSURE MODE - COS (2*PI* 1*THETA)
16 DRIVER RESPONSE FUNCTIONS USED IN FIT
128 DATA POINTS PER DRIVER RESPONSE FUNCTION
TEST FREQUENCY = 1000. HERTZ

DRIVER NUMBER	DRIVER OUTPUT SPL-DB	DRIVER PHASE DEGREES
1	122.1	302.4
2	122.4	308.1
3	120.4	308.3
4	114.8	306.8
5	87.6	214.1
6	115.0	132.0
7	119.9	131.8
8	122.6	128.7
9	123.4	130.4
10	122.2	126.5
11	120.0	129.3
12	114.6	131.2
13	78.4	17.7
14	115.2	313.6
15	120.9	311.7
16	121.3	310.8

Figure 26. Computer Output Listing Driver Amplitude and Phase for "Least-Square" (1,0) Mode Set-up

phases computed in this fashion deviate significantly from those computed from the ideal model. The test section response for the more exact set-up is shown in figure 27 and should be compared with figure 25 to show the increase in fidelity.

Finally, to show the results of the least square minimization procedure in predicting the sound pressure distribution at the source location, figure 28 displays the measured and calculated sound pressure and phase distribution after determination of the complex amplitude function, A_n. The plot is represented by

$$p(\theta) = \sum_{n-1}^{16} A_n \phi_n(\theta) \tag{61}$$

and is shown in dB amplitude and phase in degrees. The solid dots are the computed amplitude, with open triangles being the computed phase. The comparison with the measured angular distribution of these functions is quite close, as it was in all cases tested, indicating an insignificant interaction between transducers when all are operating.

Thus, in summary for this part of the investigation, the objectives of the full-scale investigation have been outlined, the facility was described and the means for simulating angular modes in the annular duct facility was described and justified in detail.

IV. SOUND PROPAGATION IN RIGID WALL ANNULAR DUCTS

The primary objective of this series of tests was to provide basic information on cut-on frequency, modal phase speed, mode shapes, frequency response of the duct, and radiation impedance of and radiation characteristics from the unflanged termination. The first three items are described in this section and the latter two are described in sections VII and VIII. Effects of flow through the duct were also determined and are included in this discussion.

The first sub-section will briefly present a description of the experiments conducted, followed by a summary of analytical predictions for the hard wall annular duct concerning cut-on frequency, phase speed, and mode shapes. Then the discussion will present experimental observations and where possible, these will be compared with theory.

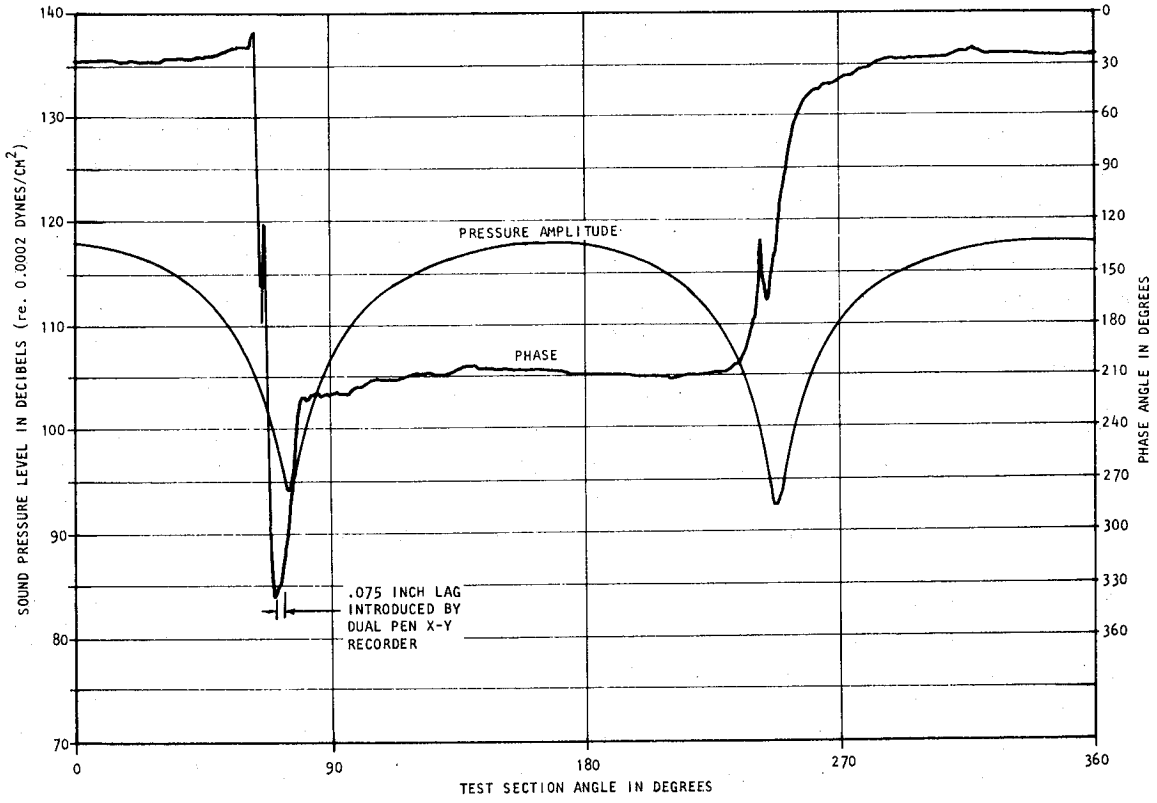


Figure 27. Angular SPL and Phase in Test Section for "Least-Square" (1,0) Mode Set-up at 1000 Hertz

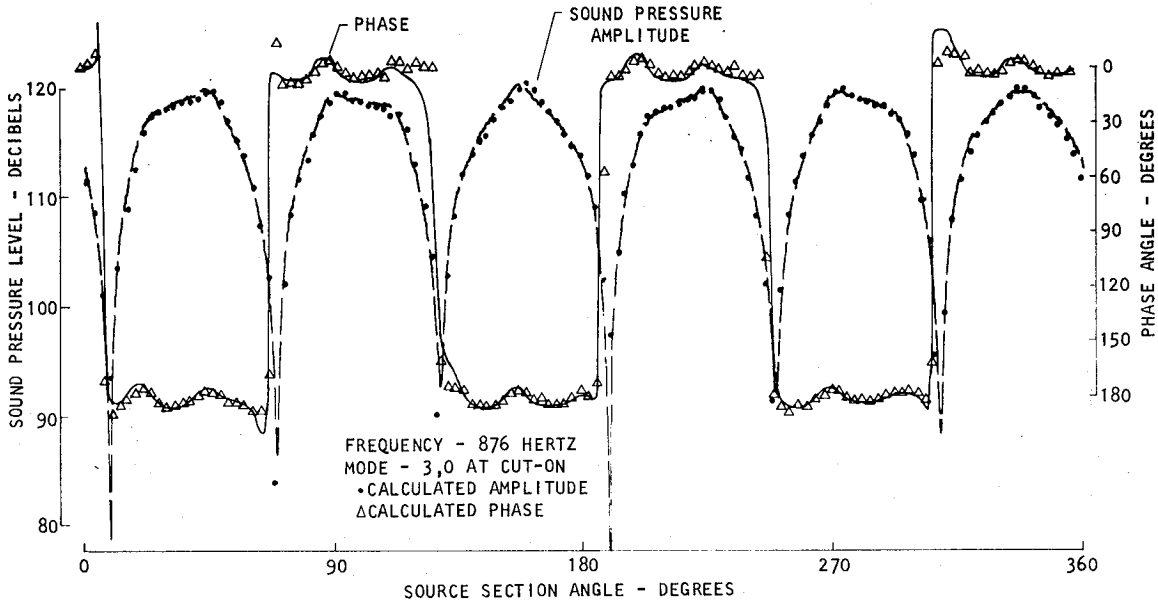


Figure 28. Comparison of Calculated SPL and Phase Distribution at Source Plane for "Least-Square" (3,0) Mode Set-up at 876 Hertz

IV.1. Description of Experiments

The fundamental parameters in the modal theory of sound propagation in rigid wall tubes or ducts are the eigenvalues and corresponding eigenvectors. The eigenvalue, in the cases of infinite or finite length ducts, is either real or imaginary, with the frequency parameter at the transition point between real and imaginary being the cut-on frequency. The first item selected for experimental evaluation was a determination of the set of cut-on frequencies for the annular duct. Two basic techniques were utilized in locating the cut-on frequency. One involved experimental determination of the frequency of peak response amplitude in the region of cut-on frequency, for a single driver simulating a point source excitation. The other involved visual examination of the circumferential or radial sound pressure distribution in the test section, for a single driver excitation, to determine which frequency resulted in a spatial response closest to the ideal modal pattern.

Next, a technique for determining the phase speed, c_ϕ, was developed. The phase speed is inversely proportional to β, i.e. $c_\phi = c/\beta$. In an infinite length duct (one in which there is no reflected wave), or a duct with a reasonably high axial attenuation rate, determination of the phase speed is a relatively simple matter. It simply involves experimental determination of the phase difference between two points with the same radial and angular coordinates but with axial separation. However, with both forward and backward traveling waves existing simultaneously, as occurs in the hard wall finite length duct, the amplitude of each wave must be determined before the phase speed can be measured.

Finally, both angular and radial mode shape measurements were accomplished for several modes at several frequencies. Although radial control of the sound pressure distribution within the duct was not possible, it was found that radial modes could be excited in relative isolation near the cut-on frequency of that mode.

The following sections will contain more detailed descriptions of the experimental procedures developed during this phase of the testing.

IV.1.1. Determination of cut-on frequency

In the early analytical treatments on sound propagation in annular ducts by Sofrin and Tyler (ref. 7) and Morfey (ref. 8), it was assumed that the source was a harmonic, distributed, pressure source. It was then shown that with a pressure source, the duct response resembles a unit step function in the region of cut-on frequency. Morfey went one step further and ran a simple experiment wherein he excited a $2\frac{1}{2}$ inch diameter duct with a siren producing a (1,0) mode pattern. The measured response is shown in figure 29.

Doak (ref. 37) conducted an analysis of a duct excited by a point velocity source and computed modal responses. An example of the space integrated

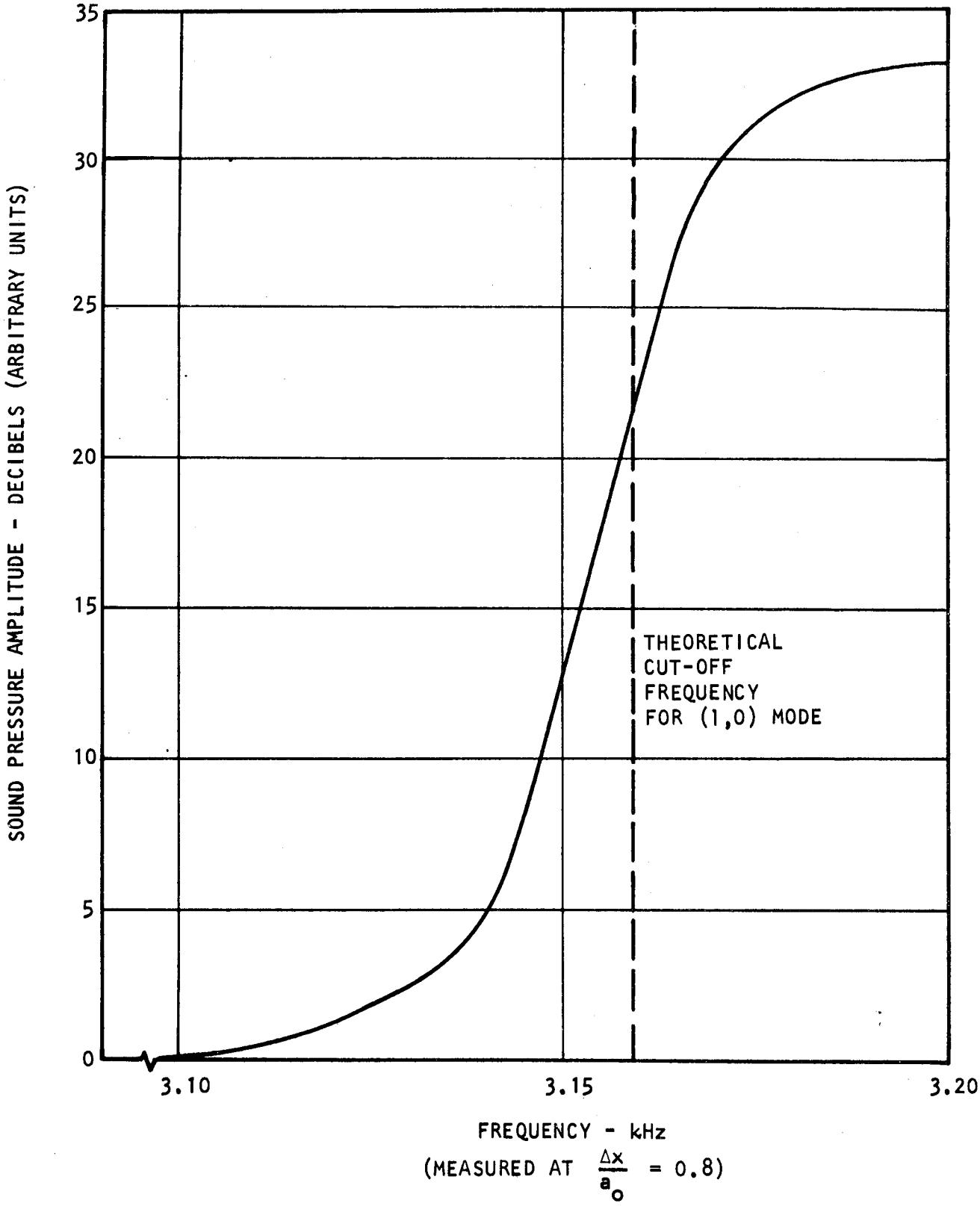


Figure 29. Cut-off Demonstration: Variation of SPL with Frequency (from Morfey, ref. 8)

mean square pressure response and the acoustic power for a source located at the center of one of the duct walls is given in figure 30.

Since the infinite duct is effectively a finite duct with a ρc termination at the ends, an escape route would appear to exist for any resonant energy that might be built up in the duct. It is perhaps surprising that the mode amplitude shown in figure 30 goes to infinity at the cut-on frequency, and is very large in the neighborhood of this frequency. Such infinite amplitudes would, of course, be expected in a completely enclosed, hard wall room at the normal mode resonant frequencies (see, e.g. Morse (ref. 38), Chapter VIII). Although this resonance effect in the duct mode case is perhaps less familiar, it nevertheless has been noted previously (e.g., Morfey (ref. 8), in the same reference in which figure 29 was presented, commented on the response to a point velocity source).

A physical explanation of the behavior is given in reference 39 (see Chapter 2). In brief, it is that, in the neighborhood of cut-on, the mode wave motion is almost (completely so, at cut-on) a pure two-dimensional standing wave, just like a two-dimensional standing wave in a hard walled room, in fact. Therefore as no energy is required to maintain motion of such a standing wave in a lossless medium, the amplitude tends to infinity when the mode motion is forced by a volume velocity source at the cut-on frequency. At the same time, however, the impedance presented by the mode to the source also becomes infinite, so that to maintain, in practice, any finite volume velocity amplitude, Q_o, of the source, would require application of an infinite force at the cut-on frequency. Thus, the back reaction of the mode on the source can be large at frequencies near the mode cut-on frequency.

Therefore, in practice, the amplitude reached by a mode at the cut-on frequency is determined by two factors: not only the rather obvious factor of the wall absorption (neglected here), but also the effective internal impedance of the source mechanism.

Morfey has shown theoretically that, for a constant pressure amplitude source (the other extreme from the constant volume velocity source used here), the mode frequency response factors corresponding to those shown in figure 30 approach the asymptotic values of unity from below, as $\omega_{mn}/\omega \to 0$, without the resonant peaks at $\omega_{mn}/\omega = 1$, as shown in figure 29.

In practice, therefore, without specification of the source type, one can expect mode response behavior near cut-on to lie somewhere between the two extremes: either a violent overshoot for sources behaving nearly like constant volume velocity sources as shown in figure 30, or asymptotic behavior for sources acting more like constant pressure sources, as illustrated in figure 29.

An example of the measured response in the annular duct facility due to a single driver excitation on the wall is shown in figure 31 (ref. 40). Based on the preceding discussion, it can be assumed that the source is a reasonable approximation to the point velocity source. In recording this response, the source pressure amplitude was held constant with frequency. It is obvious

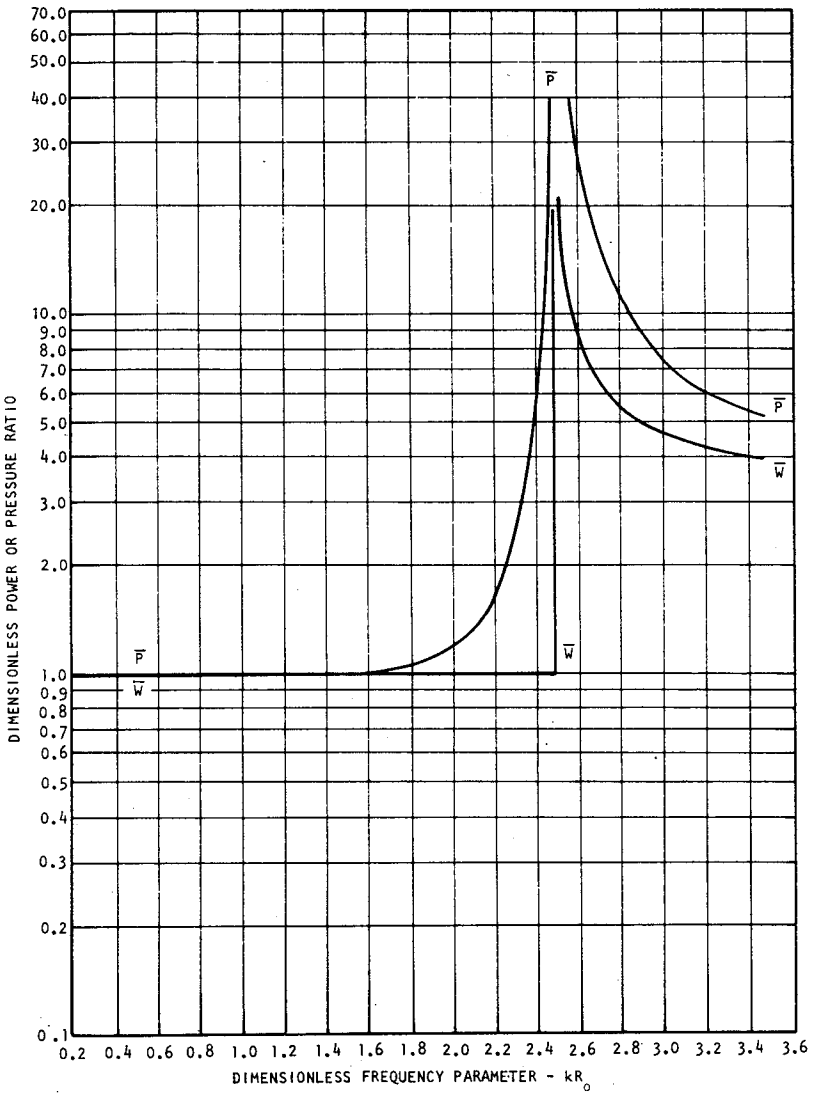


Figure 30. Dimensionless Acoustic Power and Space Integrated Mean Square Pressure for Source at Position x = a/2, y = b (see figure 19) (from Doak, ref. 37)

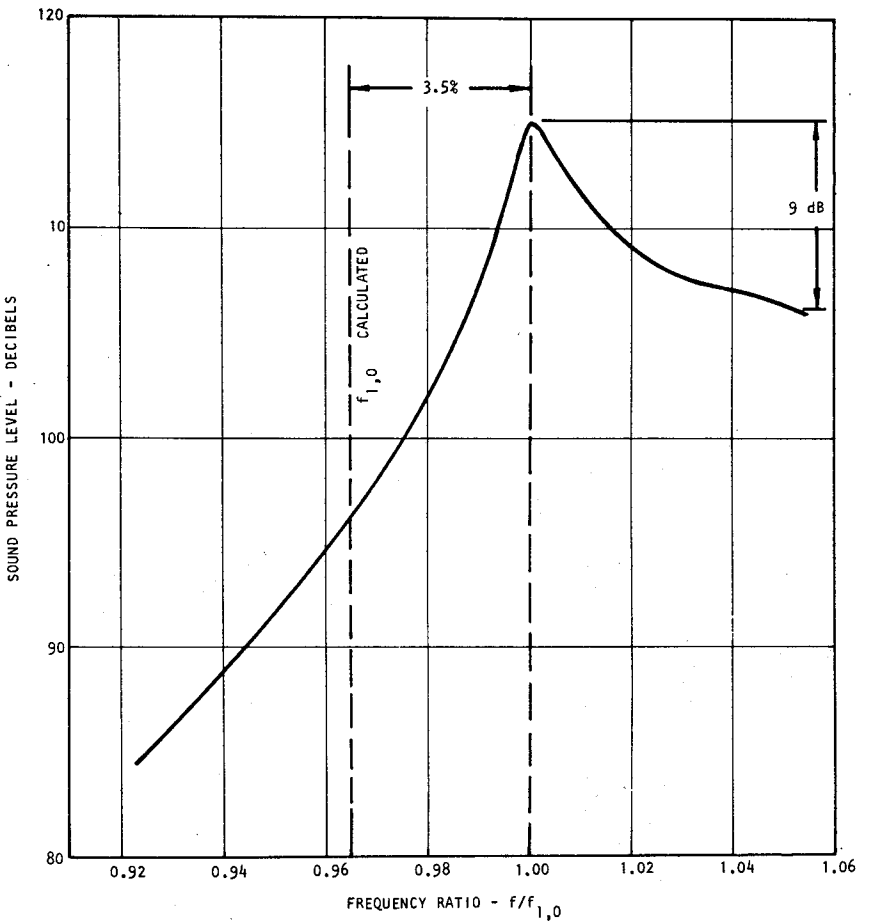


Figure 31. Variation of Annular Duct Acoustic Response in the Vicinity of the First Angular Mode (1,0) Cut-on Frequency (from Plumblee and Dean, ref. 40)

that, as expected, the response amplitude is not infinite. Damping mechanisms, not accounted for in the model, as discussed, limit the response amplitude and increase the frequency of maximum response.

The analogy of the modal response to a point velocity source is that of a damped accelerometer with a base harmonic displacement. The physical analogy is shown in figure 32(a) and the response is illustrated in figure 32(b). From this analogy, two useful data analysis tools can be extracted. First, the ratio of the peak amplitude of response to the final "steady-state" response amplitude is

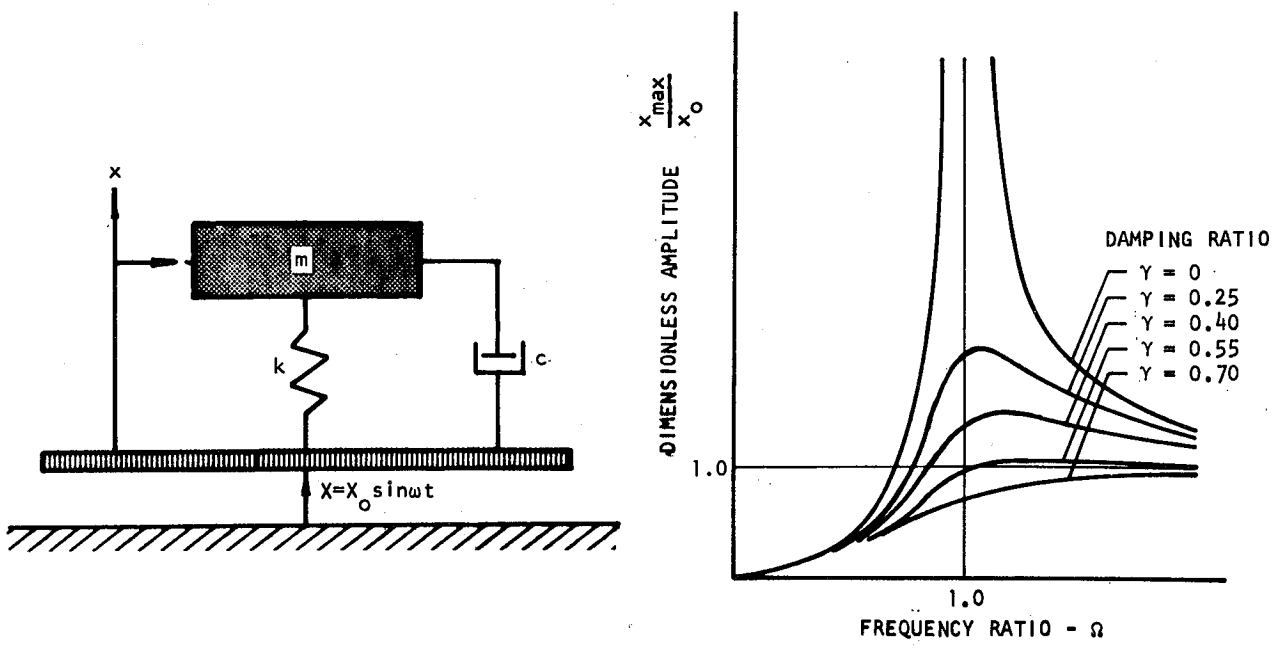
$$\frac{X_{max}}{X_o} = \frac{1}{2\gamma\sqrt{1-\gamma^2}} \quad . \tag{62}$$

On examination of figure 31, it is seen that the peak pressure amplitude is approximately 9 dB above the "steady-state" pressure amplitude at higher frequency (for constant pressure vs frequency excitation at the source). This measurable quantity can be used to determine an "effective" damping ratio, γ, for the mode from the above relationship. With a 9 dB ratio, $X_{max}/X_o = 2.82$ and $\gamma = 0.18$. The frequency at which peak response occurs is

$$\Omega = \frac{\omega_p}{\omega} = \frac{1}{\sqrt{1 - 2\gamma^2}} \quad . \tag{63}$$

For a value of $\gamma = 0.18$, a frequency ratio, Ω, is determined to be 1.035. That is, the frequency of peak response, based on an experimentally determined damping ratio, is 3.5% greater than the calculated undamped natural frequency. As will be shown later, this is the exact ratio of experimentally determined peak frequency to calculated cut-on frequency, as shown by the dashed line in figure 31..

Another useful technique for identifying mode cut-on frequency was also adopted for this study. This method involved examination of the circumferential sound pressure response in the test section, for a single driver excitation, at various frequencies above and below cut-on frequency. In figure 33, angular SPL response patterns in the test section at the outer wall are shown for three frequencies; one below peak response, one at peak response and one above peak response. In determining the cut-on frequency of a mode, once again it is assumed that the response of a mode at cut-on will significantly exceed the response of all other modes for a point velocity source excitation. In figure 33, this assumption is confirmed. The peak response is virtually all (2,0) mode while at 5 Hz below peak response the mode contribution is virtually all due to the (0,0) and (1,0) modes. At 5 Hz above cut-on the mode contribution is primarily (2,0) but the response amplitude



(a) Physical Schematic

(b) Response Amplitude

Figure 32. Accelerometer Response Characteristics (from Scanlan and Rosenbaum, ref. 41)

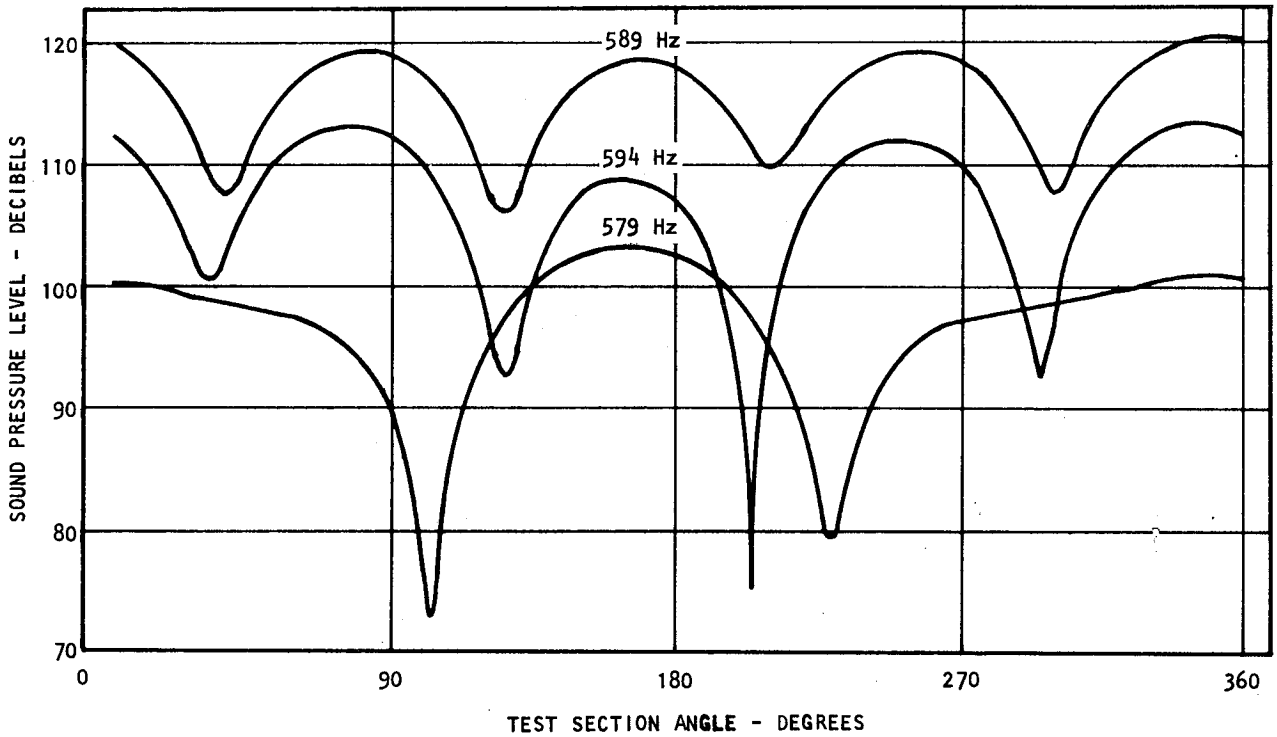


Figure 33. Angular Acoustic Response of Test Section Showing Behavior of (2,0) Mode at Cut-on Frequency (589 Hz) and ±5 Hz about Cut-on.

is significantly reduced from that at 589 Hz. Using this criterion to determine mode cut-on frequency, a series of circumferential SPL distributions was made for small increments in frequency and then a judgment was made, based on a visual balance of peak response amplitude and distortion of the mode shape, to determine the cut-on frequency.

Both of the above techniques were used extensively during this program as a means of determining cut-on frequency. The latter technique, as described, involved more judgment on the part of the experimenter than the first method; however, it does give a more positive identification to a response peak.

IV.1.2. Method for experimentally determining phase speed

The analytical form for the axial propagating wave is given as

$$e^{-ik\beta z}$$

where β is the wavelength constant. Both the axial wavelength and the propagation speed are inversely proportional to β, i.e. $\lambda_{m,n} = \lambda/\beta_{m,n}$ and $c_{\phi m,n} = c/\beta_{m,n}$ where m,n refers to the mode number and λ is the free space wavelength for a particular frequency, f, at a speed of sound, c. Thus, in the case of the finite length duct, wherein a standing wave pattern exists in the axial direction (assuming reflection occurs at the open end), the most straight forward technique for measuring $\beta_{m,n}$ is to accurately measure the frequency, speed of sound, and the axial standing wave pattern for a mode in relative isolation. This method was suggested by Morfey (ref. 8).

The primary problem in implementing this technique was the lack of an axial traversing microphone. Thus, measurements were made at discrete points in the direction of the axial coordinate, by inserting a microphone in the microphone probe holes shown in figure 14, and recording an angular sweep of sound pressure distribution such as is shown in figure 27. These were recorded at each of 33 axial positions and the peak amplitude was determined from the angular SPL plots.

A plot of the resulting axial standing wave amplitude and phase is shown in figure 34 for the (0,0), (1,0), (2,0), and (3,0) modes. A least square curve fit routine, using the assumed forward and backward wave system was used to determine the best representation of the composite wave. This is shown by the curves plotted through the data points. Examining the phase plots, it is observed that as the reflection coefficient becomes very small, as in the case of the (1,0) mode, the phase increases almost linearly with axial distance; but as the reflection coefficient approaches unity as for the (3,0) mode, the phase variation approaches the ± 180 degree square wave function characteristic of the pure standing wave. The phase change with distance can be used to determine β, only when no reflected (or standing) wave component exists, as mentioned earlier.

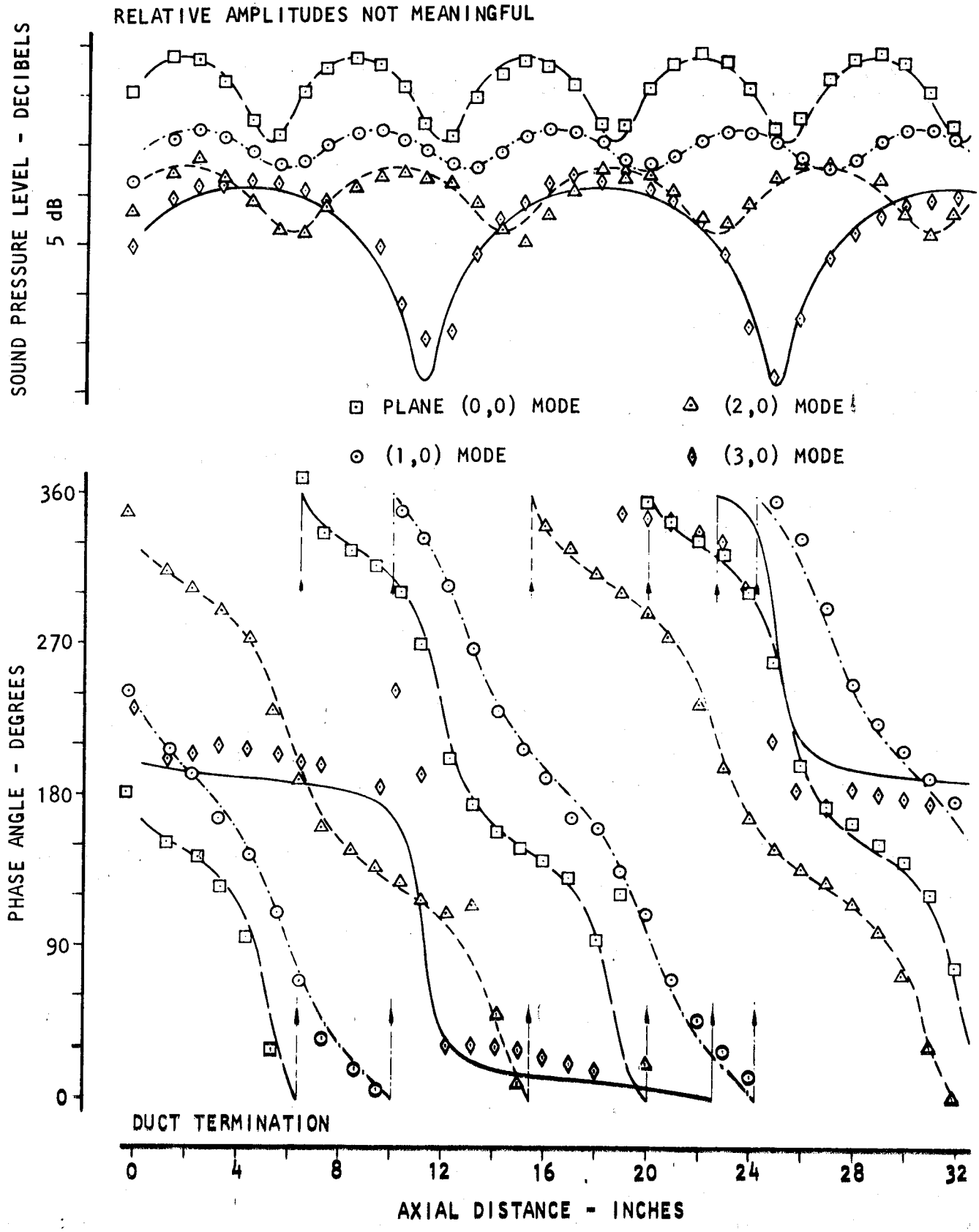


Figure 34. Measured Axial Variation of SPL and Phase for (0,0), (1,0), (2,0) and (3,0) Modes in Hard Wall Test Duct at 1000 Hertz

The propagation or wavelength constant β_{mn} is determined by measuring the distance between minima, and the relationship,

$$\lambda_{mn} = \lambda/\beta_{mn},$$

is used to determine β_{mn}.

IV.1.3. Mode shape measurement

The technique for measuring a mode shape was relatively simple, after it was determined that the mode was excited in isolation. Techniques for assuring this were described under cut-on frequency determination (IV.1.1).

At the frequency of peak response for a particular mode, the driver units were set up as described in the section on modal simulation and the angular and radial variations of sound pressure and phase were recorded at the appropriate stations in the test section.

IV.2. Analytical Predictions

The first analysis for prediction of the sound field in a hard wall annular duct is that by Tyler and Sofrin (ref. 7). Their analysis resulted in a tabulation of the characteristic numbers for the E functions, which are the radial mode shapes. The characteristic numbers, which are a function of the hub-tip ratio, are directly related to the cut-on frequencies.

The numerical analysis, described in a following section on sound propagation in lined annular ducts degenerates to the Sofrin-Tyler analysis when presented with rigid wall boundary conditions and no mean flow. The results are solutions to the following set of equations:

$$E_m(k') = J_m'(k') + Q_{m\mu}^{(\sigma)} Y_m'(k') = 0 \tag{64}$$

$$E_m(\sigma k') = J_m'(\sigma k') + Q_{m\mu}^{(\sigma)} Y_m'(\sigma k') = 0 \tag{65}$$

where primes denote differentiation with respect to the argument, σ is the hub-tip ratio, k' is the characteristic number and J and Y are Bessel functions of the first and second kind. The computer solutions also yield the propagation constant, β, which is a function of k'.

IV.2.1. Mode shape predictions

The mode shape in the hard wall annular duct is a combination of a sinusoidal function in the angular direction and the E function in the radial direction. Because of complications in the angular wave form which can be introduced by 'noise' in the set-up procedure, a single mode might be excited in isolation, but the resulting waveform might appear to be very different from the theoretical shape. Occasionally, a mode set-up will visually appear to contain a distortion in shape, evidenced by a low peak to minimum ratio. This is illustrated in figure 35. However, upon analysis of the waveform using the technique described in section VII on RADIATION IMPEDANCE, it is observed that this type of behavior is usually the result of combining a spinning mode and standing mode of the same mode number. An analysis which reduces the combined wave to its spinning and standing mode components was programmed on a digital computer. The results of this for the waveform shown in figure 35 are displayed in figure 36. It shows that the spinning wave is approximately 7 decibels below the standing wave. A somewhat trivial observation is that the minimum level of the combined wave is equal to the spinning mode component, if no other modes are involved.

A generalized complex Fourier computer analysis was written to determine the Fourier components of the angular sound pressure distribution. An example of the computer printout is shown in figure 37. The first line identifies the axial position in the test duct and the second line gives the necessary information for identifying the data run. Next, the results of the Fourier analysis are listed, giving the amplitude and phase angle for the cosine and sine components. Finally, these cosine and sine components are combined to give the amplitude and phase of the combined wave, the amplitude and phase of the standing and spinning wave components and in the last column, the angular location in the test section corresponding to the first minimum of the combined wave. In this particular example, the set-up at the source plane corresponded to an equal amplitude in the first four modes [(0,0), (1,0), (2,0), and (3,0)]. The analysis shows that this first condition still exists with ±2 dB at station 36, which is the entrance to the test section. Furthermore, the (4,0) mode is 25 dB below the plane mode component, which indicates the degree of isolation achieved in the mode simulation procedure.

IV.3. Comparison of Experiment with Theory

IV.3.1. Cut-on frequency

Using the methods described in the previous section, the non-dimensional cut-on frequency, kR_o, was measured for nine modes and is indicated by asterisks in table I. The computed eigenvalues are shown in the table for the (0,0) mode through the (6,2) mode. In all cases, the experimental value is higher than the computed value, with the percentage ranging from 3.6 percent to 0.7 percent. The decrease in error is consistent with increasing mode number, indicating a correlated effect such as ascribed to damping in the simple one-dimensional model presented in the previous section.

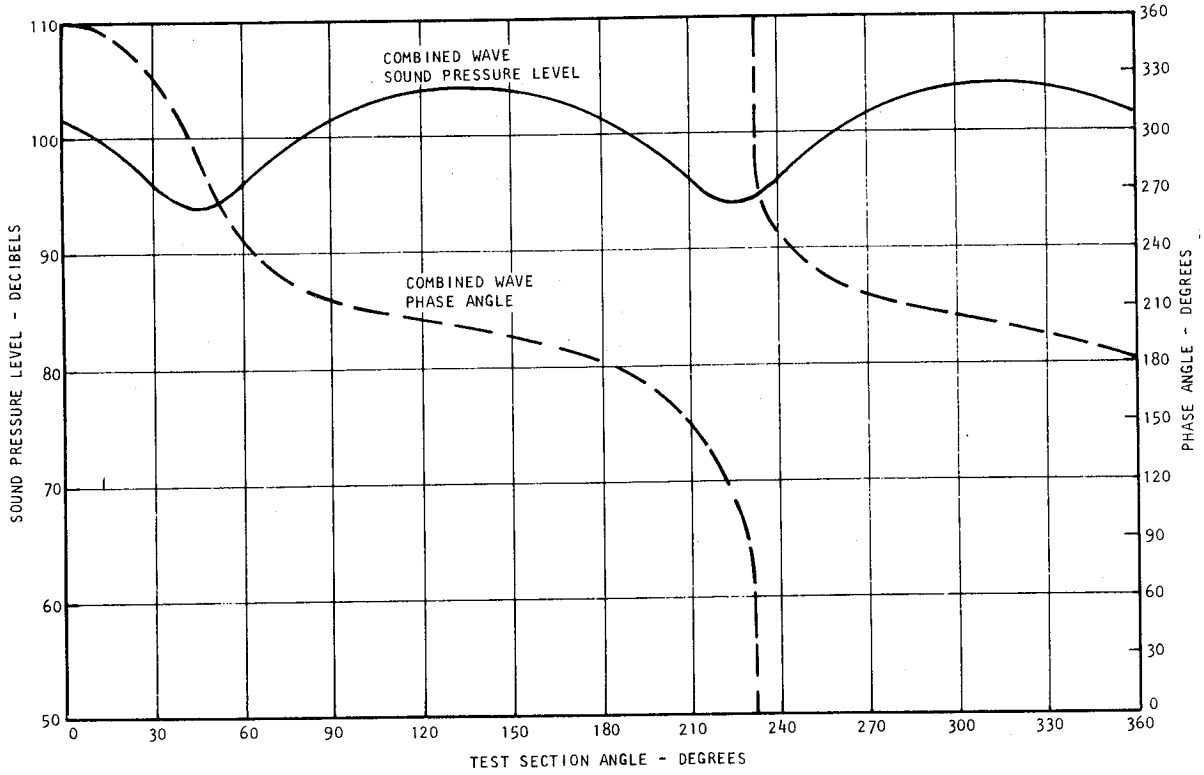


Figure 35. Typical Angular Mode "Distortion"

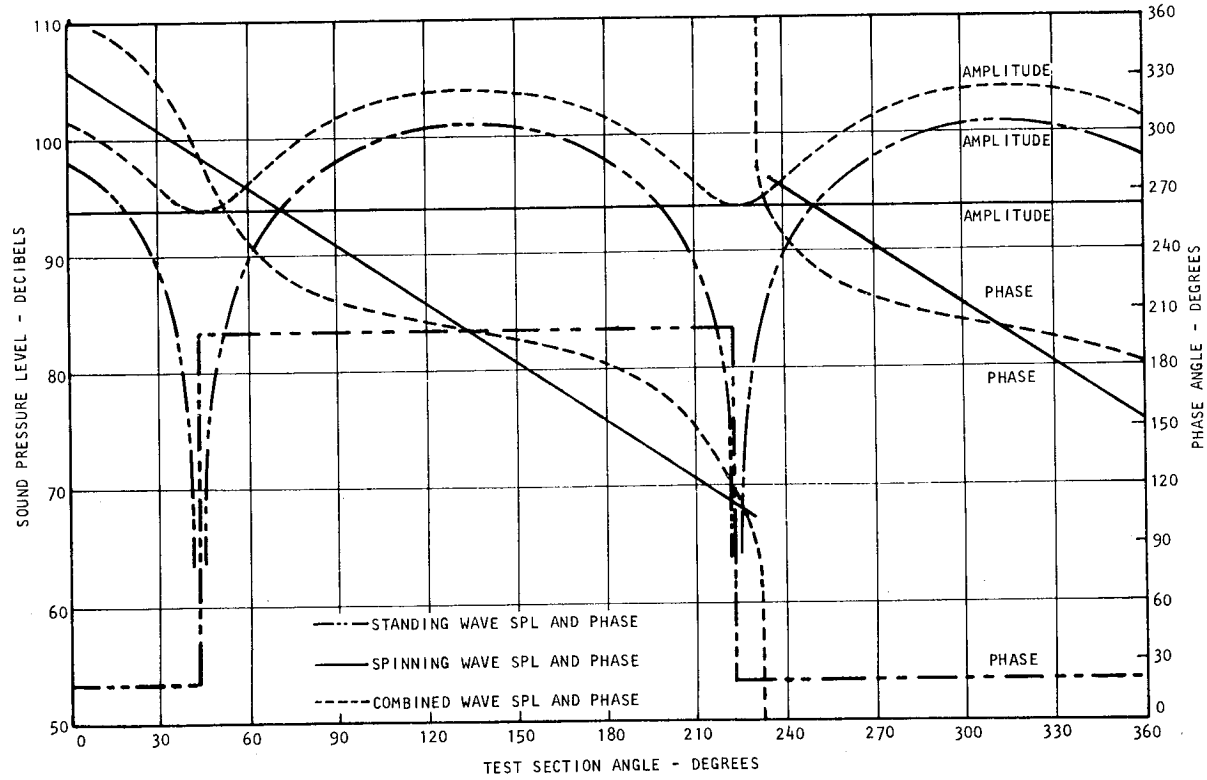


Figure 36. Components of Stationary and Spinning Modes Contributing to Angular Mode "Distortion"

HOLE NUMBER 36 MODE SET (4 MODES, EQUAL AMPLITUDE)

FREQ 1000.0 HZ TEMP 72.0 DEG F PHASE REF 0 DEG

MODE NO.	COS AMP DB	COS PHASE DEG	SIN AMP DB	SIN PHASE DEG
0	109.6	207.1		
1	107.3	133.3	109.6	315.9
2	97.5	193.2	113.1	173.8
3	113.2	143.2	106.9	129.1
4	84.0	330.4	77.3	146.6

NUMBER	COMBINED WAVE AMPLITUDE DB	COMBINED WAVE PHASE DEG	SPINNING WAVE AMPLITUDE DB	SPINNING WAVE PHASE DEG	STANDING WAVE AMPLITUDE DB	STANDING WAVE PHASE DEG	PHASE SHIFT DEG
1	111.64	314.97	78.43	82.53	111.45	314.97	127.56
2	113.20	174.28	87.84	255.32	112.72	174.28	81.05
3	114.07	140.57	93.68	165.83	113.20	140.57	25.26
4	84.85	149.77	52.94	125.02	85.07	149.77	155.25

Figure 37. Computer Output Illustrating Fourier Spinning/Stationary Mode Analysis

TABLE I

COMPARISON OF THEORETICAL AND EXPERIMENTAL HARD-WALLED ANNULAR DUCT EIGENVALUES (σ = 0.566)

$\lambda = \frac{2 f_{mn} R_o}{c}$, f_{mn} - cut-on frequency, R_o - duct outer radius, c - speed of sound

Radial Mode No. n	Circumferential Mode No., m						
	0	1	2	3	4	5	6
0	0.0	*1.3384 1.2922	*2.5976 2.5716	*3.8550 3.8268	*5.0895 5.0492	*6.2783 6.2351	7.3860
1	7.3219	7.4509	*7.9022 7.8282	8.4284	9.2173	*10.2948 10.1587	*11.2913 11.2167
2	14.5155	14.5776	14.7627	15.0672	*15.6355 15.4855	16.0108	16.6358

*Experimentally determined value

The computed values of 'equivalent' single-degree-of-freedom damping ranged from 8% to 18% for the various modes. The computed ratio of pressure at damped resonance to the 'steady-state' pressure, well above cut-on, varied from 9 dB to 16 dB for the modes measured above. This ratio was not measured for all the modes and no consistent comparison such as that given for figure 31 has been made. This comparison could only be made if the mode is excited in isolation. When a point source frequency response curve was used as a means of looking at cut-on behavior, usually more than one mode was excited.

IV.3.2. Axial propagation constant

In order to determine the propagation constant, β, a number of SPL and phase measurements were made as described in Section IV.1.2 and illustrated in figure 34. The curves drawn through the data points in figure 34 are the result of a least square curve fit through the data points at the theoretical value of β. In some cases, it appeared that a longer or shorter wavelength, corresponding to different values of β (or more basic, different values of cut-on frequency), would provide a closer fit to the measured data. As a means of determining the accuracy of the curve fit, and the 'goodness' of the theoretical propagation constants, the 'standard error of the estimate' (the square root of the 'sample variance') was computed. This computation is described in more detail in the section on RADIATION IMPEDANCE.

In attempting to determine the best value of β to fit the measured data, the curve-fit routine was used repetitively and incremental values of β were used. The error was examined for each computation and the β value which produced the minimum error was taken as the optimum value.

This procedure seemed inherently prone to the whims of experimental error, since one bad data point could result in a minimized value of error at a cut-on frequency (or wavelength) significantly removed from the actual value. After examining the results, it was found that the theoretical value of propagation constant gave the 'best' fit to the measured data points in most cases. The conclusion from this was that within minor error limits, the propagation constant is as computed, within experimental tolerance, and thus, the theory agrees exceptionally well with experiment.

IV.3.3. Mode shapes

Sound pressure distributions in both the angular and radial coordinate directions were measured for several thousand combinations of the controlling variables, which were: (1) frequency, (2) transducer mode simulation, (3) axial position, and (4) radial position for angular plots and angular position for radial plots. In most cases, the data were plotted on an X-Y recorder and also recorded on digital tape.

Several modes were studied extensively, in order to determine axial standing wave ratios, propagation speed, mode purity and comparison with theory. It was difficult to determine how much of this data could usefully be presented. Finally, it was decided to present only one angular and/or one radial plot for each mode studied, exactly as that plot was recorded and to show the calculated mode shape in comparison with that measured data. Mode shapes are presented for the (0,0), (1,0), (2,0), (3,0), (4,0), (5,0), (2,1), (5,1), and (6,2) modes in figures 38 through 52. These modes were recorded at various frequencies as noted.

Figure 38 illustrates the angular sound pressure distribution for a plane mode simulation at 1000 Hertz. There is a variation in the angular direction of 2 decibels and 15 degrees phase angle, indicating the presence of other modes at very low level. At the frequency of this test, three other higher order modes, i.e. the (1,0), (2,0), and (3,0) were also cut on. Thus, this plot demonstrates the ability to excite one mode in exclusion of other propagating modes. Figure 39 demonstrates the radial behavior of the plane mode and shows no discernible variation from the theoretical shape.

Figures 40 through 47 demonstrate the purity of both angular and radial mode shapes for higher order angular modes in combination with the lowest order radial mode. The angular variation of the (1,0) mode is shown in figure 40, with the computed amplitude and phase shape represented by solid circles and triangles. The measured phase shape is relatively true to the theoretical shape except in the region of very low amplitude. This deviation is not surprising, since at this low amplitude, other spuriously excited modes and

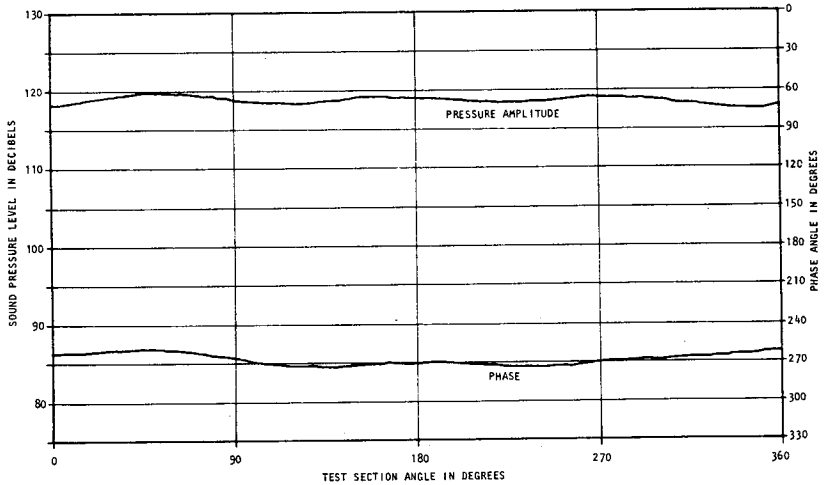


Figure 38. Angular SPL and Phase Distribution in Test Section for Plane Mode Simulation at 1000 Hertz

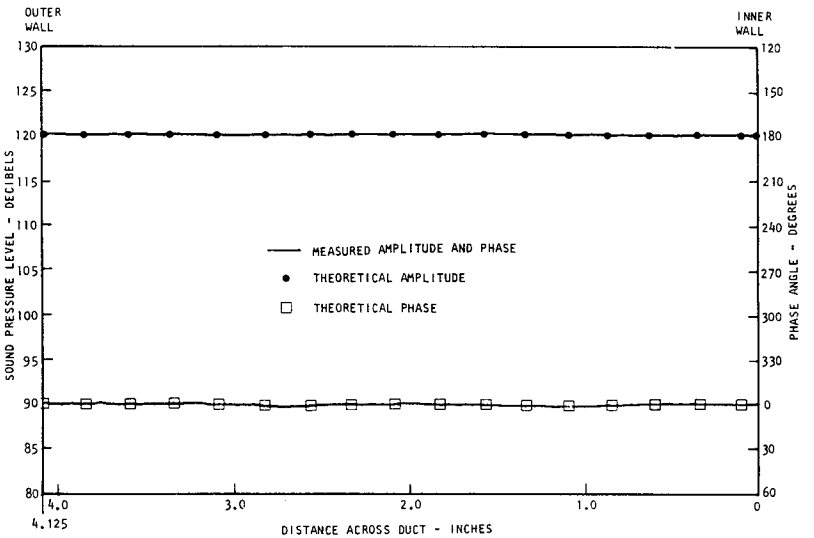


Figure 39. Comparison of Experimental and Theoretical SPL and Phase for Radial Hard Wall (0,0) Mode Shape at 1000 Hertz

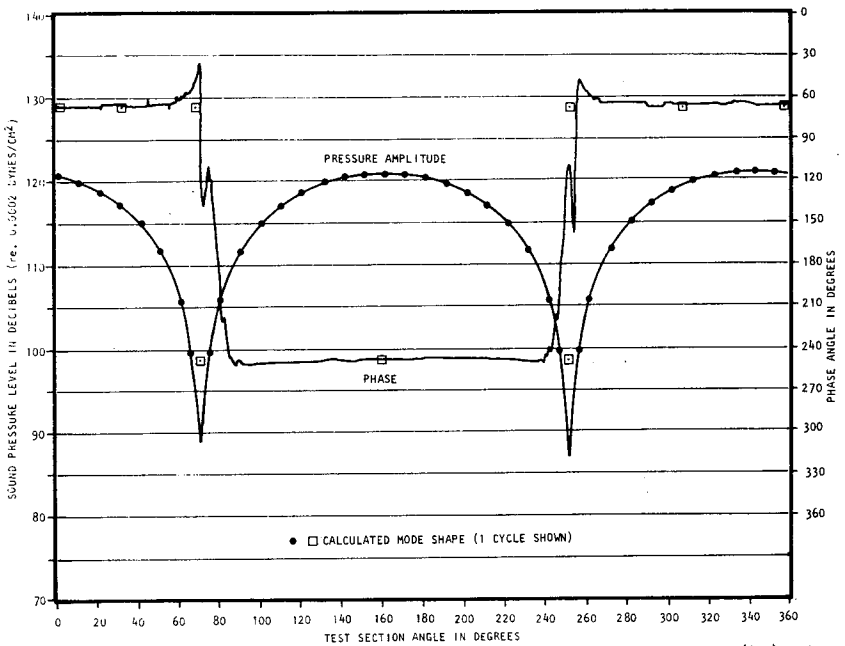


Figure 40. Comparison of Experimental and Theoretical SPL and Phase for Angular Hard Wall (1,0) Mode Shape at 304.3 Hertz

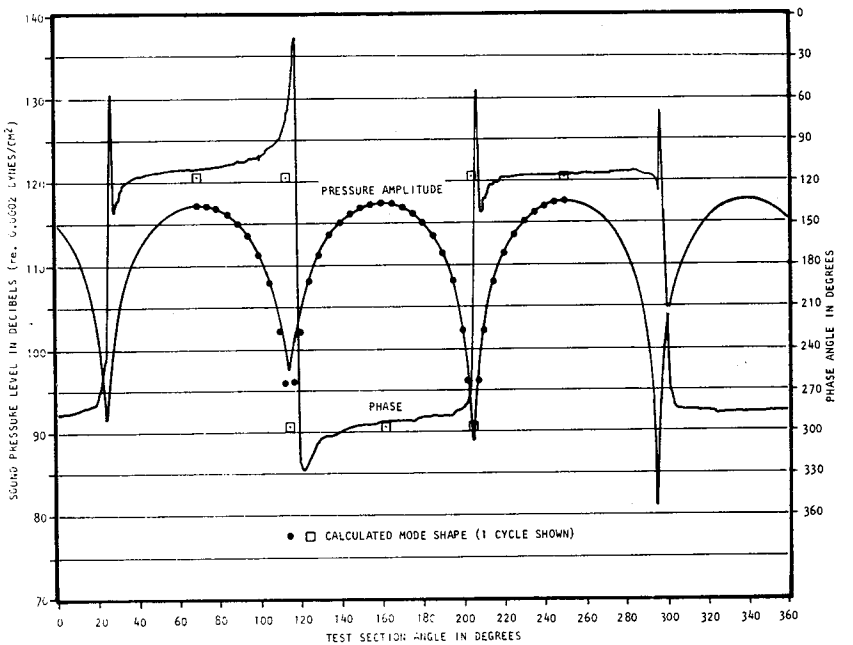


Figure 41. Comparison of Experimental and Theoretical SPL and Phase for Angular Hard Wall (2,0) Mode Shape at 590.6 Hertz

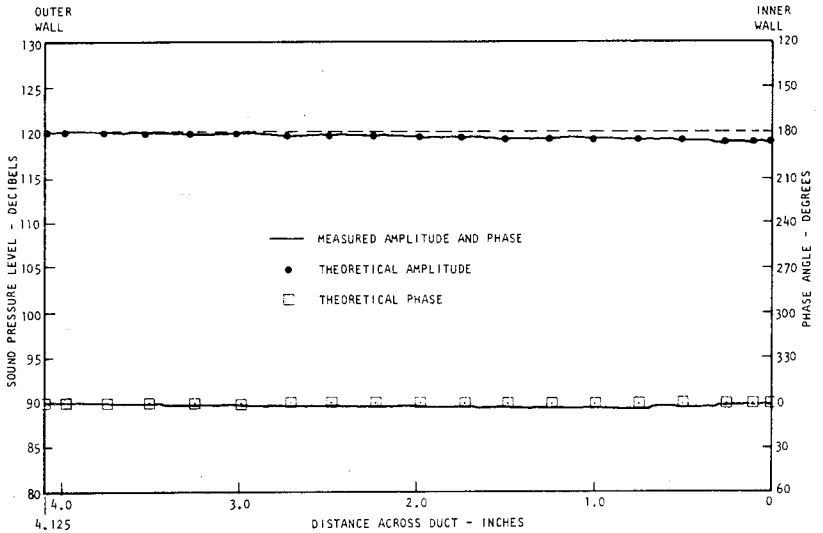


Figure 42. Comparison of Experimental and Theoretical SPL and Phase for Radial Hard Wall (2,0) Mode Shape at 590.6 Hertz

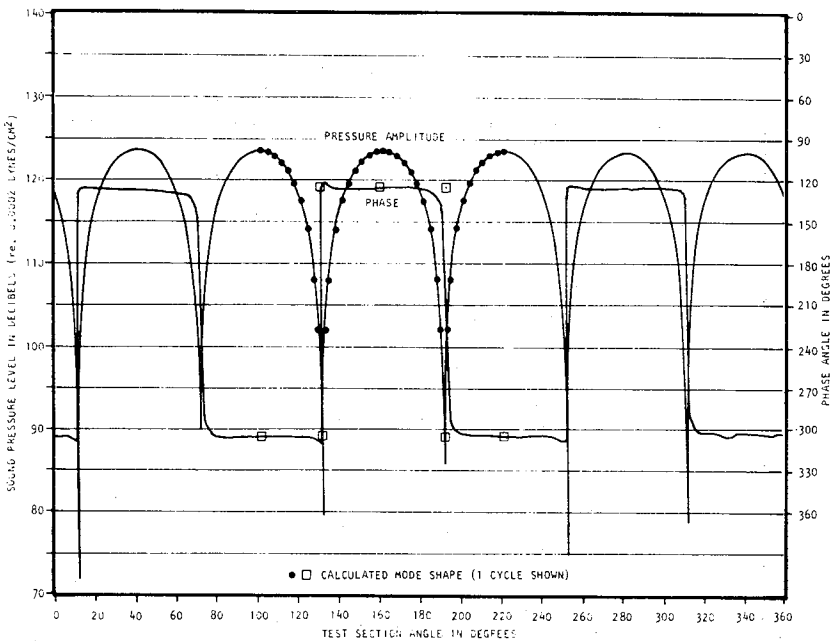


Figure 43. Comparison of Experimental and Theoretical SPL and Phase for Angular Hard Wall (3,0) Mode Shape at 878.6 Hertz

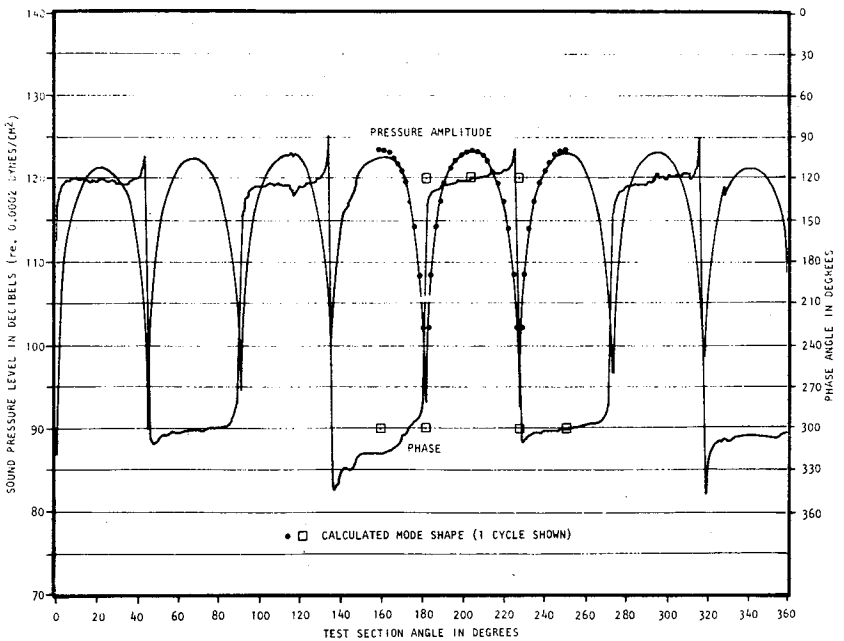


Figure 44. Comparison of Experimental and Theoretical SPL and Phase for Angular Hard Wall (4,0) Mode Shape at 1156.5 Hertz

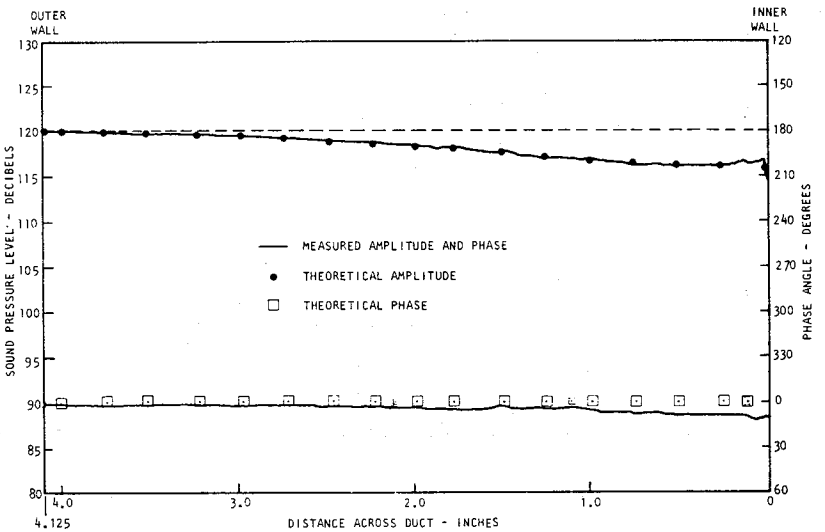


Figure 45. Comparison of Experimental and Theoretical SPL and Phase for Radial Hard Wall (4,0) Mode Shape at 1156.5 Hertz

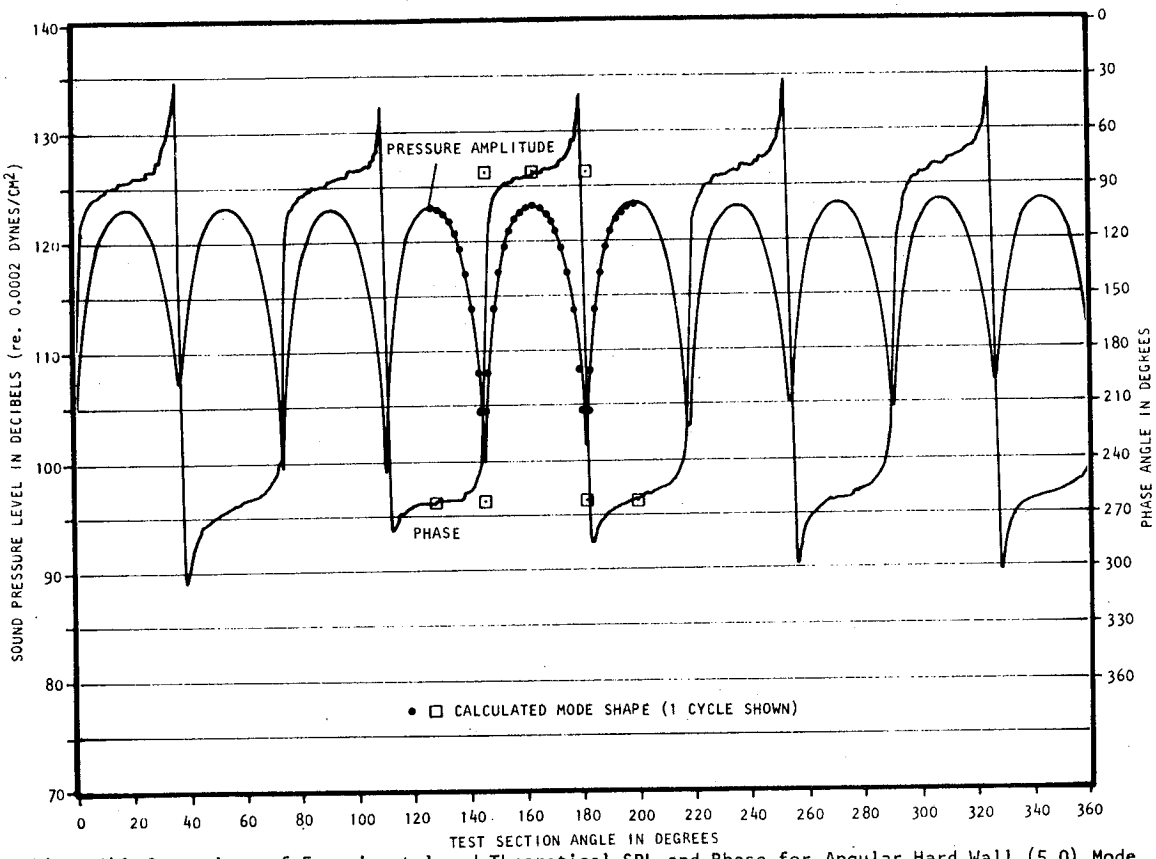


Figure 46. Comparison of Experimental and Theoretical SPL and Phase for Angular Hard Wall (5,0) Mode Shape at 1428 Hertz

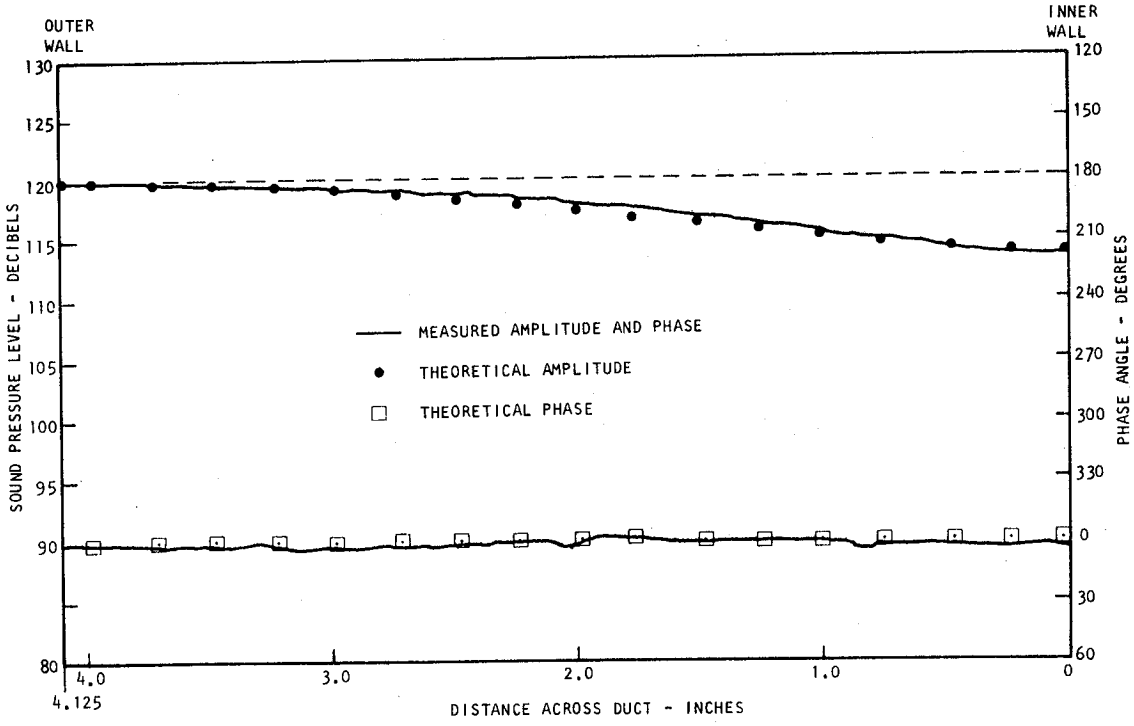


Figure 47. Comparison of Experimental and Theoretical SPL and Phase for Radial Hard Wall (5,0) Mode Shape at 1428 Hertz

spinning mode components not evident in the amplitude plot can seriously affect the phase meter output.

Figures 41 and 42 show the comparison between theory and experiment for the (2,0) angular and radial mode shapes. Note that the predicted 1 dB lower amplitude at the inner wall as compared to the outer wall for the radial shape is reproduced by the experiments with great fidelity. Comparisons with similar accuracy are shown in the cases reproduced in Figures 43 through 47.

Three higher order radial modes were studied. Results from these tests are illustrated in Figures 48 through 52. Figure 49 is, of course, similar to Figure 41, however, it is excited at a frequency very near the (2,1) mode cut-on frequency. The radial behavior is shown in Figure 48. The comparison is quite good with the exception of a zero shift. This is, in all likelihood, due to a small content of (2,0) mode, which when summed with the (2,1) mode, would result in the observed zero shift. A similar observation can be made about the comparison between the (5,1) theoretical and experimental radial mode shapes. Finally, a radial mode with two minima, the (6,2) mode, is shown in Figure 52. Here, the comparison is exceptional, especially considering that this test was conducted at 3778 Hertz.

In summary, it can be concluded that duct modes in a rigid wall annulus are quite accurately predicted by the theory, both in shape and cut-on frequency.

IV.3.4. Frequency response in hard wall duct

It was shown earlier in this section that the cut-on frequency could be determined from the frequency of peak response and the ratio of peak to steady state response amplitude for a single mode, such as shown in figure 31. In order to obtain a curve such as shown in figure 31, it was necessary to excite the mode of interest in isolation. This is very difficult to do, since the mode set-up is dependent on frequency, remembering that the drivers have different characteristic functions (illustrated by figure 21) as frequency varies. Thus, to conduct a frequency sweep of more than 30-50 Hertz range for a single mode excitation would be very tedious, since the mode set-up procedure would have to be repeated every 30-50 Hertz.

However, another frequency response curve, which produces informative results, is obtained by driving the duct with a single transducer, simulating a point velocity source on the wall, while maintaining the sound pressure output of that transducer at a constant level with increasing frequency. At low frequencies, where only a few modes are cut on (and propagating) the cut-on characteristics of each mode can be examined. Figure 53 is an example of the hard wall duct frequency response from 280 Hertz to 3000 Hertz. The mode cut-on frequencies are indicated for those which are clearly identifiable.

The peaks following the primary cut-on peak are a result of interference between multiple modes, due to the differing wavelengths (caused by differing propagation speeds). This is more clearly illustrated in figure 54 for

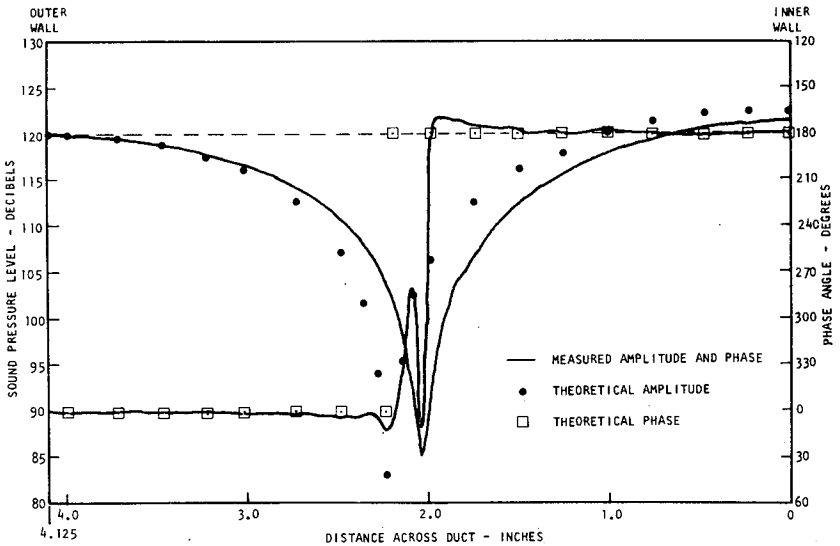


Figure 48. Comparison of Experimental and Theoretical SPL and Phase for Radial Hard Wall (2,1) Mode Shape at 1795 Hertz

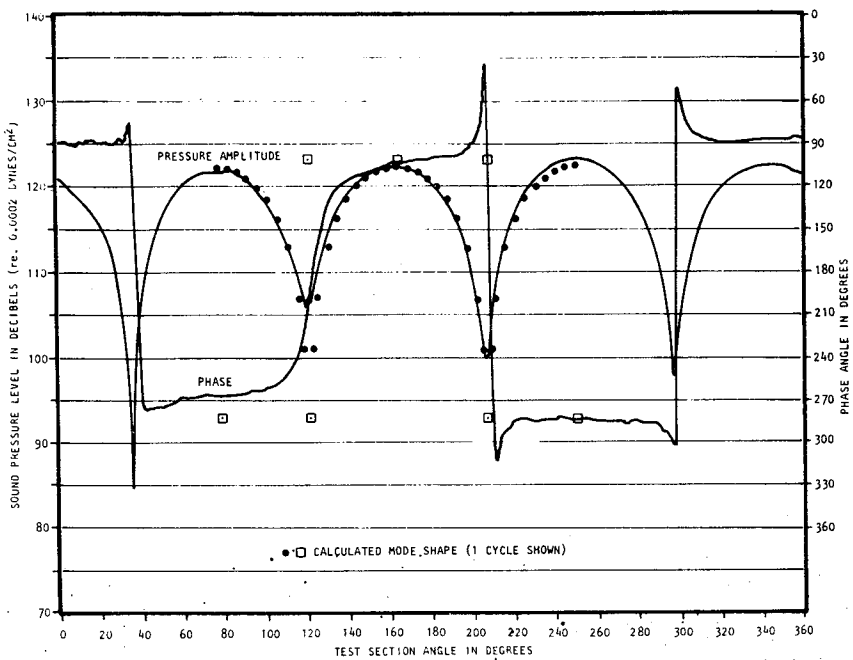


Figure 49. Comparison of Experimental and Theoretical SPL and Phase for Angular Hard Wall (2,1) Mode Shape at 1795 Hertz

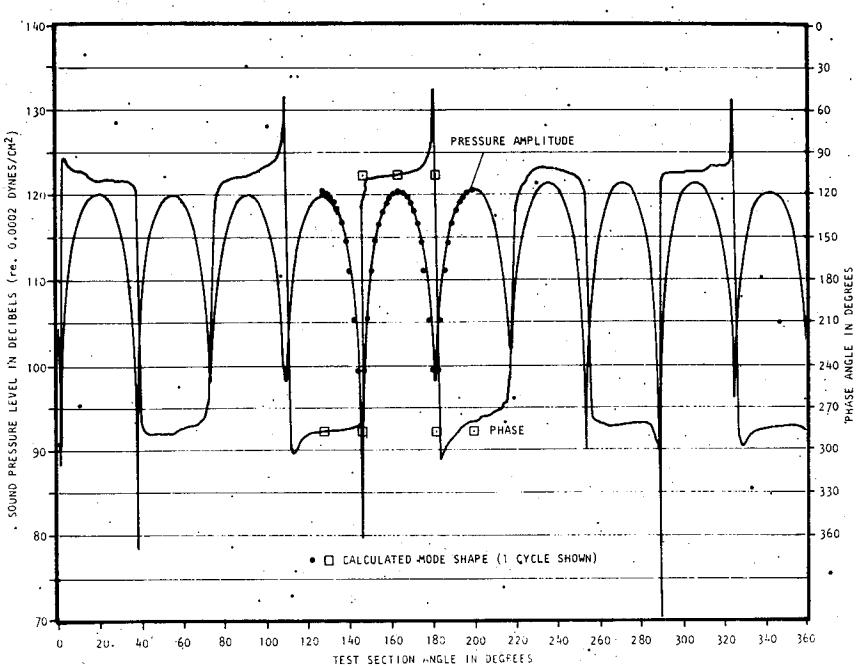


Figure 50. Comparison of Experimental and Theoretical SPL and Phase for Angular Hard Wall (5,1) Mode Shape at 2335 Hertz

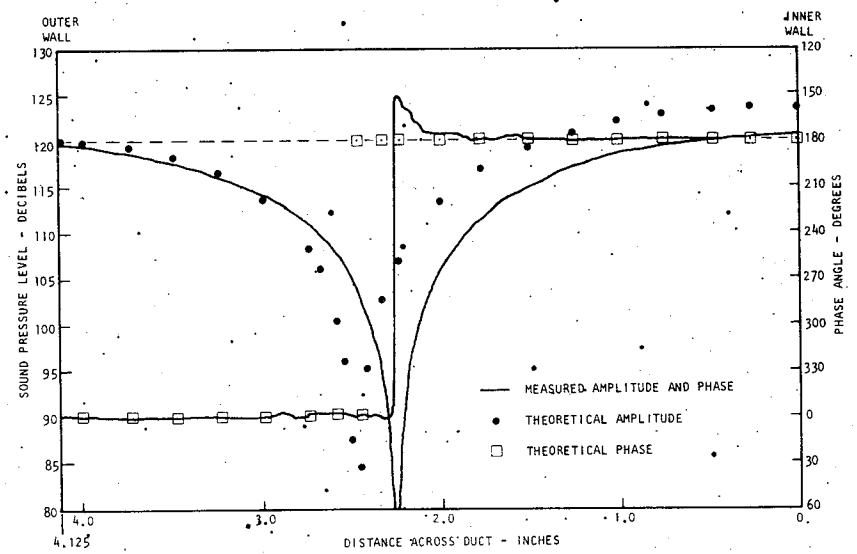


Figure 51. Comparison of Experimental and Theoretical SPL and Phase for Radial Hard Wall (5,1) Mode Shape at 2335 Hertz

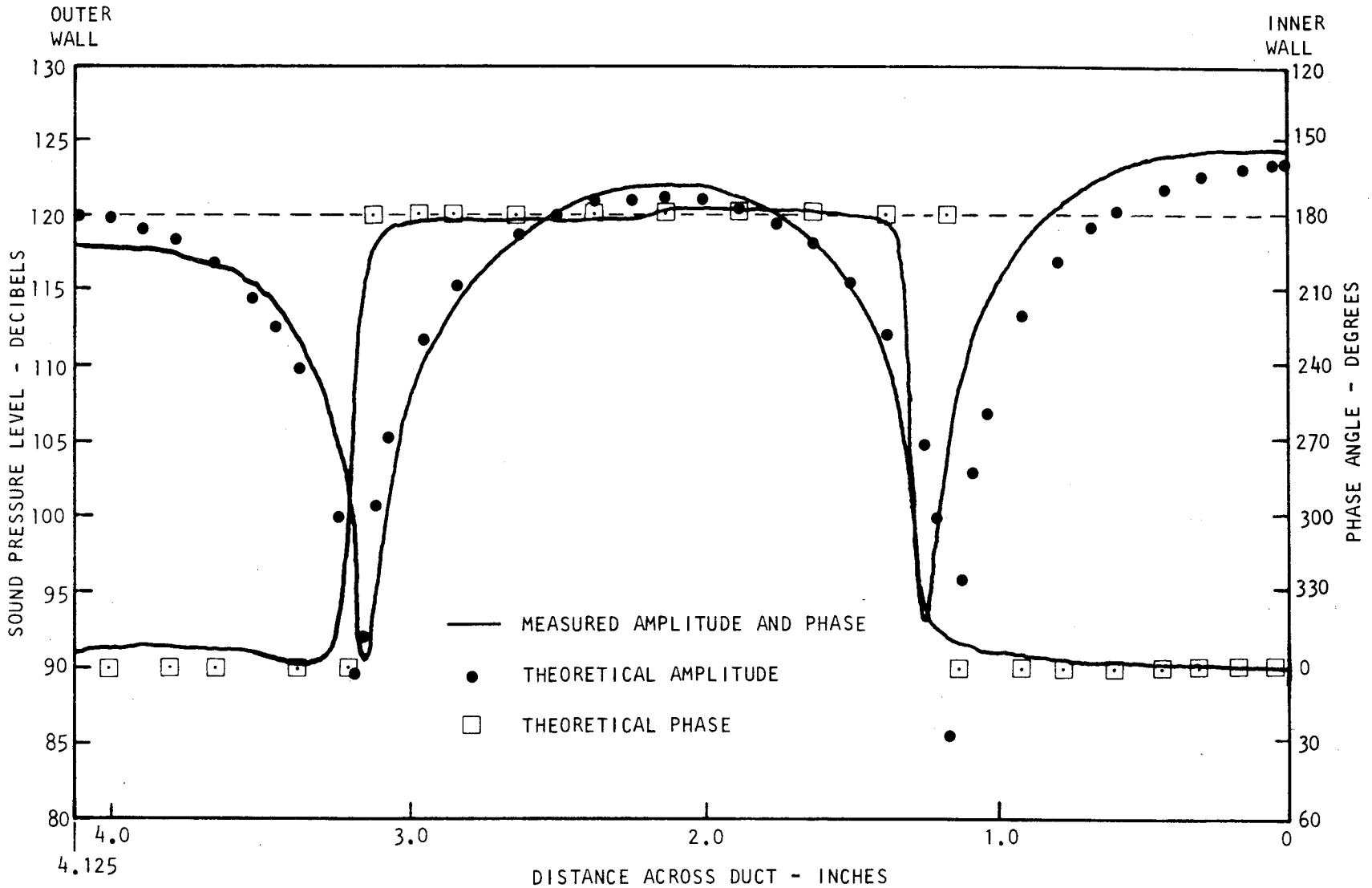


Figure 52. Comparison of Experimental and Theoretical SPL and Phase for Radial Hard Wall (6,2) Mode Shape at 3778 Hertz

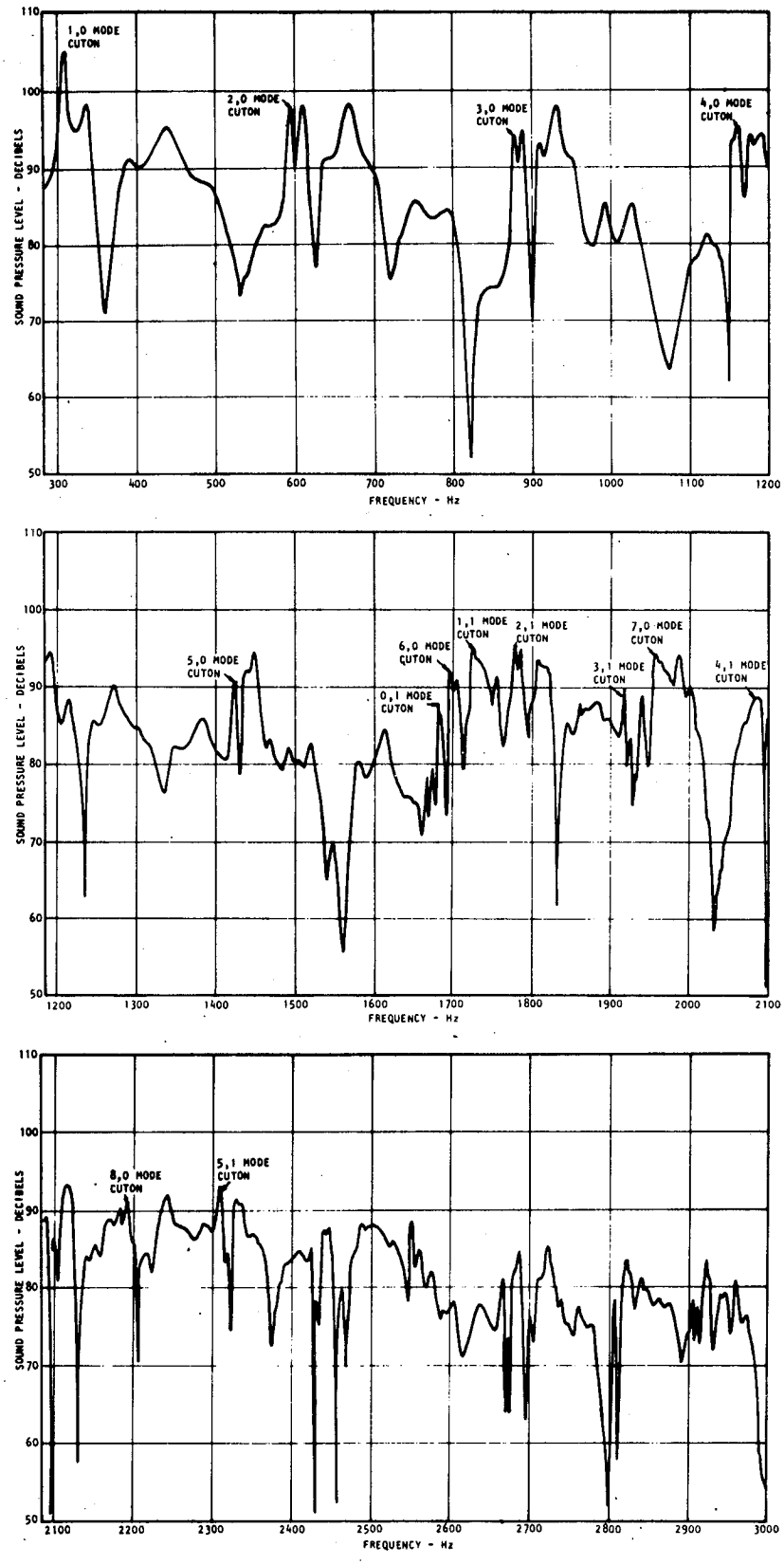


Figure 53. Duct Acoustic Response for One Driver Excitation

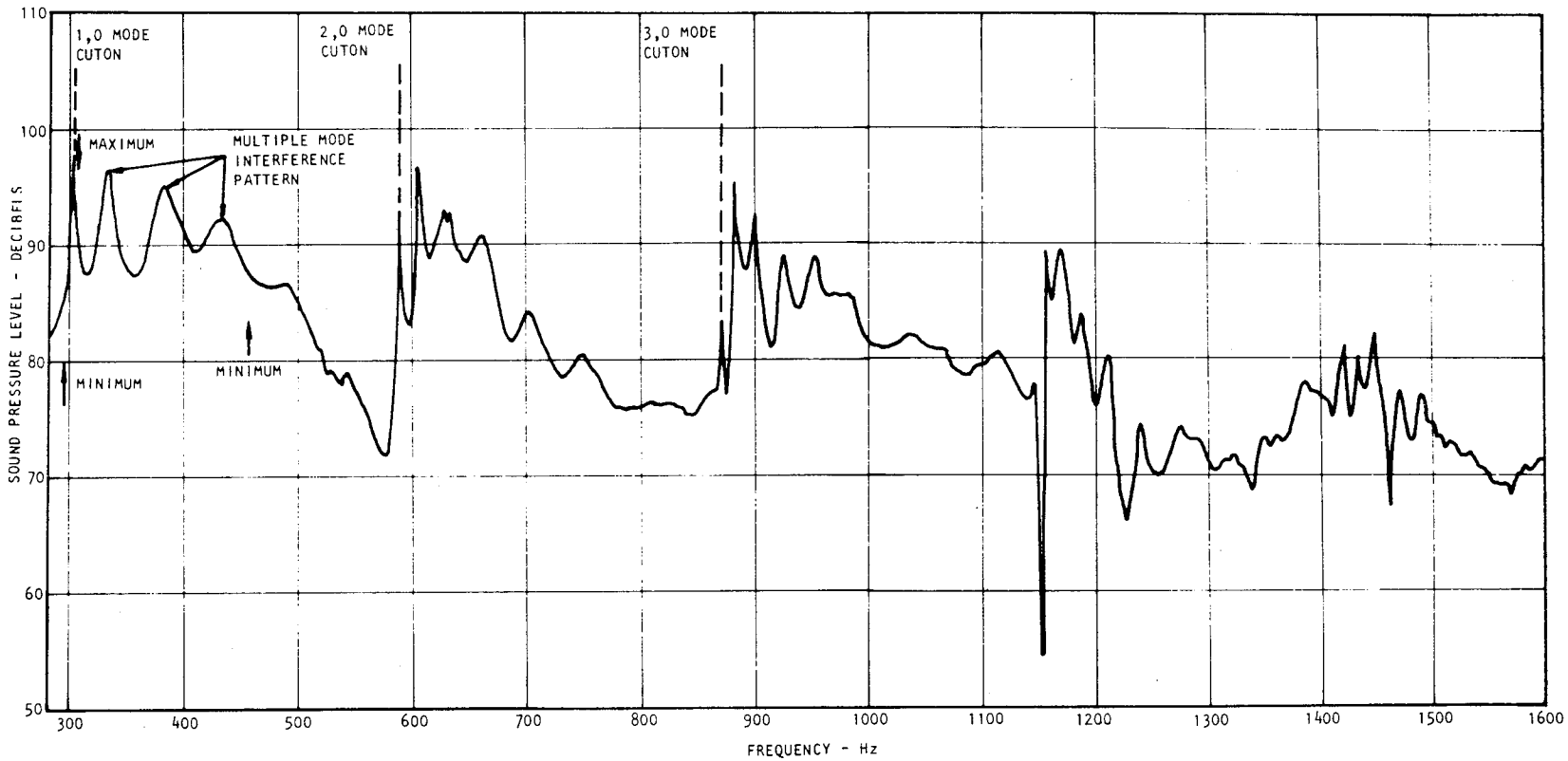


Figure 54. Duct Acoustic Response for One Driver Excitation at an Axial Location of 5.3 Feet from Driver

another position in the duct. Only the first four modes are involved in this illustration. At the cut-on frequency of the (1,0) mode the wavelength constant, β_{10} is zero, thus the axial wavelength is infinite. As frequency increases, this wavelength decreases very rapidly with the wavelength of the plane mode remaining inversely proportional to frequency. The wavelength for the higher order modes, λ_{mn}, is equal to

$$\lambda_{mn} = \frac{c}{f\sqrt{1 - (f_{mn}/f)^2}} \tag{66}$$

This relationship is illustrated in figure 55 for the plane and (1,0) modes, showing the axial wavelength differences near cut-on.

A very simple theory is hypothesized to explain the response peaks following the cut-on response maximum value. Assume the duct extends to infinity in both directions. Then the phase difference between two modes at z, excited by a point source at z = 0, is, assuming that the two modes are in phase at the source,

$$\phi = (k_1 - k_2)z. \tag{67}$$

It is seen that when this phase difference is 0, 2π, 4π, ..., reinforcement between the modes occurs and when the difference is π, 3π, 5π, ..., cancellation results. Thus, in the infinite hard wall duct, assuming no attenuation, the relationship,

$$n\pi = (k_1 - k_2)z, \tag{68}$$

will result in either a maximum or a minimum if n is even or odd. If k_1 is assumed to represent the plane mode and k_2 a higher order mode, then

$$n\pi = \frac{2\pi f}{c} z\ (1-\beta), \tag{69}$$

recognizing that $\beta = \sqrt{1 - \left(\frac{f_n}{f}\right)^2}$, where f_n is the cut-on frequency. Solving this relationship for the frequency, f, which corresponds to a value of n, the result is

$$f = \frac{f_n^2 z}{nc} + \frac{nc}{4z}\ . \tag{70}$$

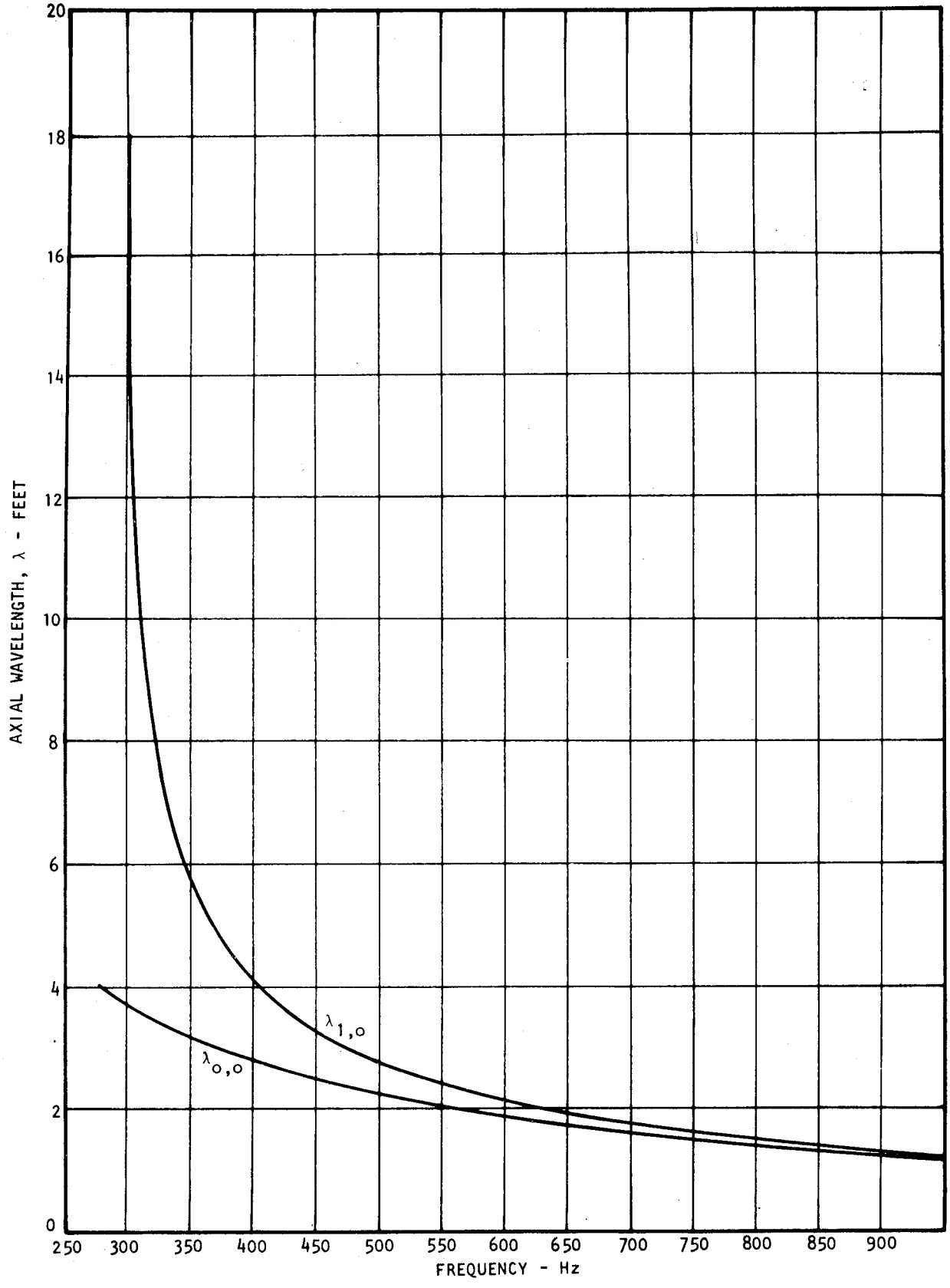


Figure 55. Illustration of Modal Axial Wavelength

For the (1,0) mode, which has a cut-on frequency of 293.4 Hertz at a temperature of 66.9°F (corresponding to a speed of sound of 1124.9 fps), the frequencies for constructive and destructive interference at a point z = 5.30 feet from the center of the source are given in the following table.

TABLE II

FREQUENCIES FOR CONSTRUCTIVE AND DESTRUCTIVE INTERFERENCE

n	f (Hertz)
0	∞
1	458.8
2	309.0 ↑
3	294.4 corresponds to positive β
4	313.6 corresponds to negative β
5	346.3 ↓
6	385.9
7	429.2
8	475.0
⋮	⋮

Solutions in the table show that as n is increased, the frequencies first decrease and then increase. The values of n corresponding to increasing values of frequency represent waves traveling in the direction opposite to the plane wave, but still in phase with the plane wave at z = 0. These solutions are meaningless in the infinite duct and misleading in the finite length duct unless the end had a rigid termination at a distance from the measuring point equal to the distance from the measuring point to the source (i.e., an image source). Thus, only three values have any meaning in this comparison. A minimum is predicted at 458.8 Hz, and it appears that this is reasonably reproduced by the experiment. The maximum predicted at 309 Hz is also in reasonable comparison with experiment as well as the minimum at 294 Hz. However, it is obvious that several more maxima and minima exist in the actual situation. The only possible explanation for these is end reflection, resulting in waves propagating in both directions. An analysis similar to the one just presented could similarly be performed, accounting for the waves reflected

from the termination and the phase shift introduced by the radiation impedance. No doubt with this added complication, frequencies of all the other maxima and minima could be predicted.

IV.3.5. Flow effects on cut-on frequency and mode shape

It has been shown that the duct mode cut-on frequency is a function of both the space averaged value of mean flow through the duct as well as the wall shear layer (Mungur and Gladwell, ref. 3). But for the range of velocity, boundary layer thickness and frequency encountered in the tests described, it would also be expected that the plug flow velocity effect derived by Morfey (ref. 20) would apply equally well. Morfey showed that the mode cut-on frequencies are shifted by the flow as follows,

$$k_{mn_f} R_o = \sqrt{1-M^2}\; k_{mn} R_o. \tag{71}$$

The introduction of flow into the test facility usually resulted in a significant drop in temperature, of the order of 10 to 20 degrees Farenheit. This, of course, resulted in a very significant change in cut-on frequency. However, after temperature was stabilized at the test velocity, a new cut-on frequency was determined by one of the methods described in section IV.1.1. After the test, the results were converted to dimensionless frequency, kR_o.

As described in section IV.1.1, the location of the exact cut-on frequency relies, to a great extent, on the judgment of the experimenter. During this series of tests, a different investigator was conducting the cut-on frequency determinations. Because of this, the values of cut-on frequency at no-flow were higher than determined in the previous no-flow cut-on frequency tests and reported earlier in this section. The cut-on frequency test results from both series of tests are shown in figure 56, for the (1,0), (2,0), (3,0), (5,0), (2,1), and (5,1) modes. The lower curve for each mode is a plot of the above cut-on relationship, based on the theoretical value of no-flow cut-on frequency. This shape is then transferred for comparison with measured data.

The trends displayed by the measured data certainly confirms the relationship presented by Morfey. While there is some scatter in the data, it must be realized that this scatter about the theoretical shape is less than 0.5% for all data recorded and except for 2 data points (the no-flow data for the (2,1) and (5,1) modes), the scatter is less than 0.2% and generally follows the predicted $\sqrt{1-M^2}$ shape.

Theoretically there is no effect of flow on mode shape in the hard wall duct if the plug flow type of analysis, such as Morfey used, is chosen. There is, however, the possibility of a significant effect due to the wall shear layer. The numerical analysis described in the next section was used to compute mode shapes for the experimental flow velocity profiles. The modification of the mode shape due to the very thin shear layer for this facility was

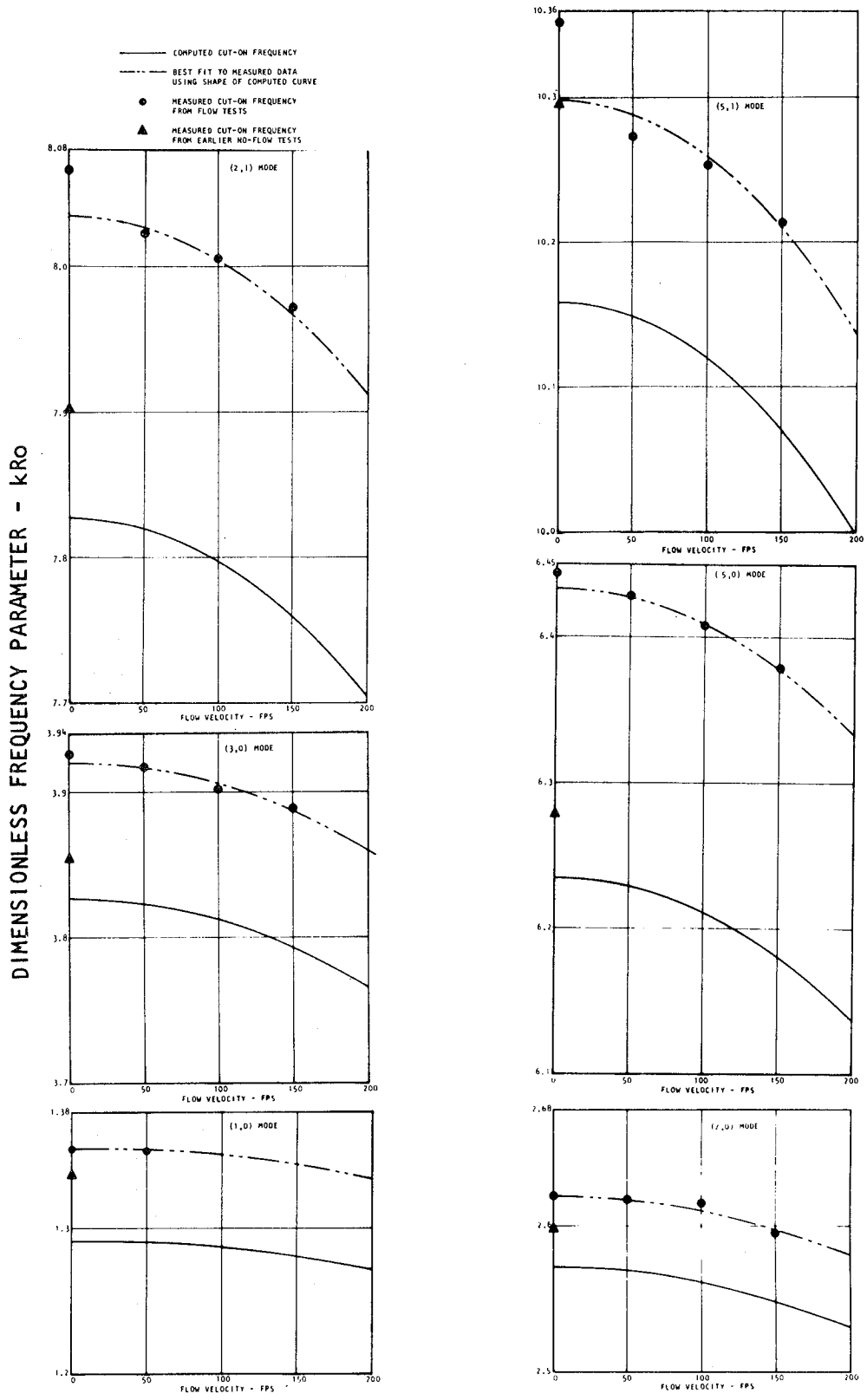


Figure 56. Comparison of Experimental and Theoretical Mach Number Effects on Cut-on Frequency

computed to be insignificant. Examples of experimentally determined mode shapes for the (3,0) angular mode and the (5,1) radial mode at various velocities are shown in figures 57 and 58. The degradation of shape with increasing velocity is due to flow noise, either present in the duct or else generated by the microphone probe. The data, as presented, were filtered through a 2 Hertz narrow band filter. The shapes in figures 57 and 58 are the plots recorded at the experimentally determined value of cut-on frequency. The radial shapes in figure 57 confirm that the effect of flow on the shape is insignificant, if the flow noise effects are ignored.

V. WALL IMPEDANCE MEASUREMENTS

The prime requirement, as defined in section VI for the accurate prediction of acoustic attenuation in a lined duct is an accurate determination of the boundary conditions (in this case, the acoustic impedance) at the wall.

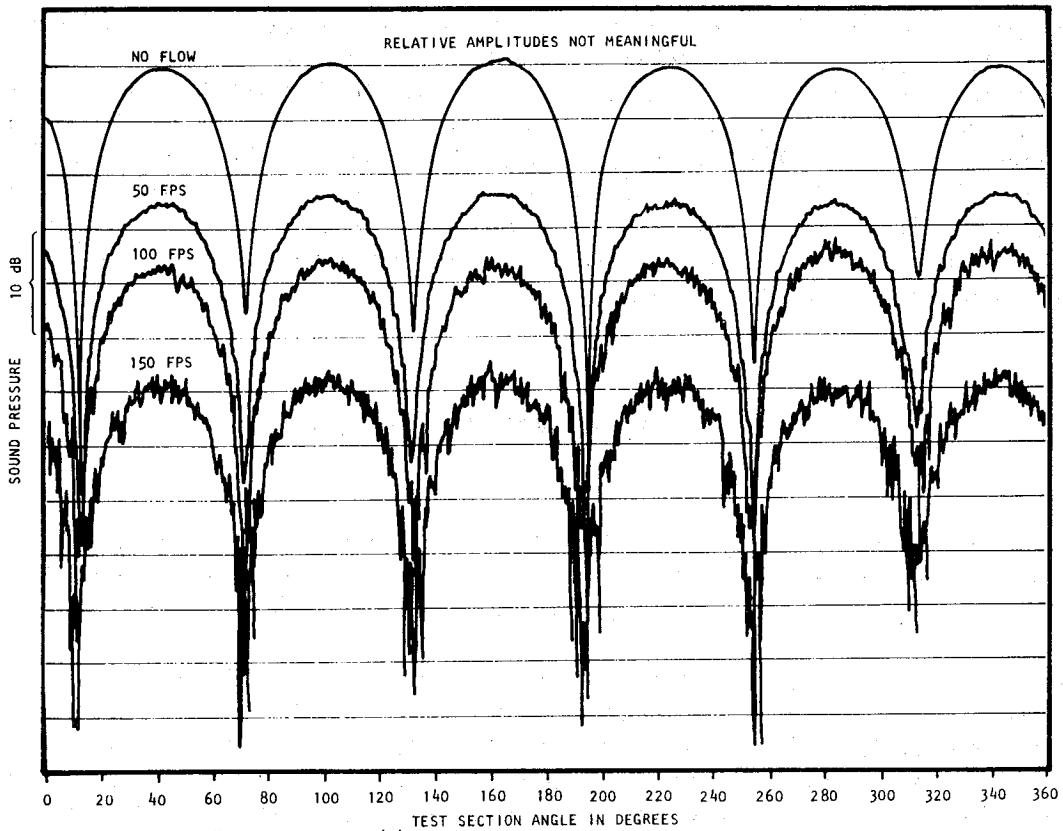
The following method of wall acoustic impedance measurement, commonly termed the "two microphone" method has been developed using as a rationale the fact that impedance values measured in the duct environment would be more representative than values determined from any other technique. That is to say, other types of impedance measurements (e.g., from an impedance tube test) have been made in the past and found to be inadequate for the duct application, particularly when mean flow or peculiar duct geometries are used in the attenuation tests.

The two microphone method was first suggested by Sivian (ref. 42), but for some reason was not considered practical until recent times when Philips (ref. 44) first attempted to use the method (although in his case the position of the measurement locations has raised some questions on the validity of his results). Soon after this, this method was used by Binek (ref. 45) with some success, using a turbulent boundary layer as the source pressure excitation.

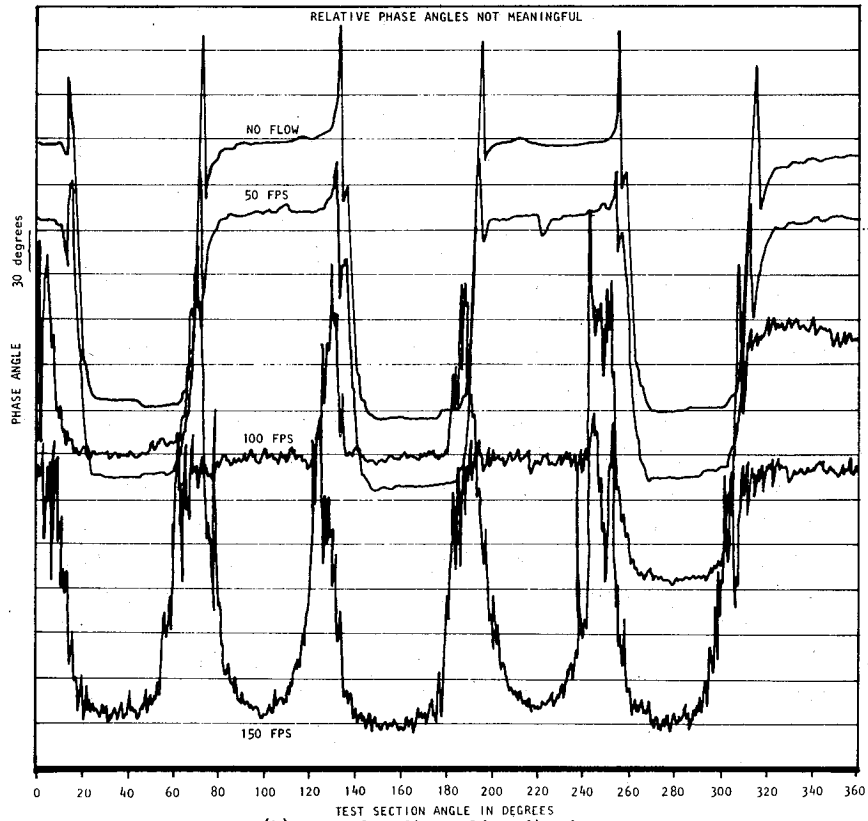
In this report the theoretical justifications (together with the implied limitations) follows that given by Tester and Dean (ref. 46) and will only be briefly summarized here. The method is based on the fact that a simple relationship between acoustic pressure and particle velocity exists. It is assumed that the particle velocities on either side of the cavity surface layer (considered to be infinitely thin) are identical.* The condition of application for this method is that the liner is locally reacting, i.e. that the wavelength is large compared to the cavity cross dimensions and that there is no transmission through the lining in a direction parallel to the liner face (rigid cavity walls). Only two measured quantities are required for the two microphone method: (1) the acoustic pressure at any point in the cavity, (2) the acoustic pressure above the cavity surface and its phase relationship with the cavity pressure.

---

*This discussion particularly concerns a resonant cavity type of liner.

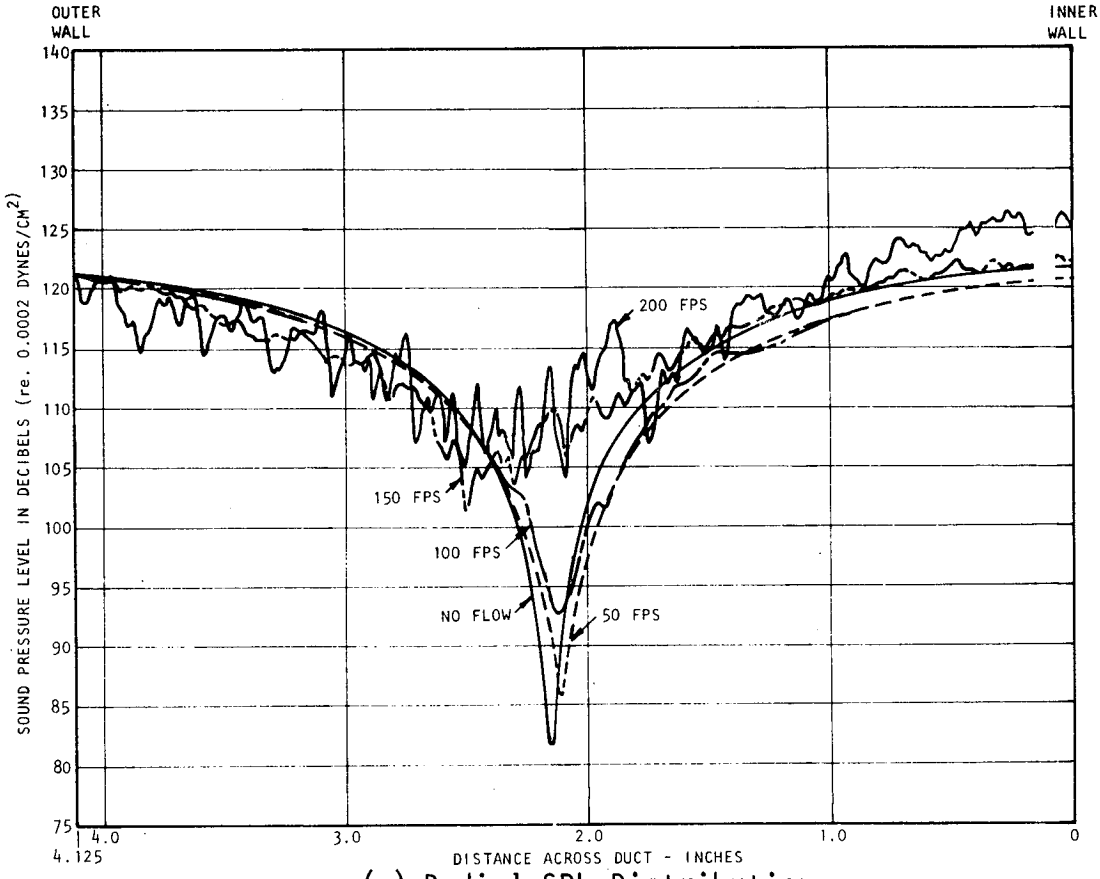


(a) Angular SPL Distribution

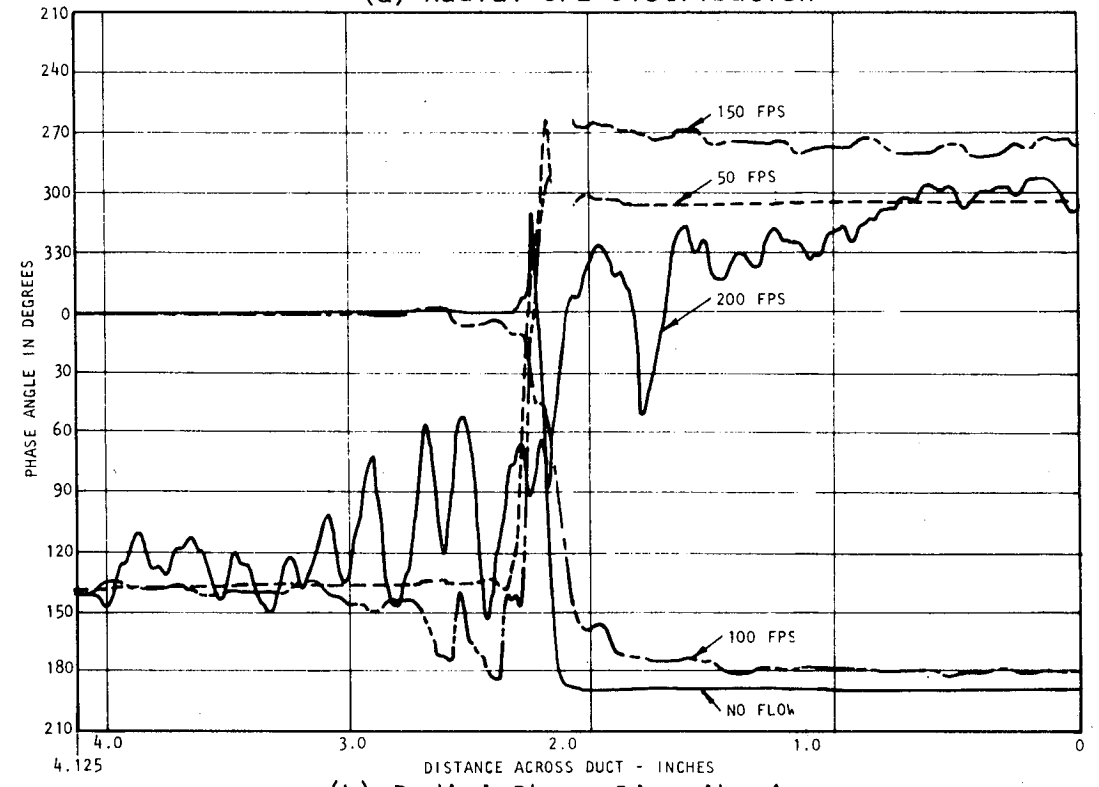


(b) Angular Phase Distribution

Figure 57. Effect of Flow Velocity on Angular Hard Wall (3,0) Mode Shape



(a) Radial SPL Distribution



(b) Radial Phase Distribution

Figure 58. Effect of Flow Velocity on Radial Hard Wall (5,1) Mode Shape

V.1. Basic Theory of Local Impedance Measurement - Two Microphone Method

Consider a lining as in Figure 59 with a y-axis origin at the back wall. The liner consists of a porous surface and an air space backing with transverse dimensions less than a half-wavelength; i.e., wave motion is in the y direction only.

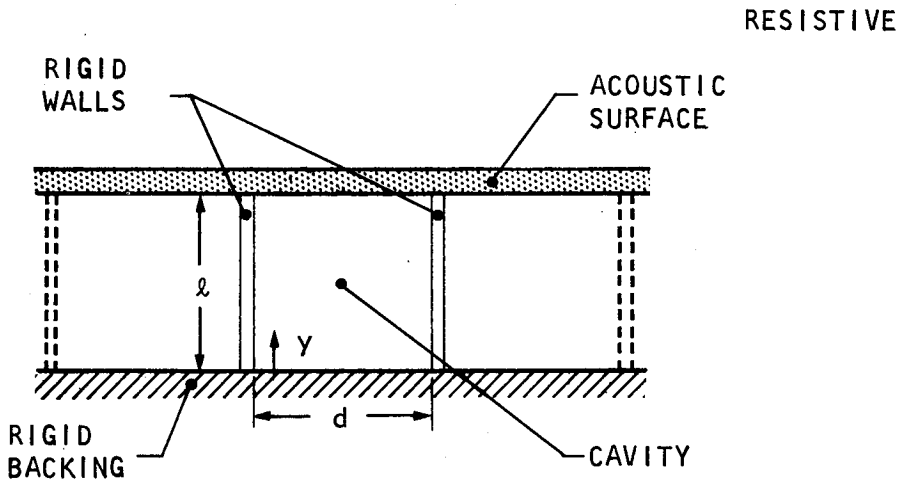


Figure 59. Classical Resonant Cavity Liner Element

The acoustic pressure in the cavity is given by,

$$P = 2\, P_B e^{j\omega t} \cos(ky), \tag{72}$$

where P_B is the cavity back wall acoustic pressure; but

$$\rho \frac{\partial u}{\partial t} = \frac{-\partial P}{\partial y} \quad \text{(the linearized momentum equation)}. \tag{73}$$

This results in the following expression for particle velocity, u,

$$u = \frac{-j}{\rho c} 2\, P_B e^{j\omega t} \sin ky, \tag{74}$$

The impedance, Z, is the ratio of pressure to particle velocity,

$$Z = \frac{P}{\rho c u} = -j \cot(ky), \tag{75}$$

with Z being the impedance at any cavity point y behind the resistive facing, normalized to ρc.

The normalized acoustic impedance at the front surface of the resistive facing is

$$Z = \frac{P_F}{u} = \frac{-jP_F e^{j\phi}}{P_B} \operatorname{cosec}(kl), \tag{76}$$

where ϕ is phase angle between P_F and P_B.

In terms of sound pressure level measurements, the impedance is

$$Z = -j\ 10^{(SPL_F - SPL_B)/20} e^{j\phi} \operatorname{cosec}(kl). \tag{77}$$

The resistive and reactive components are

$$R = 10^{(SPL_F - SPL_B)/20} \frac{\sin\phi}{\sin(kl)} \tag{78}$$

$$X = 10^{(SPL_F - SPL_B)/20} \frac{\cos\phi}{\sin(kl)} \tag{79}$$

V.2. Measurement Error Effects

V.2.1. General considerations

There are two major disadvantages associated with the two microphone method. First, the measurement position of the microphone in front of the liner must be close to the liner surface; that is, at a distance small compared with the wavelength (otherwise the amplitude and phase measurements will be in error, depending of course on the properties of the duct acoustics field). But it must not be so close that an unrepresentative pressure is measured; for example, if the liner is a simple perforate, then close to the surface the pressure adjacent to a rigid part of the surface will differ from that adjacent to a hole. Thus, the effective measuring point must be in the

"far field" of the liner but still at a distance small compared with the wavelength. Thus, it is even possible that this proper measurement point may not exist.

The second disadvantage concerns a similar difficulty; that is, if this distance from the measurement point to the surface is comparable with the boundary layer thickness, then the basic assumptions of the 'two microphone' method are invalidated and the impedance estimate will, strictly speaking be incorrect. In addition, the measurement of an acoustic signal within the boundary layer becomes difficult in terms of separating the acoustic signal from the other pressure components of the turbulence in the boundary layer. It should also be noted that the two microphone method can strictly be applied only to 'simple lumped systems' adhering to the laws of homogeneous isotropic media.

V.2.2. Error effects on two-microphone method evaluations

For the expected values of resistance, R, with a nominal 40 rayl (felt-metal) liner with a 1/2 " cavity depth, the changes in sound pressure level between the front and back walls of the cavity are very small, particularly at the low end of the frequency range, thus considerable care in measurement is required. The necessary increase in accuracy was accomplished by subtracting the two signals (filtered through a 2 Hz filter) with an analog computer and then amplifying the difference signal. The result was recorded from a digital voltmeter to an accuracy of ± 0.03 dB.

The phase differences between each probe microphone are small in the low frequency region and thus the resistance (proportional to sin $\Delta\phi$) is very sensitive to phase inaccuracies (the meter used has, for all practical purposes, an accuracy to 0.6 degrees). From the theory presented earlier the other two major variables are temperature (which controls the speed of sound) and microphone position* from the back wall. Temperature is capable of being measured to an accuracy of 0.2 degrees F and microphone position (measured by a precision potentiometer) to better than 0.005 inch.

Figure 60 shows the percentage errors of resistance and reactance versus frequency for a 10% variation in each of the above variables for the 40 rayl Brunsmet liner with a 1/2" cavity depth. The sign interactions for these changes are given below in Table III from which it can be seen that positive changes in any error quantity lead to positive resistance errors and negative reactance errors.

---

*i.e., this equals the cavity depth for the two microphone evaluation.

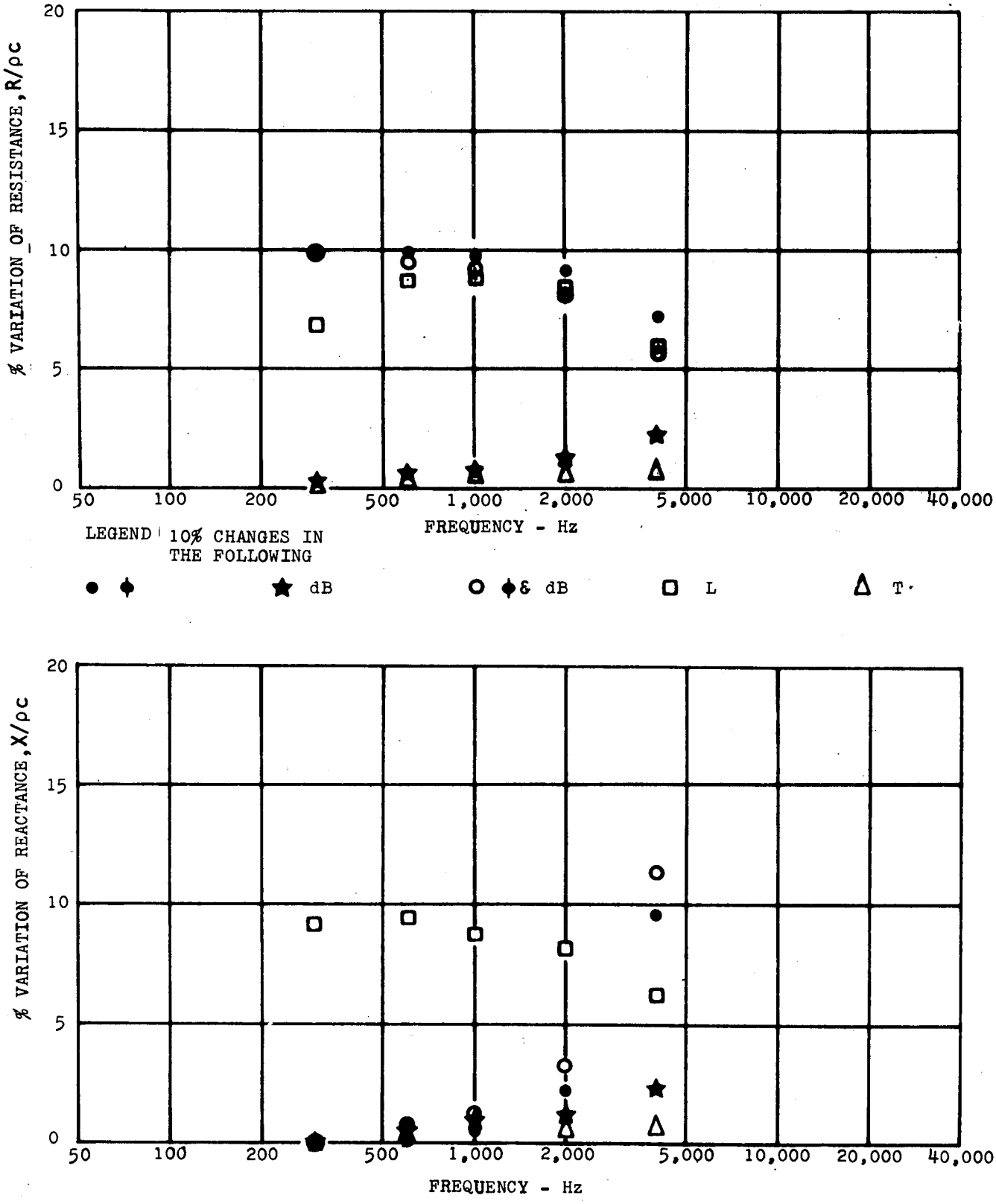


Figure 60. Effect of 10% Variation in SPL, Phase Angle, Temperature and Cavity Depth on a Nominal 40 Rayl Liner with 1/2" Cavity Depth

TABLE III

SIGN CHANGES OF ERRORS IN IMPEDANCE

Error Quantity	Sign of Error Quantity	Sign Change of Impedance	
		R	X
Sound Pressure Level (dB)	+	+	-
	-	-	+
Phase Angle (Degrees)	+	+	-
	-	-	+
Temperature (°F)	+	+	-
	-	-	+
Cavity Depth	+	+	-
	-	-	+

The effect of a 10% phase variation can be seen to cause a change of almost 10% in resistance for all frequencies up to about 2 kHz with the error reducing to about 7½% at 4 kHz. The effect of this change on reactance, on the other hand, is very small at low frequencies, rising to about 2% at 2 kHz and then sharply rising to 10% at 4 kHz.

A 10% change in the sound pressure level difference results in a slowly increasing frequency characteristic for both resistance and reactance, producing in each case changes of only 2½% at 4 kHz. The combined effect of 10% deviations in both SPL and phase differences was also estimated and can be seen to reduce the variations in resistance and to increase the reactance changes compared to the 10% phase only changes.

The variation of temperature affects only the speed of sound. A 10% change in degrees Fahrenheit would not be expected to have much effect. This can be seen to be less than 1% with an increase in both resistance and reactance noted.

On the other hand, a 10% variation in cavity depth produces a peaked resistance characteristic (of about 9% at 1000 Hz) and a decreasing reactance characteristic with frequency (from 10% at 300 Hz to 6% at 4 kHz). Of the four variables it appears that cavity depth (or microphone position) is a most important parameter being capable of affecting both the resistance and reactance roughly in proportion to its own variability. The conclusion is therefore, that precise cavity construction is necessary to produce the desired impedance values or conversely, adjacent cavities of different depths

will cause proportionate changes in both resistance and reactance, which could be an effective means of constructing a broad-band liner.

V.3. Experimental Configurations

Two distinct two-microphone measurement configurations were used, depending on the two different cavity depths, viz 1/2 inch and 1-1/2 inches, respectively. For the 1/2" depth cavity liners figures 61 and 62 show the layout of the probes in the test duct. The microphone voltages were filtered through a 2 Hz filter, converted to logarithmic DC voltages (as described earlier in the facility description) and then input to the analog computer circuit of figure 63. This produced an amplified difference signal which was measured by a digital voltmeter (or by a probability density analysis on a real-time correlator, if fluctuations caused by low signal to noise ratios existed when high air flows were present). The phase angle was measured between each microphone with a digital phase meter, using the filtered amplified microphone outputs directly.

Calibration of the microphone and amplifier amplitude and phase characteristics were achieved by placing the two microphones at a point where they would be measuring the same acoustic field. For convenience, this point was chosen as the back wall of the liner cavity. (The liners can be considered to be locally reacting, thus the acoustic field is normal to the back wall of the cavity.)

For each chosen frequency the procedure is as follows. First, the front wall microphone is set such that the probe tip is at the same point as the fixed back wall microphone. Then, the amplitude and phase calibrations are carried out. Next, the front wall microphone is moved until it is just flush with the inner (duct) surface of the liner. The amplitude and phase differences are again measured and the differences between these values and the calibration values are used to evaluate the wall impedance.

This method was used on both the 20 Rayl and 40 Rayl liners at 6 different hole positions, i.e. hole numbers 16, 18, 22, 24, 28, 30 (the hole number represents the distance in inches from the exit plane of the duct liner). Three values of mean flow velocity were tested, i.e., zero, 50 ft/sec, 150 ft/sec.

For the 1-1/2" cavity depth liner a slight modification of the fixed two microphone technique described above was used. One microphone was traversed from the back wall to the front wall and out into the duct and sound pressure amplitude and phase were recorded directly with an X-Y recorder. The wall pressure amplitude and phase values (phase was measured relative to an oscillator) were taken directly from this traverse by reading from the plots at the appropriate location. In order to eliminate any probe end effects, the probe tube was modified, as shown in figure 64 such that the liner surface hole was always filled with the probe tube. The sound pressure was detected by two small holes drilled in the probe tube at a right angle to the flow.

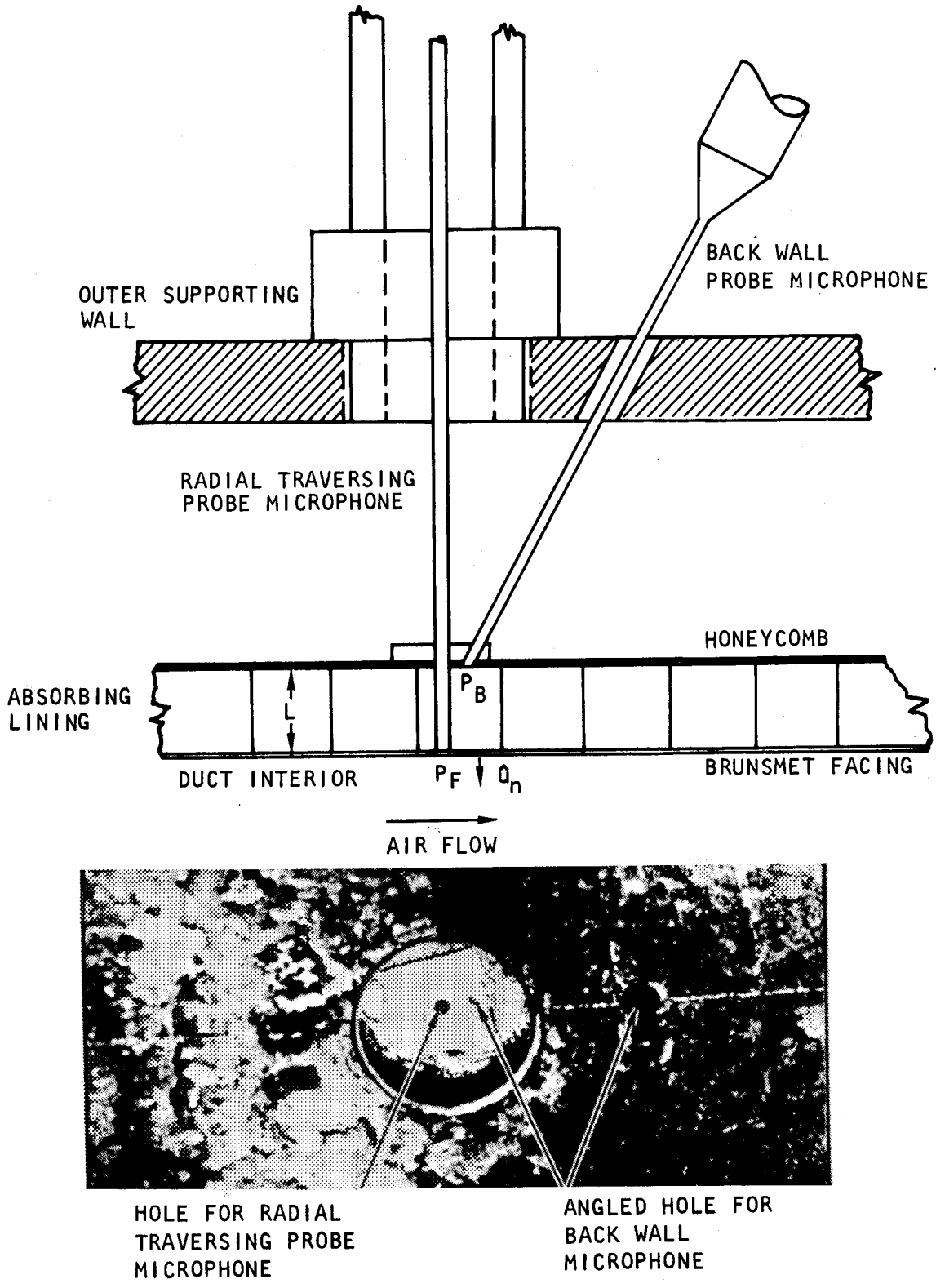


Figure 61. Schematic and Photograph of Two-Microphone Test Arrangement

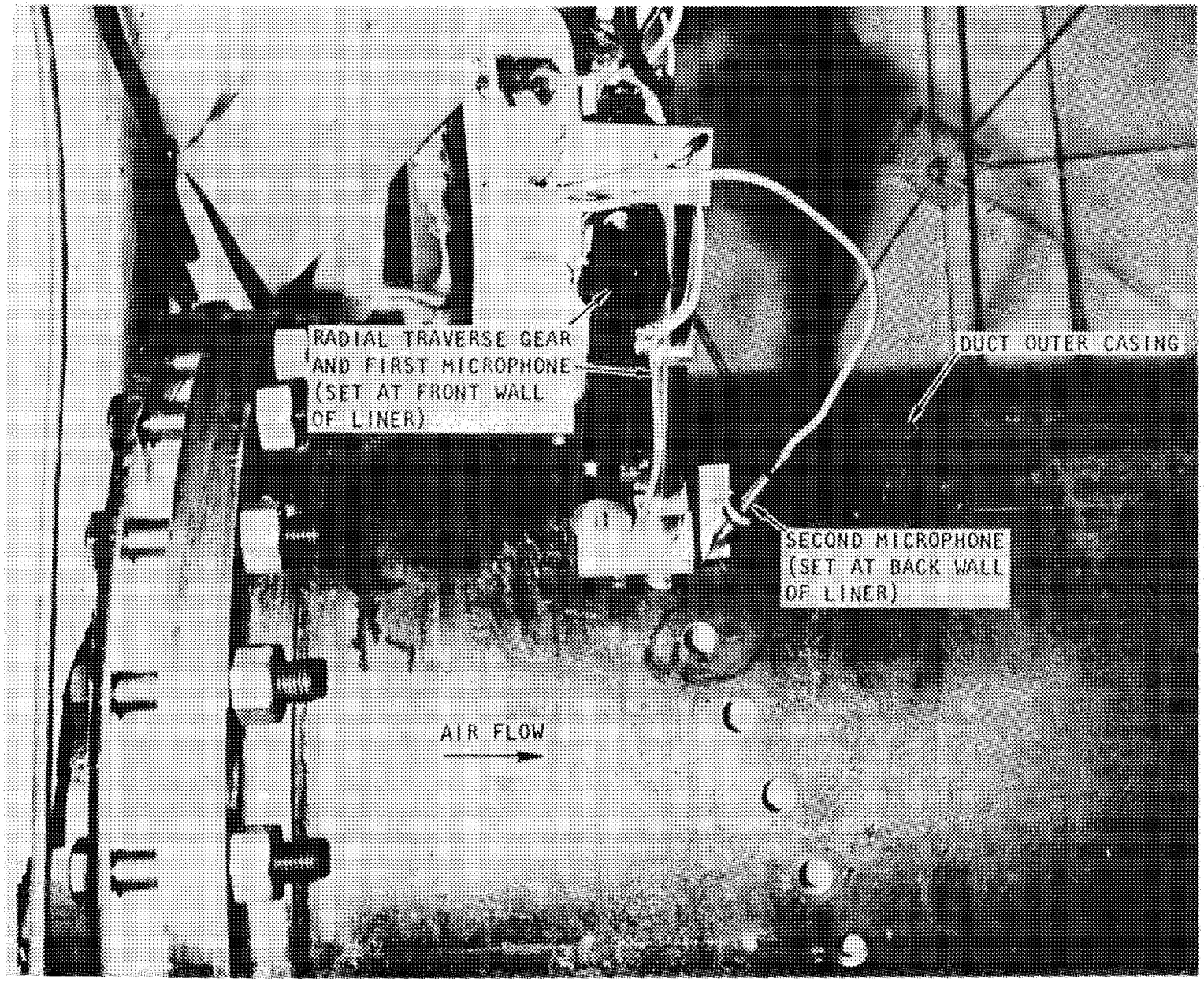


Figure 62. Overall View of Two-Microphone Test Installation

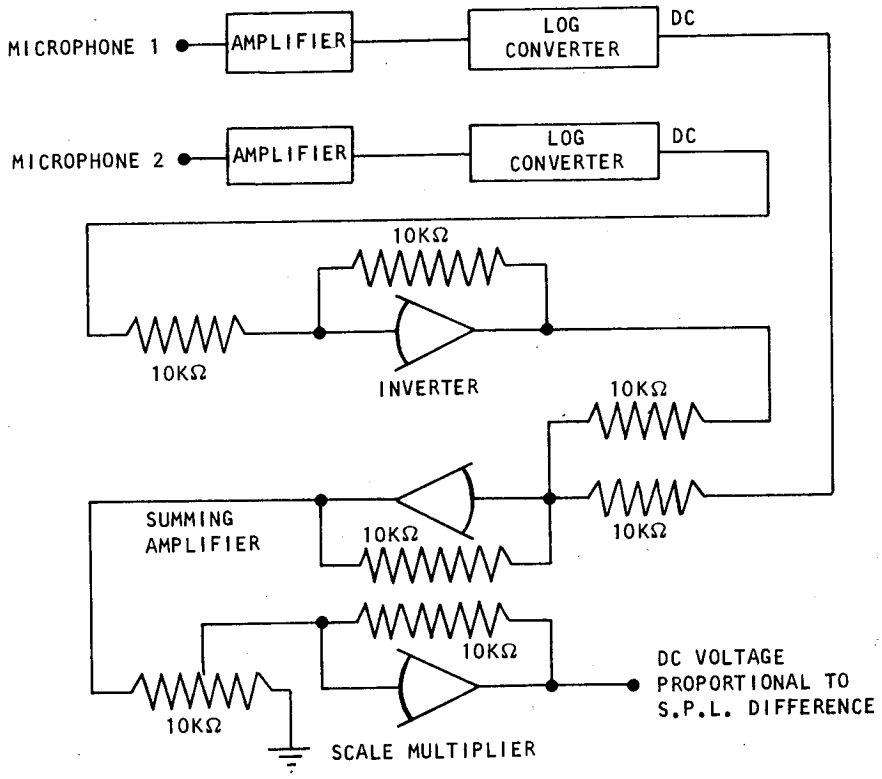


Figure 63. Analog Computer Circuit for Accurate Measurement of Two-Microphone Difference SPL

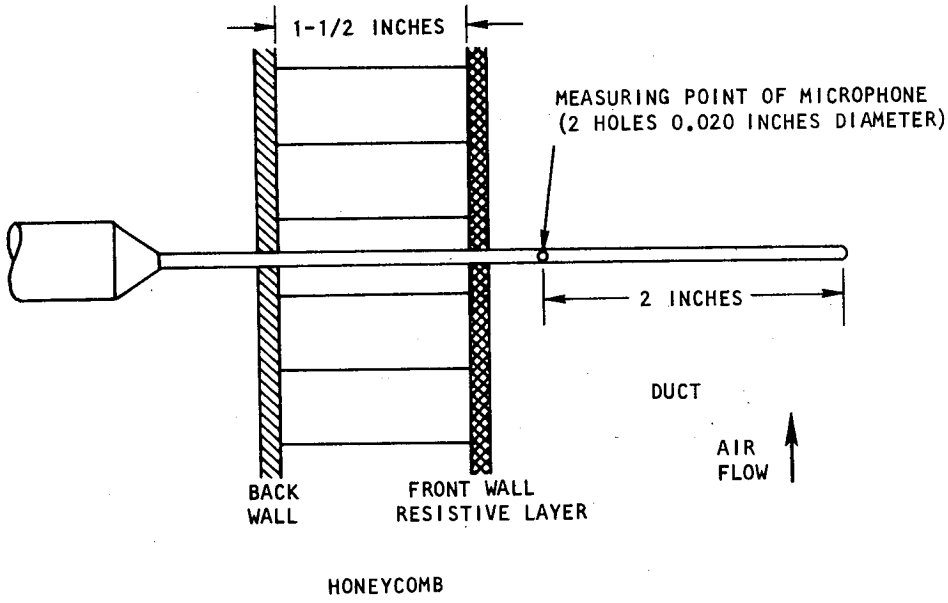


Figure 64. Traversing "One-Microphone" Modification of Two-Microphone Impedance Measuring Method

This procedure was used for this liner as the honeycomb core (necessary to satisfy the local reactivity assumption) had a transverse dimension of 1/8 inch (little more than twice the probe diameter), making the installation of a second microphone in the back wall of the same cavity exceeding difficult, without communicating with adjacent cavities. Figures 65 and 66 illustrate some typical pressure and phase traverses at different frequencies. The theoretical (or "classical") behavior of the sound pressure in the cavity can be demonstrated by a comparison with a plot of 20 log (cos kl) superimposed on the curves (with an arbitrary vertical displacement for clarity). In all cases up to about 0.1 inch from the liner surface the theoretical and measured curves are parallel thus implying that the "lumped" impedance concept of the liner surface is valid with quite well defined edges and that the liner is essentially locally reactive. In figure 66 the 180 degree phase change within the cavity, expected in a standing wave situation, is shown particularly well, the pressure minimum being outside the dynamic range of the recorder thus producing a "flat" on the pressure traverse wave at this point.

The determination of the back wall and front wall points which define the values of pressure and phase to be used require careful consideration.

The back wall situation is relatively simple: as the probe tube is moved in, the measurement holes are progressively exposed, thus the pressure level very rapidly rises, then, after complete exposure, the cavity level decreases with distance, initially at a very slow rate (in fact at l = zero the gradient of pressure, proportional to sin(kl), is zero). Thus, the back wall pressure can be estimated from the peak level which will occur approximately within one half of a measurement hole diameter from the geometric back wall point (i.e. within 0.010 to 0.020 inches). As an additional check the phase changes are also very rapid until the measurement holes are fully exposed after which point the phase will level off (unless some cavity dissipation is present due to wall flexure or bond leakage). The front wall situation is slightly more difficult. The obvious starting point is the geometric front surface, however, immediately prior to that point, the pressure and phase traverses through the resistive layer will almost invariably show a high rate of change, thus, after the measurement holes are exposed on the duct side of the surface, a pronounced "knee" occurs followed by a finite pressure and phase gradient. The point of measurement is thus taken to be that termination point of the "knee" just before the commencement of the relatively shallow pressure and phase gradients on the duct side of the surface. Reference to figures 65 and 66 show this point to be approximately 0.010 to 0.020 inches away from the surface.

In the cases when mean flow is present this point is subject to a little more uncertainty (see figure 67) due to the fact that the boundary layer produces some distortion and turbulence induced fluctuations of pressure and phase on the duct side of the surface. However, the "knee" point is still quite obvious and can be used to estimate accurately the surface pressure level and phase, the level differences for each flow case being quite marked (see figure 67 for the zero flow and 50 ft/sec. comparison at 1000 Hz and a 3000 Hz, 50 ft/sec. case for comparison with the zero flow case shown on figure 66). This "knee" estimation problem becomes more difficult in those cases where small standing wave pressure gradients occur near the surface,

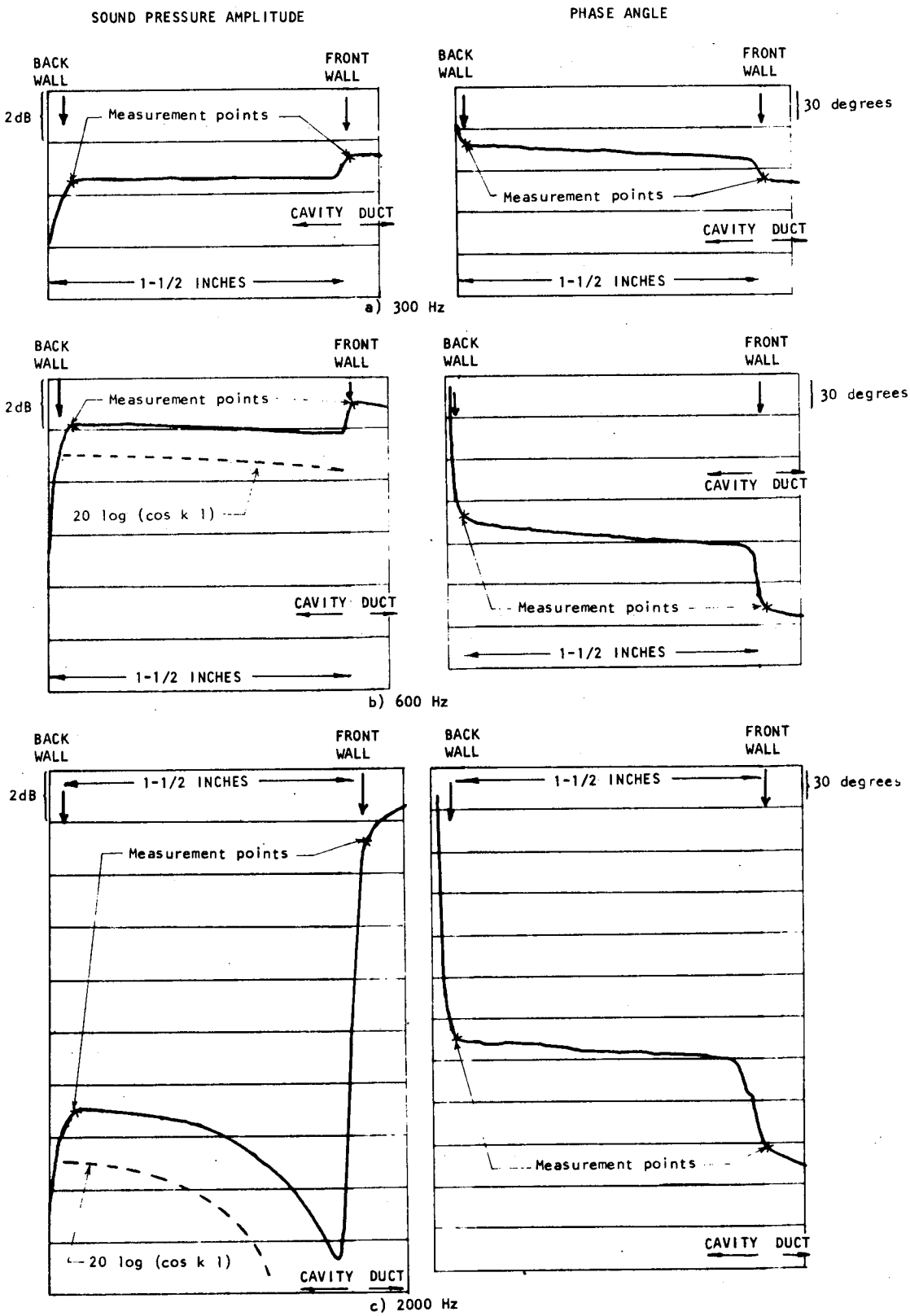


Figure 65. Effect of Frequency on SPL and Phase Angle Traverse Measurements for Welded Fibrous Metal Liner with 1 1/2 Inch Cavity Depth (300 - 2000 Hz)

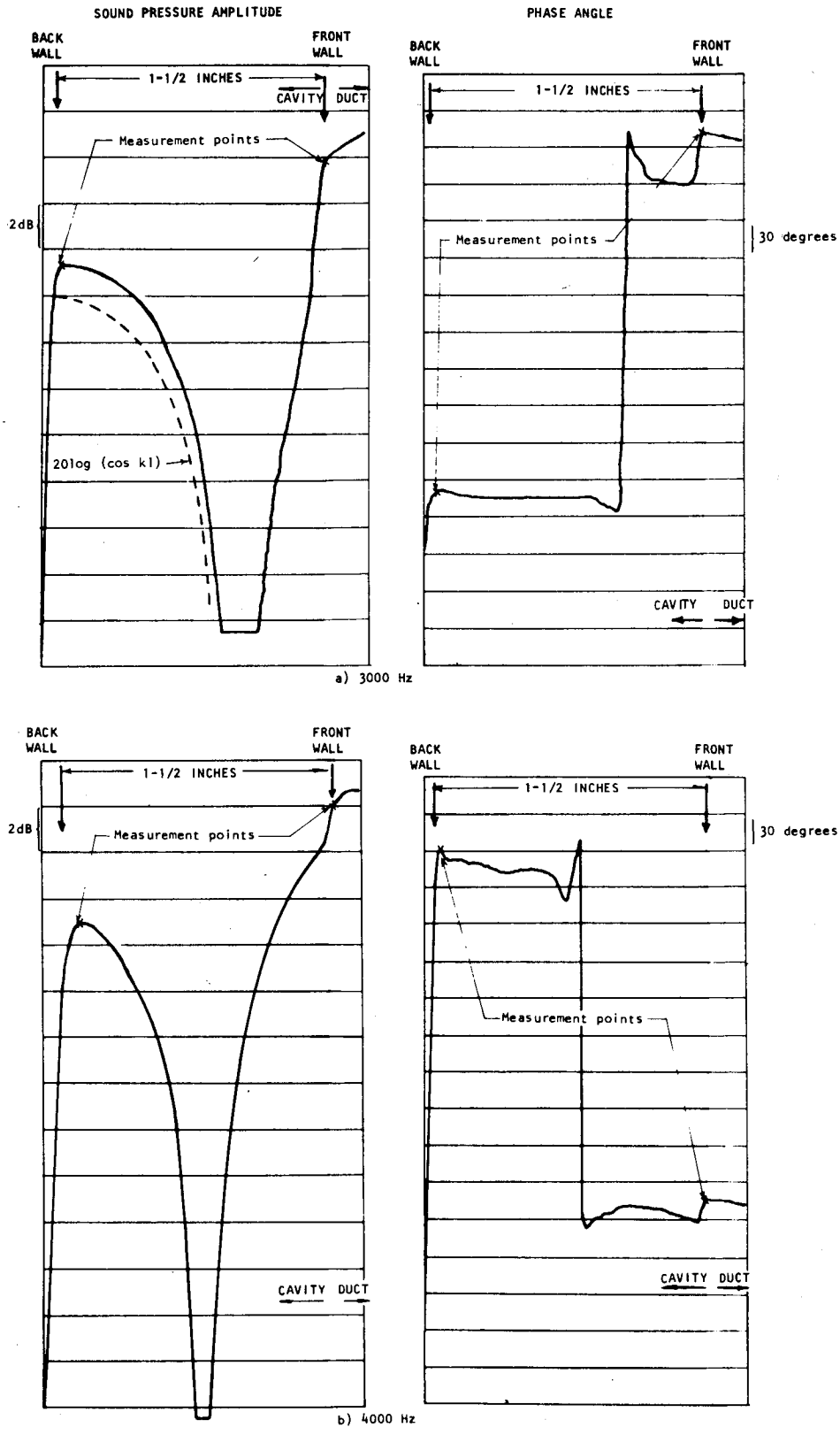


Figure 66. Effect of Frequency on SPL and Phase Angle Traverse Measurements Welded Fibrous Metal Liner with 1 1/2 Inch Cavity Depth (3000 and 4000 Hz)

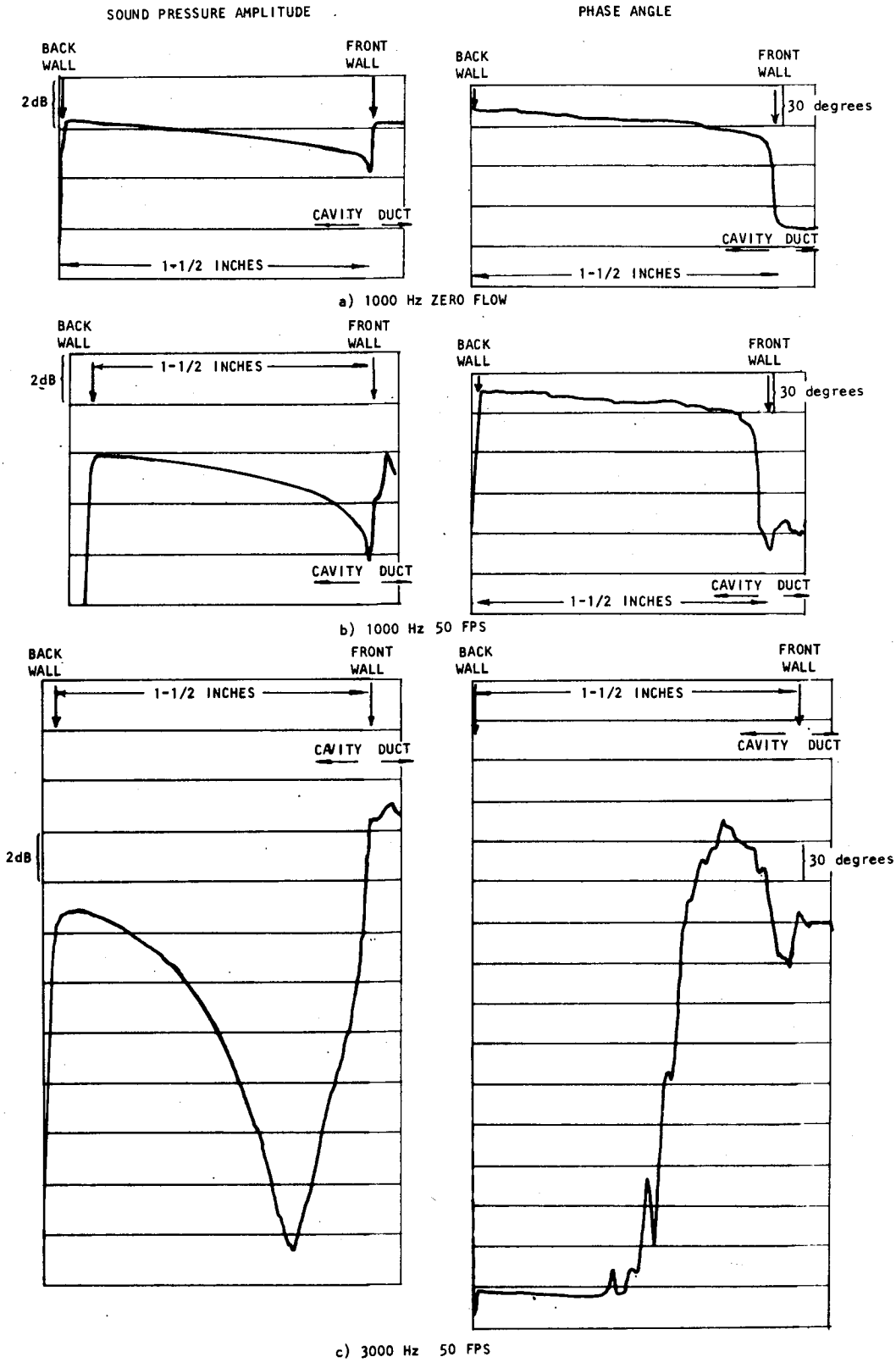


Figure 67. Effect of Velocity on SPL and Phase Angle Traverse Measurements for Welded Fibrous Metal Liner with 1 1/2 Inch Davity Depth

i.e. at low frequencies where the wavelength is more than ten times the cavity depth or at higher frequencies where the wavelength is approximately equal to cavity depth and the standing wave pressure minimum is near the middle of the cavity. In these cases the pressure and phase charges through the liner surface are small and the knee points are difficult to determine accurately. It should be emphasized that in these cases 2 Hz filtering is necessary in order to reduce the turbulent flow distortions.

Figure 68 is included as an example of the traverse variations encountered. The first case exhibited the problem of drilling holes in the liner for the probe. The traverse shown is typical of a torn cavity side wall. The remaining traverses show evidence (as variations from hole position to hole position of pressure level and phase) of surface non-uniformities and/or sealing imperfections between the honeycomb edges and the surface resistive layer.

Some variations between hole positions will always occur due to experimental error so the individual hole measurement must be averaged to produce a representative answer. However, it should be emphasized that an "average" impedance will only represent the "average" properties of the liner if the variability of the measured wall impedance is of small scale and spatially random in character. Any mean axial trends or variations should be looked for, particularly as these could produce marked changes in the modal propagation constants associated with the acoustic field. The acoustic properties of commercially available materials commonly exhibit large scale 'patchiness' with resistance variations possibly even greater than ±25%, thus any quoted value should be treated cautiously.

In some high frequency tests of the 1/2" cavity depth liners at high flows, for holes far downstream, the signal to noise ratio was so low that peculiar results (originating from turbulent pressures) appeared; these were ignored in the averaging process. In one case at hole 16 of the 20 Rayl liner, all the values were in considerable disagreement. This test was repeated and the same answers resulted, the implication being that, at this point, there exists a gross manufacturing defect in the surface resistive layer. Figure 69 shows examples of imperfections such as large scale voids and surface warping. Results from these regions were not included in the averaging process since they were not considered as representative of the important liner region further upstream.

V.4. Results of Measurements

V.4.1. General comments

Five different linings were tested, three of the resonant cavity type (locally reacting) and two of a non-locally reacting porous homogeneous plastic foam. Two of the resonant cavity linings were constructed to have 1/2 inch cavity depth with felt-metal resistive surface facings of, nominally, 20 Rayls and 40 Rayls flow resistance, respectively. The third sample of this type had a cavity depth of 1½ inches with a surface resistance layer of welded

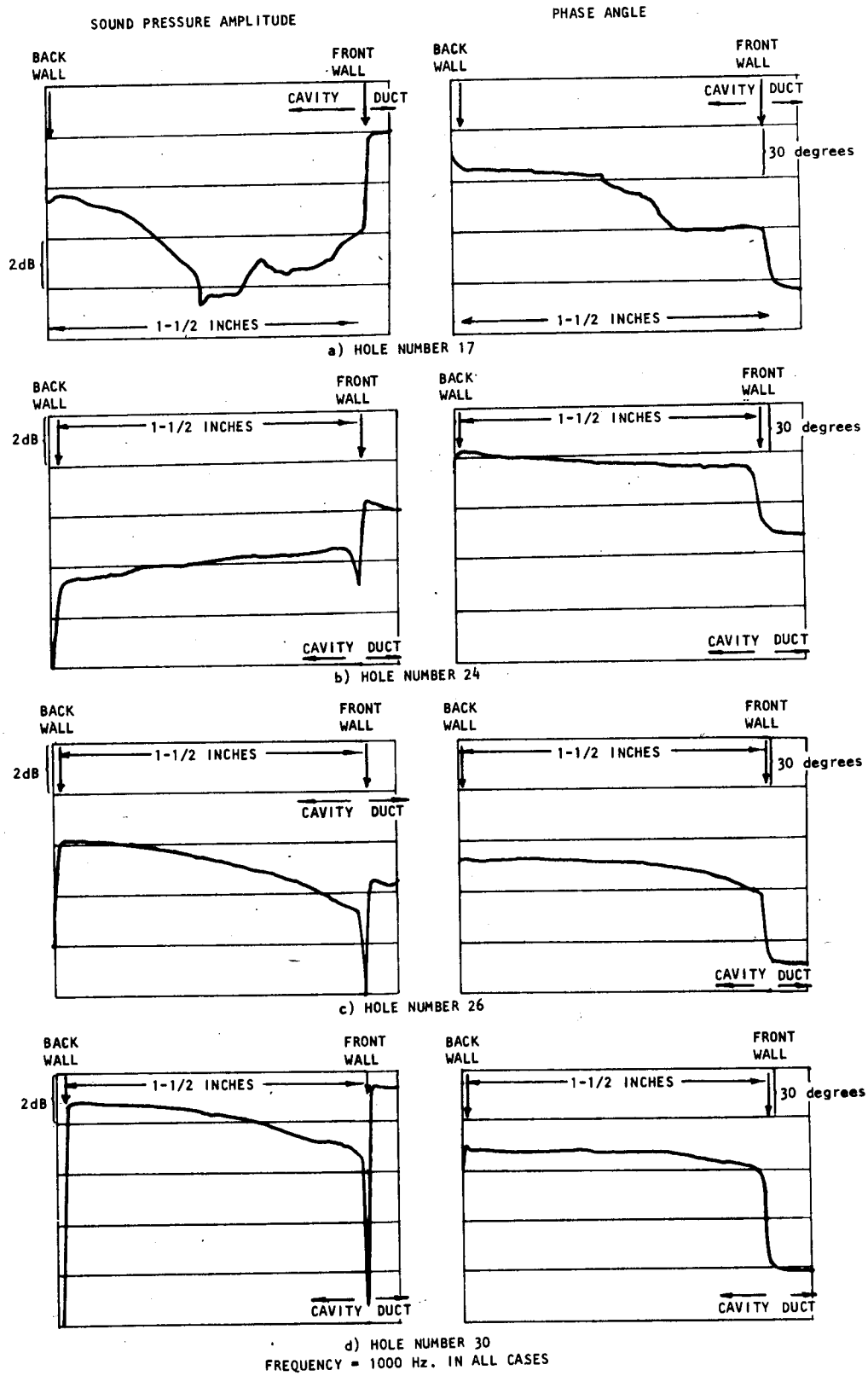
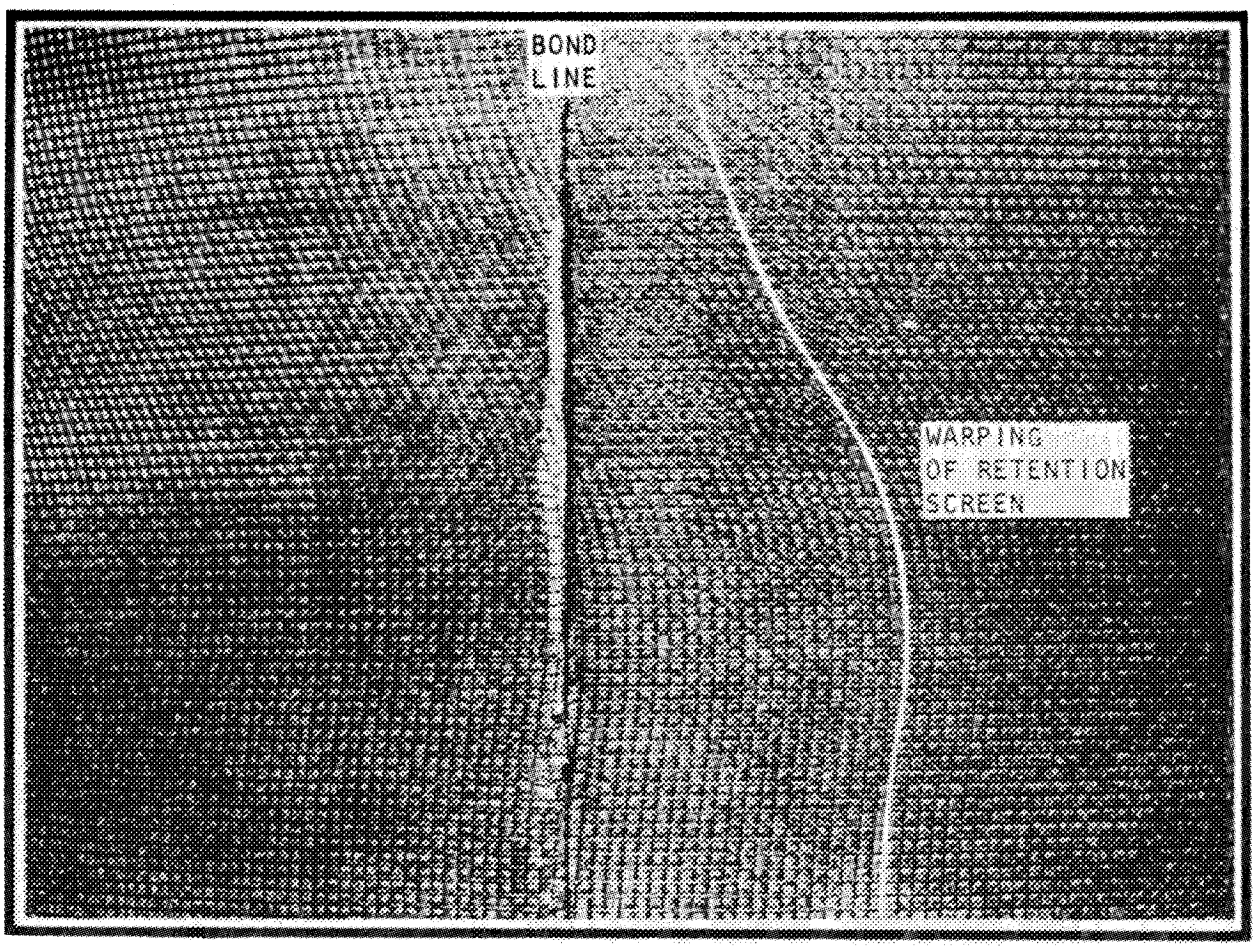


Figure 68. Effect of Material Non-Uniformities on SPL and Phase Angle Traverse Measurements for Welded Fibrous Metal Liner with 1 1/2 Inch Cavity Depth



COMPRESSION OF FIBERS DUE TO SEVERE WARPING

LARGE SCALE VOIDS IN SURFACE MACROSTRUCTURE

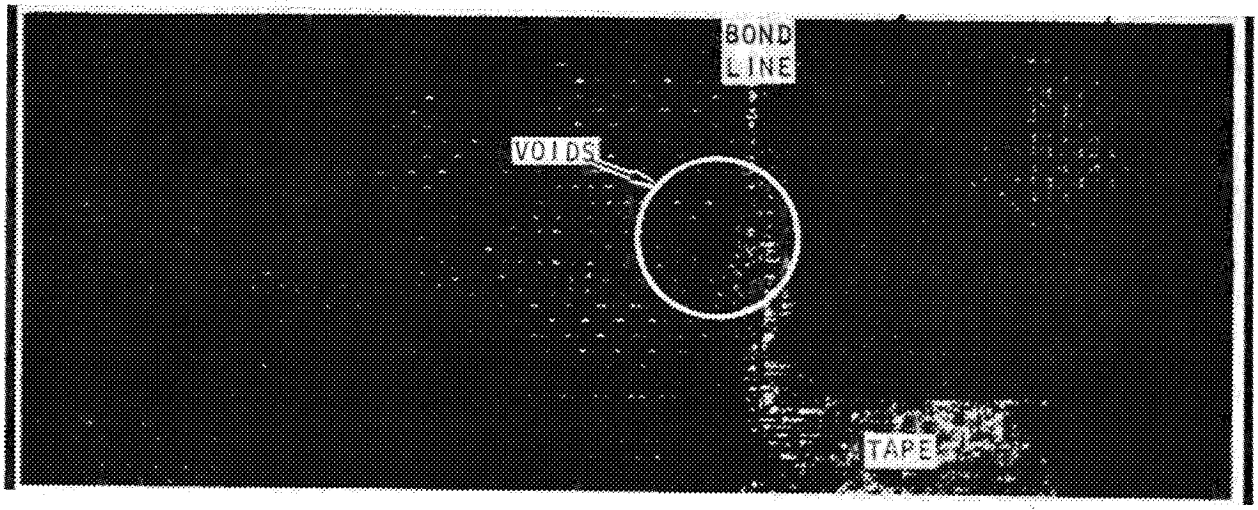


Figure 69. Examples of Surface Non-Uniformities in Felted-Metal Acoustic Lining Material

random fibers. The plastic foam liners were both 2 inches in thickness, from two different companies, one of them being a controlled manufacture acoustical foam.

The two microphone method of impedance evaluation was used for all the resonant cavity type liners, while the standard impedance tube method was used for the homogeneous plastic foam liners (this method was also used as a check on the zero flow values of the resonant cavity type liners). For the 20 Rayl and 40 Rayl liners with 1/2 inch cavity depth, both the impedance results (from the two microphone method) expressed as a mean over all measurement holes, and the standard deviation, can be seen in figures 70-75. Two examples of different hole impedance curves (representing a 'bad' measurement case and a 'good' case, respectively) are also presented (figures 76 and 77) and it can be seen from these that local variations of material properties are present, particularly in the resistance. This is to be expected, considering the sensitivity exhibited by this parameter in the error analysis. The averages over all holes for these two liners are presented in figures 78 and 79 as the zero flow case.

The reactance can be seen to be far more stable, probably due to the uniformity of the cavity depth between the various test positions. The reactance consists of a negative stiffness (the cot(kl) term) plus a positive mass term associated with the liner surface. This latter term is very small for the felted metal materials (shown by the difference between the measured total reactance and cot(kl) curves) and is not consistent between holes due to non-uniformities of the resistive surface material.

In addition to the in-duct measurements, 4 flat samples of the lining resistive surface layer bonded to plastic honeycomb were evaluated in an impedance tube. These measured values should be equivalent to the "in-duct" (figures 78, 79) measurements at zero flow and from figures 80 and 81, good agreement can be seen (considering the variations possible in the surface layers) in all the samples tested. However, in the welded fiber metal sample sheet used on the 1-1/2" facing, the derived impedance, as shown in figures 82 and 83, appears to be considerably larger (of the order of 0.2 or greater) and frequency dependent, with an increase at the low and high end of the frequency range, especially for the mass reactive terms.

Considerable variability of resistance was also experienced, as the small cell size of the honeycomb used was of the same order of magnitude as the surface density striations of this material. Thus some honeycomb cavities, at the points of measurement, were covered by a high flow resistive facing and others by a low flow resistive facing.

V.4.2. Effect of material property variations

In many of the impedance tests, a standard deviation of the impedance difference between various measurement positions was computed. In all cases the standard deviation observed for both resistance and reactance decreased with increasing frequency. These deviations incorporate both material

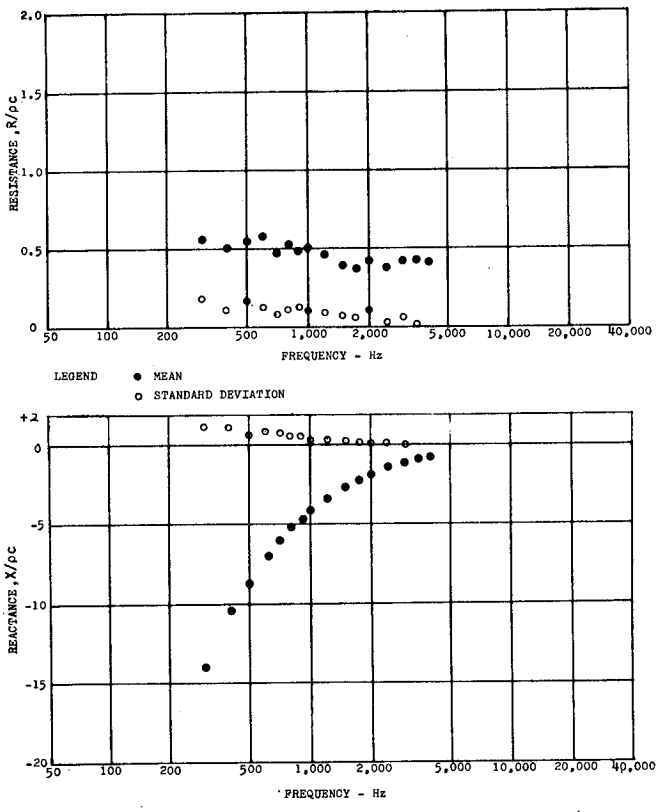


Figure 70. Two-Microphone Wall Impedance Measurements for Liner 2 (20 Rayl - 1/2 Inch Cavity Depth) Without Flow

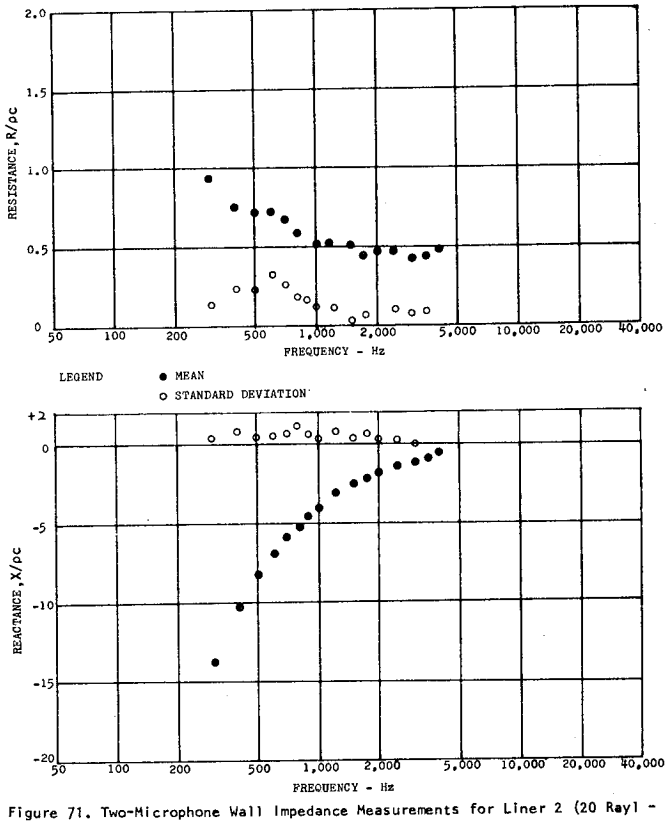


Figure 71. Two-Microphone Wall Impedance Measurements for Liner 2 (20 Rayl - 1/2 Inch Cavity Depth) at 50 fps Mean Flow Velocity

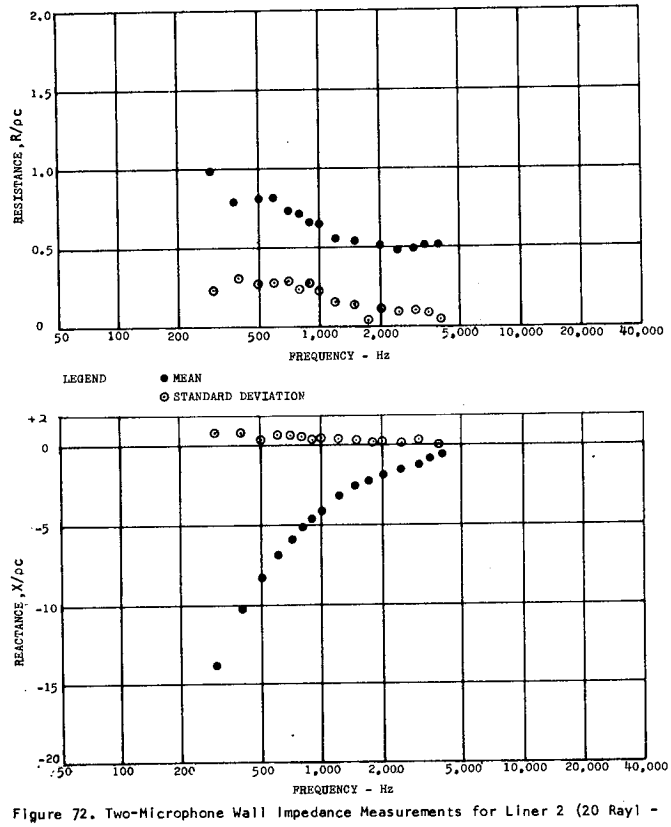


Figure 72. Two-Microphone Wall Impedance Measurements for Liner 2 (20 Rayl - 1/2 Inch Cavity Depth) at 150 fps Mean Flow Velocity

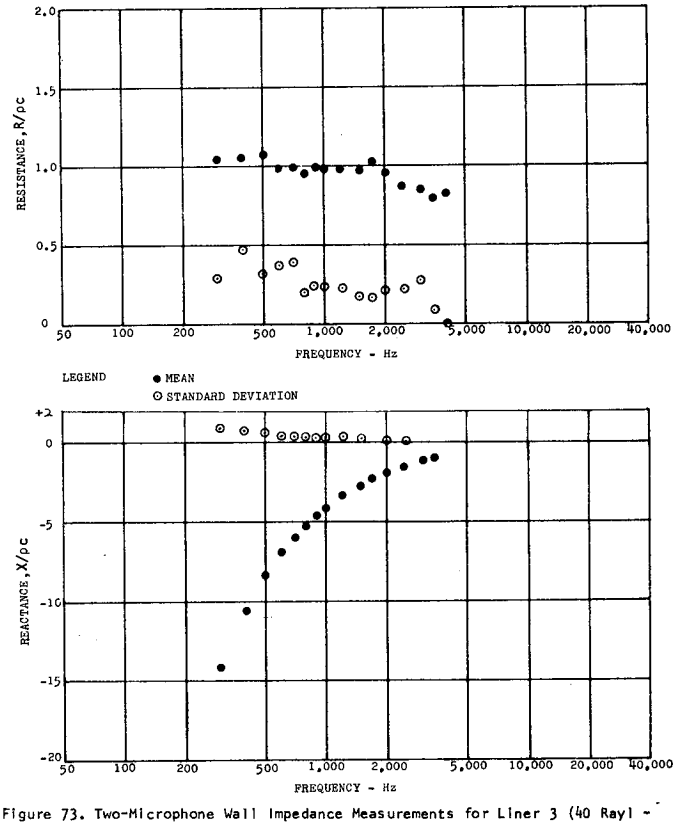


Figure 73. Two-Microphone Wall Impedance Measurements for Liner 3 (40 Rayl - 1/2 Inch Cavity Depth) Without Flow

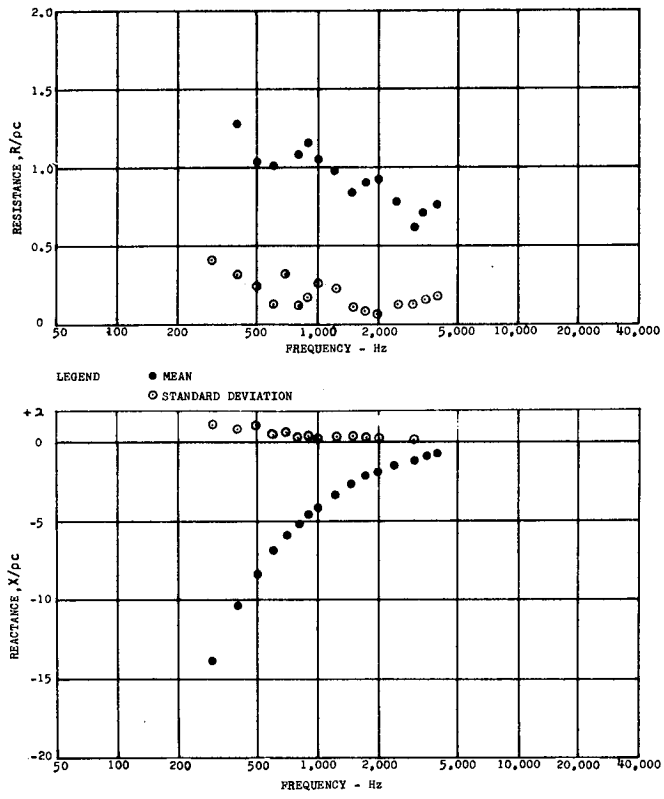


Figure 74. Two-Microphone Wall Impedance Measurements for Liner 3 (40 Rayl - 1/2 Inch Cavity Depth) at 50 fps Mean Flow Velocity

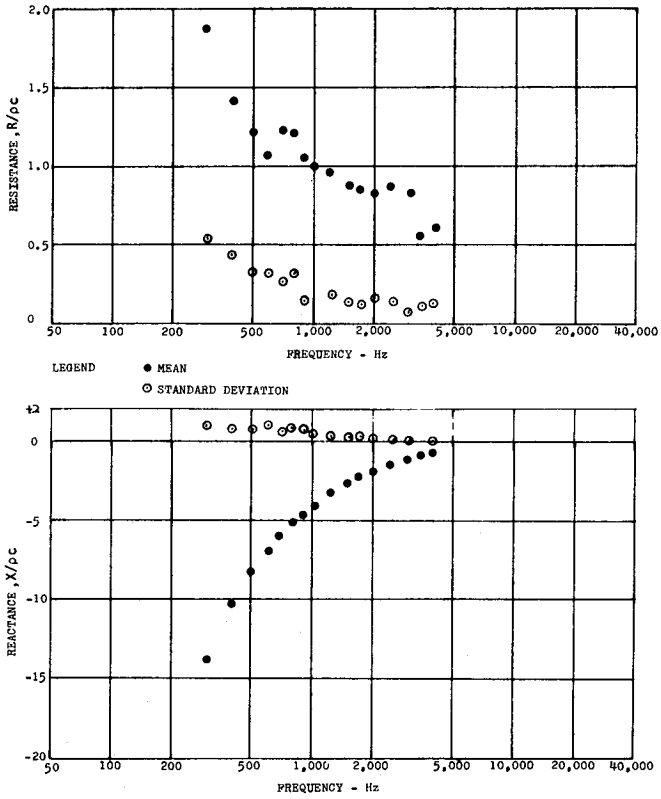


Figure 75. Two-Microphone Wall Impedance Measurements for Liner 3 (40 Rayl - 1/2 Inch Cavity Depth) at 150 fps Mean Flow Velocity

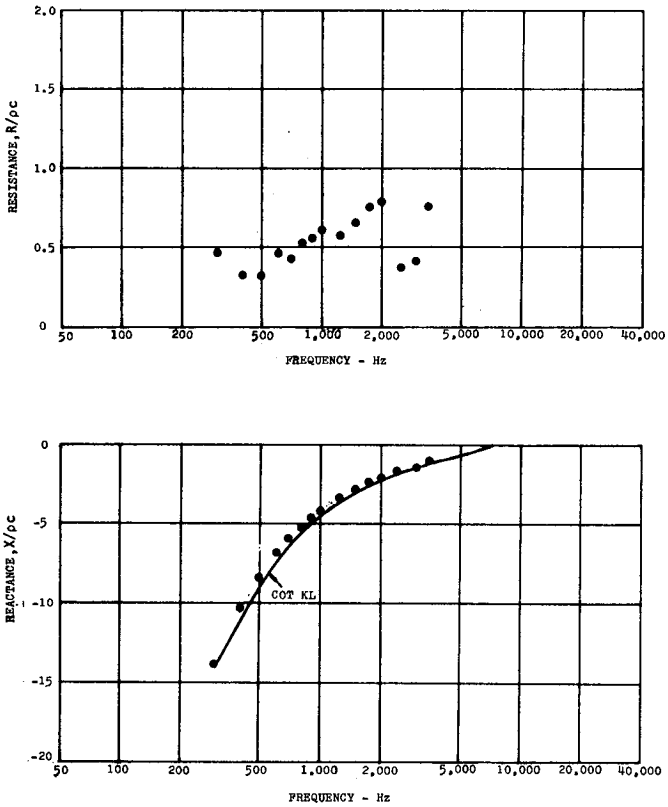


Figure 76. Two-Microphone Wall Impedance Measurements for Liner 3 (40 Rayl - 1/2 Inch Cavity Depth) at Hole Number 22, Illustrating a "Bad" Measurement

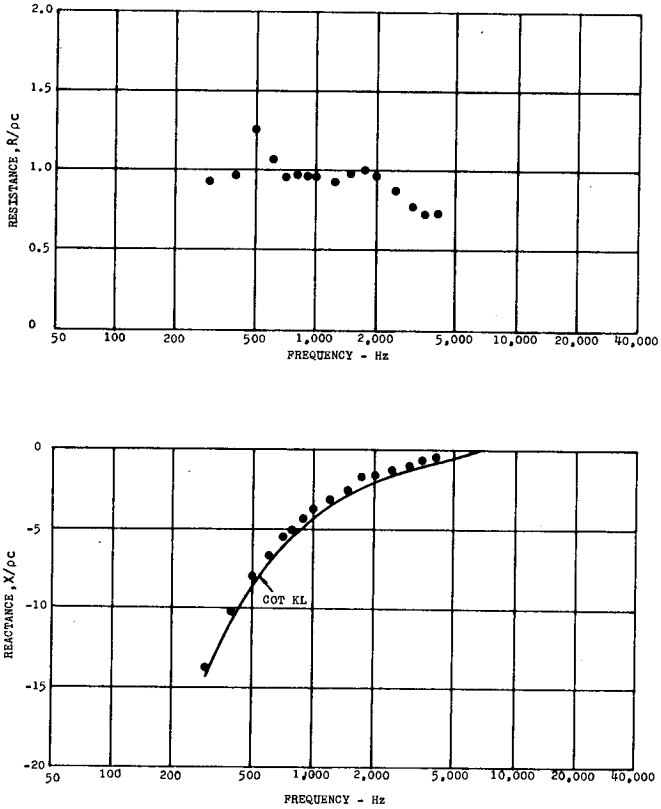
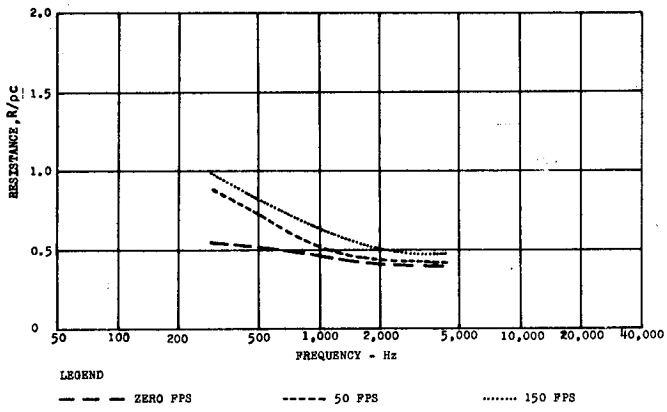


Figure 77. Two-Microphone Wall Impedance Measurement for Liner 3 (40 Rayl - 1/2 Inch Cavity Depth) at Hole Number 20, Illustrating a "Good" Measurement



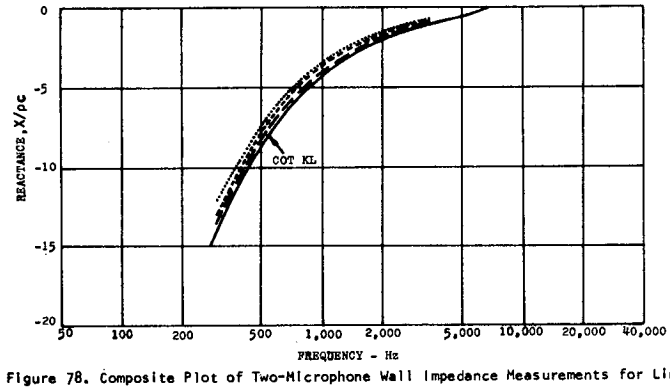
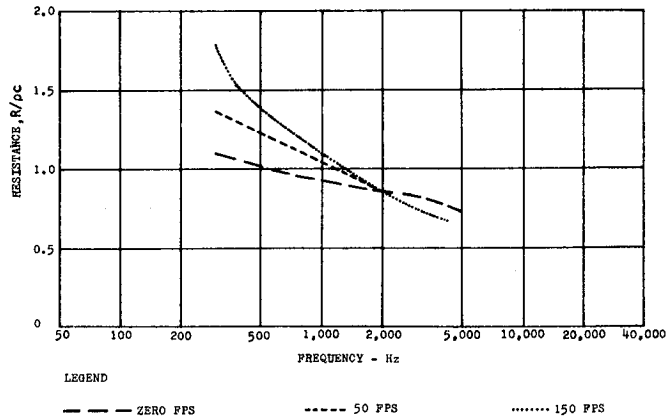


Figure 78. Composite Plot of Two-Microphone Wall Impedance Measurements for Liner 2 (20 Rayl - 1/2 Inch Cavity Depth) Showing Effect of Velocity



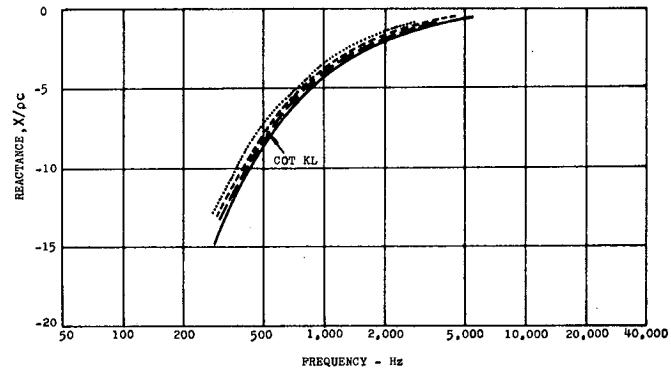
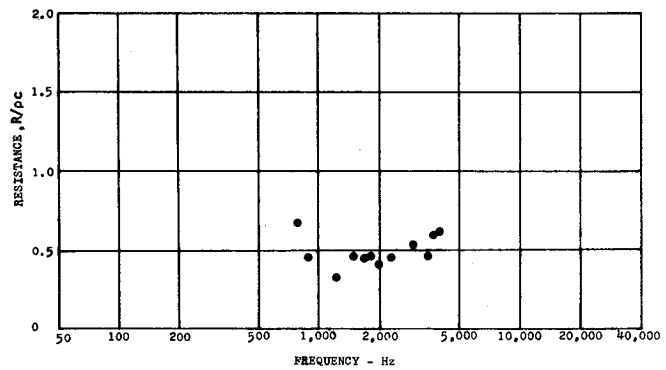


Figure 79. Composite Plot of Two-Microphone Wall Impedance Measurements for Liner 3 (40 Rayl - 1/2 Inch Cavity Depth) Showing Effect of Velocity



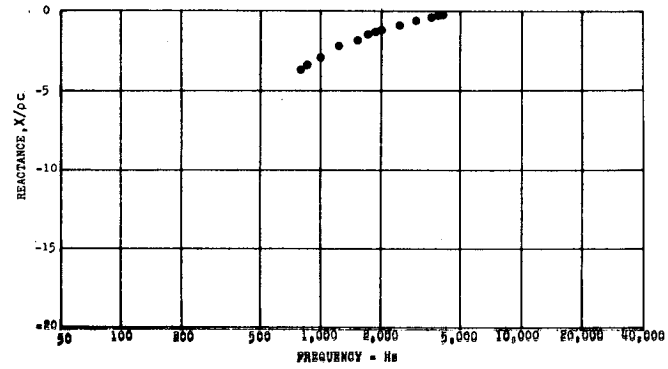
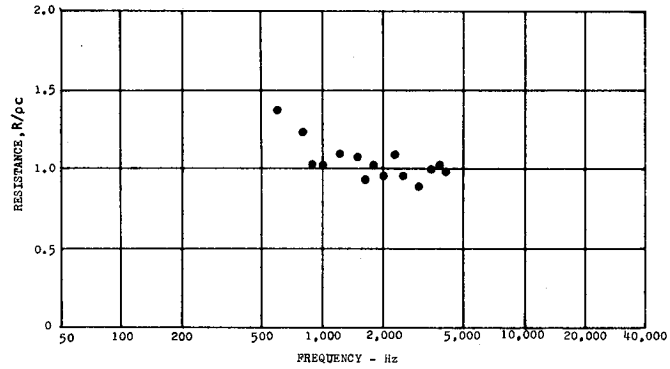


Figure 80. Average of Standard Impedance Tube Measurements for Two Liner 2 (20 Rayl - 1/2 Inch Cavity Depth) Samples



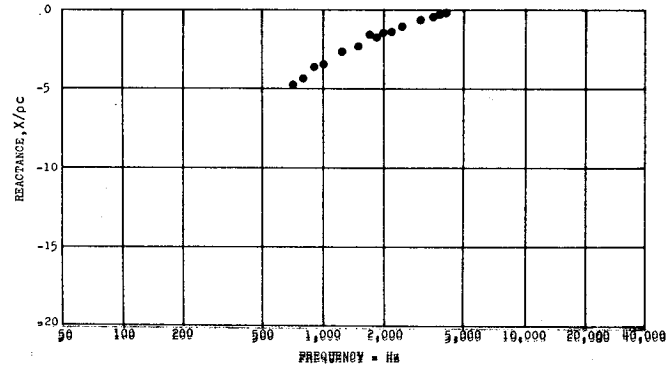


Figure 81. Average of Standard Impedance Tube Measurements for Two Liner 3 (40 Rayl - 1/2 Inch Cavity Depth) Samples

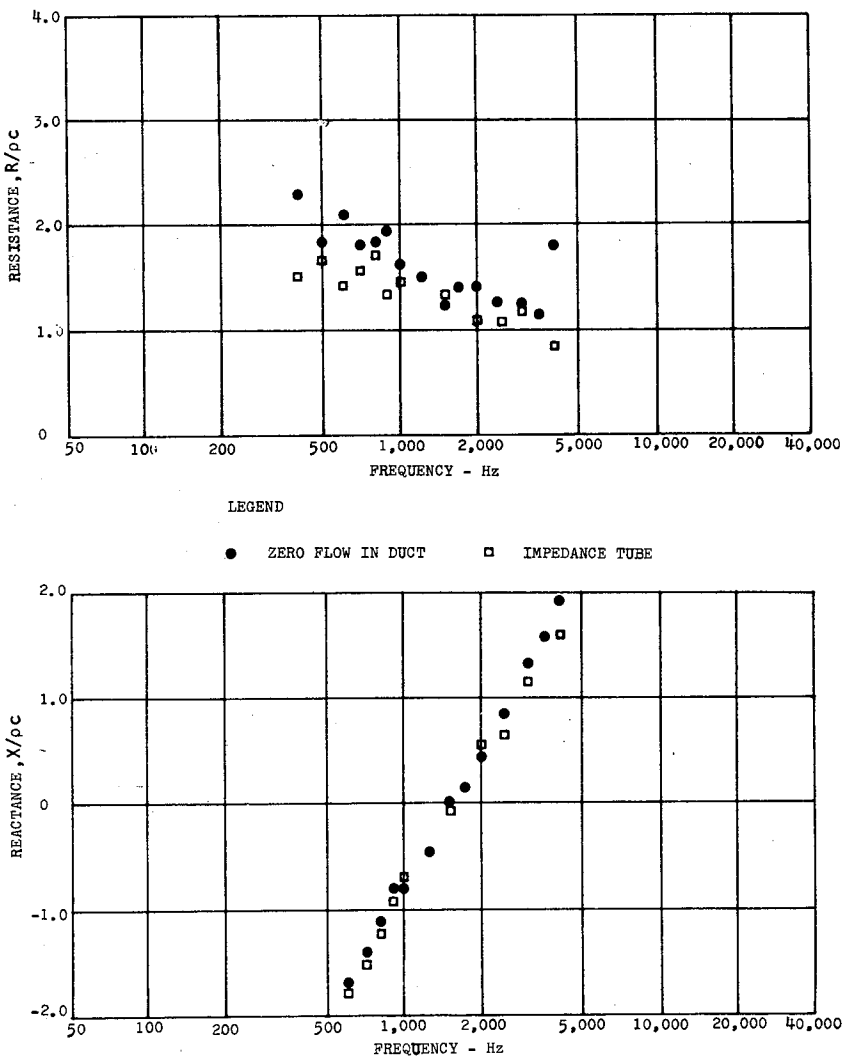


Figure 82. Comparison of Impedance Tube and Two-Microphone Impedance Measurements for Liner 1 (Welded Fibrous Metal - 1 1/2 Inch Cavity Depth) Without Flow

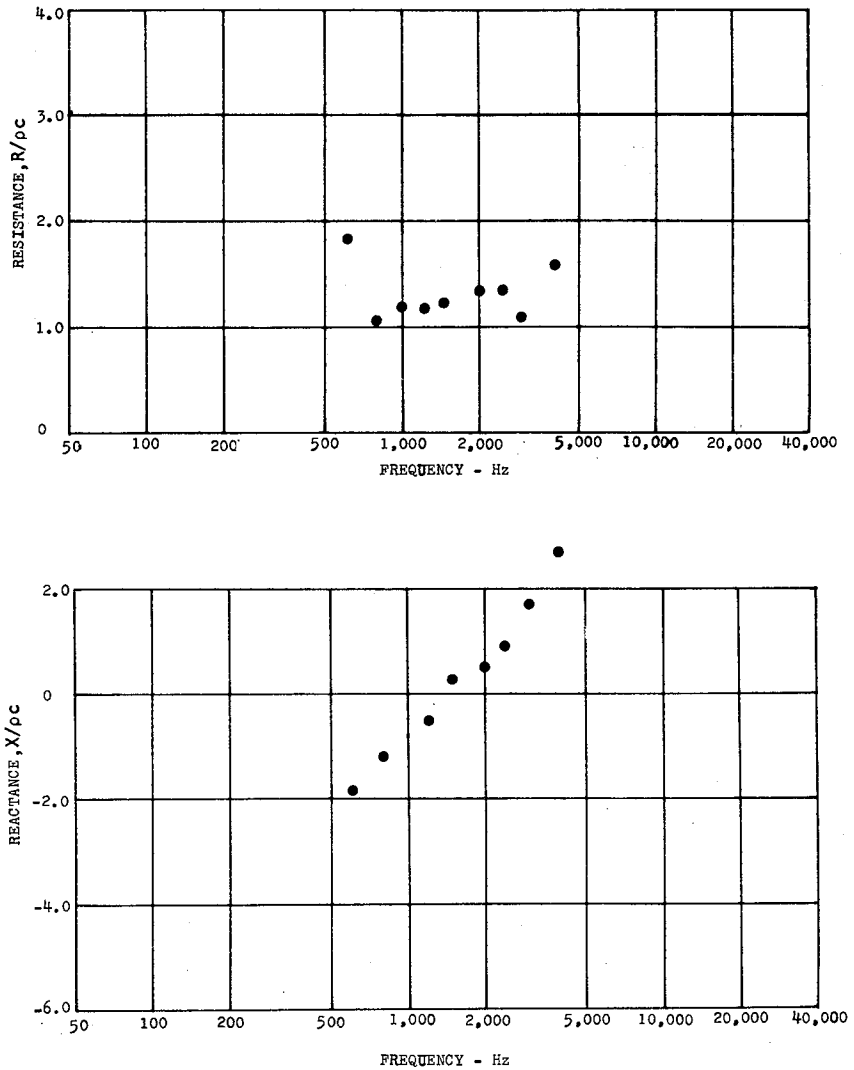


Figure 83. Two-Microphone Wall Impedance Measurement for Liner 1 (Welded Fibrous Metal - 1 1/2 Inch Cavity Depth) at 50 fps Mean Flow Velocity

property variations and measurement errors, which from the earlier evaluations are most likely to be caused by phase errors and/or cavity depth errors for the resistance deviations, and cavity depth errors for reactance deviations. However, these will be quite small (of order of 5% at low frequencies) in comparison to the observed low frequency deviations of resistance of 20-25% in the 20 Rayl liner zero flow case, and 20-30% in the 40 Rayl liner case. Thus, it appears reasonable to ascribe these deviations to gross changes of the porous surface material properties.

The effect of a flow velocity of 50 feet per second over the surface is to increase the resistance deviations in the low frequency region, particularly with the 20 Rayl liner where a 5% or more increase can be seen by comparing figures 71 and 72. In contrast, the reactance deviations are little affected, thus implying, from the earlier analysis, that phase changes are the cause of this increase. It is also interesting to note that when the mean flow velocity is increased to 150 feet per second the low frequency deviations are increased but not in proportion to the flow velocity. However, the magnitude of the resistance increased as well, thus the percentage deviations remained constant or were even reduced.

The 40 Rayl felted-metal liner resistance deviations remained largely unaffected with flow velocity, although the increase in mean values produced a reduction in percentage error. This implies (from the assumption that bulk flow properties in the duct are not affected by the liner change) that the variations observed with the 20 Rayl liner could be flow interaction with the materials, this interaction having varying degrees of effect depending on the local variations near the test holes. Again, with this liner as with the 20 Rayl liner the reactance variations remained essentially independent of flow velocity.

The welded fiber metal liner was not as extensively tested as the 20 Rayl and 40 Rayl felted metal liners; however, its mode of construction produced striations of varying flow resistance, which can be seen as a cyclic variation in resistance, as shown in the multiple hole test data at 1000 Hz in Figure 84.

The impedance of the plastic foam linings was determined from samples cut from a large sheet and tested in an impedance tube by the standing wave method. The results for the two materials are given in Figures 85-86. As can be seen from Table IV, one of the two foams exhibited considerable variations between supposedly identical test samples at 1000 Hz. This is unusual for "acoustic" foams and as such was considered undesirable test material. The other foam did not exhibit such variations.

The impedance of the controlled manufacture acoustic foam is shown in figure 86. This material, which has the same peaked characteristic in impedance, did not exhibit the impedance variability of the foam previously discussed.

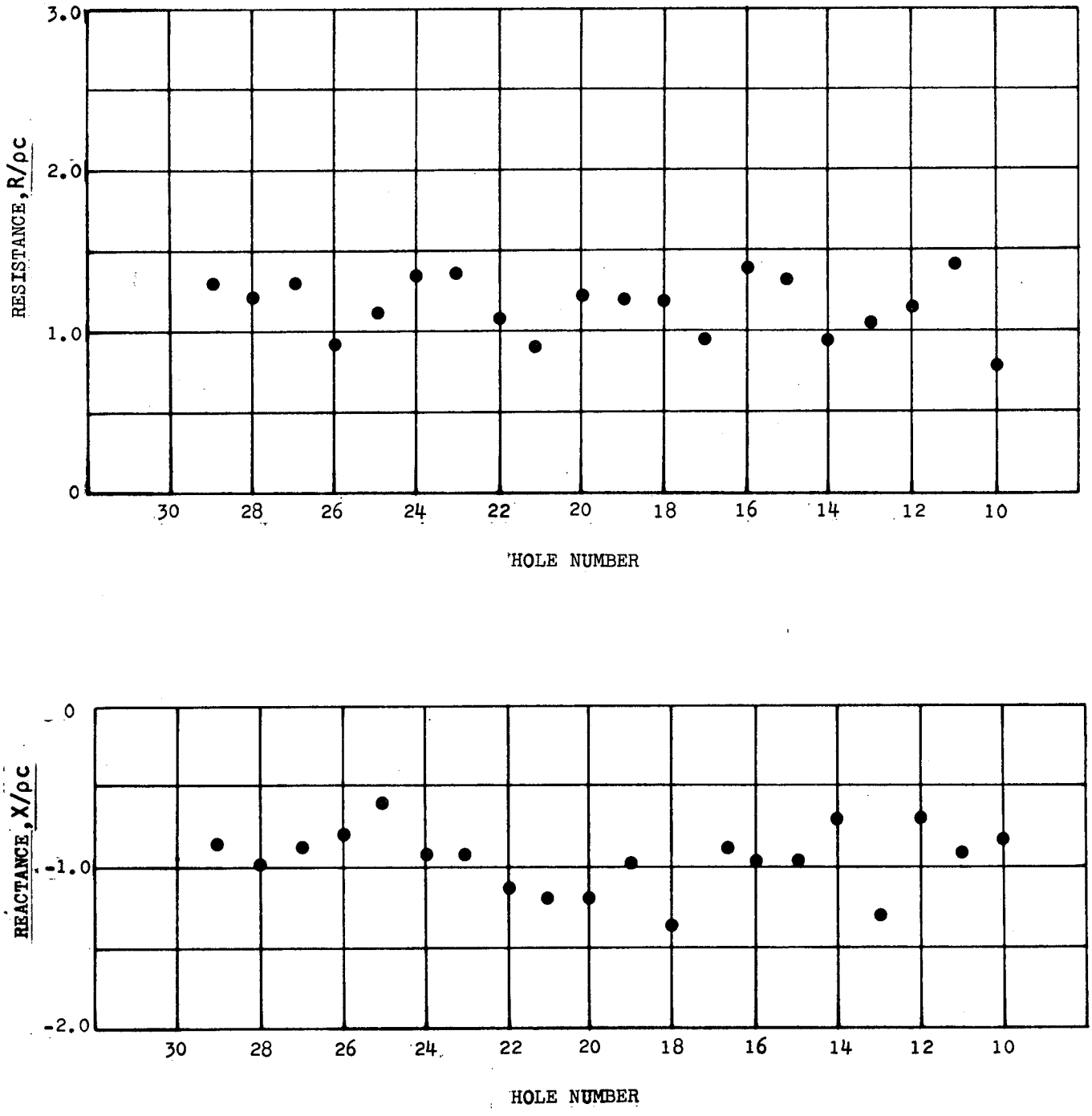


Figure 84. Effect of Axial Measurement Position on Wall Impedance for Liner 1 (Welded Fibrous Metal - 1 1/2 Inch Cavity Depth) Without Flow, f = 1000 Hz

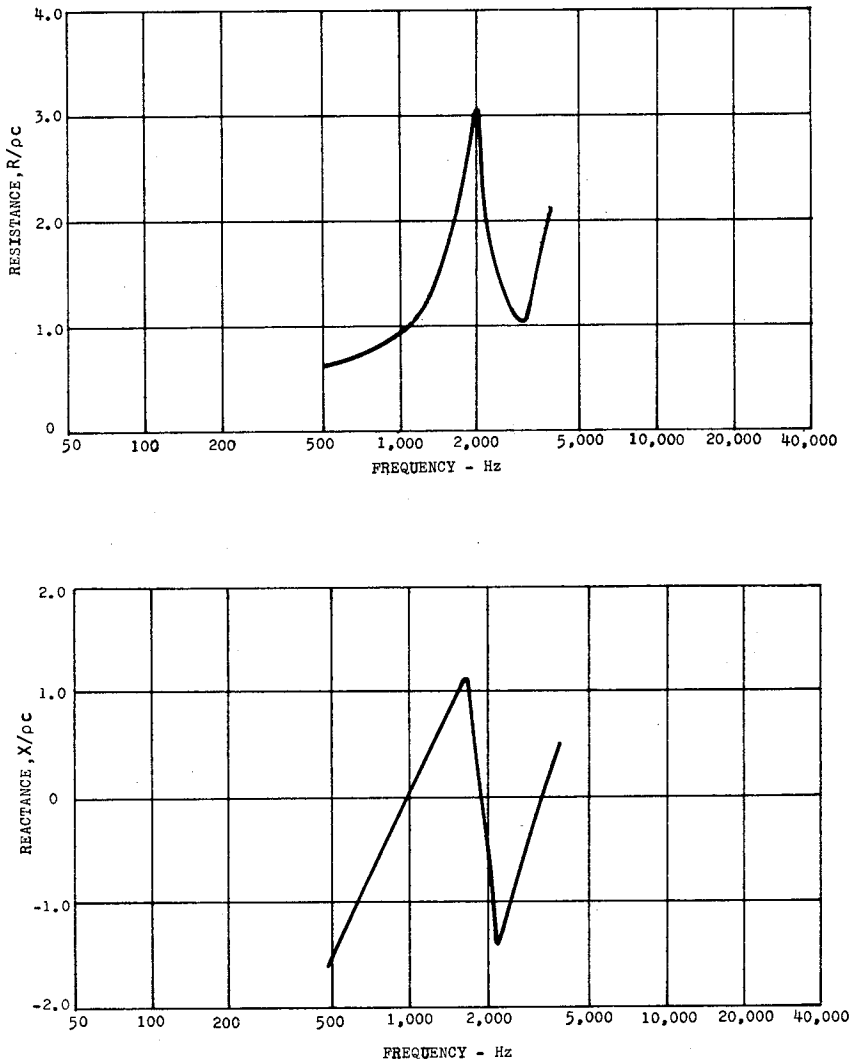


Figure 85. Average of Standard Impedance Tube Measurements for Five Liner 4 (Commercial Foam) Samples

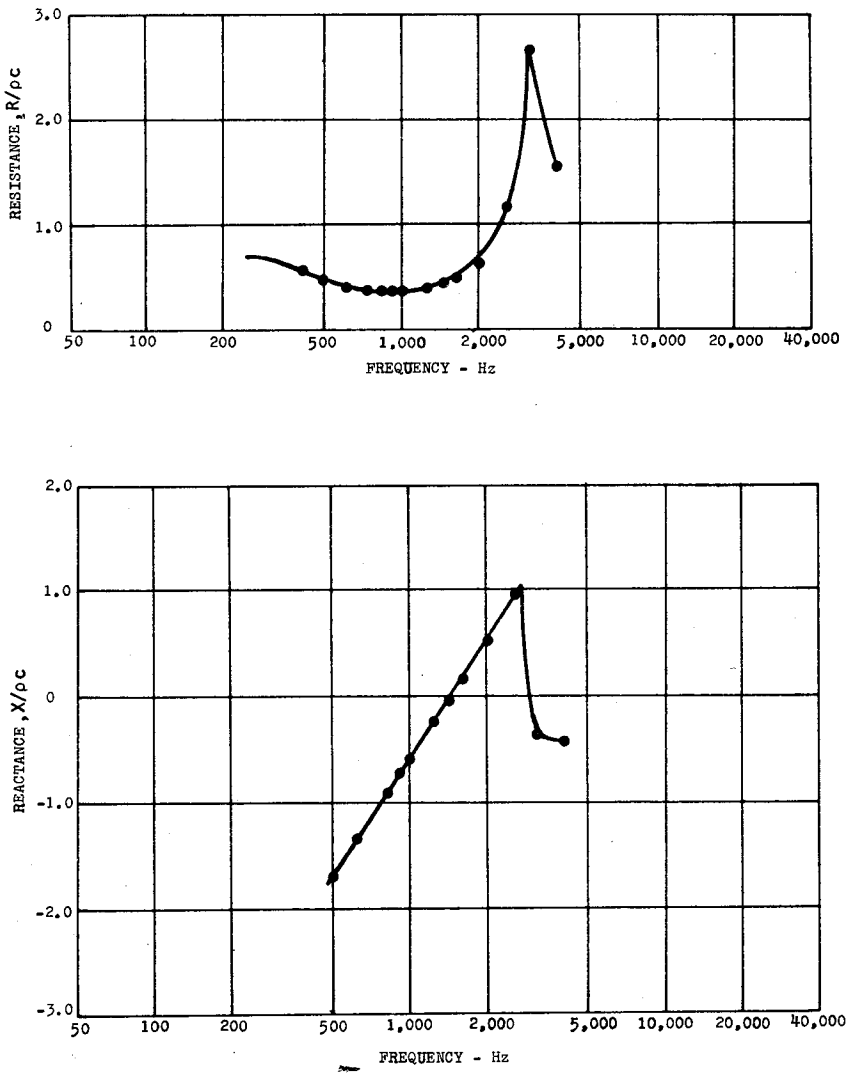


Figure 86. Average of Standard Impedance Tube Measurements for Three Liner 5 (Acoustic Foam) Samples

TABLE IV

IMPEDANCE VARIATIONS OF SIX SAMPLES OF
2" THICK POLYURETHANE FOAM AT 1000 Hz

SAMPLE	RESISTANCE R.	REACTANCE X
1	.755	.056
2	.983	.168
3	.712	.042
4	.809	.034
5	.863	.086
6	.830	-.078

V.4.3. Mean values and related flow effects

Figures 78 and 79 summarized the effects of flow on the 20 Rayl and 40 Rayl liners. A marked frequency effect exists in the resistance values in both cases; this being a preferential increase in the low frequency region. The 20 Rayl case appears remarkable at 300 Hz as this increase is almost 100% and then tapers off to 20% at 1000 Hz. It should be remembered, however, that percentage increases in this case are perhaps not particularly meaningful. On considering the 40 Rayl case (a material of similar construction), almost the same magnitude increases (with flow at various frequencies) can be seen, implying that the increase in flow induced resistance can be considered as an additional "lumped" element, dependent only on the mean flow.

The effect of flow on reactance appears small and of a positive nature and is often difficult to estimate as it is of the order of the natural material reactance variations. However, it is possible to conclude that the mass reactance of the liner increases with velocity, this increase then decreasing in magnitude with increasing frequency. The cavity reactance term ($\cot(kl)$) is also shown, and as expected dominates the total reactance except, of course, near the resonance frequency. It should be noted that these observations apply only to the 1/2" liners where all frequencies of interest are below resonance and thus the cavity reactance term, by definition, is negative in sign.

The welded fiber metal liner was not studied as comprehensively as the other two resonant cavity types, thus work concentrated only on a few frequencies and flows up to 50 feet per second. However, from a comparison of figures 82 and 83, the resistance increases little (if any) and the reactance curves shift slightly to the left (implying a higher mass term). The drop in resonance frequency (where reactance is zero), compared to the 1/2" liners, is due to the increased cavity depth of 1-1/2" for this liner.

V.5. Conclusions

From the theoretical discussion and the results presented earlier, the following comments can be made. First, the in-situ impedance measurement technique is a viable one, the success of its implementation being governed by an appreciation of the effects of errors, and a regard for the necessary equipment for minimizing these errors.

Secondly, the importance of uniformity in the construction of the acoustic surface liners has been made clear. The variability of the properties of the surface layers is currently too large for precise classification of the wall impedance, thus implying extreme difficulty in making precise attenuation predictions. Large sample area tests (such as in an impedance tube) serve only to "smear out" the local variations which influence any grazing acoustic field application, such as duct linings. However, for some practical situations the "average" wall impedance, as presented, could be "adequate" for design purposes.

Finally, the effects of mean flow over the surface of the liners tested appears to increase the acoustic resistance (with a low frequency bias) and to reduce the reactance slightly. The quantifying of these effects is a prerequisite for the successful prediction of the attenuation of the sound field in a duct.

VI. SOUND PROPAGATION IN LINED ANNULAR DUCTS

The primary objective of this series of experiments was to provide a sufficient amount of data to validate the theoretical predictions for sound propagation and attenuation in an acoustically lined annular duct sustaining a radially non-uniform mean flow. This involves validation of both the eigenvalues (which consist of the propagation constant, β, and the attenuation constant, α) and the eigenvectors (or natural mode shapes). In addition, other factors which influence the eigenvalues and eigenvectors such as the wall impedance boundary conditions, the termination radiation impedance, the sound pressure distribution at the source plane, and the mean flow and temperature distributions, must be experimentally determined in order to completely define the experiment conditions.

The experiments conducted in the facility with sound attenuating liners provide the nucleus for comparison of annular duct theoretical predictions with measured data. Experiments were conducted with five different sets of liners. The parameters varied for each liner configuration were: (1) angular pressure distribution, (2) frequency, and (3) flow velocity.

The pressure distribution studies are divided into two regimes; the first being below the first higher order radial mode (0,1) cut-on frequency and the second being equal to or greater than that frequency. At frequencies below

the first higher order radial model cut-on in the hard wall source section (1620 Hertz), the radial pressure distribution at the entrance to the lined duct is determined by the angular pressure distribution, if it is assumed that higher order mode reflections at the interface between the lined and unlined sections are negligible. From experimental observations, this assumption seems to be reasonable as long as no higher order radial modes will propagate. Thus, because of the control which can be exercised over the angular pressure distribution, it is possible to drive, in relative isolation in the source section, the plane and higher order angular modes, up to and including the (5,0) mode, without the presence of higher order radial mode response.

VI.1. Description of Experiments

The experiments conducted with the five liners progressed from a relatively simple low frequency test to a reasonably complex, multi-mode, high frequency test. The degree of success achieved was almost directly proportional to the complexity of the test. The most simple and probably most rewarding test in terms of useful data was that run using a felted metal over a 1½" deep honeycomb core. A series of tests was conducted at 1000 Hertz for both a plane (0,0) mode excitation and a (3,0) mode excitation. The tests were conducted with and without mean flow. The most complex and least productive tests were those conducted with a felted metal liner over a ½" deep honeycomb core at high frequencies.

VI.1.1. Liner description

The five liners used in the test series and illustrated previously in figure 14 are briefly described below:

(1) Liner set 1 was a single liner for the outer wall consisting of one layer of nominal 40 Rayl felted metal over a 1½" deep honeycomb with 1/8" cell diameter. The honeycomb was closed at the back with a .050" thick aluminum plate. The honeycomb was bonded to the aluminum plate and was tightly squeezed around the acoustic inner surface, thereby eliminating any change in porosity due to the adhesive. The inner wall consisted of a ½" thick steel pipe.

(2) Liner set 2 was a 20 Rayl felted metal over a ½" core. This configuration was used to make up both an inner and outer liner for the annulus. The rigid closure for the honeycomb was a 0.050" thick layer of cured resin-impregnated fiberglass cloth.

(3) Liner set 3 was the same as (2) above with a 40 Rayl felted metal (not the same manufacturer as for the acoustic material of (1) above).

(4) Liner set 4 was made up of commercially available polyurethane foam covering the inner and outer annular walls. No specifications were available on the foam, other than the measured impedance. The inner liner was 2.3" thick and the outer liner was 2.0" thick.

(5) Liner set 5 consisted of the outer wall covered with a 2" thick commercially available acoustic foam with closely controlled pore size, with the inner wall surface a ½" thick steel pipe.

VI.1.2. Data requirements

The type of data recorded varied from test to test, depending on the motivation for a particular test. In all cases, the circumferential sound pressure distribution was recorded for the outer wall position in the plane of the drivers. This was used to compare with the computed circumferential distribution of sound pressure at the driver plane, for a particular mode simulation, to determine the validity of the test set-up and to determine if the presence of the liner had introduced any distortion in the driver plane sound pressure distribution.

The sound pressure distribution in the plane at the intersection between the lined and unlined section was recorded in as much detail as possible. The SPL at this plane was chosen as the source distribution. Angular SPL distributions were recorded at nine equally spaced radial locations from the outer wall to inner wall. Also, continuous radial SPL distributions were recorded at several angular locations. Further, for several of the tests, these measurements were made at four axial positions.

In tests where one mode was responding in isolation, it was possible to measure the axial decay and propagation speed of that mode by measuring the peak amplitude at the inner and outer walls for a number of axial stations.

In addition, temperature, humidity, and barometric pressure were recorded for most of the tests conducted. No particular effect was related to changes in humidity or barometric pressure, but very significant changes in mode response amplitude, cut-on frequency and modal attenuation were observed for very slight changes in temperature within the duct. In fact, as noted previously, when conducting tests with flow, it was found to be necessary to introduce a temperature compensating circuit which maintains a constant value of wave number ($k = 2\pi f/c$).

VI.1.3. Phenomena to be verified

The most important phenomena to be considered in the lined duct tests are listed and briefly discussed below.

(1) Natural acoustic pressure mode shapes.

(a) Angular modes. Provided the liner has no variation of properties in the angular direction, and if no angular non-uniformity exists in the mean flow, then the angular mode shape should remain in a sinusoid variation. This, however, required experimental verification.

(b) The radial mode shape can be critically dependent on both the value of wall impedance and the flow velocity profile. Radial mode predictions must be verified for as many combinations of wall impedance and flow as possible.

(2) Complex propagation constant. In rigid wall ducts mode propagation is very distinctly defined. The propagation constant is either real (propagating) or imaginary (exponentially decaying). The presence of an attenuating liner results in a complex propagation constant, the real part normally corresponding to the rigid-wall propagation constant with the imaginary part representing the sound attenuation in the duct. The presence of mean flow further modifies the propagation constant. Both phenomena are subjects of study in the experiments for the lined annular duct.

(3) Radial acoustic velocity mode shape. Analytically, this was given as a solution to the radial momentum equation. The radial acoustic velocity is a function of both the acoustic pressure mode shape, the propagation constant and the mean velocity and mean velocity profile (or shear). The intent was to make radial measurements with a hot-wire probe and compare with the predictions. However, difficulties in processing the hot-wire signals precluded any useful observations.

(4) Effect of termination impedance on wave field in duct. If the duct radiation impedance is not well matched, significant reflections occur at the termination. The effect of this on the energy attenuation rate and the standing wave in the duct was investigated.

(5) Effect of mean flow on wave field in duct. Flow affects the wave field by convection through the duct and by refraction due to the flow profile. For certain conditions, either or both effects can be very significant. Also, they can either add or cancel according to the direction of propagation with respect to the flow direction.

(6) Effect of locally reacting vs non-locally reacting liners. For the honeycomb type liners, there is no appreciable sound propagation through the liner, parallel to the duct axis, and use of the locally reacting impedance assumption appears to be valid. However, for certain of the foam and fiberglass liners, propagation through the liner material occurs, with significant alteration in the overall attenuation performance of the liner. Tests and comparisons with theoretical predictions illustrate this point.

VI.2. Analytical Predictions

The theoretical study of sound propagation in acoustically lined ducts is a very complex subject. An experimental program of the type described in this report would be impossible without guidance from theoretical predictions. Therefore, before a detailed description and presentation of the experimental results, a series of numerical studies which display the predicted behavior of the parameters of interest and which were used in designing the experimental study, is felt to be useful.

The numerical studies are presented in graphical form to aid understanding of the effects. The graphs will show contours of equal attenuation and phase speed for individual modes and combinations of modes. Attenuation vs. frequency behavior for one of the liners is shown. Radial sound pressure distribution as a function of distance along the duct axis is studied, showing effects of variation and sensitivity to wall impedance on that radial pressure distribution. Also, the effect of wall impedance on the axial power level attenuation is studied.

A computer program, based on the theory presented in the analytical review section of this report was prepared within the Lockheed-Georgia Company under IR&D funding. Before entering a detailed discussion of the numerical studies, a brief description of the computer program is useful.

VI.2.1. Features of computer analysis for sound propagation in ducts

Basically, the computer program provides mode shapes and eigenvalues of the convected wave equation (equation (14)) for sound propagation in ducts of rectangular, circular, or circular annular geometry with axisymmetric, radially non-uniform mean flow. A brief discussion of each feature of the program input and solution features follows.

(1) Geometry. As stated above, the geometry may be either rectangular, circular, or circular-annular.

(2) Wall impedance. The wall impedance may be arbitrarily specified. For a rectangular duct, different values of wall impedance can be specified for opposite walls. The other pair of walls is assumed to be rigid. For the annular duct, the inner and outer walls may have different impedance.

(3) Circumferential or cross-mode order. Specification of the circumferential mode ("spinning mode") order for circular ducts or the cross-mode for rectangular ducts is arbitrary. The presence of rigid radial splitters can be included by specifying non-integer values for the circular geometry mode order.

(4) Radial mode order. This input is arbitrary. Any number of modes can be calculated, up to the number of finite difference stations,

however, accuracy requirements would keep the number of modes at a factor of 5-10 below the number of computational stations.

(5) Flow velocity and velocity profile. One of three options is available:

(a) Experimental values may be input at the finite difference computational stations;

(b) Mean velocity and boundary layer thickness can be specified, using a half-sinewave to simulate the boundary layer profile;

(c) A number of experimental data points can be input and the velocity and shear profiles close to the wall can be computed using a modified version of the universal law of the wall.

(6) Frequency. This may be arbitrarily specified and can be input as real frequency or non-dimensional wave-number parameter.

(7) Source sound pressure distribution. This has two options. One assumes a uniform sound pressure in the radial direction. Only radial modes of a particular angular mode order may be considered at any one time. A two-dimensional curve fit was not built into this program. The other option allows manual input of sound pressure distribution in the radial direction at each of the computational stations. A complex least-square curve fit routine is used in a Fourier type analysis to determine the mode amplitudes at the source location in order to simulate a specific source sound pressure distribution.

The computer program also includes effects of finite length, but in the present studies no end reflection is included. Thus, the results given are for an infinite length duct.

VI.2.2. Numerical studies

VI.2.2.1. Effects of wall impedance without flow. The parameter of primary usefulness in a design study is the total attenuation expected per unit length of duct. However, this cannot be specified unless the sound pressure distribution, and thus the amplitudes of the various modes, is specified at the duct entrance. Analytical studies in the past have resorted to various techniques for determining this total attenuation per unit duct length based on assumed modal distributions or initial pressure distribution. Feder and Dean (ref. 48) experimented with three assumptions for the modal distribution. These were (1) to assume that all the energy propagates in the least attenuated mode, (2) to assume that all the propagating modes initially (at the liner entrance) have equal energy, and (3) to assume that all the propagating modes initially have equal pressure amplitude. Another assumption introduced by Rice (ref. 49 was a sound pressure distribution at the liner entrance which conformed to the hard

wall plane (0,0) mode or else was specified from measurement. For a single frequency of excitation, this assumption is more realistic, especially for comparison with experiments where the initial pressure distribution can be measured.

In the discussion immediately following, it was assumed that the sound pressure distribution was confined to a particular angular mode set and that the sound pressure in the radial direction at the entrance to the lined section was plane. For purposes of comparing with experimental data from the facility, this condition is very closely approximated at frequencies below 1620 Hertz. The numerical studies in this sub-section will concentrate on the attenuation in an annular duct with hub-tip ratio of 0.566 and an unlined inner cylinder. It is quite difficult to display the relationship between the complex impedance and the complex eigenvalue without resorting to a contour map. Two types of these are used in practice. Morse (ref. 1) used the eigenvalue as the axis and ordinate of the complex plane plot and the complex impedance as the contour parameter. It seems more convenient, when studying a particular mode or a sum of modes to display the contours of constant eigenvalue on an impedance plane plot. Thus, effects of variation of impedance can easily be studied.

In the presentation to follow in this section, several modes and combinations of modes will be displayed in an impedance plane plot with attenuation and phase speed the plotting parameters. These plots will be used to show the effect of, and sensitivity to, wall impedance. Because of the multiplicity of combinations which could occur if inner and outer wall impedance varied independently, the inner wall is either considered as rigid or else its impedance is set equal to that of the outer wall.

Figure 87 illustrates the attenuation predicted for the 3rd angular mode set with the assumption of a plane radial sound pressure at the liner entrance. This computation, which displays the power level attenuation at one duct width downstream is at a frequency of 1000 Hertz ($kL = 1.915$). Several interesting facts can be gleaned from this contour map. First, examination of the data which resulted in the attenuation contours revealed that the contribution of each mode, necessary to simulate the plane radial distribution at $z = 0$, varies for each value of impedance on the complex plane plot. This results from the fact that mode shapes are highly dependent on the wall impedance boundary conditions. In this particular study, only the outer wall contains an acoustic material, with the inner wall specified as rigid. Second, the result of this study shows that for the particular annular geometric configuration, the optimum impedance is approximately $Z/\rho c = 0.05 - 0.10i$ with a power level attenuation greater than 30 decibels at one duct width downstream.

An interesting study, which illustrates the characteristics of the modes contributing to the contours of Figure 87, is presented in Figures 88-91. Figure 88 is an impedance plane contour plot of the complex eigenvalue. The attenuation contours are $Attn(dB) = 8.68\ kL\alpha$ and the contours normal to the attenuation are the real part of the propagation constant, β. The details of this curve provide data which can be directly compared with measurements from the facility. At frequencies below 1620 Hertz, the hard wall (3,0) mode can

Frequency - 1000 Hz, kL = 1.915; Hub-Tip Ratio = 0.568;
Hard Inner Wall; Acoustically Lined Outer Wall

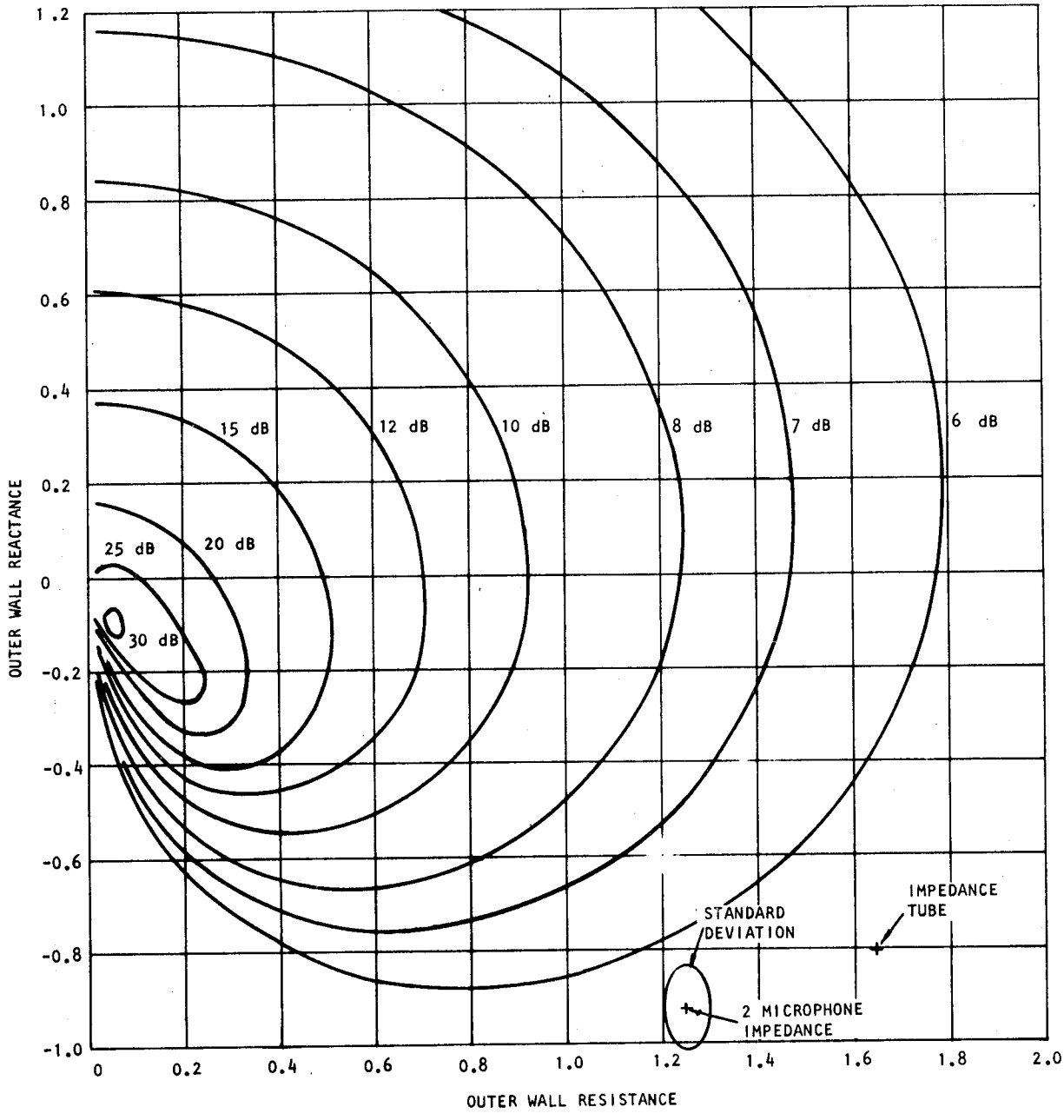


Figure 87. Isocontours of Sound Power Level Attenuation One Diameter Downstream in Annular Duct, for Plane Radial - Third Angular Mode Set

Frequency - 1000 Hz; kL = 1.915; Hub-Tip Ratio = 0.568
Hard Inner Wall; Acoustically Lined Outer Wall

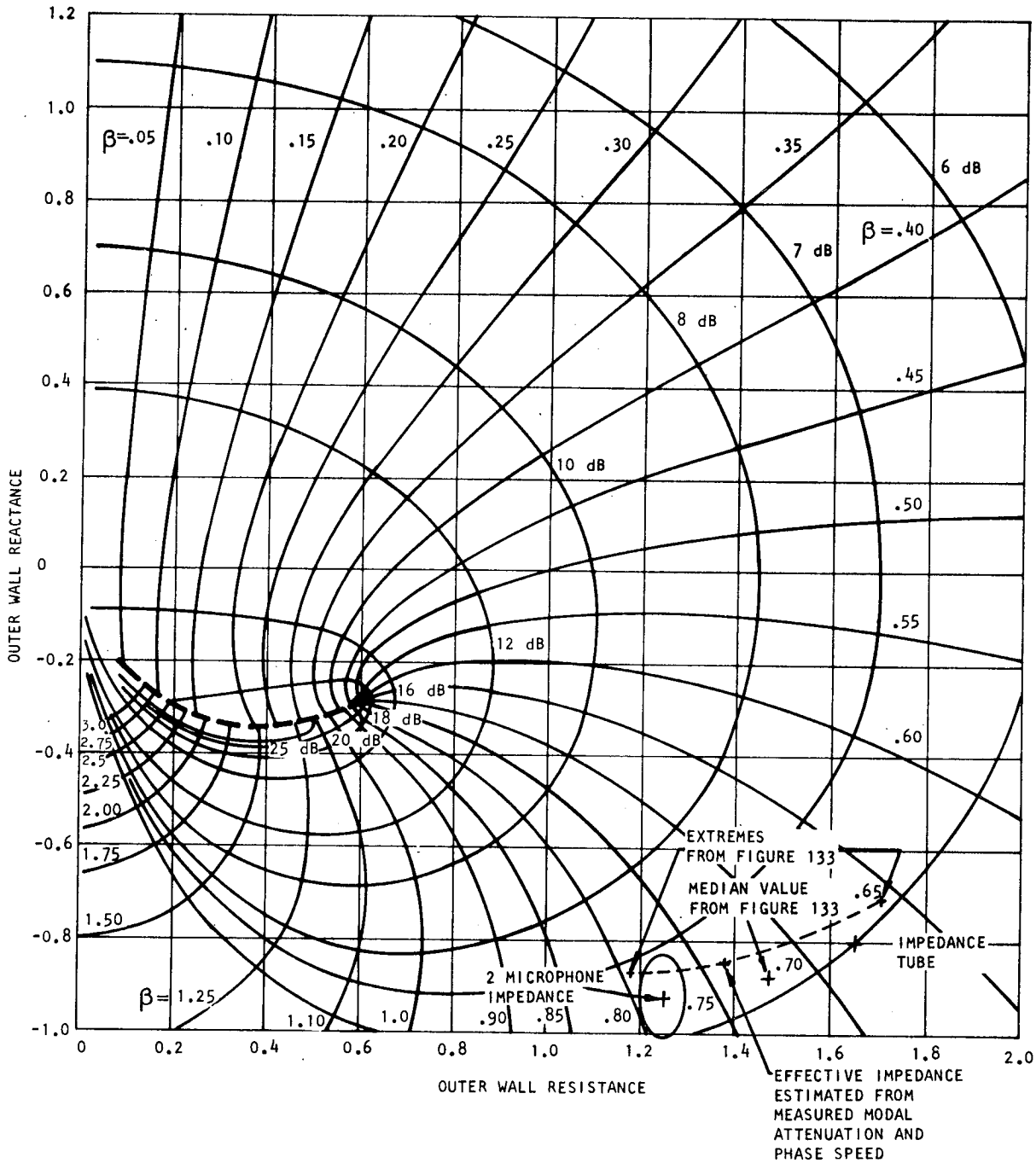


Figure 88. Isocontours of (3,0) Modal Attenuation and Propagation Constant, β, in Annular Duct

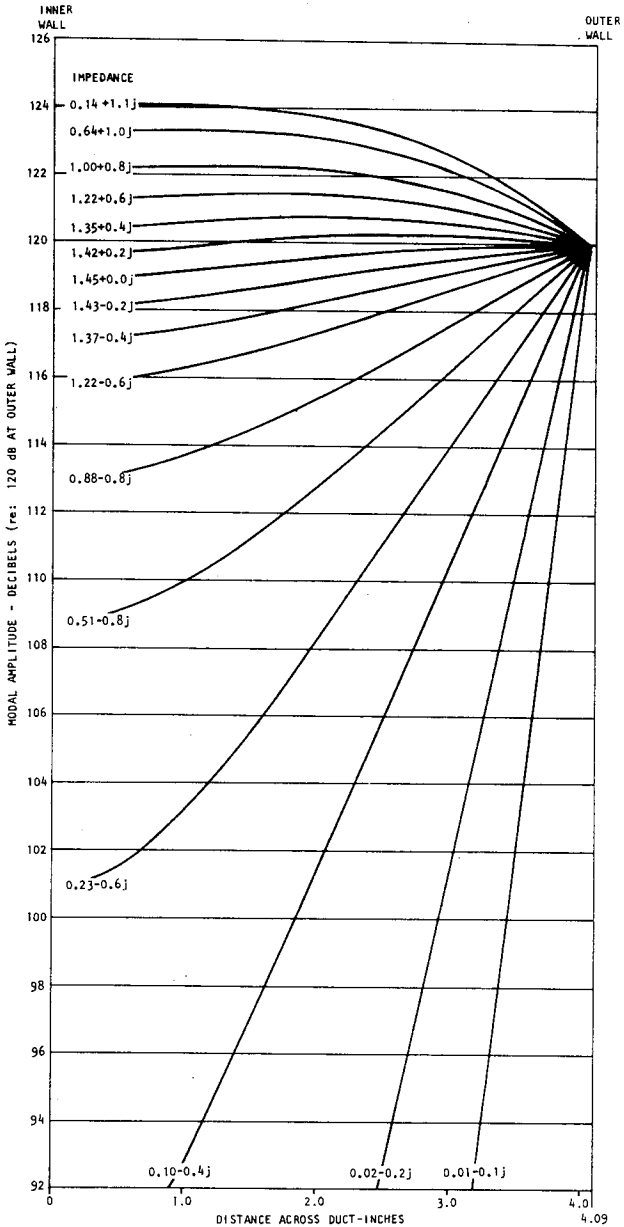


Figure 89. Variation of (3,0) Modal Amplitude Along Trace of 8 dB Contour in Figure 88

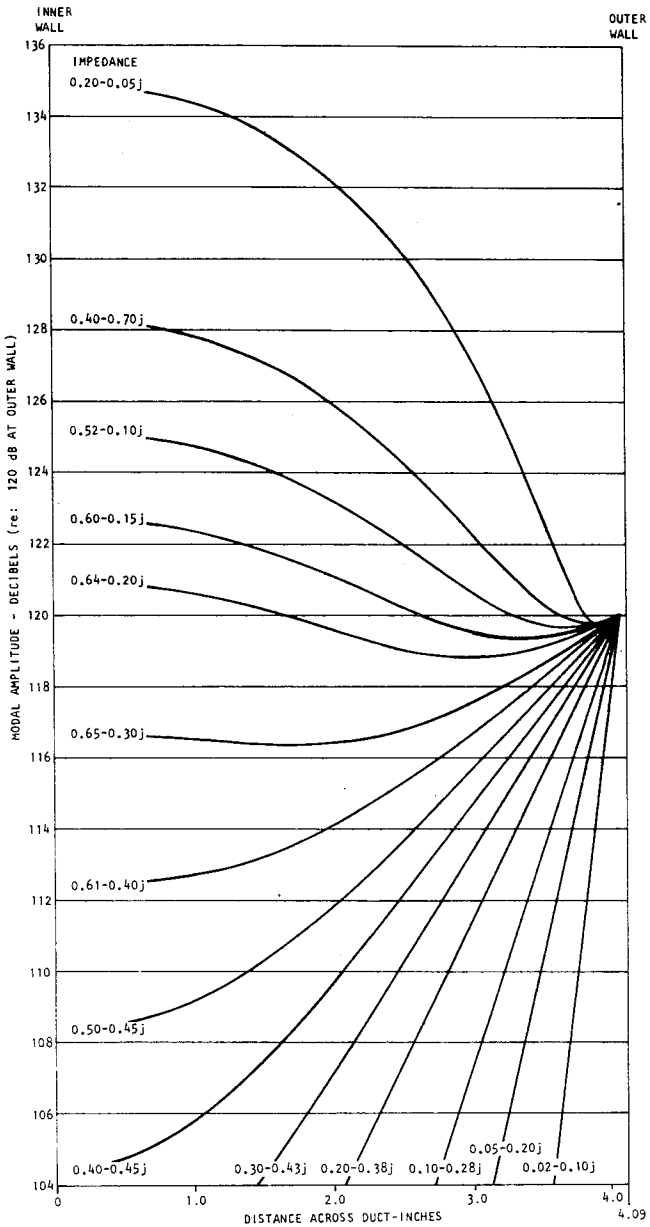


Figure 90. Variation of (3,0) Modal Amplitude Along Trace of 16 dB Contour in Figure 88

be simulated in the 3' long source section. This hard wall (3,0) mode, after entering the test section, which is nine duct widths long, rapidly converts to the (3,0) lined duct mode for most values of impedance on the contour chart. Thus, except for impedance values below the branch line, down to reactances of approximately -0.6, the (3,0) lined duct mode can be set up in relative isolation at about two duct lengths from the entrance, since all the higher order softwall modes decay much more rapidly than the zero order mode. In the region excluded, other modes may have less attenuation than the (3,0) mode. In all but the excluded region, it should be possible to measure both the attenuation rate and the propagation speed of the (3,0) softwall mode.

The phase velocity of propagating modes is $c_\phi = c/\beta$, where c is speed of sound and β is the propagation constant. It is quite intriguing in examining figure 88, to note that at resistances less than 0.73, the propagation constant exceeds 1.0 for most reactance values below the branch line. The physical interpretation of a mode with a propagation constant greater than 1.0 is that the mode is "slow." That is, the phase speed, c_ϕ, is less than the speed of sound. It is not known if these modes have been experimentally detected previously, but the possibility of their existance was noted in a conversation with Mungur in 1969. One physically significant point associated with the slow propagation speed is that the axial wavelength is reduced at a particular impressed frequency (i.e., $\lambda_{mn} = c/f\beta_{mn}$).

It was mentioned earlier that while the contours of figure 88 display the attenuation and axial propagation characteristics for the (3,0) mode, the radial shape of the (3,0) mode changes drastically for various positions in the impedance plane. Figures 89 and 90 illustrate the changing character of the mode shape as two of the constant level contours are traversed in a clockwise direction. Mode shape amplitudes are shown in figure 89 for various positions in the impedance plane, corresponding to intersections of the 8 dB contour and reactance lines beginning at 1.1 and progressing in a clockwise direction in steps of 0.1 magnitude in reactance. The mode shapes are normalized to 120 decibels at the outer wall. For large positive values of reactance, sound pressure is greater on the inner hard wall, than on the outer soft wall. However, for the low positive and all negative values of reactance, the pressure is lower on the hard wall, than on the lined wall. At first glance, this is adverse to physical concept since one would expect the lined wall to have a lower sound pressure for all modes. However, this adverse skewing of the mode shape is due to the effect of the reactance. It is observed that the influence of the hard wall on forcing a zero gradient at the wall extends quite a long way toward the center of the channel. In fact, in some impedance regions finite sound pressure exists only near the wall. The mode is very similar to a surface wave which decays exponentially away from the wall. Consistent with this, the value of sound pressure on the hard wall in the region of small resistance and negative reactance appears to approach zero in the limit of zero resistance. It is noted, however, that this would violate the boundary conditions.

The set of mode shapes in a clockwise direction around the 16 dB contour are very similar, except for a slight dip in some of the shapes. This dip sometimes makes mode identification very difficult, especially in the region of the branch line.

A characteristic of this first order mode, which is very easy to measure, is the SPL and phase difference between the inner and outer walls. These parameters are also fairly easy to plot as contours, somewhat similar to the plots of eigenvalue. In figure 91, the differences between outer wall and inner wall SPL and phase are plotted as contours of constant level. At first glance, the usefulness of a plot of this type appears to be minimal, but as will be described later, it provides a check on the effective value of wall impedance also obtained from other experimental data.

A considerable volume of published results deal specifically with the least attenuated mode. Also, as mentioned, much of the current and previous liner design work is based on the least attenuated mode results. Thus, it is of interest to study this mode both analytically and experimentally and also to compare the (0,0) mode eigenvalue with that of the (3,0) mode previously discussed. First, the (0,0) mode is not always the least attenuated mode. For certain reactance values immediately below the branch line, the (0,1), or in some cases the (0,2) mode will be least attenuated.

In the comparison of the (0,0) (figure 92) and (3,0) mode (figure 88) contours of equal attenuation, it is immediately obvious that at low resistance, for positive values of reactance, the contours are normal to the branch line for the (0,0) mode and normal to the zero resistance axis for the (3,0) mode. The most useful observation is that the (0,0) mode attenuation is generally less than that for the (3,0) mode for a particular value of impedance. Probably the most significant difference between the impedance plane eigenvalue contours is the location of the branch point. The lower order mode branch point lies closer to the zero reactance axis. Also, for any value of impedance, the phase speed is much slower.

The propagation of a plane wave of zero angular order is shown in figure 93. If this is compared with figure 87, two distinct differences can be observed. First, the attenuation for most values of impedance is significantly lower. The maximum attenuation for the plane mode is of the order of 15 dB at the optimum, while the 3rd order, plane radial shape has a maximum attenuation of over 30 dB. Second, the optimum value of impedance appears to be approximately, $Z = 0.15 - 0.3i$, compared to $0.05 - 0.1i$ for the 3rd order plane mode of figure 87.

Two sets of the test liners have both inner and outer attenuating walls. Figures 94 and 95 show the contours of constant attenuation for the (2,0) and (2,1) modes at 1800 Hz over a range of impedance encompassing the test values for those liners. For this particular impedance-frequency range, both modes are propagating with predicted attenuations from 0.5 to 9 decibels.

VI.2.2.2. Effects of frequency without flow. Another parametric study which is of interest, is given in figure 96 and shows the functional behavior of the 20 Rayl configuration with frequency with both inner and outer walls lined. This chart illustrates the attenuation-frequency characteristics of the first three radial modes, for a $\sin(2\theta)$ angular mode variation, up to a frequency of 4000 Hertz. Average values of measured impedance were used in

Frequency - 1000 Hz; kL = 1.915; Hub-Tip Ratio = 0.568;
Hard Inner Wall; Acoustically Lined Outer Wall

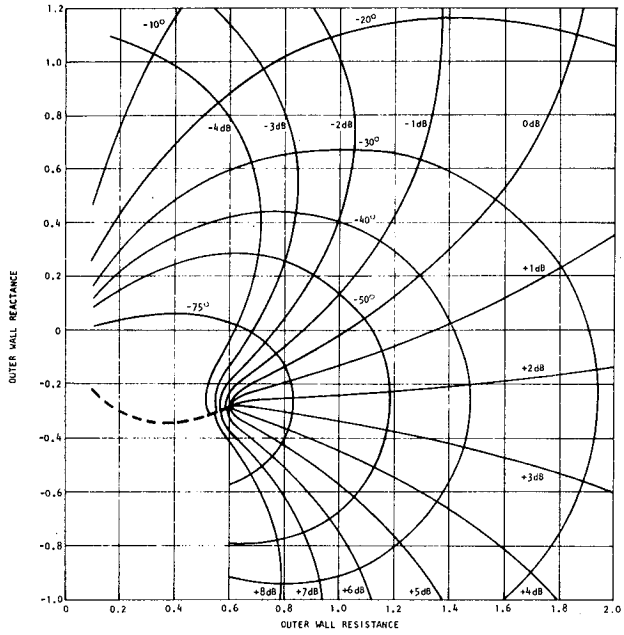


Figure 91. Isocontours of (3,0) Mode Amplitude and Phase Angle Differences Between Inner and Outer Walls (re. Outer Wall) of Annular Duct

Frequency - 1000 Hz; kL = 1.915; Hub-Tip Ratio = 0.568;
Hard Inner Wall; Acoustically Lined Outer Wall

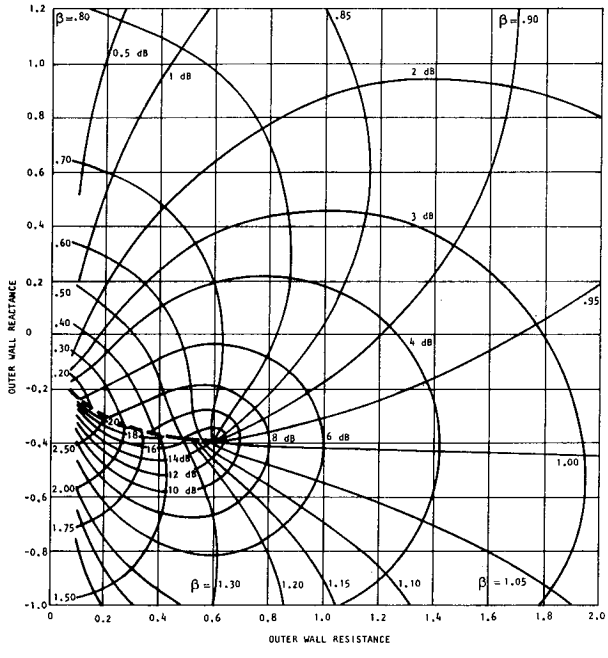


Figure 92. Isocontours of (0,0) Modal Attenuation and Propagation Constant, β, in Annular Duct

Frequency - 1000 Hz; kL = 1.915; Hub-Tip Ratio = 0.568;
Hard Inner Wall; Acoustically Lined Outer Wall

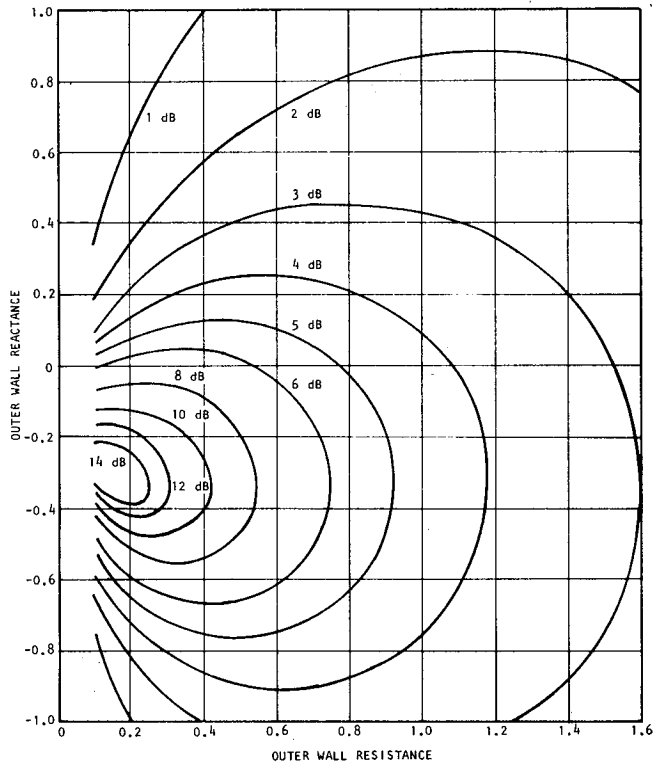
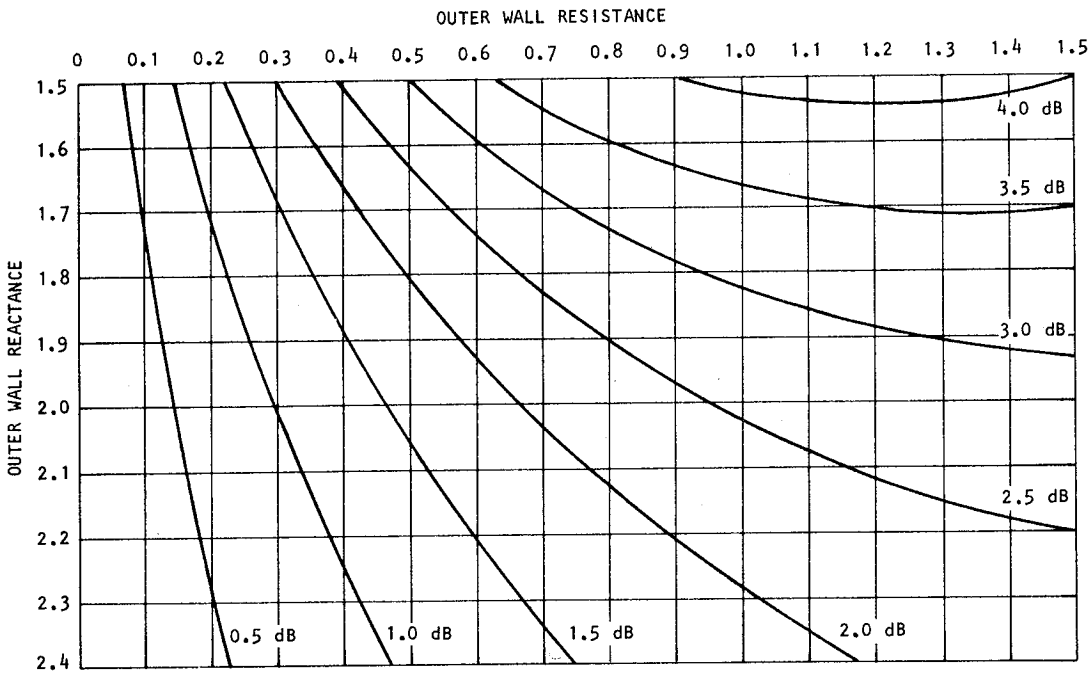
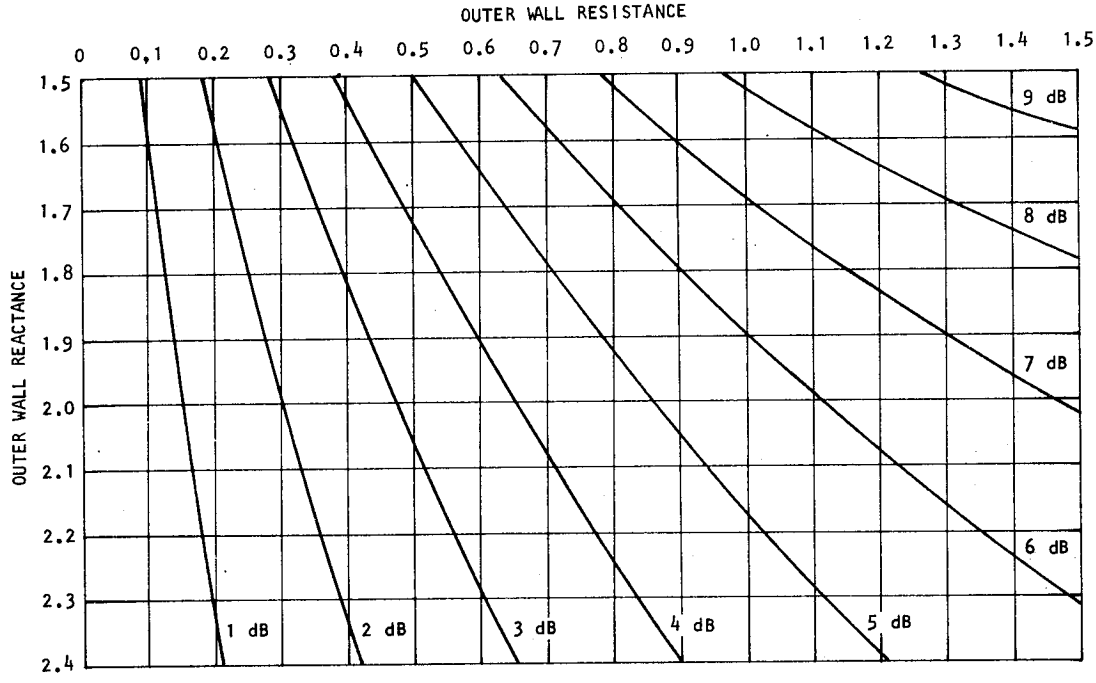


Figure 93. Isocontours of Sound Power Level Attenuation One Diameter Downstream in Annular Duct for Plane Radial - Plane Angular Mode Set



Frequency - 1800 Hz; kL =3.44; Hub-Tip Ratio = 0.566; Acoustically Lined Inner and Outer Walls

Figure 94. Isocontours of (2,0) Modal Attenuation in Annular Duct



Frequency - 1800 Hz; kL =3.44; Hub-Tip Ratio = 0.566; Acoustically Lined Inner and Outer Walls

Figure 95. Isocontours of (2,1) Modal Attenuation in Annular Duct

computing this frequency response. Similar modal attenuation curves are shown in figures 97-99 for the plane (zeroth), fifth and sixth angular modes.

The most interesting result from this study concerns the least attenuated mode. If the criterion chosen was that the least attenuated mode dominates the liner attenuation, then the maximum attenuation at any frequency for this liner would be 6 dB per duct width, with the peak at 2900 Hz, where the wall impedance is approximately 0.4 - 1.2i. However, if a radial source pressure distribution is assumed, which is independent of frequency , a completely different trend results at frequencies above the first radial mode cut-on frequency. This demonstrates the necessity, once again, for more detailed knowledge of the in-duct sound pressure distribution due to the noise source.

In this numerical study a plane radial shape was introduced for all frequencies. Coefficients of each mode were determined to give the best approximation to the plane wave at the liner entrance. This procedure was repeated at each frequency and the resulting sound power attenuation was computed at three axial stations (i.e. 1, 2, and 3 duct widths downstream). Similar results are shown for the other angular mode sets in figures 96-99 with the curves being identified in the legend. It is very interesting to note how the power attenuation at one duct width adhers to the attenuation of the least attenuated mode up to approximately 3000 Hertz, but then becomes considerably greater than the attenuation of that mode (which incidently has switched from the zero order radial mode to the 2nd order radial mode). It is in this region (i.e. the region near liner resonance) that the picture of modal attenuation becomes very confusing and it is considered an absolute requirement that an initial sound pressure spatial distribution must be given.

Another interesting feature of the power attenuation curves for an initial plane wave is the tendency of the frequency of peak attenuation to shift as a function of axial distance. This is a result of the modes with high attenuation losing effectiveness at distances further downstream from the source plane.

VI.2.2.3. Effects of flow. In previous numerical studies, flow effects on attenuation rate and propagation speed have been found to be very significant. In addition, mean flow indirectly affects liner performance by modification of liner impedance. These effects on liner impedance were discussed in Section V.

A study which duplicates the data of figure 88, but with 50 fps mean flow velocity through the annulus, is shown in figure 100. This chart is a constant level contour plot in the impedance plane for the (3,0) mode at 1000 Hertz. The mean flow profile is that of a quarter-sine wave in the 2% thick boundary layer (2% of annulus width) and uniform flow elsewhere. General observations are that for negative reactance values the attenuation is reduced by approximately 1 decibel and that the branch line has shifted to more positive values of reactance.

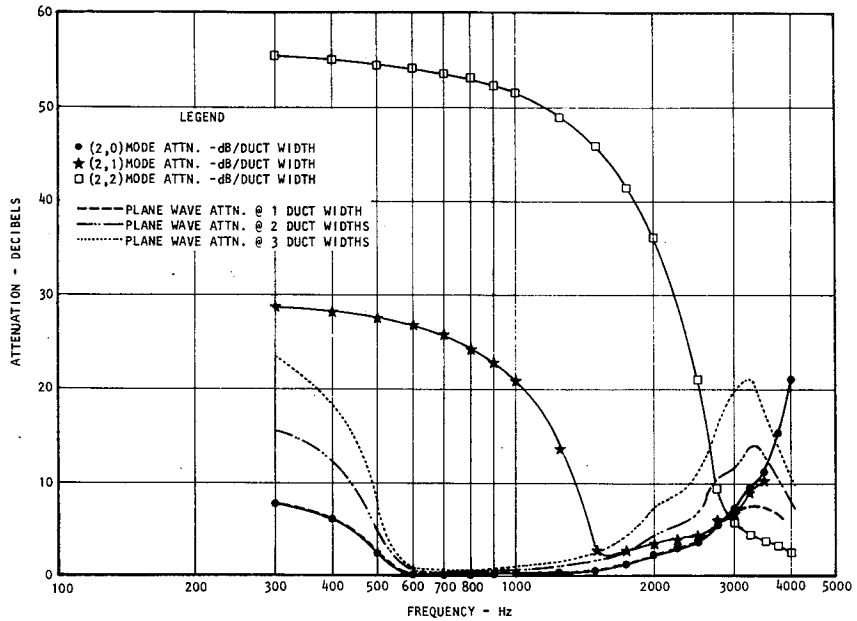


Figure 96. Modal and Power Level Attenuation Frequency Response for Liner 1 - Second Angular Mode Set

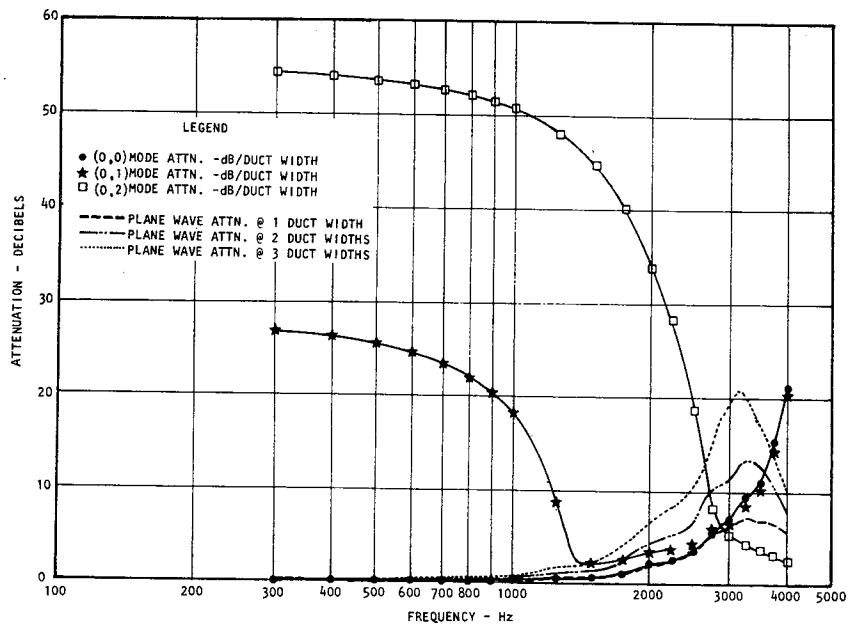


Figure 97. Modal and Power Level Attenuation Frequency Response for Liner 1 - Plane Angular Mode Set

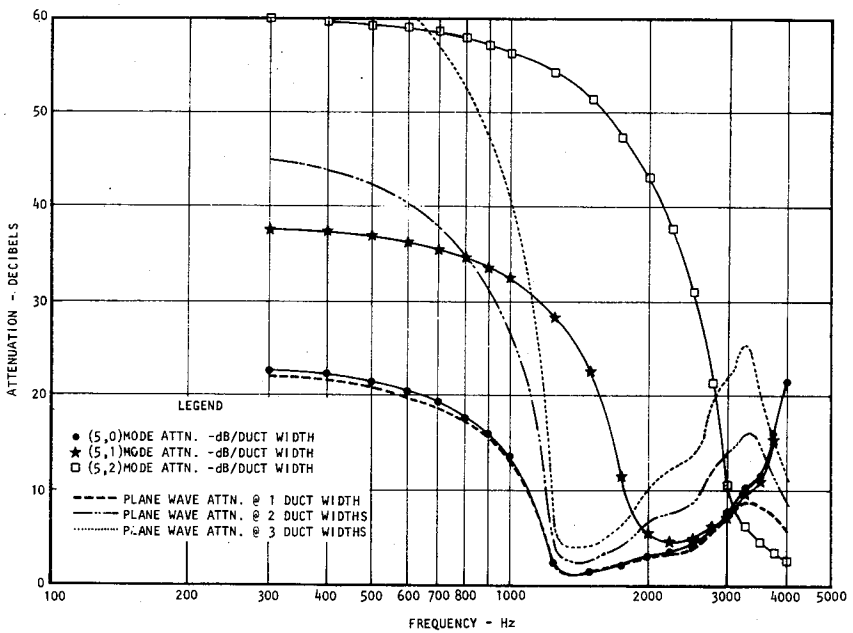


Figure 98. Modal and Power Level Attenuation Frequency Response for Liner 1 - Fifth Angular Mode Set

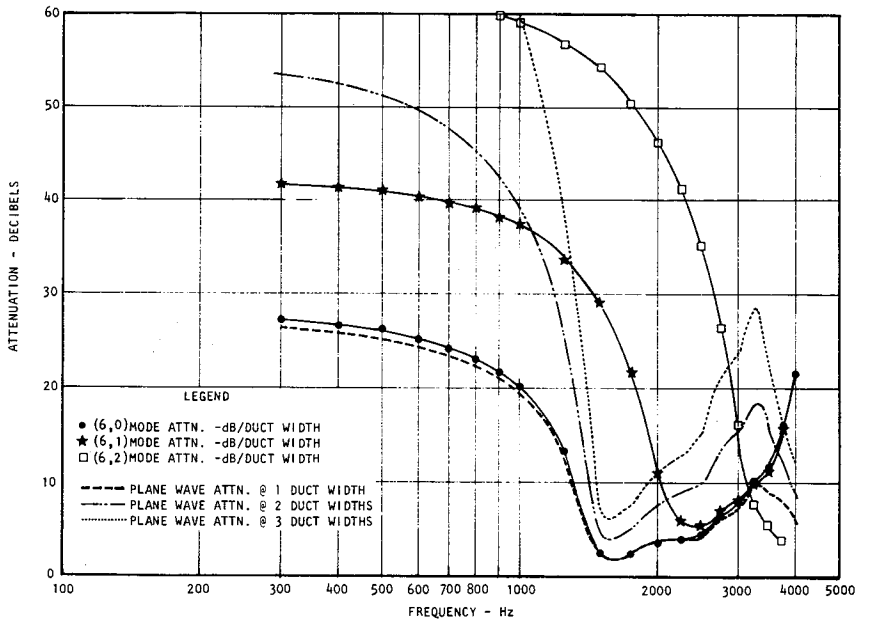


Figure 99. Modal and Power Level Attenuation Frequency Response for Liner 1 - Sixth Angular Mode Set

Figures 101-103 show the attenuation contours for an initial radial plane distribution (derived by Fourier summing 10 radial modes at the source plane) for the third angular mode at 50 fps, with 2% boundary layer, for three different downstream positions. Figure 101 at one duct width downstream is comparable to figure 87 for no-flow. An overlay of the two plots would show that the position of the optimum impedance with flow has shifted upward and toward greater positive values of wall resistance. At the same time the maximum attenuation appears to have been reduced. Figures 102 and 103 are similar to figure 101 at two and three duct widths downstream. The contours in figure 102 are plotted in multiples of two times the values of attenuation used for contour plotting increments in figure 101. A multiple of three was used in plotting the contours at three duct widths downstream. Thus, when comparing the attenuation contours at the three positions, the deviation from a linear attenuation rate can be ascertained. It is apparent that at distances further downstream, the optimum value of impedance for maximum attenuation shifts to a higher value of resistance. This effect is a result of the fact that modes with greatest attenuation are, for all practical purposes, completely decayed at 3 duct widths downstream. Thus, the optimum shifts from the lower resistance, associated with higher order modes, to the higher resistance optimum value, characteristic of the least attenuated mode.

Finally, in order to provide further comparison data for the test results, contours for the (3,0) mode complex propagation constant are plotted in figure 104 and the 3rd order plane mode are shown in figure 105 for a flow velocity of 150 fps. The predominant effect of flow on the (3,0) mode complex eigenvalue is a reduction in propagation constant, β, as would be expected for the downstream propagating mode and as can be seen by comparing figures 88 and 104. The data necessary to fill in the area in the vicinity of the branch line was not computed because of the extra computer run time required for that region. In examining the plane mode attenuation for the 3rd angular set, the 150 fps data of figure 105 should be compared with figures 87 and 101. Although the area of the optimum impedance was not bracketed, it appears that the value of optimum impedance has increased in resistance and the reactance has assumed a more positive value, when compared to the no-flow case.

VI.2.2.4. Sound pressure distribution across the duct. An example of the effect of wall impedance on the pressure distribution in the duct is shown in figures 106-109. These curves at the four axial stations, for each impedance value, originate as plane waves at $z/L = 0$ and ultimately revert to the shape of the least attenuated mode. In figure 106, the shape remains relatively plane at all axial positions, however, the attenuation per duct width is not linear. A glance at figure 110 reveals the behavior of this non-linear attenuation vs axial distance, and a study of the propagation constants reveals that mode "beating" is the reason for the non-linear behavior. The case studied in figure 106 has two modes with almost equal attenuation but with significantly different propagation speeds as shown in the tabulation at the top of figure 110. This particular situation results in the two modes slowly moving in and out of phase as the pattern propagates down the duct. Figures 107-109 show variations of the downstream pressure distribution for different values of impedance in the region near the optimum

Frequency - 1000 Hz; kL = 1.915; Hub-Tip Ratio = 0.568
Hard Inner Wall; Acoustically Lined Outer Wall;
Velocity Profile ¼ Sine Wave; Boundary Layer Thickness 2%

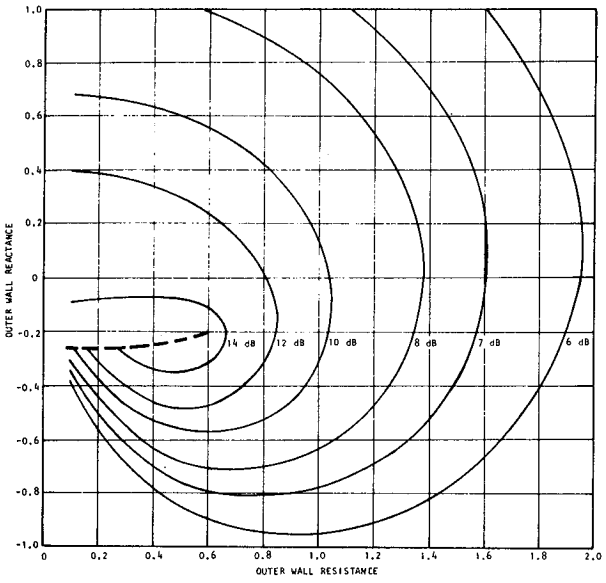


Figure 100. Isocontours of (3,0) Modal Attenuation in Annular Duct with 50 fps Sheared Flow

Frequency - 1000 Hz; kL = 1.915; Hub-Tip Ratio = 0.568
Hard Inner Wall; Acoustically Lined Outer Wall;
Velocity Profile ¼ Sine Wave; Boundary Layer Thickness 2%

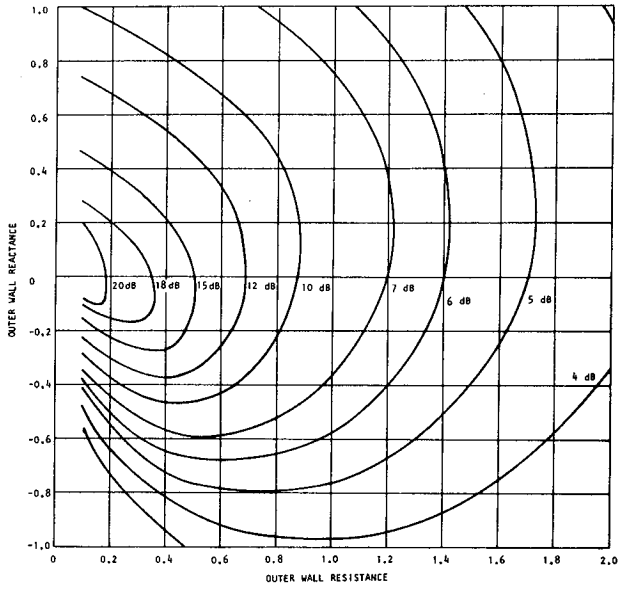


Figure 101. Isocontours of Sound Power Attenuation One Diameter Downstream in Annular Duct for Plane Radial - Third Angular Mode Set with 50 fps Sheared Flow

Frequency - 1000 Hz; kL = 1.915; Hub-Tip Ratio = 0.568
Hard Inner Wall; Acoustically Lined Outer Wall;
Velocity Profile ¼ Sine Wave; Boundary Layer Thickness 2%

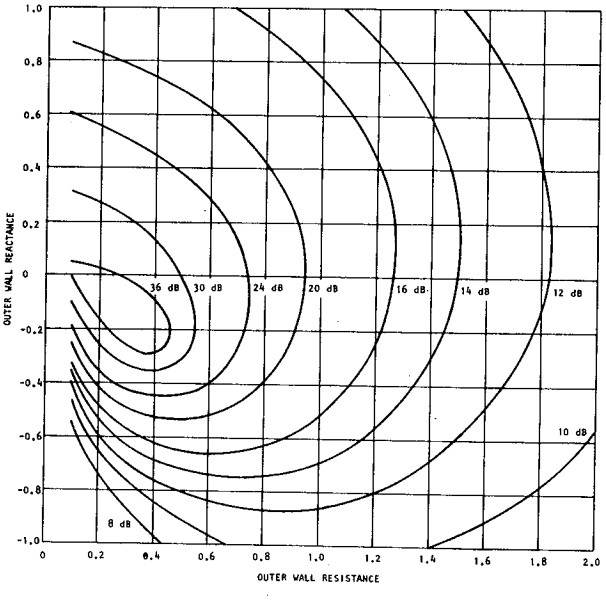


Figure 102. Isocontours of Sound Power Attenuation Two Diameters Downstream in Annular Duct for Plane Radial - Third Angular Mode Set with 50 fps Sheared Flow

Frequency - 1000 Hz; kL = 1.915; Hub-Tip Ratio = 0.568
Hard Inner Wall; Acoustically Lined Outer Wall;
Velocity Profile ¼ Sine Wave; Boundary Layer Thickness 2%

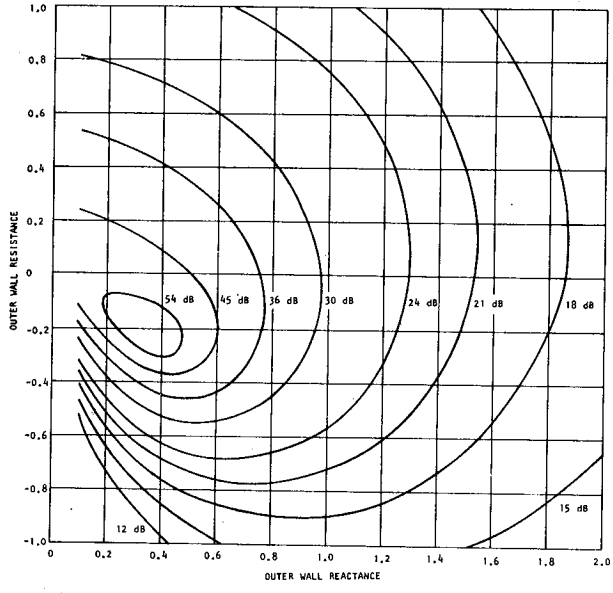


Figure 103. Isocontours of Sound Power Attenuation Three Diameters Downstream in Annular Duct for Plane Radial - Third Angular Mode Set with 50 fps Sheared Flow

Frequency - 1000 Hz; kL = 1.915; Hub-Tip Ratio = 0.568
Hard Inner Wall; Acoustically Lined Outer Wall
Velocity Profile ¼ Sine Wave; Boundary Layer Thickness 2%

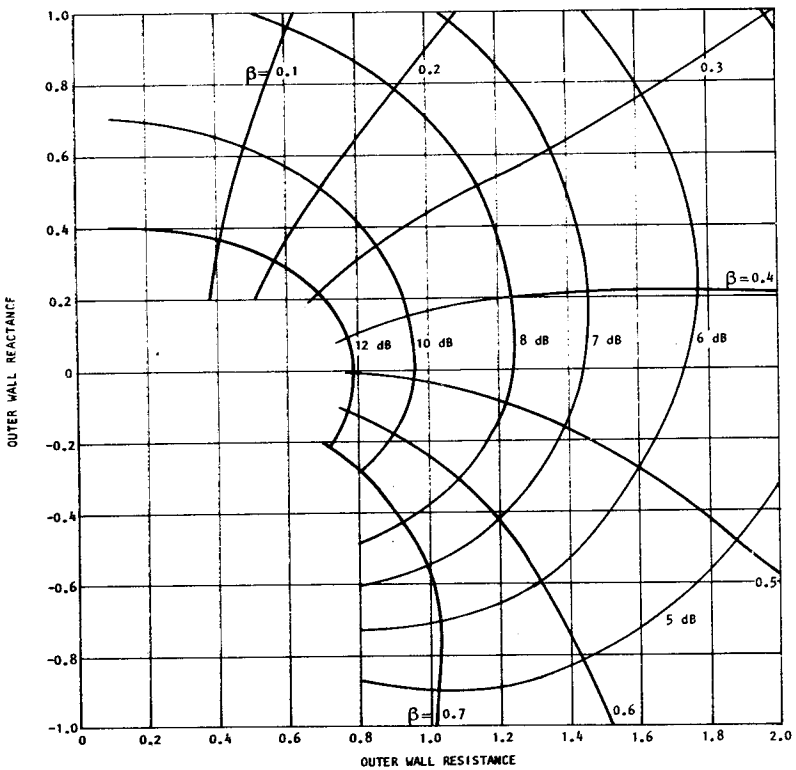


Figure 104. Isocontours of (3,0) Modal Attenuation and Propagation Constant, β, in Annular Duct with 150 fps Sheared Flow

Frequency - 1000 Hz; kL = 1.915; Hub-Tip Ratio = 0.568
Hard Inner Wall; Acoustically Lined Outer Wall;
Velocity Profile ¼ Sine Wave; Boundary Layer Thickness 2%

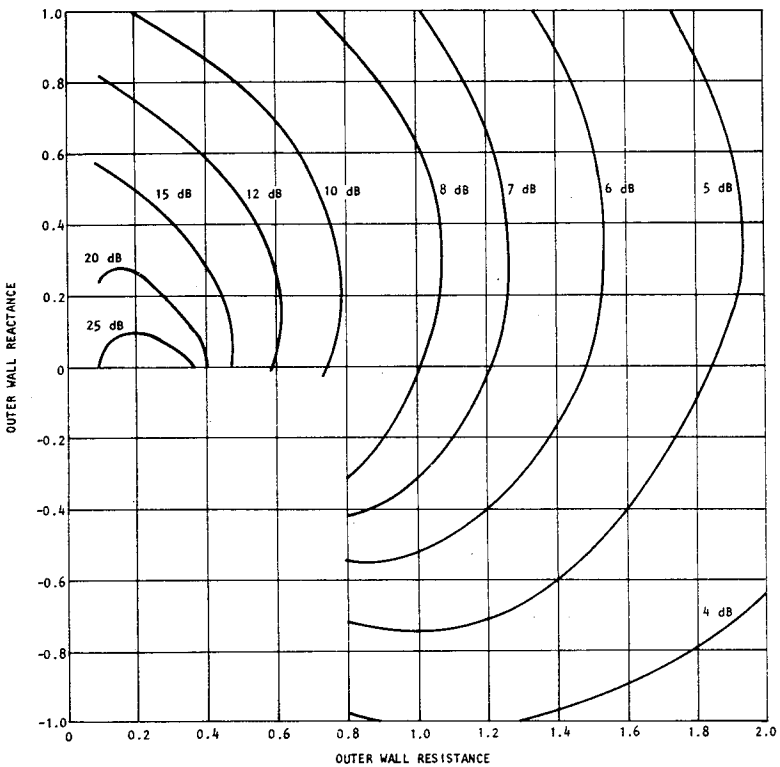


Figure 105. Isocontours of Sound Power Attenuation One Diameter Downstream in Annular Duct for Plane Radial - Third Angular Mode Set with 150 fps Sheared Flow

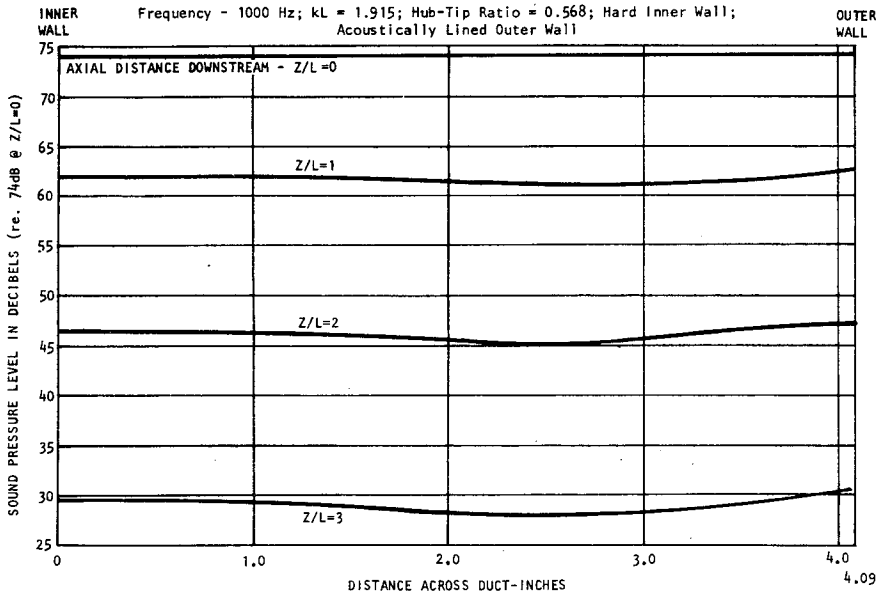


Figure 106. Downstream Sound Pressure Distribution in Annular Duct for Z = 0.6 - 0.2i

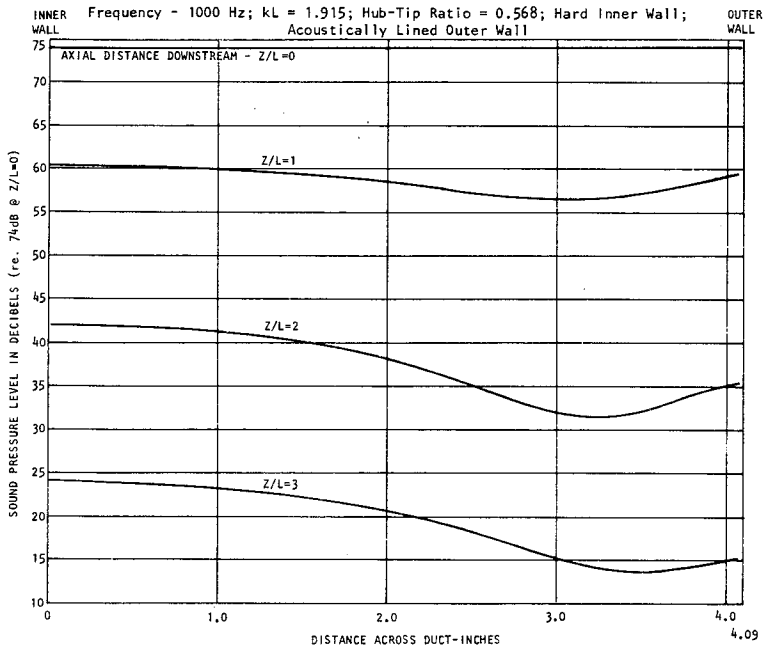


Figure 107. Downstream Sound Pressure Distribution in Annular Duct for Z = 0.4 - 0.2i

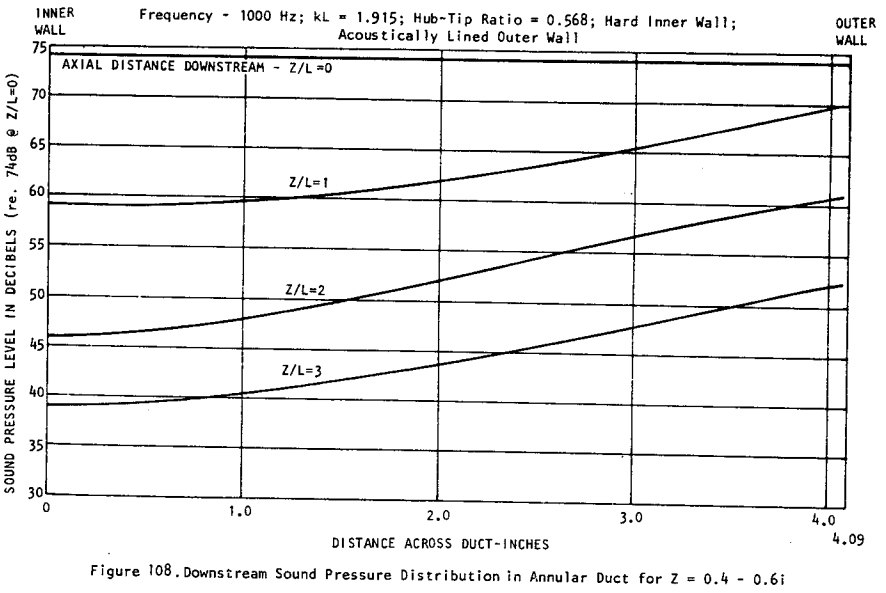


Figure 108. Downstream Sound Pressure Distribution in Annular Duct for Z = 0.4 - 0.6i

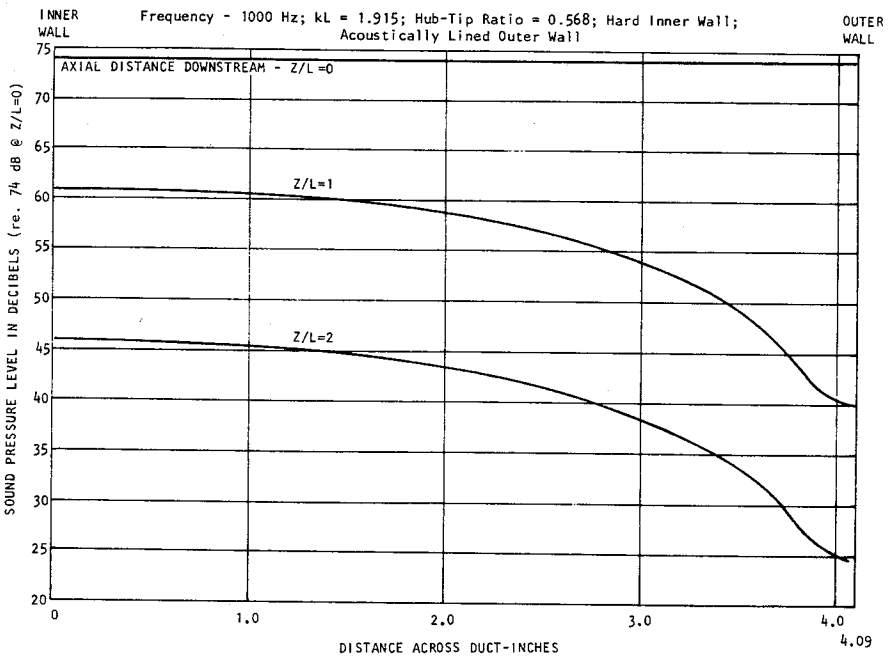


Figure 109. Downstream Sound Pressure Distribution in Annular Duct for Z = 0.1 + 0.0i

SYMBOL	IMPEDANCE		EIGENVALUES							
	R	X	α_1,dB	β_1	α_2,dB	β_2	α_3,dB	β_3	α_4,dB	β_4
— — — —	0.6	-0.2	19.38	0.475	19.82	0.664	51.57	0.136	79.35	0.026
———	0.4	-0.2	17.70	0.200	24.39	1.310	49.74	0.163	78.17	0.042
----------	0.4	-0.6	8.76	1.270	21.28	0.076	50.82	-.005	78.99	-.074
——·· ——	0.1	0	15.18	0.013	41.81	0.091	70.27	0.151	99.26	0.155

Frequency - 1000 Hz; kL = 1.915; Hub-Tip Ratio = 0.568
Hard Inner Wall; Acoustically Lined Outer Wall

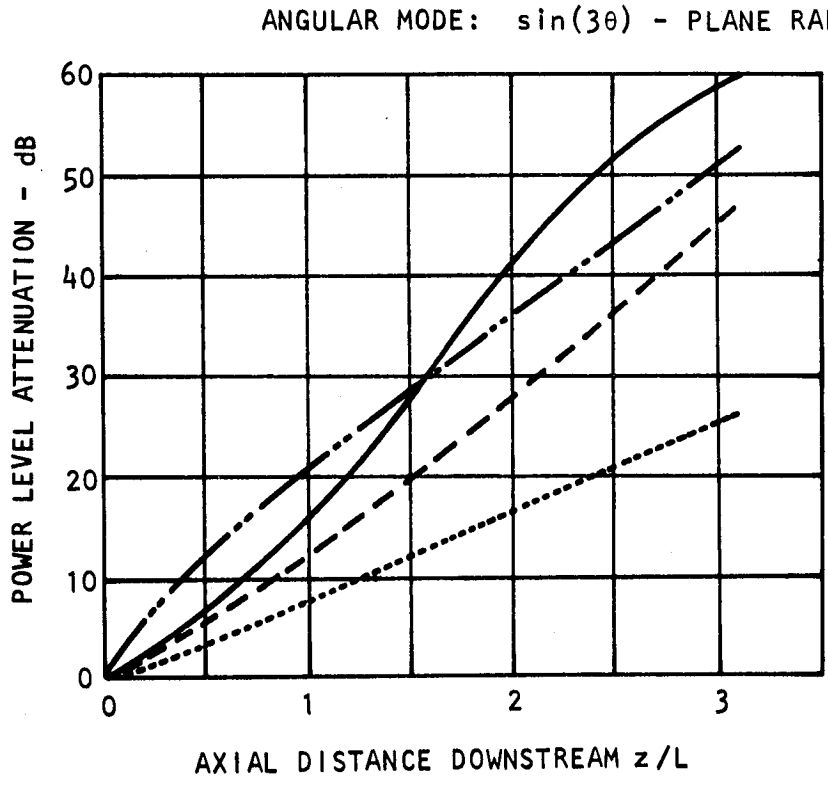


Figure 110. Effect of Outer Wall Impedance on Power Level Attenuation in Annular Duct

impedance. Note in figure 110 how the performance ranking of various liners at one duct width downstream changes for distances further downstream.

There are many interesting variations on this type of presentation; however, this serves to illustrate the nature of energy attenuation of a particular pressure distribution and how that parameter compares with modal attenuation. As an example of a ridiculous comparison, observe the modal attenuation for a wall impedance Z = 0.6 - 0.2i. The attenuation of the least attenuated mode is 19.4 dB and the next mode has 19.8 dB attenuation, with the other modes having 50 dB or greater attenuation. At first glance, it would be expected that the minimum attenuation for any type of sound pressure wave propagating down the duct would be at least 19.4dB. However, the calculated energy attenuation which is proportional to

$$1/2 \int_{R_i}^{R_o} pv^{*}RdR + \text{Mach no terms}, \qquad (80)$$

is only 12.5 decibels at one duct length and at three duct lengths becomes 45 decibels, still 13 decibels below the attenuation of the least attenuated mode. The cause for this significant disparity is due almost entirely to mode phasing.

VI.3 Comparison of Theory with Experiment

The previous sub-section on analytical predictions has served to illustrate the type of results expected from the experiments. Also, in the introduction to this section, the major phenomena for experimental consideration were listed. These were (1) propagation constant (attenuation and phase speed), (2) sound pressure mode shapes, (3) radial acoustic velocity mode shapes, (4) effect of end impedance, (5) effect of mean flow, (6) effect of wall impedance, and (7) effect of locally reacting vs non-locally reacting wall impedance.

In this section, a detailed set of measurements are presented, followed by the relevant comparisons of those measurements with theoretical predictions. The fundamental parameters derived from basic theory are the modal eigenvalue and eigenvector. Thus, the complete section will be devoted to various comparisons with either the eigenvalue or eigenvector, singularly or in combination, together with studies of the effects of flow and wall impedance on those parameters.

A considerable portion of the work which follows is devoted to comparisons in lined ducts without flow. These tests were multi-purpose. First, it was necessary to develop the necessary test techniques and data analysis methods prior to introducing the additional complication of mean flow, and second, it was necessary to verify the theory for the no-flow case prior to testing with flow.

Thus, the following major sub-sections are devoted to no-flow eigenvalue comparisons of theory and experiment, no-flow eigenvector comparisons of theory

and experiment, and the effect of flow on both the eigenvalue and eigenvector.

VI.3.1. Modal attenuation and propagation constant - no flow

In the introduction to this section, it was implied that at frequencies below the first radial mode cut-on it would be relatively easy to measure the mode attenuation rates and propagation constants, but that at higher frequencies, where more than one radial mode is propagating, determination of the characteristics of individual modes would require a more sophisticated experimental technique. Because of the different requirements of the experimental procedures, results of tests from two different frequency regimes will be described separately.

VI.3.1.1. Single lower-order radial mode. Liner 1 was designed to have maximum attenuation in the frequency range below the first higher order, hard-wall, radial mode cut-on frequency. Thus, with this liner, a series of angular modes could be studied in isolation in both the hard wall source section and in the lined test section.

In comparisons of experiment and theory, the numerical predictions utilized the measured values for impedance as discussed and presented in Section V.

Liner 1 was very useful in two ways. Because of its impedance-frequency characteristics, much useful data for comparison of theory and experiment for the lowest order radial mode was developed from this liner. It was also used for developing data analysis techniques for measurement of higher order radial mode characteristics. This will be discussed in the sub-section immediately following.

A useful series of basic tests was conducted with the liner 1 configuration. A 3rd order angular mode ($\sin 3\theta$) was set up in the source section. Radial sound pressure surveys were conducted at an angle corresponding to a peak value of the angular mode at a large number of axial stations. An interesting parameter is the axial variation of the sound pressure amplitude and phase. Figure 111 shows SPL and phase at the inner and outer wall for three frequencies plotted versus axial distance down the duct. Examining the sound pressure amplitude decay characteristic for 884 Hertz, it is observed that the SPL at the inner wall falls more rapidly than does that at the outer wall. The radial pressure pattern at the liner entrance has a 2.5 dB difference between the inner and outer wall, which is approximately the level difference expected for the hard wall (3,0) mode excited at the source plane. As this wave enters the lined section, the natural modes abruptly assume a new radial shape. Thus, some of the energy transfers into the least attenuated radial mode and some transfers into higher order radial modes. In the first 4" - 6", the effect of these higher order modes can be detected by observing that the attenuation rate on the outer wall is non-linear, signifying that the modes are decaying at different rates. In figure 111(c) for 1430 Hertz, it is found that the outer wall now has a lower sound level

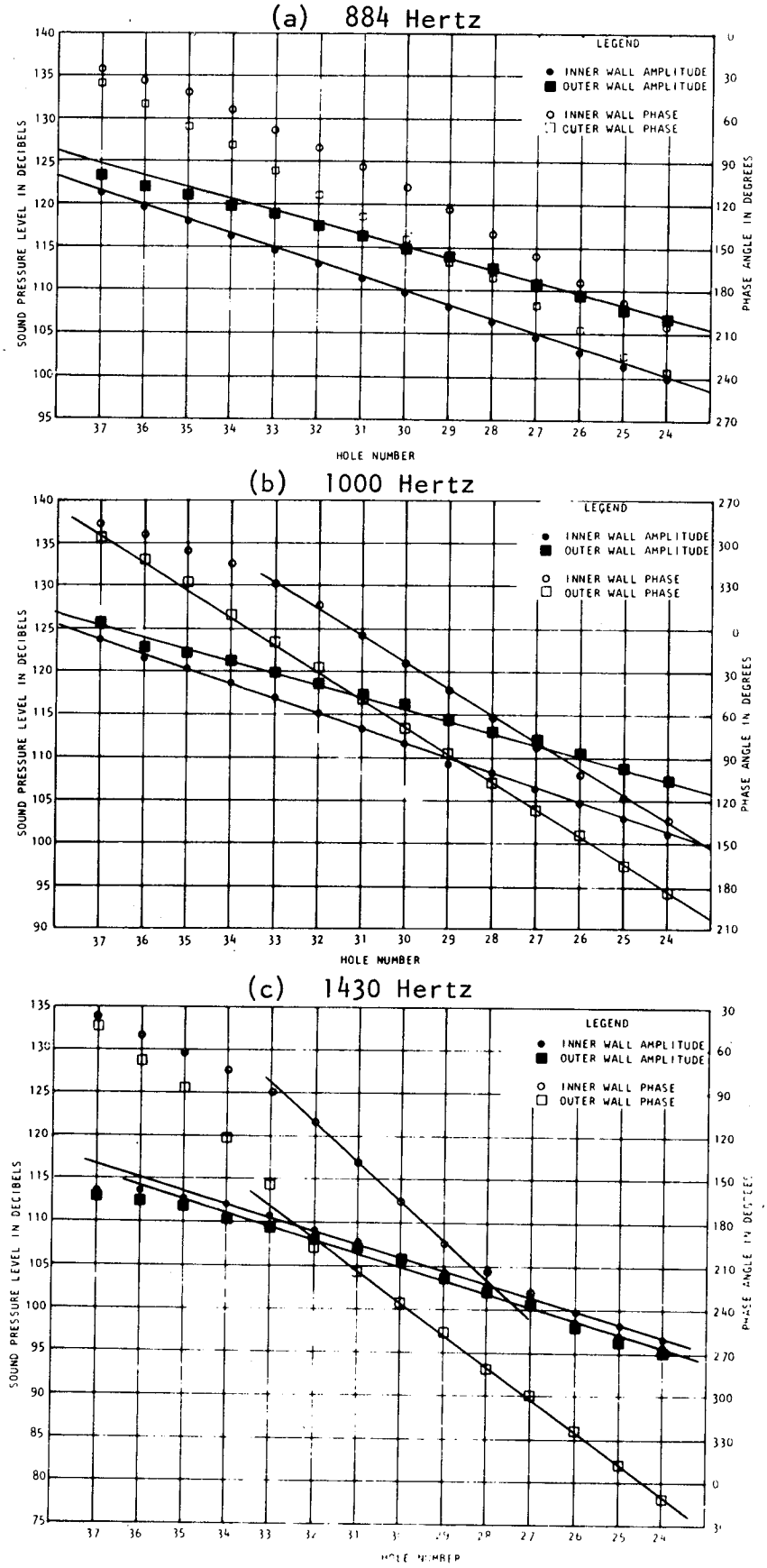


Figure 111. Sound Pressure Level Decay and Phase Change for Liner 1 for (3,0) Mode at Various Frequencies

than the inner wall. This is primarily attributed to the change in the shape of the least attenuated mode, which will be shown later. It is emphasized that this data is acquired in the first 12" of the duct liner in order to avoid any waves which may be reflected from the open end. As the attenuation at these test frequencies is of the order of 1.5 dB per inch, the attenuation from station 24 to the open end would be 36 dB, with a further 36 dB for the reflected wave traveling back to station 24. Thus, at 24" any reflected wave from the open end would be at least 70 dB below the incident wave.

If one attempts to determine the linear attenuation rate for these frequencies, it is wise to use the slope between 32" and 24", since the higher order modes have, for all practical purposes, decayed and little chance for a reflected wave exists. The attenuation rates of the inner wall, the outer wall, and an average between these two is given in table V.

TABLE V

COMPLEX PROPAGATION CONSTANT FOR 40 RAYL, 1.5" DEEP LINER FOR (3,0) MODE

Frequency Hertz	INNER WALL		OUTER WALL		AVERAGE	
	Attenuation dB/Duct Width	Wave Length Constant	Attenuation dB/Duct Width	Wave Length Constant	Attenuation dB/Duct Width	Wave Length Constant
884	6.5	.665	5.6	.644	6.0	.654
1000	6.8	.705	5.5	.733	6.2	.719
1430	6.3	.710	6.3	.585	6.3	.648

The computed attenuations and wavelength constants are compared with the average measured values in table VI, using the impedance values derived from impedance tube measurements as the boundary condition for the computer program which solves the convected wave equation in the duct.

Two values are given for the computed attenuation at each frequency. The first is the modal attenuation and the second is the power level attenuation associated with a wave which was radially plane at the test section entrance, but which decayed to the shape of the (3,0) mode, as the higher order lined duct modes were attenuated. The computed wavelength constants are for the same conditions. The comparison between measured and calculated values of attenuation is excellent. It would be difficult to achieve a more accurate measurement or comparison. The wavelength (or propagation) constant, β, comparison is not nearly as good, but on the whole this comparison is also quite satisfactory.

TABLE VI

COMPARISON OF CALCULATED AND MEASURED COMPLEX PROPAGATION CONSTANT

(3,0) MODE

Frequency Hertz	ATTENUATION			WAVELENGTH CONSTANT, β		
	COMPUTED		Avg. Meas.	COMPUTED		Avg. Meas.
	Modal	Power Level For Plane Wave		Modal	Plane Wave	
884	6.2	6.1	6.0	.556	.571	.654
1000	6.0	6.0	6.2	.679	.698	.719
1430	5.8	6.0	6.3	.682	.698	.648

The usual indicator of a liner's performance is its frequency response (or attenuation) curve. Figure 112 is a plot of the power level attenuation at three axial stations for the frequency range 400-4000 Hertz for an assumed radial plane wave at the duct entrance. The attenuation, as stated in a previous discussion, is not a linear function of axial distance because of the different exponential decay rates and phase speeds of the various modes contributing to a particular pressure distribution. Thus, the average attenuation at each of these three axial stations is determined from figures 111(a) - (c) at stations 32, 28, and 24. These data are plotted in figure 112 in a direct comparison with the computed attenuation, and reflects the excellent comparison made in table VI above, using impedance tube data for the calculation. However, if anything, the comparison in figure 112 is better, in that it shows the non-linear effect due to radial mode combinations, necessary to match the test section entrance pressure distribution. It is unfortunate that a test was not run at 1200 Hz to show the weak peak in the liner attenuation and again at a higher frequency to show the reduced efficiency of the liner; however, the three data points shown are sufficient to give a tentative verification of the theoretical prediction method.

However, one matter of concern which must be discussed before accepting the above results at face value is that of wall impedance spatial variation. A study of the impedance measurements at 1000 Hertz reveals that, by the two microphone method, the mean acoustic impedance is $Z = 1.25 - 0.93i$ with a standard deviation of 0.1 on resistance and 0.05 on reactance. If this value of impedance is entered on the curve of figure 87, the attenuation and propagation constants derived are 5.0 to 5.8 dB for a plane wave at one duct width downstream and from figure 88, a modal attenuation of 5.8 to 6.8 dB with $\beta = .76$ to .80. The plane wave attenuation compares reasonably with the measured value of 5.1 dB from figure 111(b) and the modal attenuation compares quite well with the measured value of 6.2 dB, also derived from 111(b) as discussed previously. However, the calculated propagation constant derived from the impedance measured by the two microphone method is significantly

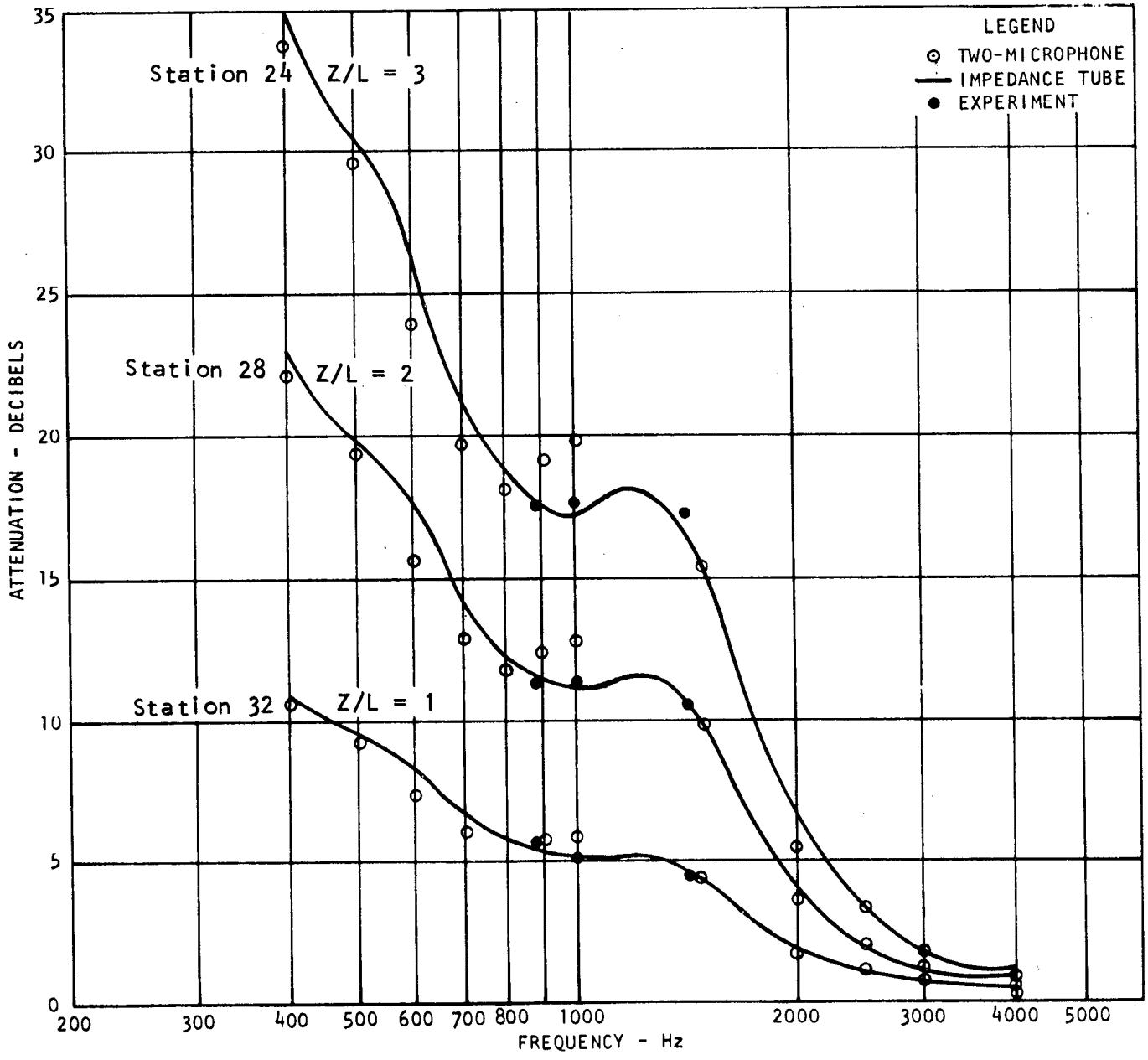


Figure 112. Comparison of Experiment and Theory for Power Level Attenuation in Liner 1

different from that calculated using the impedance tube data, and it is obvious that the measured propagation constant lies somewhere in between the two computed values. If the measured attenuation of 6.2 dB and the measured propagation constant of 0.72 is also entered on figure 88, it is seen that the measured value of complex propagation constant lies on a direct line between the two computed values. At this point a very critical observation (or perhaps hypothesis) can be made. If the measured complex propagation constant is taken as accurate, then by an inverse process an impedance value can be inferred. This impedance value would not only assume that the duct propagation theory is correct, but also that the measurement of complex propagation constant is accurate. The value inferred for the effective wall impedance for the liner is $Z = 1.47 - 0.87i$.

Thus, three values of impedance are inherent in the measurements and it becomes quite obvious that an accurate measure of the impedance is crucial. The impedance tube data could be in error, since only one sample was tested, and quite obviously there is no way of comparing the impedance tube data with a mean impedance, since the impedance of the one sample in relationship to the mean impedance of the liner is unknown.

In measurements by Melling (ref. 51), it was noted that, on average, the two microphone method results in a lower resistance and a higher mass reactance measurement than that derived from the impedance tube. Thus, it is quite possible that the value of impedance indicated for the two microphone (or one microphone traverse) method is in error by a small percentage. Melling was not able to conclude if the difference was due entirely to errors in measurement (primarily in phase) or if a real difference exists between the two techniques. Dean (ref. 52) ran a controlled test in an impedance tube on a 17% perforate in which the standing wave method, the two microphone technique and the one microphone traverse technique were compared. Figure 113 shows the results. The two microphone and impedance tube produce very nearly the same results up to 3000 Hertz, but the one microphone traverse method shows a very distinct difference. Dean attributed this difference to errors in estimating the sound pressure level and phase at the front and back surface of the cavity, as discussed in more detail in another section of this report.

VI.3.1.2. Radial characteristics of the 'plane' mode. Following the above detailed discussion of characteristics of higher order angular mode complex propagation constant, it is also interesting to briefly examine the propagation of the 'plane' (0,0) mode. The measured amplitude and phase change down the duct for an (0,0) mode simulation is shown in figure 114. Although the inner and outer wall sound pressure levels should be identical in the hard wall source section (Station 37), it is noted that the inner wall is 1.5 decibels higher than at the outer wall. This measurement is indicative of the fact that more than one angular mode exists in the hard wall section. The characteristic radial shape of the hard wall angular modes has a lower level at the inner than at the outer wall, which is in opposition to the observation of a higher inner wall level. However, with more than one angular mode present, the zero order radial mode of the various angular modes can add up to give the observed behavior. Thus, it must be concluded that a reasonable

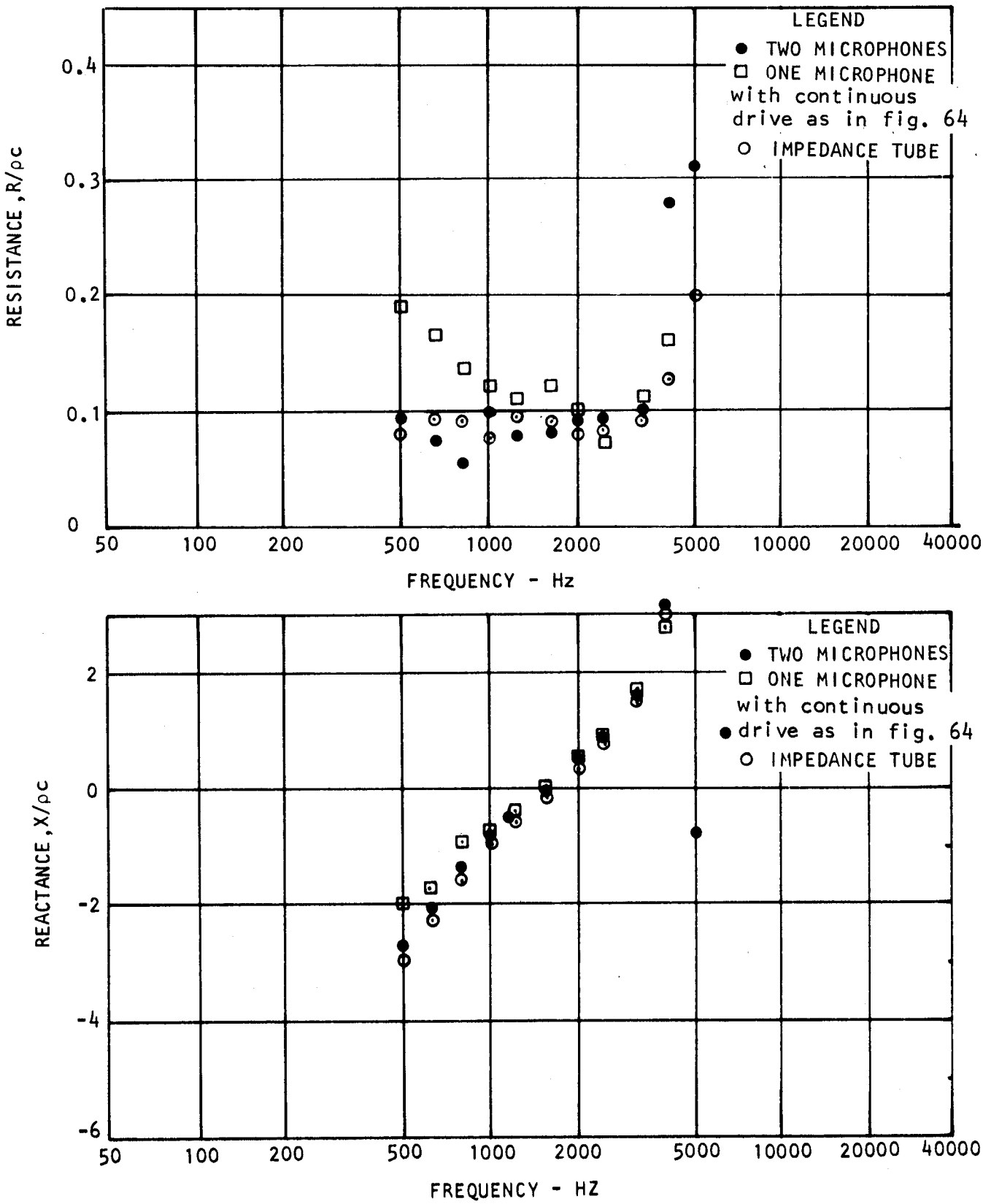


Figure 113. Comparison of Various Experimental Methods for Impedance Measurement

simulation of the (0,0) mode did not exist for this test. Figure 115 is a sample of the angular distribution of sound pressure and phase in the hard wall section of the duct. A complex Fourier analysis of this spatial distribution reveals the angular mode distributions listed in table VII.

TABLE VII

ANGULAR MODE DISTRIBUTION FOR PLANE (0,0) MODE SIMULATION

Angular Mode No.	Amplitude Decibels	Phase Degrees	Phase Shift Degrees
0	118.6	141.9	
1	103.4	190.4	92.7
2	86.8	150.8	129.4
3	100.1	83.2	134.2

Thus, the (1,0) angular mode is approximately 15 decibels below the (0,0) mode, or a linear amplitude of 0.17 when normalized to a plane mode of unity value; and the 3,0 mode, at 18.5 dB down, is 0.12 relative to the plane mode amplitude. Since these modes propagate at different speeds and have different attenuation rates (i.e., for the (3,0) mode β = .68 and the attenuation is 6 dB per duct width, compared to β = 1.08 and an attenuation of 3.5 to 4.0 for the plane (0,0) mode), it would be expected that the amplitude difference between the inner and outer wall would change down the duct until the effect of the higher order modes ceased to be important. However, at 3 duct lengths the (1,0) mode would have attenuated, at most, only 2 decibels more than the (0,0) mode, thus even at station 24, the effect of the higher order angular modes is still present and the composite decay rate should be somewhat higher than that expected for the (0,0) mode.

In spite of this higher order angular mode "noise" the (0,0) mode controls the propagation constant and compares quite well with the calculated value (viz. β = 1.08 theoretical vs. 1.08 experimental), whereas the measured attenuation rate seems to be about 1 dB higher than the theoretical value (3.8 dB theoretical vs. 4.8 dB experimental). Theoretical values are derived from effective wall impedance and experimental values are averages of inner and outer wall values. It is interesting to note that in this particular case, the mode is a "slow mode." the propagation constant being greater than 1.0 (or conversely, the phase speed, c/β, is less than the speed of sound, c, from which the 'slow mode' terminology results).

VI.3.1.3. Fourier-Bessel analysis technique for radial modes. For the case of multiple mode propagation, the computerized two-dimensional complex 'Fourier-Bessel' analysis developed to determine the complete modal content at each axial plane, was used. As a means of determining the validity of this analysis the angular spatial patterns associated with the (3,0) mode at 1000

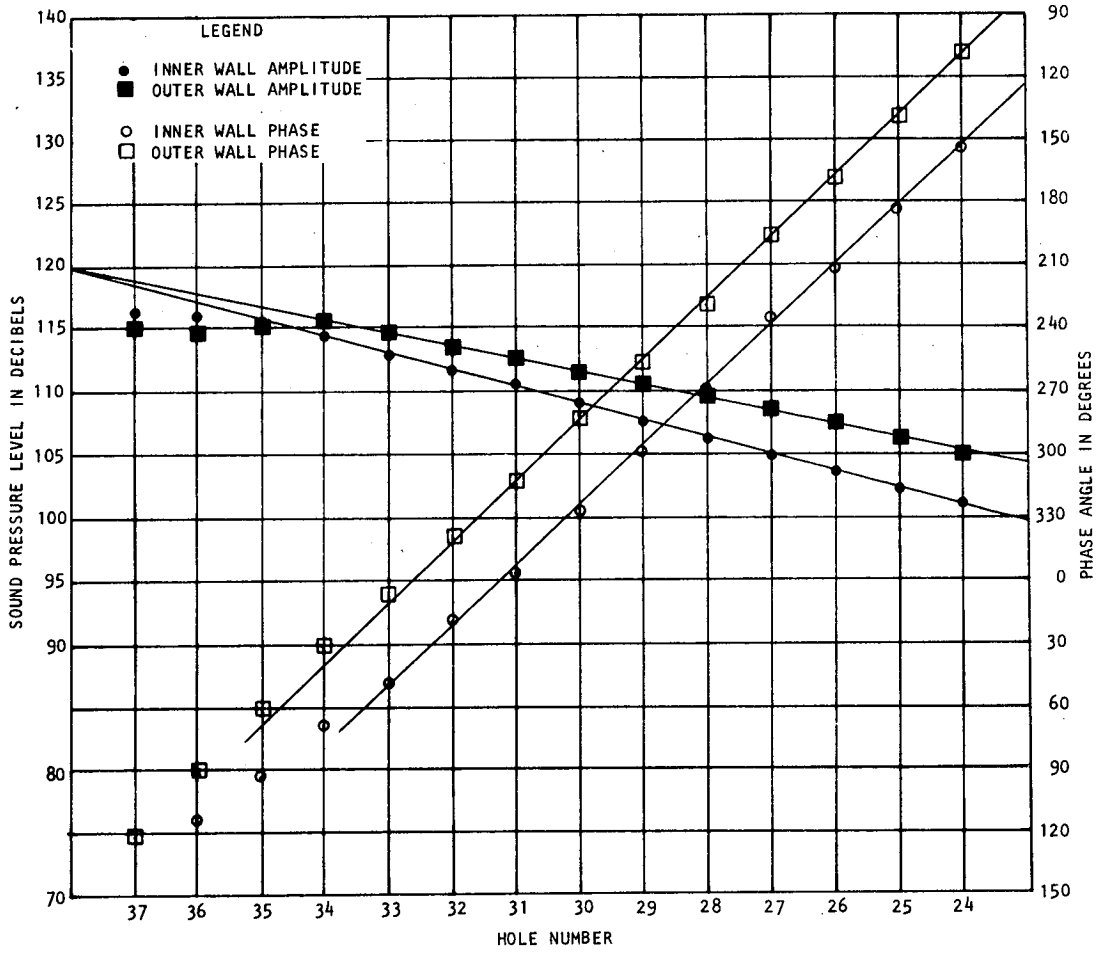


Figure 114. Sound Pressure Level Decay and Phase Change for Liner 1 for (0,0) Mode at 1000 Hz

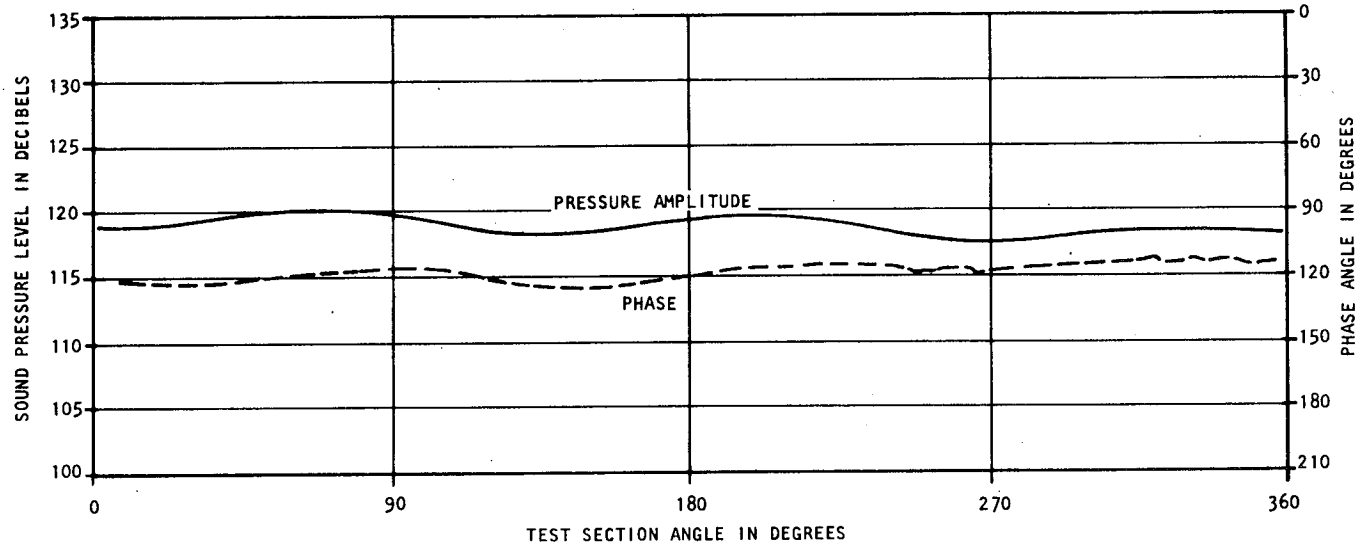


Figure 115. Example of (0,0) Mode Angular Distribution in Hard Wall Section Upstream of Liner

TABLE VIII

FOURIER ANALYSIS OF ANGULAR PRESSURE DISTRIBUTION AT NINE RADIAL STATIONS
FOR FOUR AXIAL STATIONS - (3,0) MODE SIMULATION AT 1000 HERTZ

ANGULAR MODE COMPLEX AMPLITUDE AND PHASE															
		0		1			2			3			4		
AXIAL STATION	RADIAL STATION	AMP dB	PHASE DEG	AMP dB	PHASE DEG	PHASE SHIFT DEG	AMP dB	PHASE DEG	PHASE SHIFT DEG	AMP dB	PHASE DEG	PHASE SHIFT DEG	AMP dB	PHASE DEG	PHASE SHIFT DEG
	1	89.7	121.1	93.4	287.7	158.0	98.7	32.4	31.2	120.3	329.5	104.8	79.1	76.9	95.7
	2	86.9	114.9	92.0	271.0	162.2	98.1	66.6	43.0	120.3	325.6	104.0	87.1	119.7	157.5
	3	89.2	118.6	93.1	277.6	161.1	98.6	69.5	34.4	120.3	319.9	103.2	82.5	66.7	107.2
	4	87.9	113.4	91.3	262.1	160.9	98.2	53.7	39.8	120.1	315.6	101.2	85.5	110.6	150.7
36	5	89.7	109.4	92.9	266.0	156.7	98.1	54.2	33.5	119.6	311.6	100.1	83.1	91.1	112.3
	6	88.8	115.8	93.7	260.1	157.2	98.5	52.9	32.1	119.3	309.9	99.2	79.3	322.8	7.3
	7	91.9	78.1	93.1	254.5	158.8	97.8	54.5	39.5	118.8	311.0	103.4	84.1	128.8	179.1
	8	92.8	83.6	94.9	262.3	158.8	98.3	55.4	39.4	118.8	306.8	105.3	79.9	53.9	112.5
	9	91.8	83.7	94.5	264.8	156.8	97.6	53.7	41.0	118.8	306.5	109.1	79.7	342.9	66.2
	1	87.8	272.1	87.1	39.6	154.1	94.0	169.5	44.4	114.7	45.1	109.1	80.7	198.3	173.6
	2	87.1	265.5	85.6	23.6	155.7	93.9	161.5	44.6	114.3	39.9	109.1	80.9	199.7	172.3
	3	86.9	256.1	86.2	19.6	152.2	93.2	158.0	43.1	113.7	32.0	108.4	78.3	186.8	179.8
	4	85.1	248.7	85.5	15.1	154.0	93.4	150.2	39.4	113.3	26.3	105.4	77.6	179.9	179.4
32	5	84.7	234.9	85.6	7.7	153.5	92.8	146.5	38.1	112.8	19.5	105.2	75.0	161.0	165.0
	6	84.7	220.5	86.3	355.6	154.5	92.5	132.5	48.1	112.1	12.1	107.9	82.6	2.7	30.6
	7	83.8	211.7	85.9	342.8	158.8	92.2	126.2	50.1	111.6	6.9	108.1	83.1	358.0	31.8
	8	83.2	202.9	85.8	338.6	160.5	92.2	123.2	51.4	111.2	3.2	107.4	83.5	356.5	35.9
	9	84.7	202.5	86.6	347.2	166.0	92.2	126.3	53.3	111.1	2.0	109.0	81.0	348.2	41.3
	1	83.3	352.0	84.9	128.1	160.1	90.4	256.7	48.2	109.3	117.8	109.2	75.8	214.4	133.4
	2	82.1	326.4	85.6	101.4	167.0	89.6	246.8	45.2	108.0	103.4	115.2	68.4	181.9	117.6
	3	82.6	314.6	86.1	100.0	162.9	89.8	234.6	46.0	108.3	93.9	114.7	73.0	157.1	98.0
	4	82.7	308.3	86.2	99.5	116.3	90.1	239.6	46.7	108.2	94.6	114.7	70.8	181.3	86.9
28	5	81.8	306.2	86.2	95.3	166.4	89.2	235.5	45.8	107.3	88.6	115.0	73.4	220.7	76.1
	6	82.0	305.4	86.0	96.5	163.7	88.1	220.7	64.4	106.8	84.5	116.8	76.0	108.8	68.7
	7	80.6	306.8	83.4	95.8	159.5	87.8	217.3	69.3	106.3	81.3	116.6	77.2	82.0	31.1
	8	80.2	302.8	82.8	91.5	158.4	87.6	213.4	71.2	105.8	78.2	116.5	78.6	93.1	37.9
	9	80.1	302.6	82.8	88.8	161.4	88.0	215.9	70.6	105.8	78.7	117.7	77.6	98.0	46.1
	1	79.5	118.9	81.8	264.2	160.7	85.1	25.7	57.0	102.0	232.5	119.7	70.2	8.9	93.1
	2	78.3	109.4	80.6	248.1	163.6	84.0	15.0	54.2	100.7	224.2	119.5	70.0	18.7	132.6
	3	73.7	82.9	79.1	232.4	166.3	83.8	2.7	55.6	99.5	211.1	120.5	68.0	328.3	106.5
	4	73.7	81.2	78.0	231.3	163.8	82.7	353.2	58.7	98.2	201.8	120.7	68.4	340.4	121.5
24	5	74.1	69.9	78.7	220.3	168.5	82.3	351.2	57.4	97.3	194.7	123.5	67.9	314.5	95.5
	6	73.4	69.4	77.0	215.5	167.2	81.7	341.7	59.7	96.4	187.1	122.6	66.7	315.8	94.7
	7	73.1	67.7	76.4	211.1	169.1	81.1	339.6	59.7	95.7	182.6	122.5	67.1	315.5	117.1
	8	73.1	68.2	76.5	210.6	166.9	80.6	337.8	61.8	95.1	179.1	123.5	68.1	321.3	127.0
	9	73.7	67.3	76.2	211.1	164.4	80.3	337.2	62.9	94.9	178.3	123.0	69.0	326.2	131.6

Hertz were digitized at the nine radial stations indicated in figure 116 at axial stations 36, 32, 28, and 24. As previously discussed, the angular patterns were first Fourier analyzed and then the lined duct radial modes were used to compute the radial mode contribution for an angular set.

Table VIII contains the angular mode amplitude at each radial and axial station surveyed, for the (3,0) mode at 1000 Hertz. The pressure distribution which resulted from the survey will be shown in the next section. The columns in the tabulation give the modal amplitude, the phase of the mode referenced to the oscillator and the angular phase shift of the first minimum of the angular mode in question referred to zero degrees of azimuth. This is tabulated for the first five angular modes at the nine radial stations for each of the four axial locations. The 3rd angular mode, which corresponds to the mode set (3,0), (3,1), ... (3,N), which was simulated in the source section, is of the order of 20 decibels above the other modes which were spuriously excited. Closer examination of the table, however, reveals that even the unintentionally excited modes are present in a consistent manner in most cases. For instance, at station 36, the amplitude variation across the duct in the first order angular mode set ((1,0), (1,1) ...) is uniform to within 3 decibels and the phase is uniform to within 20 degrees. Further, if that mode, which is only a spurious excitation from the (3,0) mode, is followed down the duct, it is seen that the location of the first angular minimum (indicated by the phase shift column) is consistent to within about 15 degrees, indicating that even the modes which were unintentionally excited, are responding and do propagate, and also that the instrumentation system is capable of measuring over a SPL range of greater than 40 decibels.

In order to determine the radial mode content in the 3rd angular set, the data listed in table VIII for each radial station were Fourier-Bessel analyzed, using the computed radial modes for the particular frequency and wall impedance boundary conditions. Table IX gives the result of this analysis for the first two radial modes at each of the four axial stations.

TABLE IX

RADIAL MODE ANALYSIS FOR 3RD ANGULAR MODE SET

Configuration: 1½" Deep Liner with 40 Rayl Felted Metal
Frequency: 1000 Hertz
Impedance Used in Computing Radial Modes: 1.22 - 0.65i

Axial Station Inches	RADIAL MODE NUMBER					
	0			1		
	AMP dB	Phase Deg.	Phase Shift Deg.	AMP dB	Phase Deg.	Phase Shift Deg.
36	122.7	118.1	102.9	113.6	247.6	103.4
32	226.1	186.8	107.7	108.9	303.9	108.1
28	110.6	255.9	114.3	102.6	17.1	114.2
24	101.6	6.9	120.9	95.2	111.7	121.0

Examination of this data points up an inherent problem in the analysis system which may have been avoided by more radial data points. Since only nine radial points were used, what would visually appear to be minor errors, ultimately results in 'noise' of the order of 10 decibels down from the predominant radial mode. Thus, any radial mode which is more than 3-6 decibels below the predominant mode will be obscured by 'noise' generated from minor errors in the predominant mode measurement and analysis. In the case under consideration, the (3,1) mode is determined to be on the order of 8 decibels below the (3,0) mode at all stations, based on the experimental analysis technique. At the entrance to the lined section, a significant contribution of the (3,1) and even higher radial modes is expected, in order to match the hard wall (3,0) mode (which theoretically is 2.3 decibels lower at the inner wall than at the outer wall). However, since the (3,1) mode is, for all practical purposes, cut off at 1000 Hertz (the computed attenuation rate is 23 decibels per duct width), it should be insignificant at station 32. Obviously, this is not the case, as the data shows.

Now let us examine the data for the (3,0) mode and compare it with the measurements made previously as now shown in figure 117. The attenuation rate determined from this analysis for the (3,0) lined duct mode is 6.1 to 6.8 dB and the propagation constant is between 0.66 and 0.79 according to the weight given the phase data at station 24. The mean square values are 6.5 dB attenuation, with $\beta = 0.75$. These values of complex propagation constant are also shown on figure 88 for comparison with the values determined previously. The median value is very close to the effective impedance value and, in effect, justifies use of the analysis technique for higher order modes, if the 'noise' problem resulting from insufficient radial data points did not exist.

As a further test of the data analysis system, a complex angular modal pattern was set up at 1000 Hertz with liner 1 installed in the test section. The modal pattern consisted of an equal summation of the first four angular modes at the transducer plane; that is, the pressure at the source was

$$p = 1 + \cos\theta + \cos 2\theta + \cos 3\theta. \tag{81}$$

After Fourier analysis of the angular patterns at the 9 radial stations, at each of the four axial stations, the radial Fourier-Bessel analysis was conducted. The results of this analysis for the first radial mode for each of the four angular modes is listed in table X.

The most consistent method of determining the average modal attenuation rate and propagation constant from the data listed was to fit a least-square regression line through the four data points for SPL and phase for each mode. The least-square modal attenuations and β are listed in Table XI with the computed values for each mode using three impedance values, viz. that measured by the impedance tube, the modified two microphone method, and the effective impedance as described in this section.

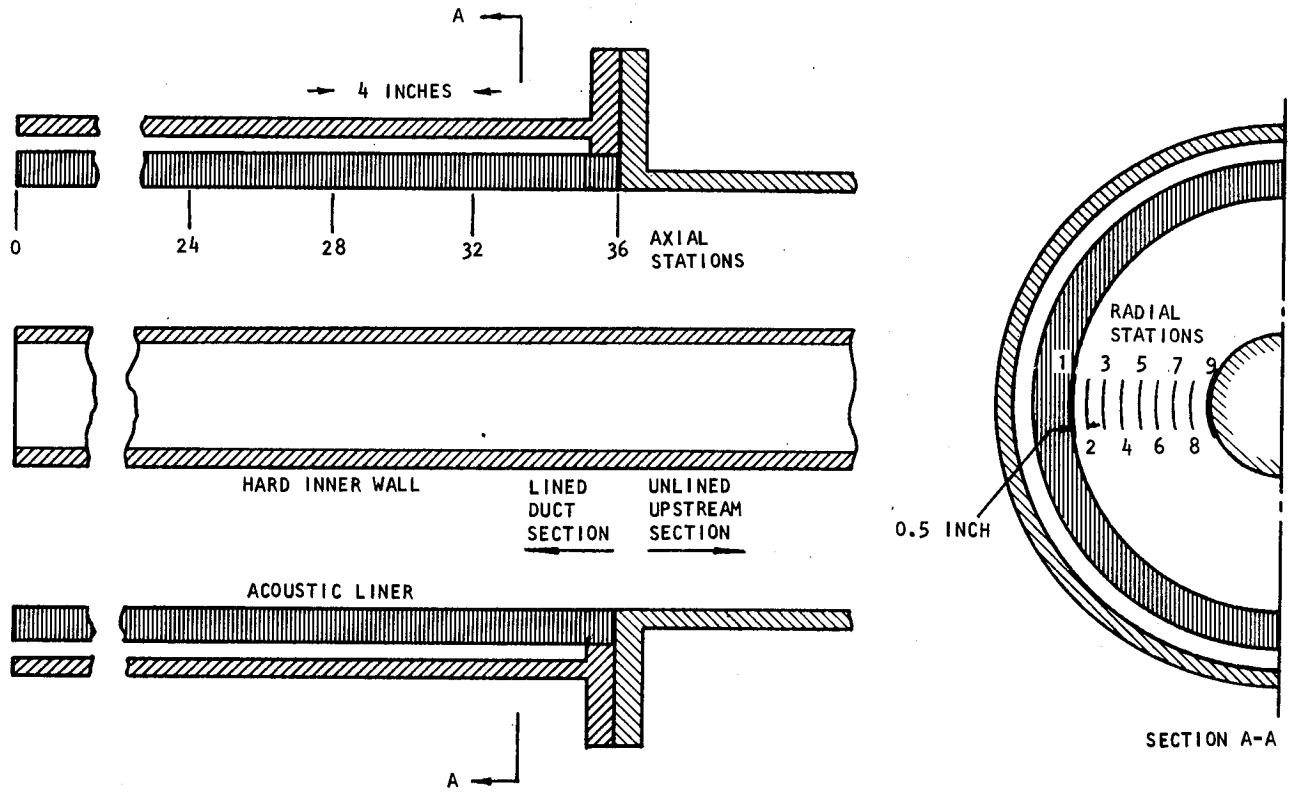


Figure 116. Measurement Locations for Two- Dimensional Digital Data Recording

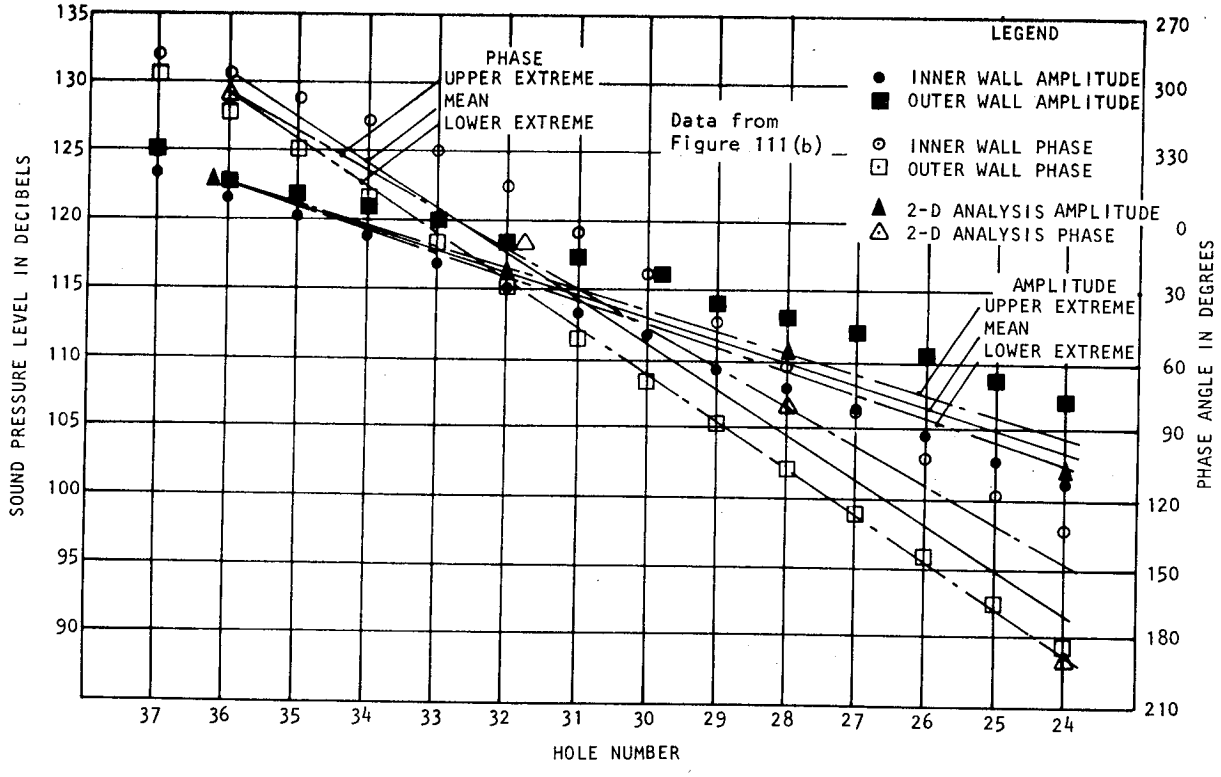


Figure 117. Comparison of Analog and Digitally Analyzed SPL Decay and Phase Change for Liner 1 (See figure 111(b))

TABLE X

FIRST RADIAL MODE FOR FOUR EQUAL AMPLITUDE ANGULAR MODES

FREQUENCY: 1000 Hz - LINER 1 - NO FLOW

Axial Station Inches	ANGULAR MODE NUMBER											
	0		1			2			3			
	Amp dB	Phase Deg.	Amp dB	Phase Deg.	Phase Shift Deg.	Amp dB	Phase Deg.	Phase Shift Deg.	Amp dB	Phase Deg.	Phase Shift Deg.	
36	112.6	180.4	114.3	106.7	128.4	116.0	150.0	82.3	116.6	117.5	26.1	
32	109.7	290.3	109.4	196.2	131.0	110.0	248.2	88.8	109.3	187.5	32.5	
28	104.0	29.9	106.4	301.9	129.8	104.5	348.6	98.2	103.0	275.0	40.0	
24	102.3	154.7	101.1	97.4	125.2	101.9	92.4	87.5	97.1	347.7	35.4	

TABLE XI

COMPARISON OF EXPERIMENTAL AND THEORETICAL ATTENUATION RATES AND PROPAGATION CONSTANTS FOR FIRST FOUR ANGULAR MODES

FREQUENCY: 1000 HERTZ - LINER 1 - NO-FLOW

MODE NO.	EXPERIMENTAL VALUES		IMPEDANCE VALUE FOR CALCULATIONS					
			Two Mike Z=1.25 - 0.93i		Effective IMP Z=1.48 - 0.88i		Impedance Tube Z=1.65 - 0.80i	
	Amp dB	β	Amp dB	β	Amp dB	β	Amp dB	β
1,0	3.77	1.034	3.85	1.100	3.60	1.070	3.40	1.047
2,0	4.39	1.091	4.10	1.055	3.94	1.020	3.70	0.998
3,0	4.93	0.832	4.78	0.958	4.78	0.914	4.54	0.891
4,0	6.68	0.733	6.45	0.780	6.20	0.720	6.00	0.680

First, it is obvious that the trends exhibited by the experimental data match the theory in almost all respects. The attenuation increases as mode number increases and the wavelength constant, β, decreases with increasing mode number. The effective impedance was chosen as being the best fit to the measured data for the (3,0) mode in isolation. Once again, this value of impedance produces theoretical results which compare well with the measured data over all the modes.

Now summarizing the results discussed to this point concerning the two-dimensional data acquisition Fourier-Bessel analysis system, two important conclusions can be reached. These are (1) the data on the (3,0) mode shown previously and the 4 angular mode situation just discussed, further strengthen

the earlier conclusion that the eigenvalue theory of sound propagation in an annular duct is adequate, and (2) it is shown that mode superposition is a valid concept -- there is no evidence of mode cross-talk for these zero order radial modes.

VI.3.1.4. Higher order radial modes. At this stage of the discussion, it is appropriate to examine the utility and accuracy of the two-dimensional measurement and analysis system for studying higher order radial modes. Liner 1 was tested at 1808 Hertz with an angular mode set-up for the (2,0), (2,1) ... etc. modes. The results from the angular Fourier analysis (i.e., the data used as input for the radial Fourier-Bessel analysis) are graphically shown in figure 118. It would appear from visual inspection that the nine radial data points follow the expected trend. At the entrance to the lined duct section, it is evident that the (2,1) hard wall mode dominates. As the mode progresses down the lined section, the radial shape rapidly assumes a new form, as does the phase distribution.

The results of the radial analysis of the nine data points are listed in table XII for experimental values of impedance determined from two methods.

TABLE XII

RADIAL MODE ANALYSIS FOR COMBINED (2,0) & (2,1) MODES

FREQUENCY: 1808 HERTZ - LINER 1 - NO FLOW

AXIAL STATION INCHES	ANALYSIS IMPEDANCE							
	Impedance Tube: Z = 1.40 + 0.22i				Two-Mike: Z = 1.22 + 0.22i			
	RADIAL MODE ORDER				RADIAL MODE ORDER			
	0		1		0		1	
	Amp dB	Phase Deg.	Amp dB	Phase Deg.	Amp dB	Phase Deg.	Amp dB	Phase Deg.
36	103.3	158.4	122.7	338.7	104.0	146.8	122.6	334.3
32	110.7	211.9	113.8	10.1	110.0	205.8	113.4	3.6
28	108.2	4.8	109.3	135.6	107.4	358.9	109.1	127.5
24	106.3	162.5	104.9	297.0	105.5	157.0	104.6	287.5

It is immediately obvious that some problem, not previously discussed, exists with the data. Regardless of the impedance data chosen, the amplitude of the (2,0) mode increases from station 36 to 32. If the data could be assumed to be absolutely accurate, this would be indicative of energy transfer between modes. It is emphasized that the analysis incorporates the same set of lined duct modes at each axial analysis point. There is no possibility of energy

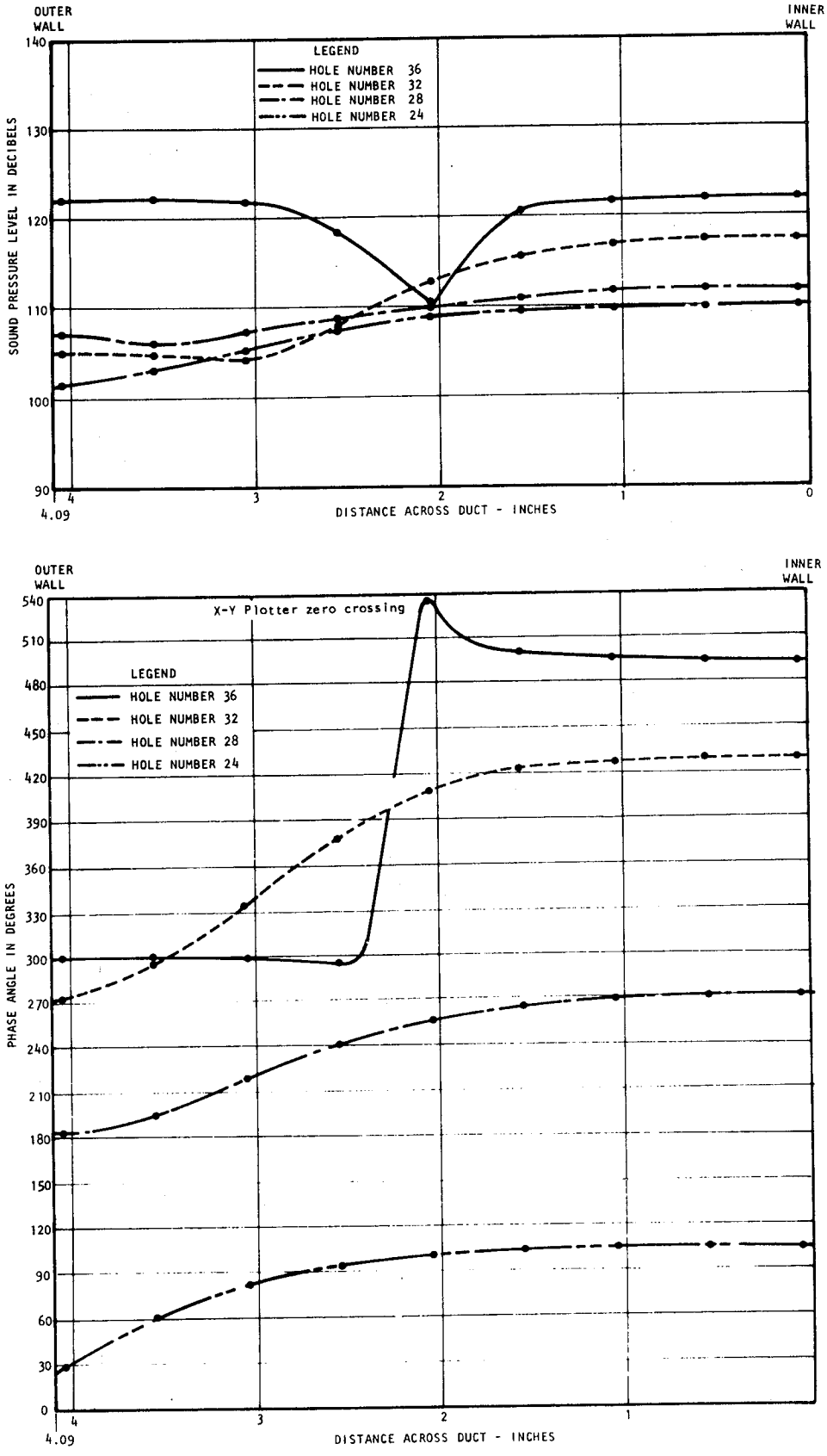


Figure 118. Sound Pressure Level and Phase Angle for Second Angular Mode Set - Derived from Digital Analysis of Angular Sweep Data-Liner 1, 1808 Hz

conversion due to switching from hard wall modes to soft wall modes (in the analysis, that is).

The computed mode attenuations range from 2.38 to 2.48 dB for the (2,0) mode and 15.31 to 16.93 dB for the (2,1) mode. If only the last three data points for the (2,0) mode are considered, an attenuation on the order of 2.2 dB results. However, the (2,1) mode attenuation resulting from these three data points is 4.5 dB; considerably less than the computed value. It is assumed that the problem discussed earlier, that of 'noise'* is indeed a reality. The only position where it would appear that the (2,1) mode is decaying much more rapidly than the (2,0) mode is near the liner entrance. This rapid decay then merges into the analysis 'noise' before reaching station 32.

Thus, it must be concluded, as suspected earlier, that the radial mode decomposition analysis method is in doubt, due to error in the measured data as a result of too few radial measurement points. Therefore, no further attempts to measure higher order radial mode decay will be presented. It is felt that the method is valid, as shown, for the lower order modes, but that either a more accurate measurement/analysis scheme must be incorporated or else more radial data points must be acquired. If the number of radial data points was increased without decreasing the number of angular points, the analysis would become prohibitively time consuming. However, it is probable that a better balance between angular and radial data points could be achieved. As it now stands, the angular analysis is probably over-accurate with 128 points. Perhaps if the 128 x 9 matrix were divided such that the same number of data points were allocated for each half-cycle of the mode, whether angular or radial, the accuracy would be optimized. With this criterion, the number of data points for each half-cycle would be

$$\frac{128 \times 9}{2 \times m \times (n+1)}. \qquad (82)$$

For a 2,1 mode, the number of angular data points would more appropriately be 48 and the number of radial points would be 24 (arrived at by allocating 12 data points to each half-cycle). However, no such system was possible at the time this measurement/analysis problem was discovered.

VI.3.1.5. Complex propagation constant measurements for non-locally reacting liners. Finally, further useful data was provided by measurements of attenuation and propagation constant with the two foam liners in place. Figure 119 is a plot of the sound pressure amplitude at the outer wall. This plot alone is a rather meaningless measure of the performance of a liner in terms of modal attenuation. It does, however, reveal rather interesting behavior.

---

*'Noise' can be defined in this context as being inherent variations of liner impedance plus digitizing errors and computational approximations; the last two components being very small in the no flow case.

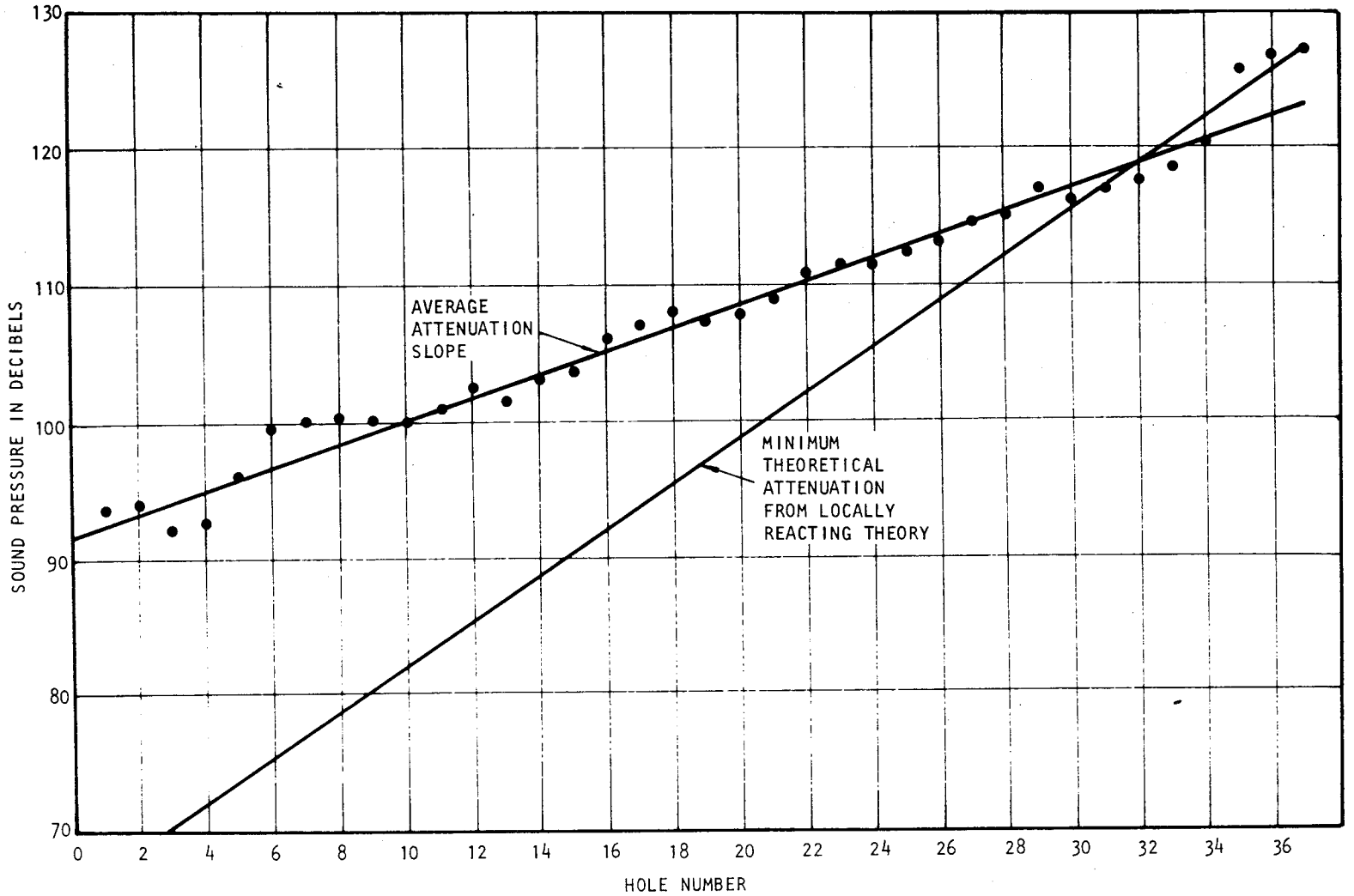


Figure 119. Sound Pressure Level Decay for Liner 4 for (0,0) Mode at 1000 Hertz

The sound field appears to have a rather strong reflected wave component, since what appear to be damped standing waves are in evidence all the way back to the test section entrance. However, as a result of the impedance measurements on the liner, which displayed a considerable variability in impedance as a function of position (of the order of ±50%), it was surmised that the reflections were the result of local changes in liner impedance.

The slope of the sound level decay curve is approximately 4 dB/duct width (for this one liner, the duct width was 4.75"). The computed value of attenuation (based on a locally reacting assumption) for the (0,0) mode ranged from 8 to 14 dB/duct width according to the combination of values selected for average impedance of the inner and outer liners.

Here, it must be concluded that the fact that the material is non-locally reacting dominates the attenuation characteristics of the duct, since the measurements were checked several times and it is believed that the results presented are accurate.

A further test was conducted using a commercially available acoustic foam on the outer wall only. The inner and outer SPL and phase are shown over an axial distance of 12 inches for 3 frequencies in figure 120. Detailed calculations for this case were not made, however, the generalized calculations of figures 87 and 88 apply for a locally reacting liner. The impedance at 1000 Hertz is, $Z = 0.35 - 0.60i$. The impedance was uniform within ±20% over the five samples measured. The calculated modal attenuation from figure 88 is of the order of 10.5 dB and β is of the order of 1.45. The measured attenuation, although not a linear decay, is approximately 4-5 dB/duct width and β is approximately 0.67. Thus, the measured data for this liner are also not in agreement with locally reacting calculations and it must be concluded that the non-locally reacting impedance effect is very significant for this particular geometry/frequency combination. Further, the effect is to significantly reduce the attenuation from that predicted by the theory.

It must further be concluded that if non-locally reacting liners are to be used, an analysis incorporating Scott's (ref. 53) assumptions and solution techniques must be used.

This concludes the presentation on propagation constant and attenuation in soft-walled annular ducts without flow. Next, the discussion will center on mode shapes and radial pressure distribution in the lined duct.

VI.3.2. Mode shapes and pressure distribution.

The previous display of comparisons between experiment and theory as pertains to the complex eigenvalues for lined annular ducts has, in effect, provided the basic substantiation for the mode theory of sound propagation in ducts. However, one critical detail of the mode theory which has been alluded to in the discussion, especially concerning the calculation of power attenuation, is the spatial distribution of sound pressure and phase for a particular mode. In this sub-section, a number of mode shape and pressure distribution

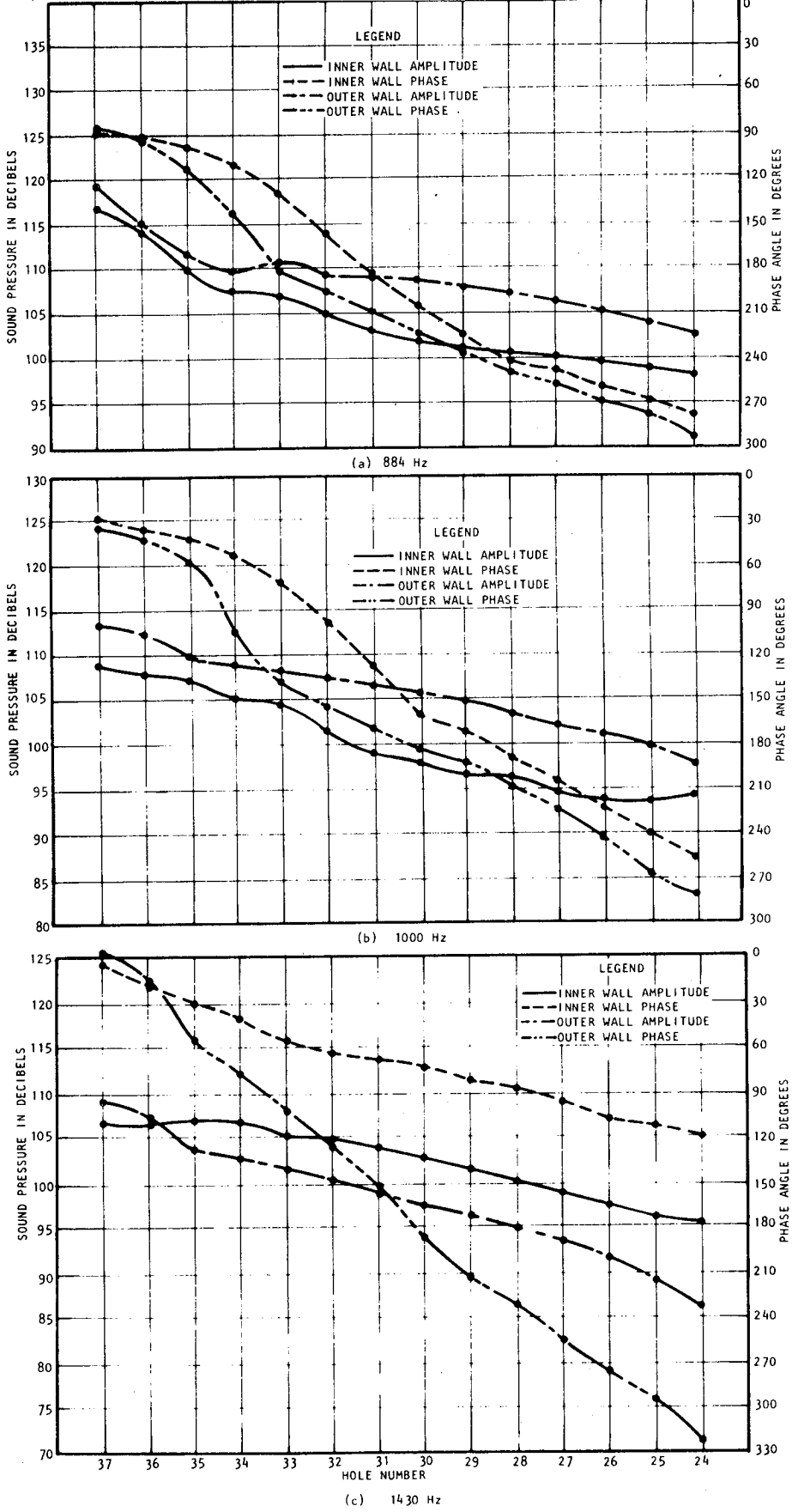


Figure 120. Sound Pressure Level Decay and Phase Angle Change for Liner 5 for (3,0) Mode at Various Frequencies

measurements for each of the liners will be presented. Also, for many of these experiments, valid comparisons with theory are possible.

VI.3.2.1. Liner 1 mode shapes. The liner 1 configuration provided a significant portion of the useful data on pressure distribution and mode shapes. The angular mode shapes are not of particular concern, since the presence of an attenuating liner, provided it has a uniform circumferential distribution of impedance, does not alter the angular pressure solutions. Because of the previous concentration on data for liner 1 at 1000 Hertz, the radial distribution of sound pressure at that frequency will be presented first.

Figure 121 is a plot of the measured radial sound pressure and phase at 1000 Hertz. The measurements were made at one inch intervals beginning one inch upstream of the liner entrance and extending twelve inches into the lined section. A 1.5 dB reduction occurs between station 37 and 36 indicating a reflection at the interface between the hard wall and lined sections. The radial pressure distribution at the entrance to the lined section is that of a hard wall (3,0) mode, which theoretically has a 2.3 dB lower level at the inner wall as compared to the outer wall. As the pressure wave progresses down the lined duct, the shape gradually changes, both in pressure and phase. At station 24, the pressure distribution is 6 dB lower at the inner wall with a 55° phase difference between the inner and outer walls. Examination of figure 91, which is for the same set of physical conditions, would imply a significantly different wall impedance, from those presented before, in order to match the mode shape. At the 'effective' impedance value, the mode shape is calculated to have a 4.5 dB lower level at the inner wall and a 33 degree phase change between walls. Thus, some differences do exist between measurement and theory. Figure 122 shows the comparison between the theoretical and experimental pressure distribution at the entrance and three axial stations spaced 4 inches apart, based on an assumed plane radial distribution at the liner entrance. The calculations are made at an impedance of $Z = 1.4 - 0.8i$, which lies approximately half-way between the two-microphone and the impedance tube experimental impedance values. While generally the comparison could be considered excellent, there are differences of up to 2 dB at station 24 in the absolute sound pressure level and up to 18 degrees absolute phase difference. It is emphasized that all the calculations are referenced to the entrance plane, thus effects of modal attenuation and wavelength constant differences, as well as differences in mode shape are involved. At station 24, the pressure distribution has decayed to the shape of the (3,0) mode, since all the higher order soft wall modes have attenuated to much lower levels.

Figures 123 and 124 illustrate the behavior at two other frequencies, consistent with the data presented in figure 112. In figure 123 for 884 Hz, the comparison with theory, calculated at an impedance of $Z = 1.90 - 0.85i$, is excellent for both amplitude and phase, down to station 24, where the comparison shows a significant disagreement in phase (of the order of 60 degrees difference) and approximately 3.5 dB difference at the inner wall. It is not known what to attribute this difference to. It is probably an experimental error, but it could also be related to a change in liner impedance between the liner entrance and station 24. The comparison at 1430 Hz generally follows

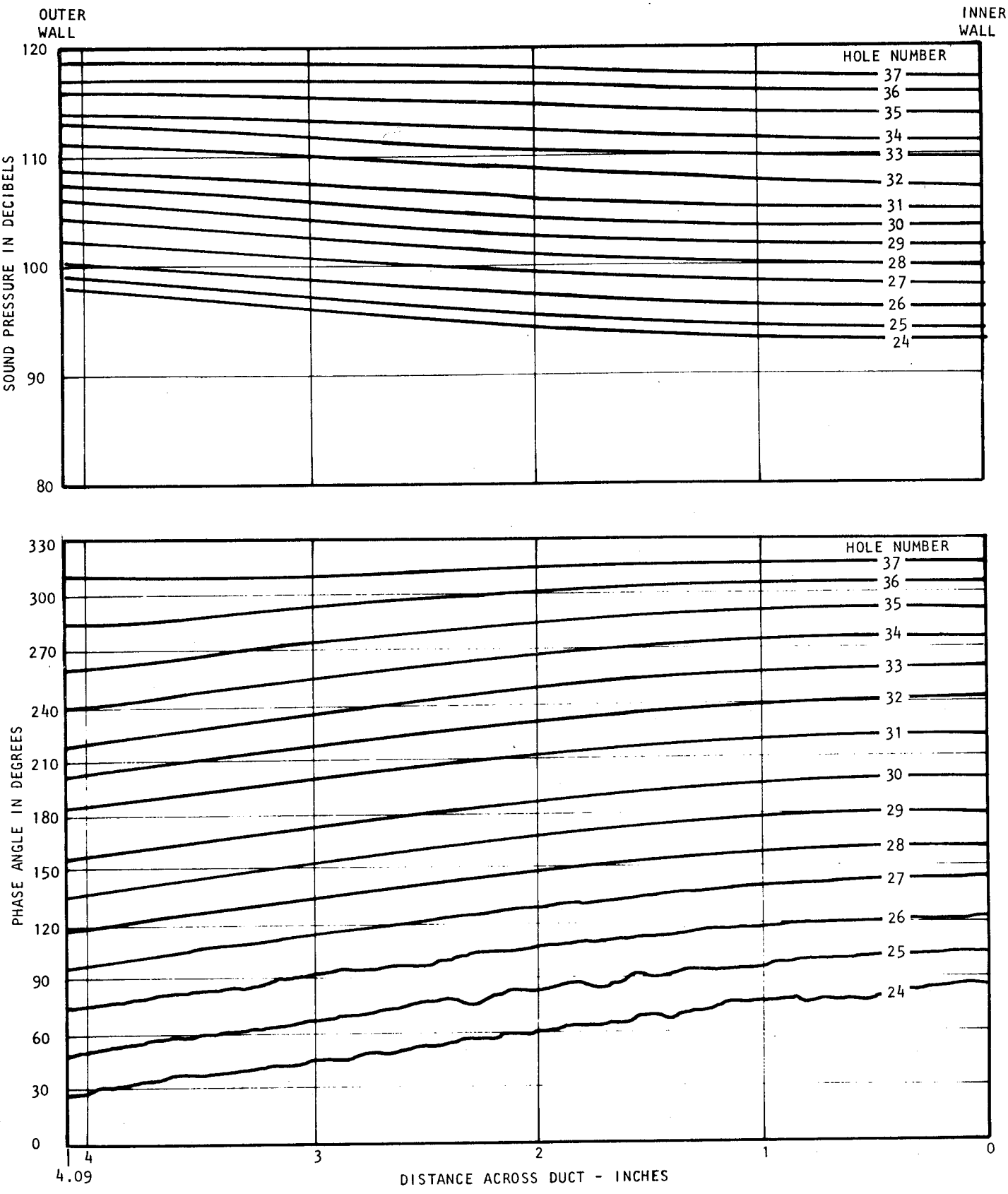


Figure 121. Measured Sound Pressure and Phase Contours for (3,0) Mode in Liner 1 at 1000 Hertz

the shape trends both in amplitude and phase. It is significant to note that the amplitude is lower at the outer wall for both experiment and theory, in opposition to the tests at 884 and 1000 Hz. The calculculations were made at a frequency of 1500 Hz, while the experiment was conducted at 1428 Hertz. This difference in wavelength would introduce approximately 15 degrees phase error between stations 36 and 24. The balance of the error is probably due to improper definition of the wall impedance due to spatial inhomogeneities of the liner material.

One further test of interest is the propagation of the (0,0) mode. Figure 125 shows the pressure and phase distribution at six axial stations one inch apart beginning at station 37 and progressing to station 32. Although the pressure distribution is not initially plane at station 36, it rapidly assumes the shape of the calculated pressure distribution, which at station 32, is predominantly the (0,0) soft wall mode. It is interesting to observe how the pressure distribution changes from a shape which is 1.5 dB lower at the outer wall to a shape which is 1.5 lower at the inner wall, in conformance with the soft wall (0,0) mode calculations.

VI.3.2.2. Mode shape and pressure distribution for liner 2. Another series of radial plots were made in the hard wall section and in the lined section with liner 2 installed. This liner, as described earlier, was comprised of inner and outer cylinders consisting of acoustic material over 1/2 inch deep honeycomb with a rigid backing. The acoustic material was a nominal 20 Rayl material. Three higher order angular-radial mode combinations were excited in the hard wall source section at the response peak corresponding to the damped cut-on frequency of the particular mode. The radial amplitude and phase plots are shown in figures 126 to 128 for the (2,1), (5,1), and (6,2) hard wall radial duct modes. No attempt has been made to provide a theoretical comparison directly on the charts. These experimental studies do, however, provide a significant bit of data for future analytical studies, such as that of Zorumski (ref. 15) on sound propagation in a two section duct. The plots are placed onto separate sections of the page for ease in discrimination between individual plots. The soft wall section begins at station $35\frac{1}{2}$ for this particular liner. The parameters defining the test condition are given on each figure.

Theoretical mode shapes in the lined section calculated at frequencies near the test frequencies and using average impedance acquired by the two-microphone method, are shown in figure 129. The frequency, impedance and computed complex propagation constant for each mode shown is given in the legend. The calculations show that the (2,1) mode should be only slightly attenuated at station 32, as is evidenced in the experimental plots (figure 126). The (5,1) mode should be attenuated by approximately 3-5 dB and this is also confirmed by the experiment (figure 127). The (6,2) mode also seems to follow the trend of the predicted attenuation of 4-6 dB (figure 128).

Comparing figures 129 and 126, it is seen that the pressure distribution for the (2,1) condition very closely matches the computed (2,1) mode shape at station $32\frac{1}{2}$, except near the minimum. From examination of figures 127 and 129, it is seen that the radial shape at station 32 for the (5,1) set seems to be a

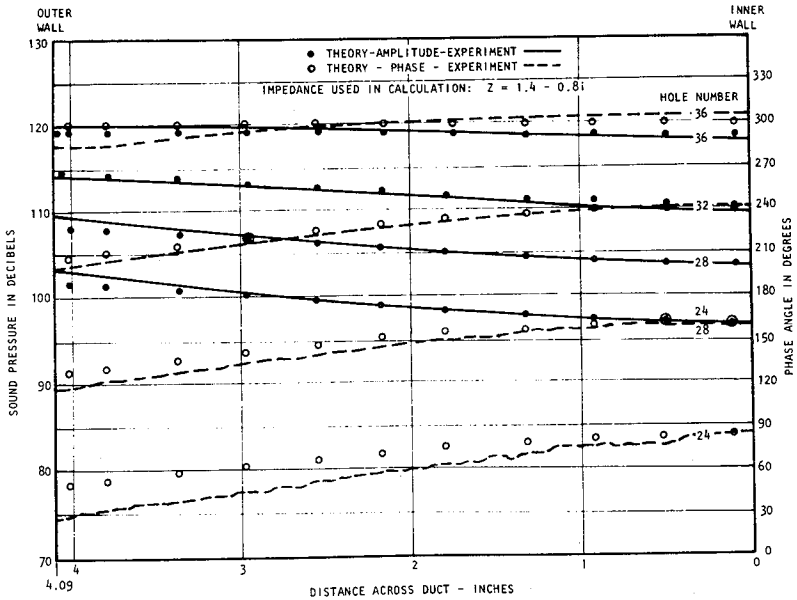


Figure 122. Comparison of Experiment and Theory for SPL and Phase Angle Contours for (3,0) Mode in Liner 1 at 1000 Hertz

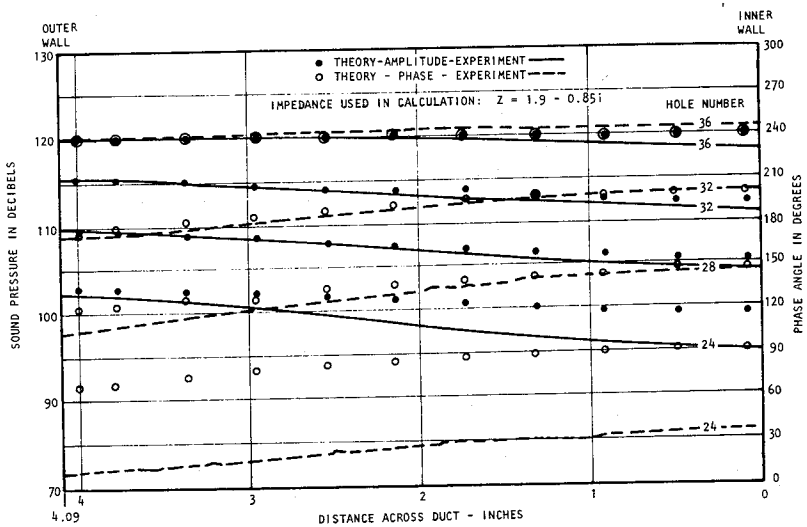


Figure 123. Comparison of Experiment and Theory for SPL and Phase Angle Contours for (3,0) Mode in Liner 1 at 884 Hertz

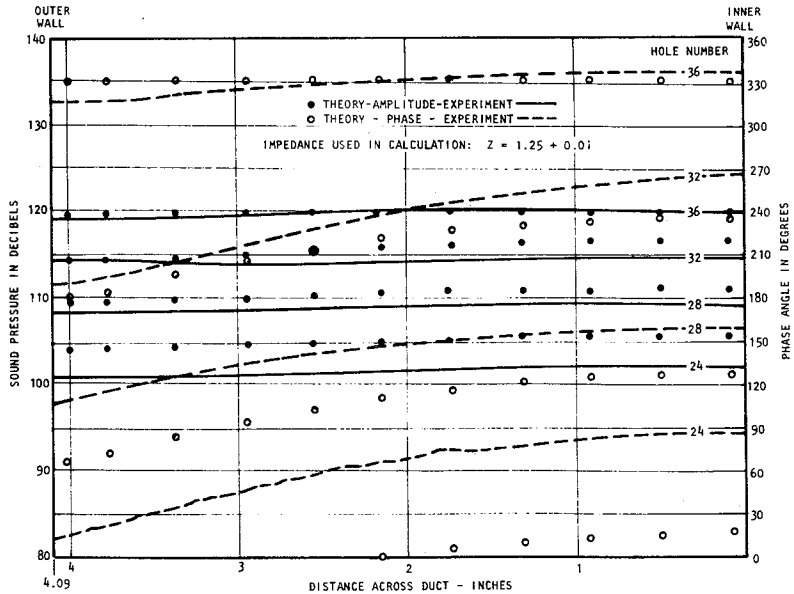


Figure 124. Comparison of Experiment and Theory for SPL and Phase Angle Contours for (3,0) Mode in Liner 1 at 1430 Hertz

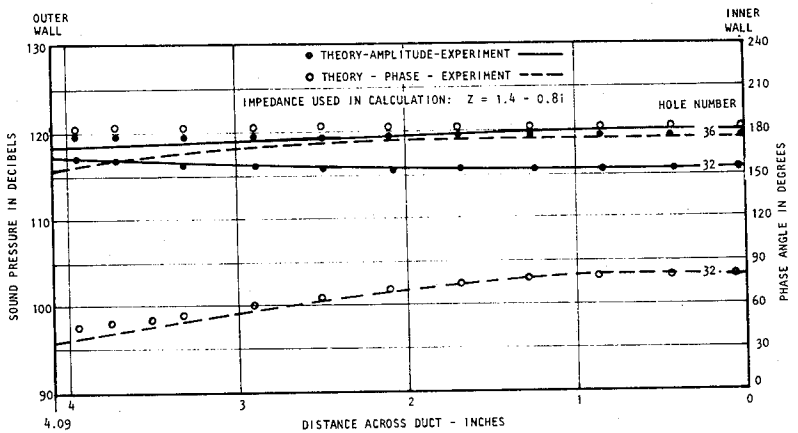
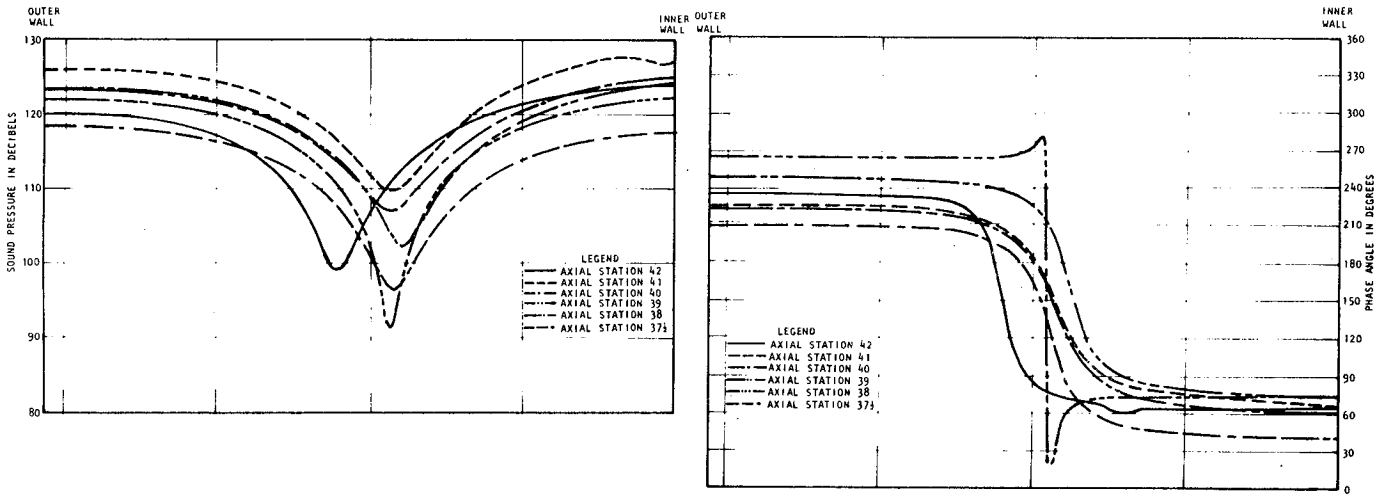
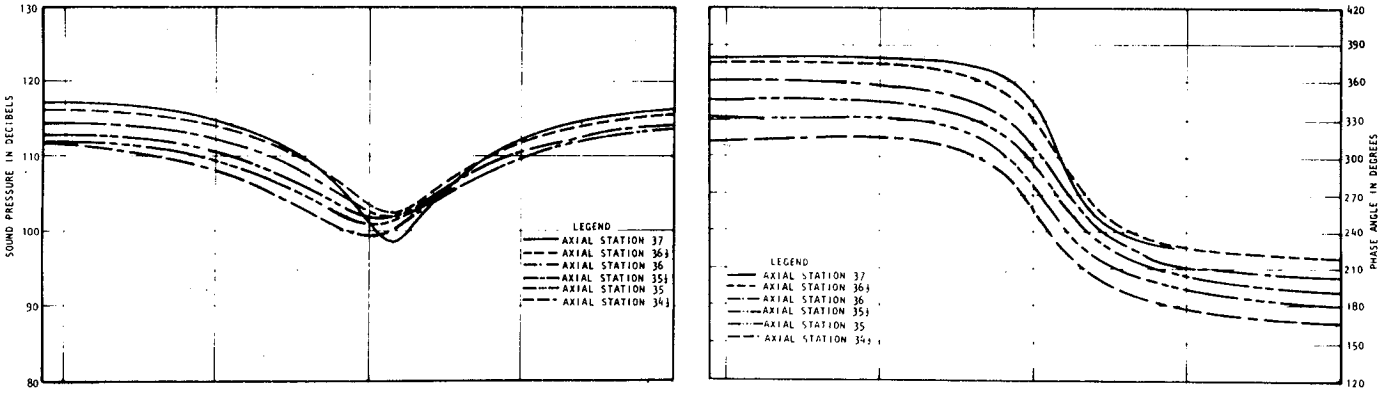


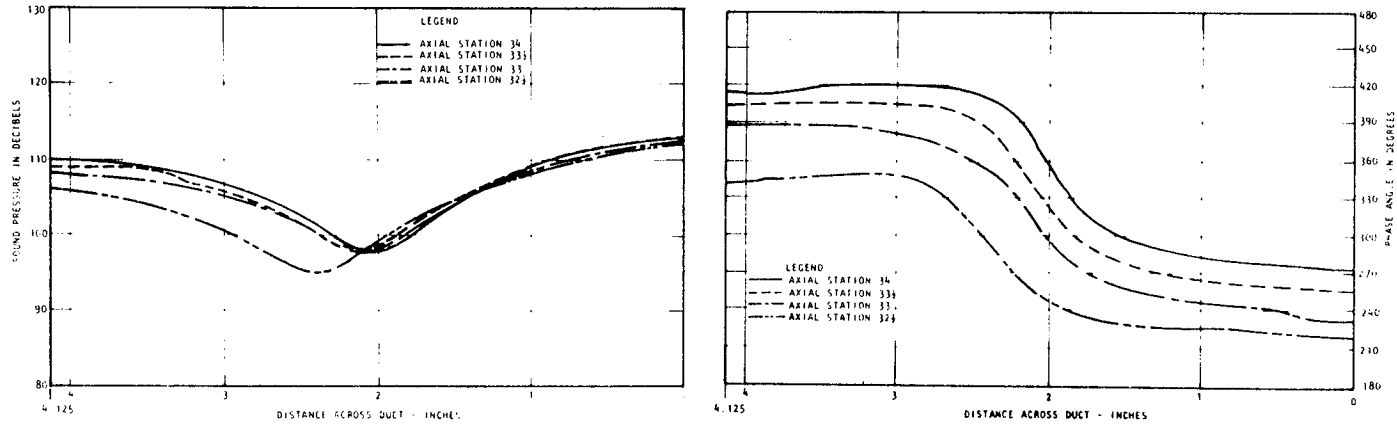
Figure 125. Comparison of Experiment and Theory for SPL and Phase Angle Contours for (0,0) Mode in Liner 1 at 1000 Hertz



axial stations 42 - 37½

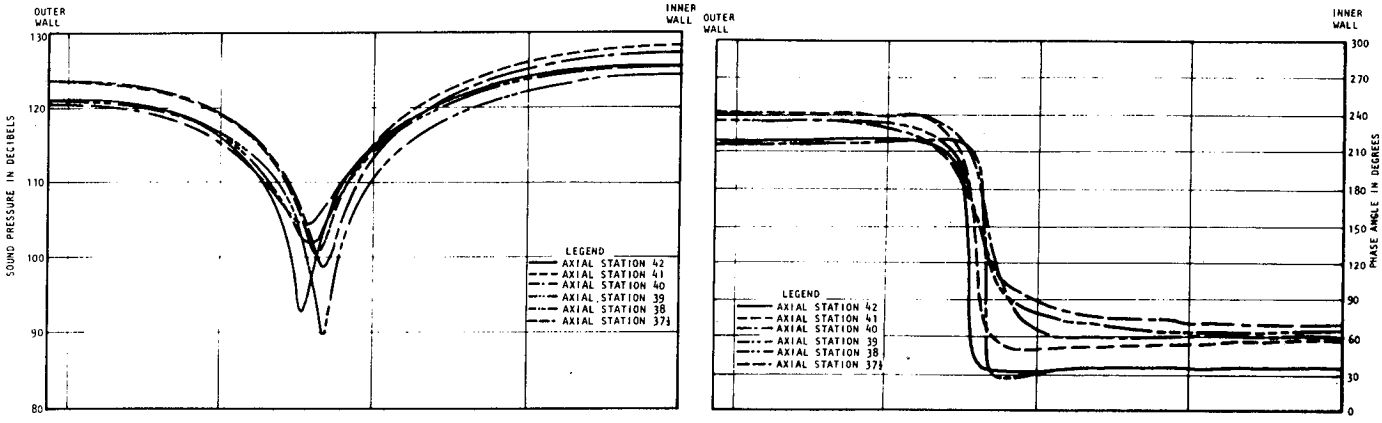


axial stations 37 - 34½

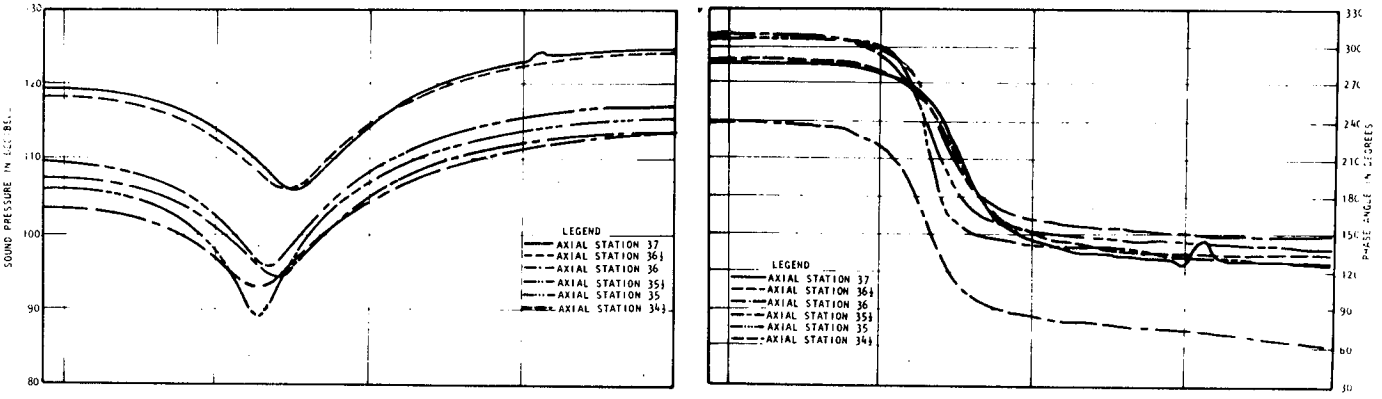


axial stations 34 - 32½

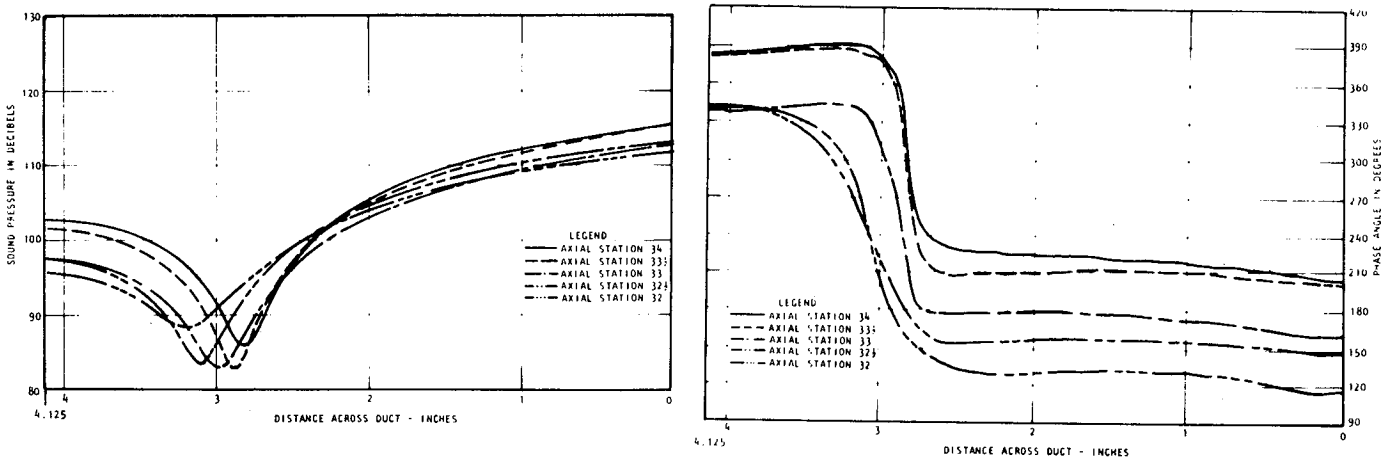
Figure 126. Radial SPL and Phase Angle Contours in Hard Wall Section and Liner 2 Test Section for (2,1) Mode at 1800 Hertz



axial stations 42 - 37 1/2



axial stations 37 - 34 1/2



axial stations 34 - 32

Figure 127. Radial SPL and Phase Angle Contours in Hard Wall Section and Liner 2 Test Section for (5,1) Mode at 2330 Hertz

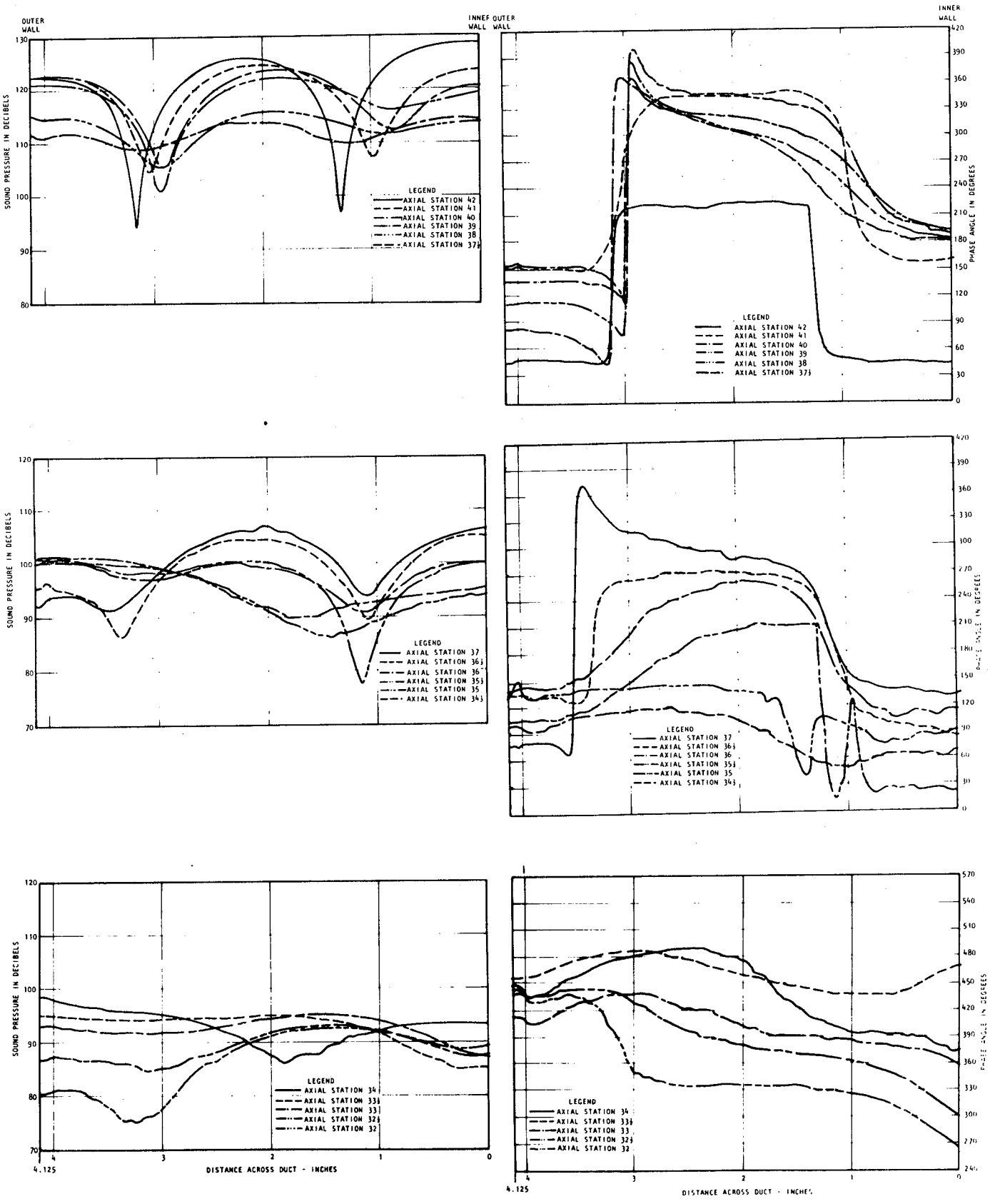


Figure 128. Radial SPL and Phase Angle Contours in Hard Wall Section and Liner 2 Test Section for (6,2) Mode at 3778 Hertz

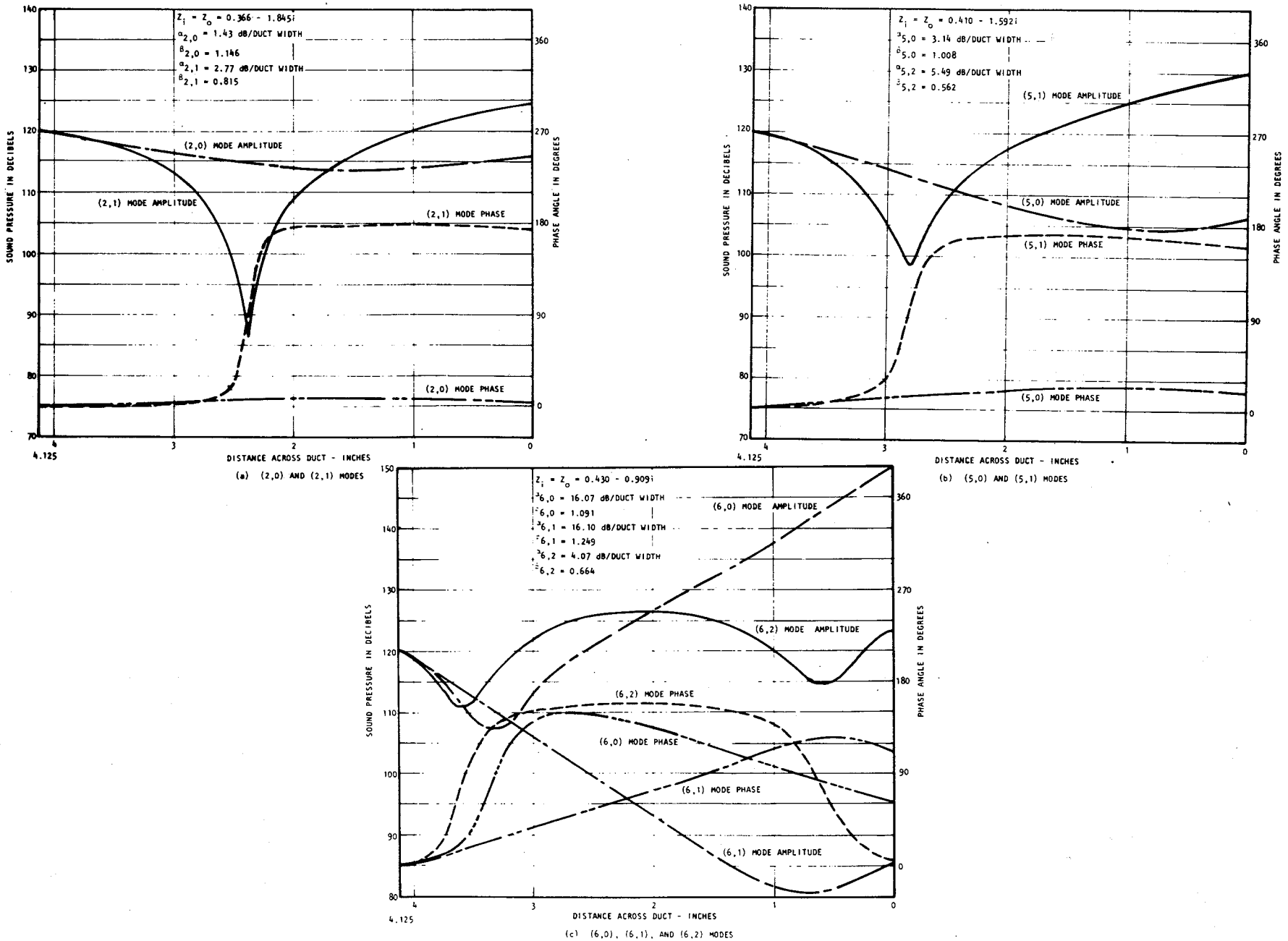


Figure 129. Calculated Mode Shapes in Liner 2 for Comparison with Experimental Data of Figures 126 through 128

a combination of the (5,0) and (5,1) soft wall modes, but is dominated by the (5,1) mode as it should be. From comparison of figures 128 and 129, the pressure distribution in the lined section for the (6,2) case does not really show any close resemblance to the (6,0), (6,1) or (6,2) soft wall modes presented in figure 129(c). Figure 130 is a calculation of the pressure distribution at one duct width downstream for an assumed radial plane wave at the liner entrance for a 6th angular mode variation. As expected, the shape has decayed to the calculated shape of the (6,2) mode, since the other two cut-on modes have attenuations of 12 dB greater than the (6,2) mode. Thus, the experimental behavior at the (6,2) mode cut-on frequency seems to be dominated by other modes.

As was demonstrated in figure 117, the attenuation derived from the two-dimensional Fourier-Bessel analysis was quite accurate for the zeroth order radial modes. Table VIII listed the Fourier analysis results associated with the summary data in figure 117. Figure 131(a)-(d) shows the angular sound pressure distribution in liner 1 at the nine radial stations for each axial location. These data are presented as an illustration of the consistency of the data acquisition and analysis system for analyzing the zeroth order radial modes. Figure 132 is included as an aid in estimating the effect of axial distance on the amplitude of the (3,0) mode as it propagates down the liner 1 configuration.

Because of the exceptionally good correlation with theory shown for the case of four equal amplitude angular modes propagating simultaneously, an example of the angular distribution of SPL and phase at the four axial stations is shown in figure 133. These angular plots were obtained at radial station 6 as shown in figure 116. The angular patterns at each axial station provide further insight into the effect of higher order mode attenuation. The SPL and phase pattern at station 36 is very complex due to addition of the four equal amplitude angular modes. But, at station 24, the (1,0) mode has decayed 2.5 dB more than the (0,0) mode, the (2,0) mode has decayed 5.0 dB more than the (0,0) mode and the (3,0) mode has decayed 11.6 dB more than the (0,0) mode. Thus, the amplitude of the (0,0) mode now dominates, as evidenced by the reasonably flat angular distribution of SPL. However, it is also evident that a strong component of the (1,0) mode still exists by examination of the phase plot.

Finally, in the interest of providing original data for future use, the radial mode shapes for liners 4 and 5 at several axial stations are presented in figures 134 and 135(a)-(c). Complete documentation concerning these measurements is given on the figures.

VI.3.3. Effect of flow velocity in lined ducts.

The most effective data for illustrating the effects of velocity were obtained in the liner 1 configuration. Two sets of data will be presented and in some cases these will be compared with theory. Figure 136 contains the inner and outer wall SPL and phase measurements at 1000 Hertz for the (0,0) and (3,0) modes at 50 fps. Figure 137 shows the radial pressure distribution

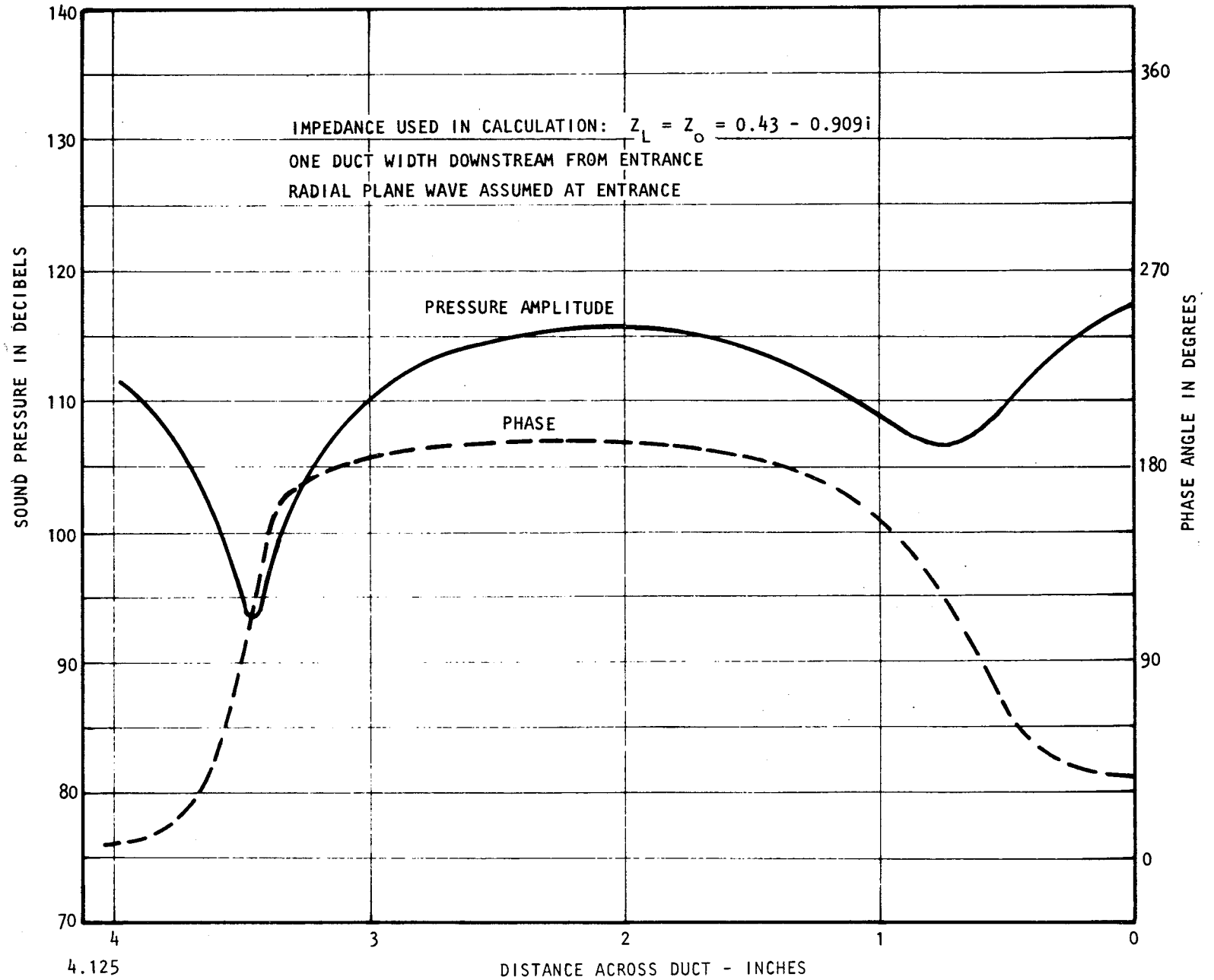


Figure 130. Pressure Distribution Across Annulus for Sixth Angular Mode Set at 3750 Hertz

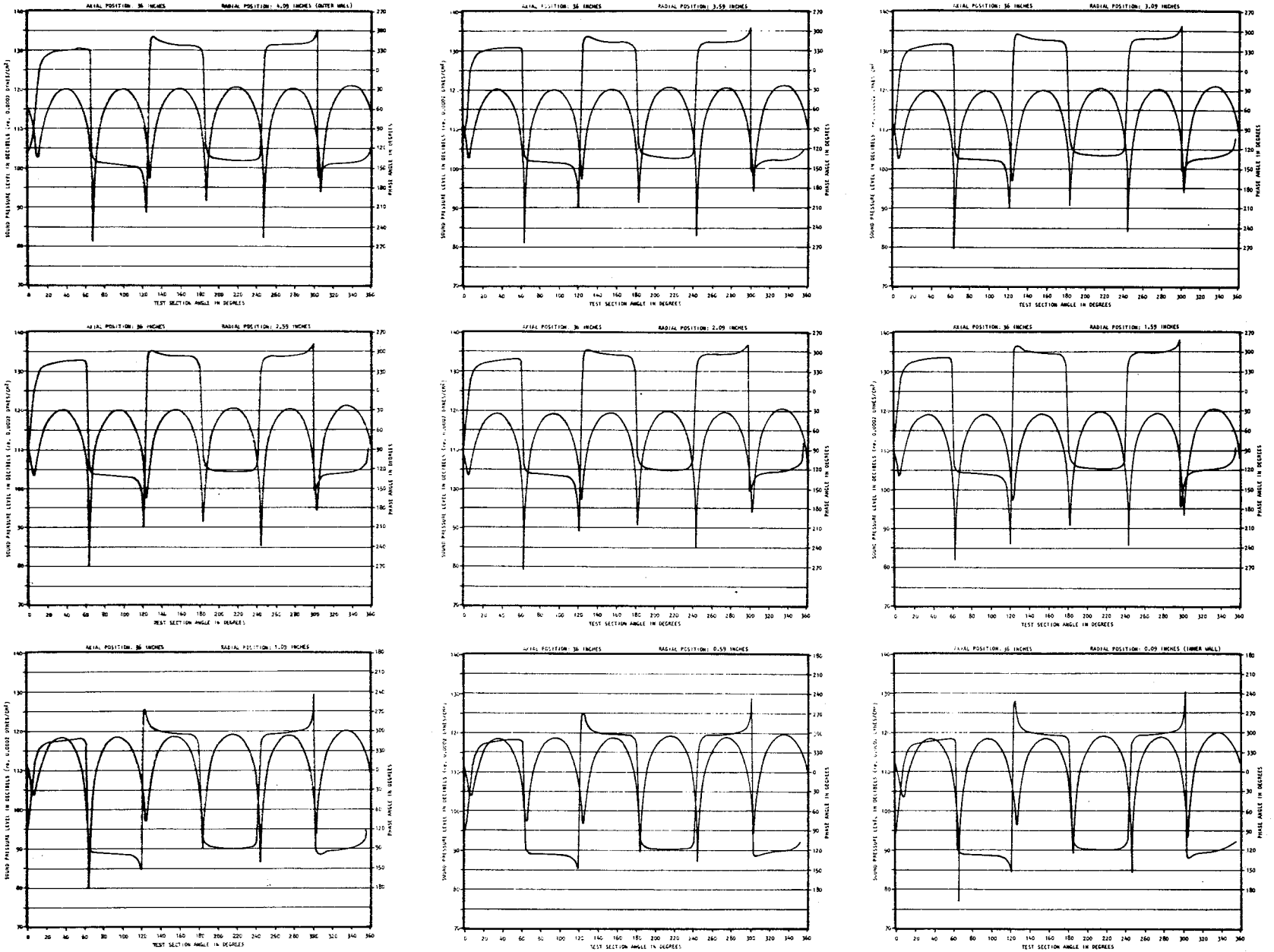


Figure 131. Angular SPL and Phase Angle Distributions in Liner 1 at 1000 Hertz without Flow for Two-Dimensional 'Fourier-Bessel' Analysis - (a) Axial Position: 36 Inches

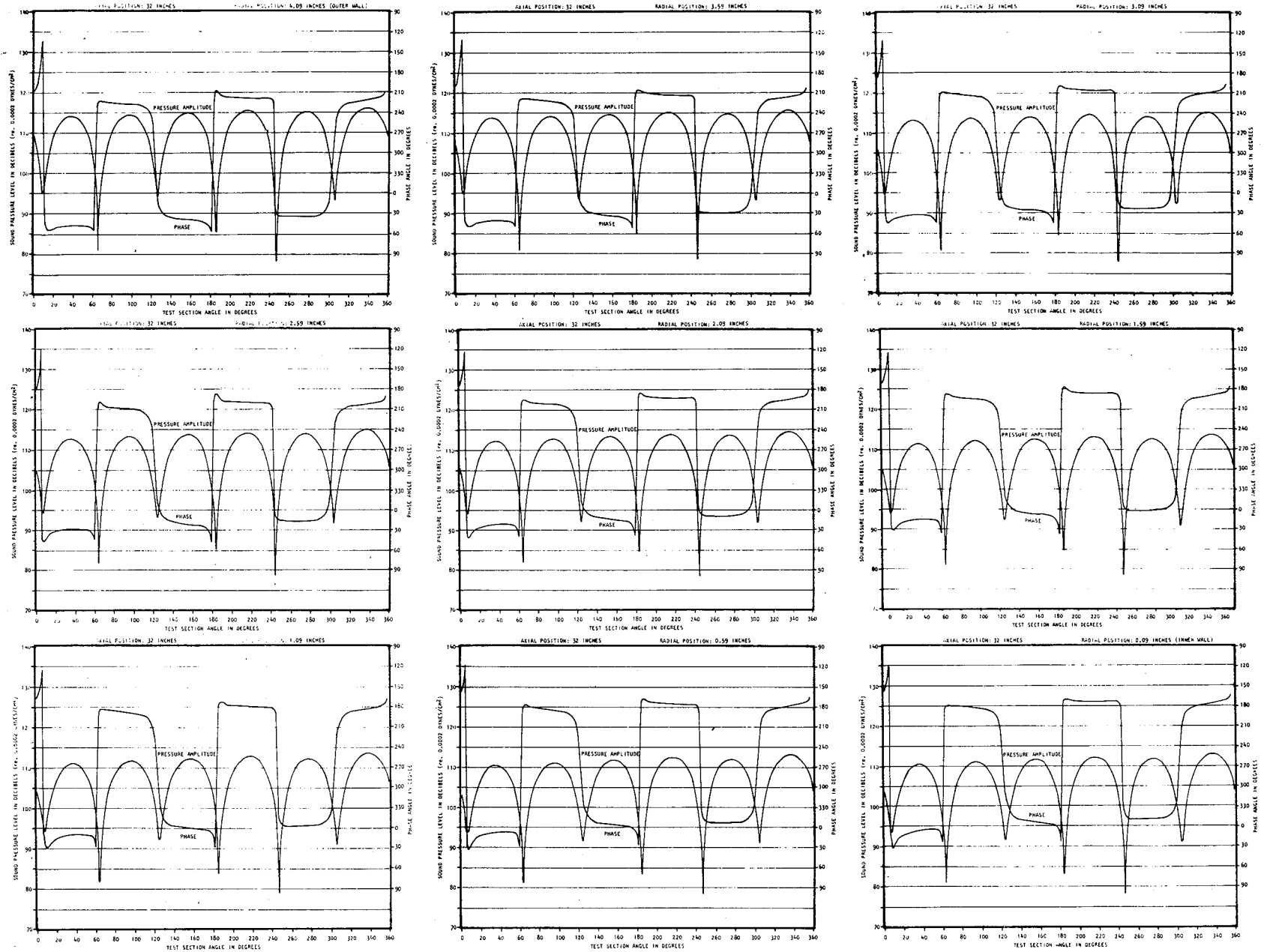


Figure 131. Cont. (b) Axial Position: 32 Inches

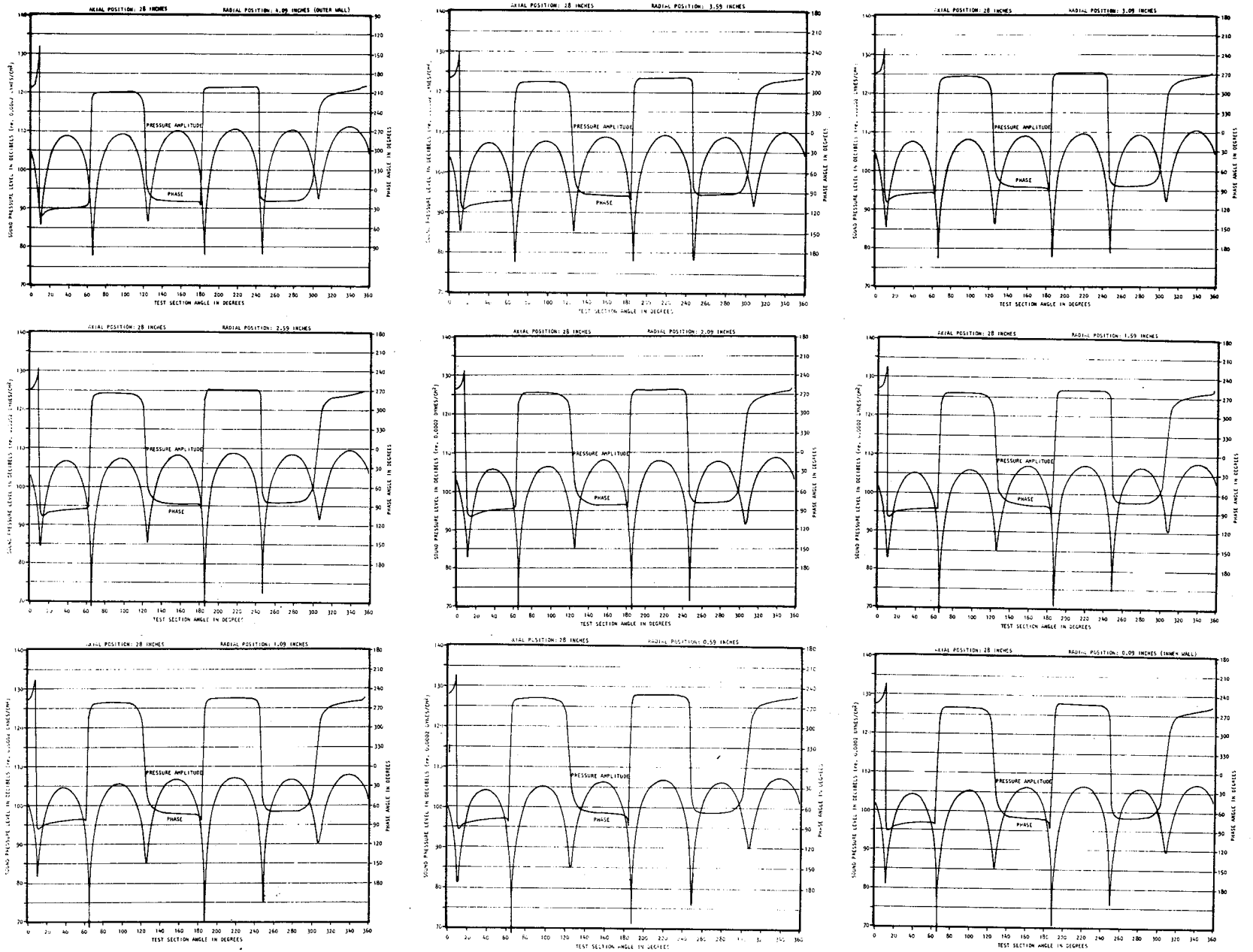


Figure 131. Cont. (c) Axial Position: 28 Inches

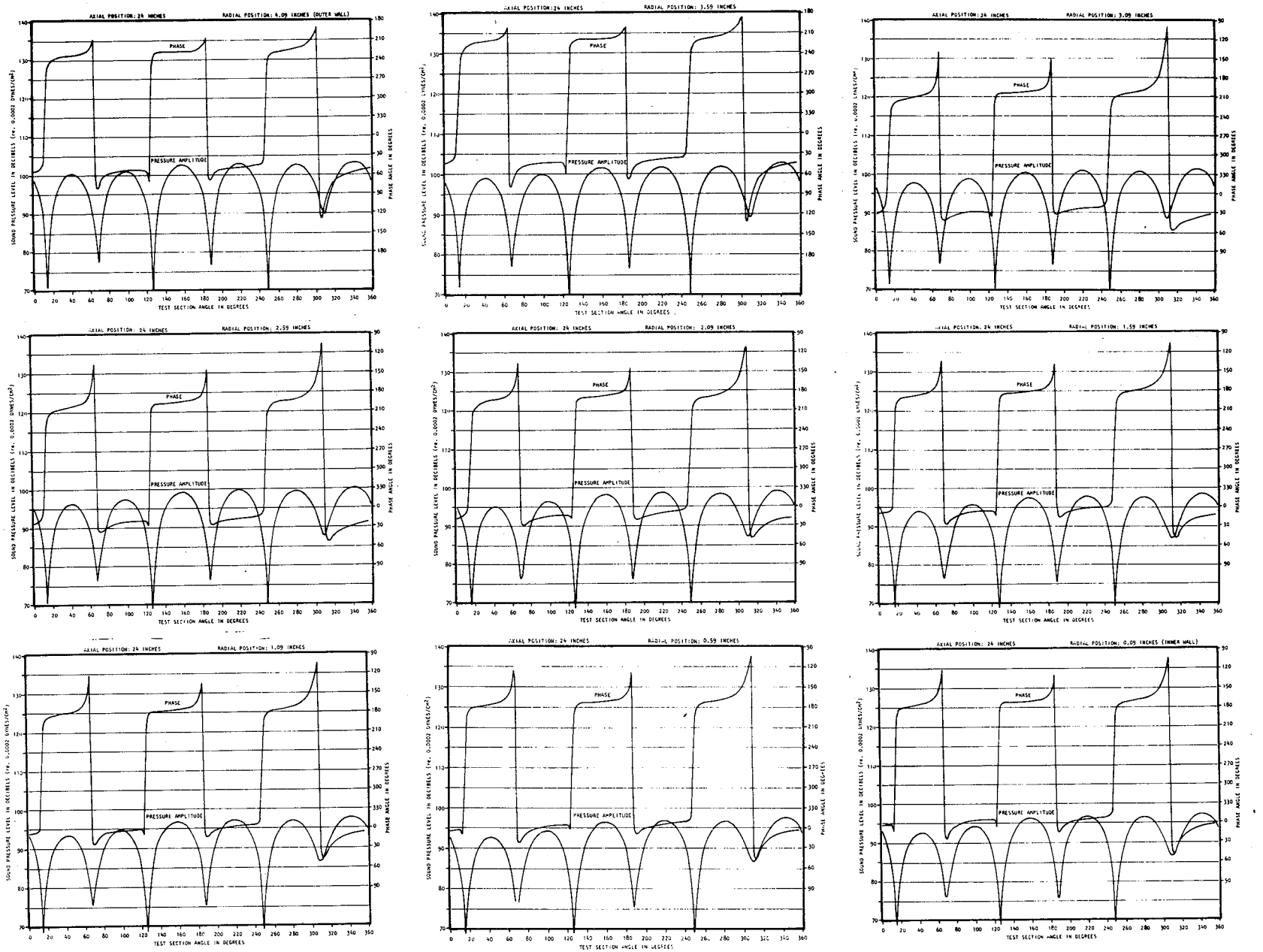


Figure 131. Cont. (d) Axial Position: 24 Inches

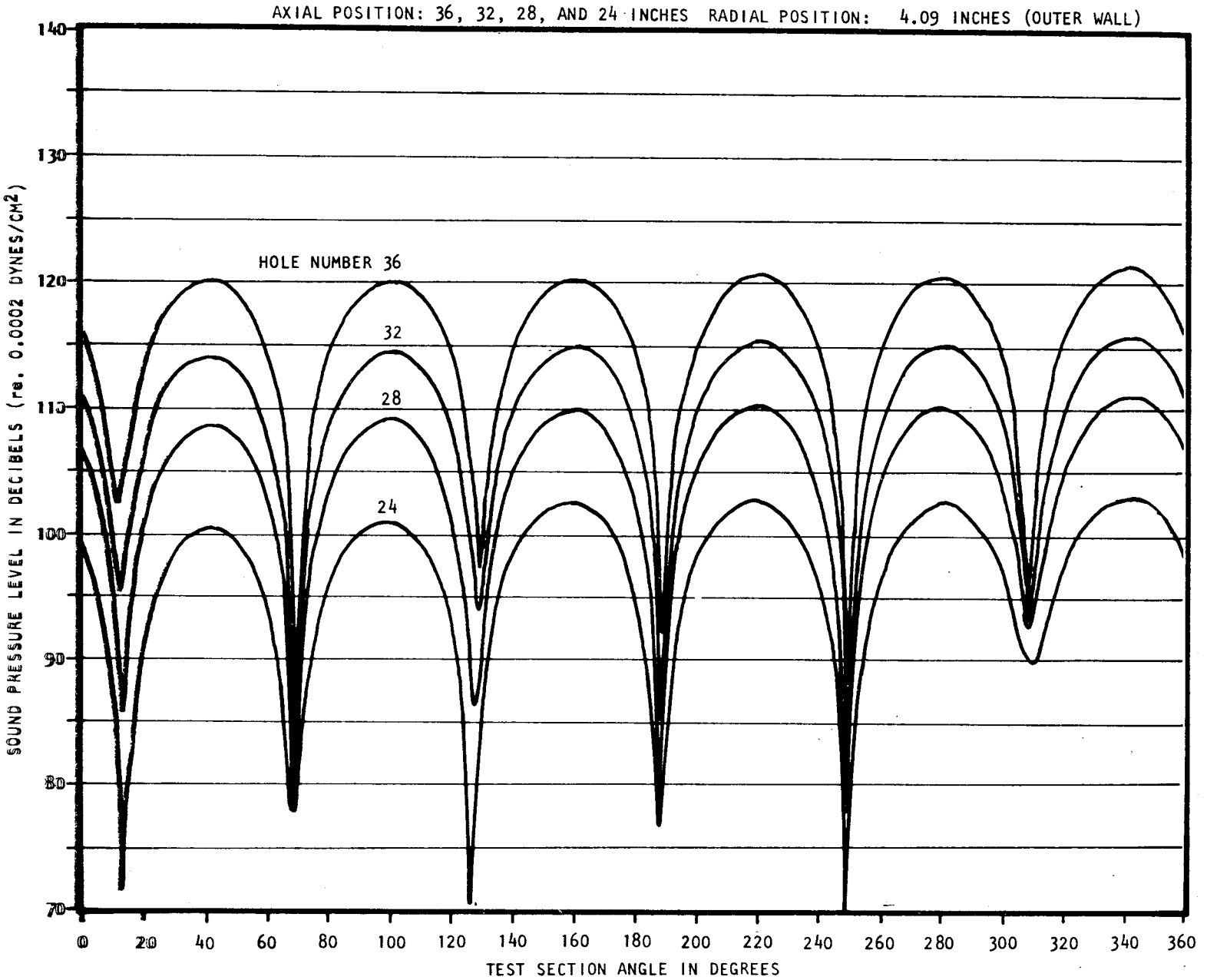


Figure 132. Comparison of Outer Wall Angular SPL Distribution for Four Axial Stations (see Figure 131)

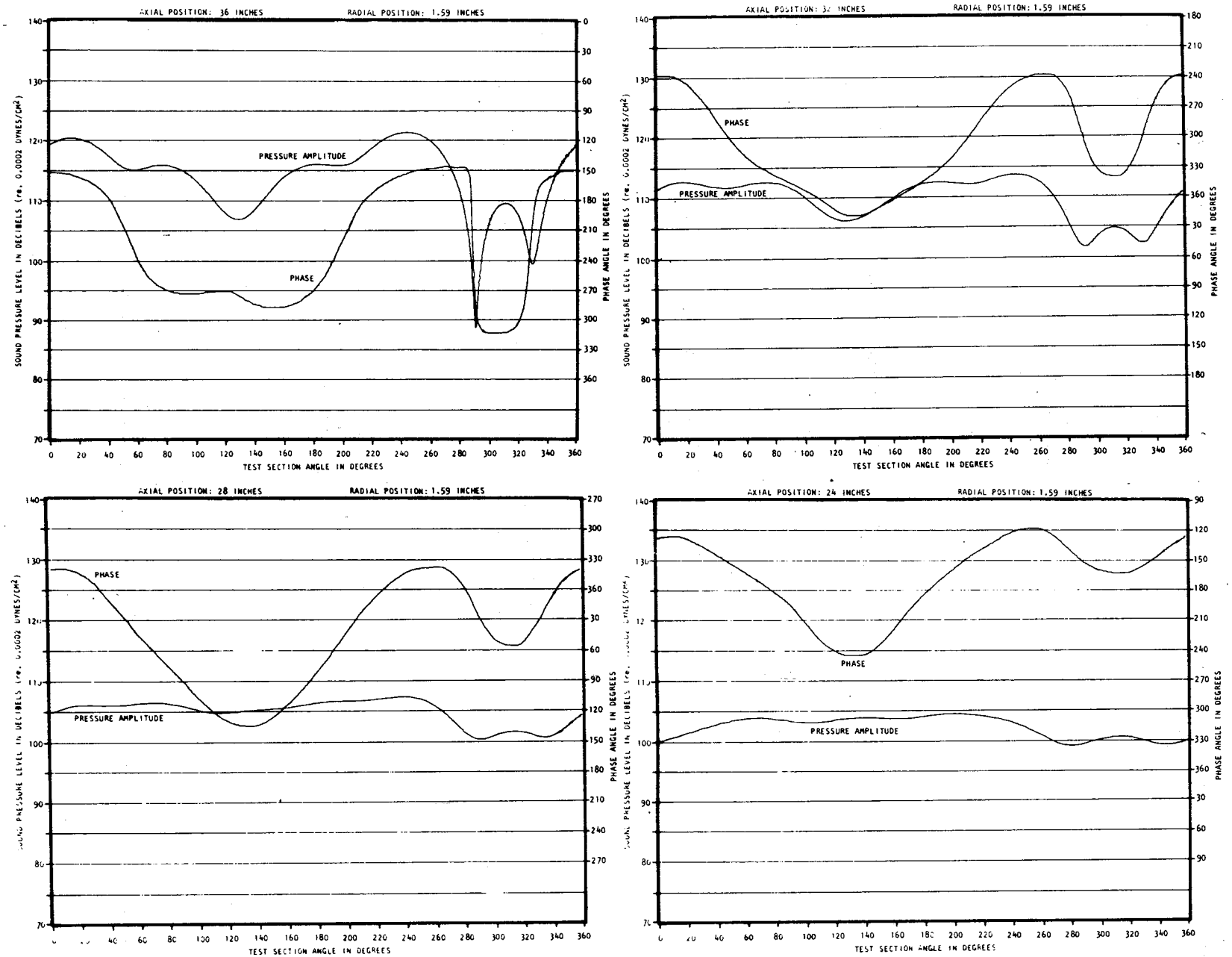


Figure 133. Angular SPL and Phase Angle Distribution in Liner 1 at 1000 Hertz for Four-Mode Combination

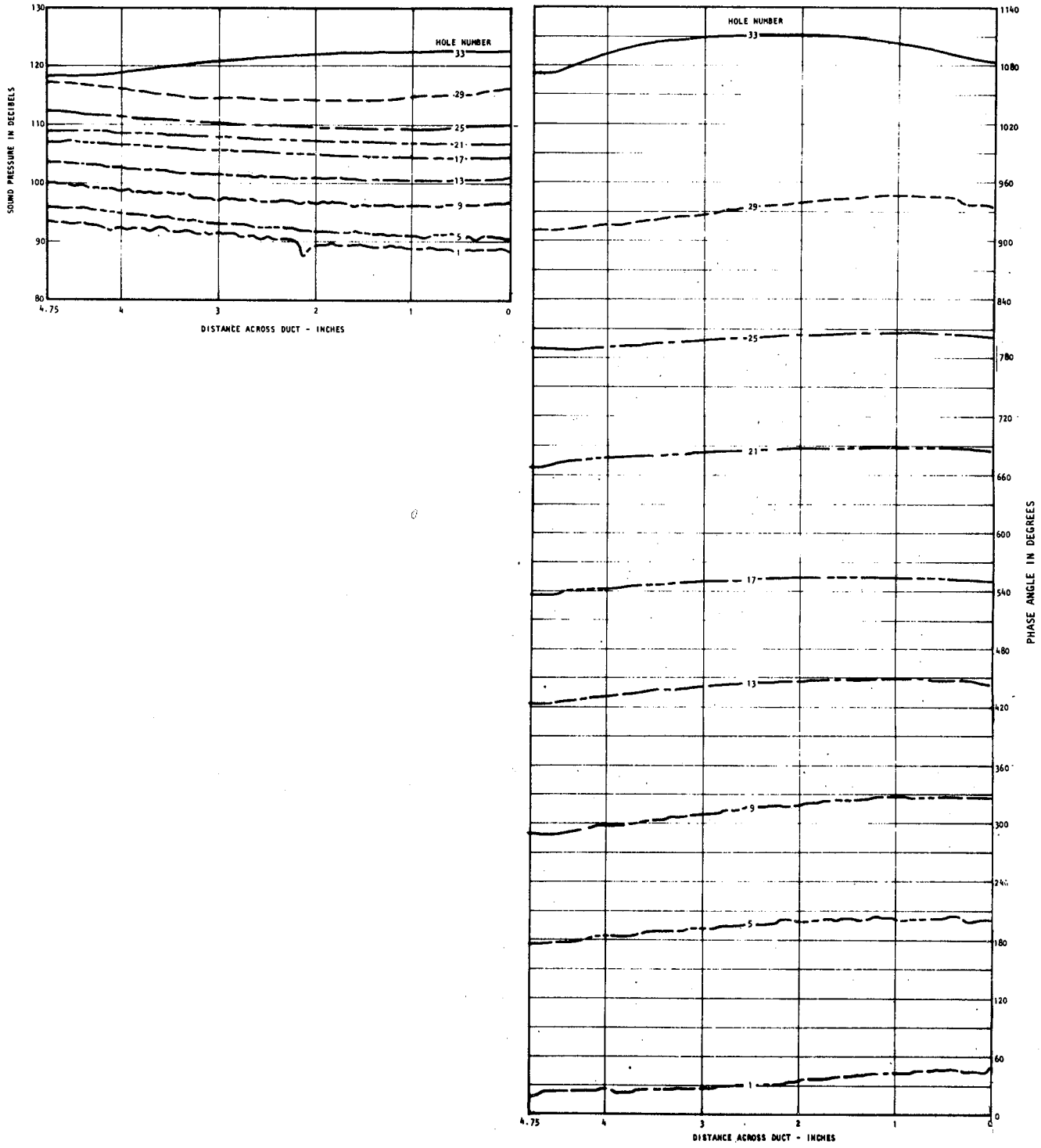


Figure 134. Radial SPL and Phase Angle Contours for the Plane (0,0) Mode in Liner 4 (two sides lined with foam) at 1000 Hertz

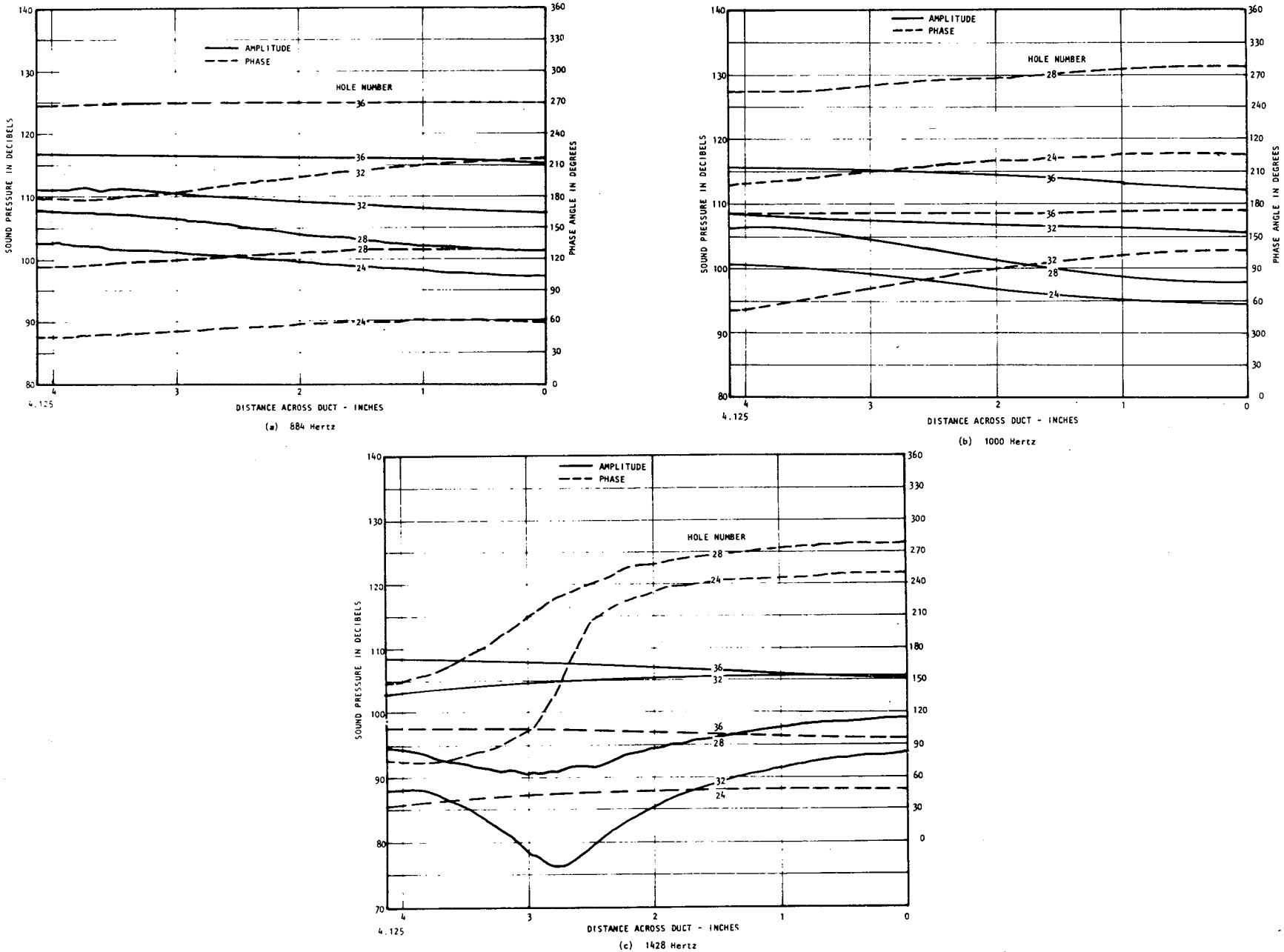


Figure 135. Radial SPL and Phase Angle Contours for the (3,0) Mode in Liner 5 (acoustic foam on outer wall) at Various Frequencies.

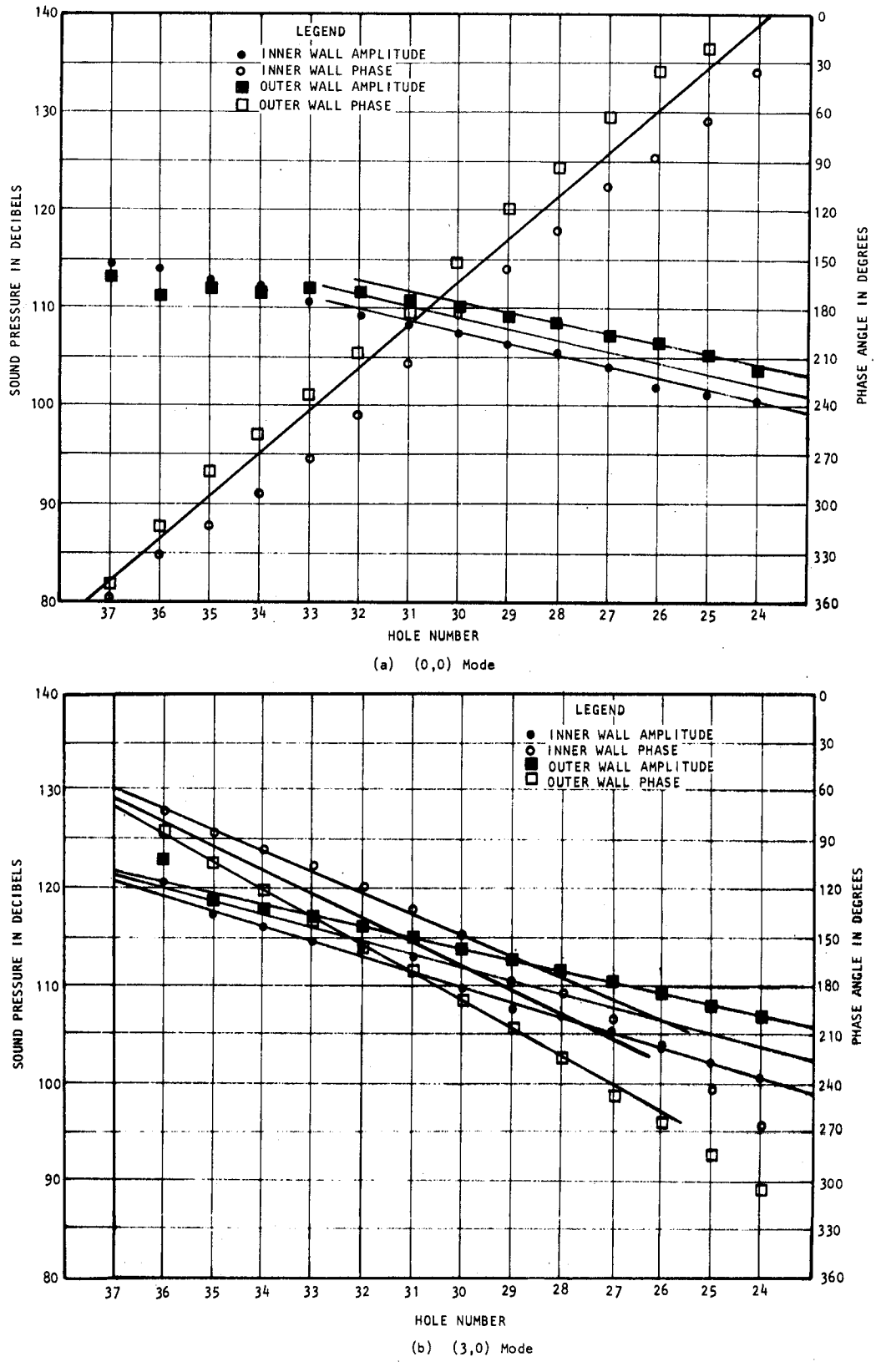


Figure 136. Sound Pressure Level Decay and Phase Angle Change for the (0,0) and (3,0) Modes in Liner 1 at 1000 Hertz with 50 fps Flow Velocity

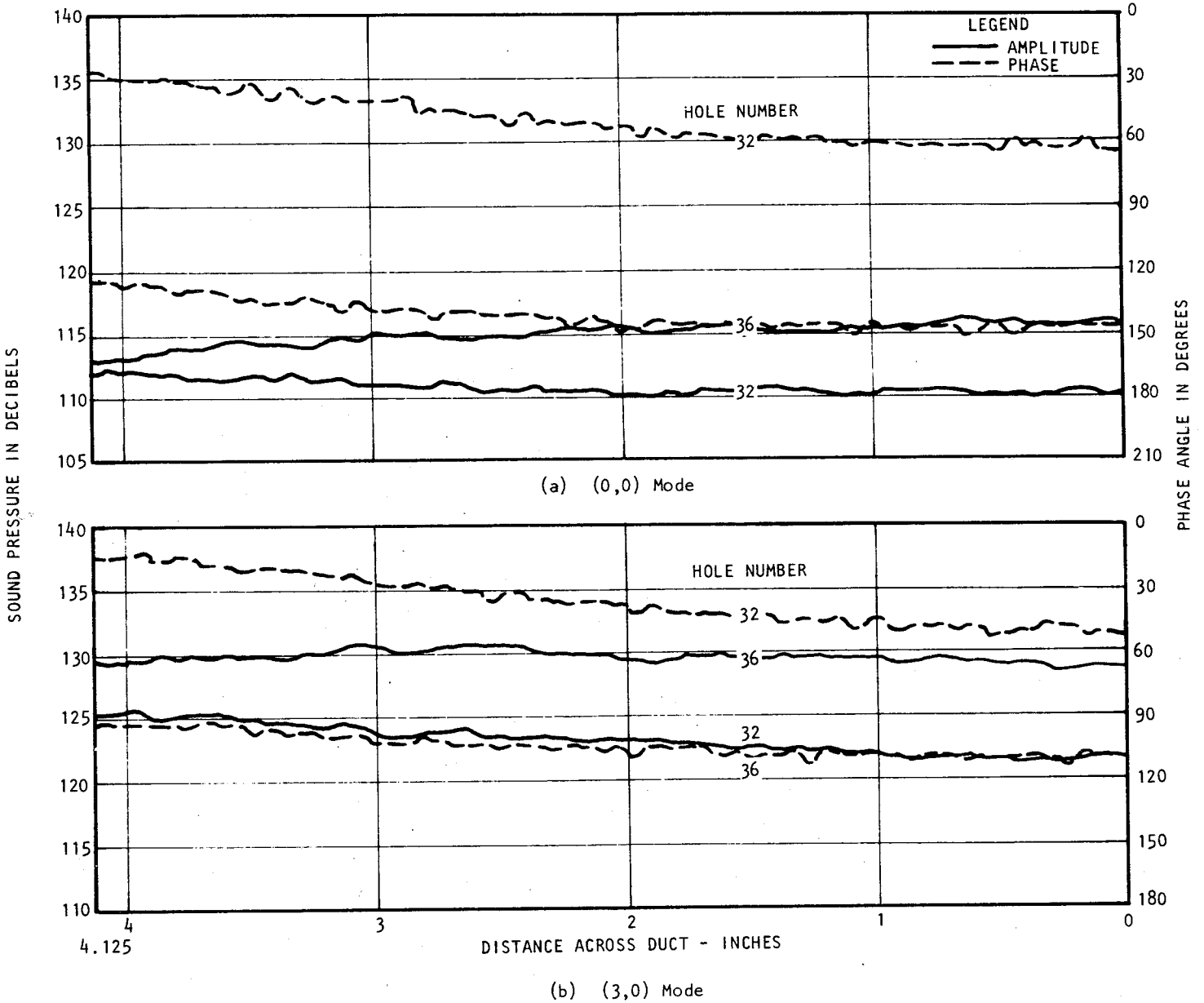


Figure 137. Radial SPL and Phase Angle Contours for the (0,0) and (3,0) Modes in Liner 1 at 1000 Hertz with 50 fps Flow Velocity

at four axial stations spaced 4 inches apart for the two conditions shown in figure 136. Figure 138 illustrates the attenuation of the (3,0) mode at 150 fps for 3 frequencies and figure 139 illustrates the radial pressure distribution at two of those frequencies.

From figure 136(a), the (0,0) mode attenuation is determined to be approximately 4.0 dB, which is essentially that obtained for the no-flow case. The propagation constant, β, has reduced from 1.08 for the no-flow case to .99 at 50 fps. Calculations were not made for comparison with the (0,0) mode case at 50 fps. Figure 136(b) shows the (3,0) mode attenuation and propagating phase slopes. The average attenuation is 5.4 dB and β is 0.551. This compares with a computed value of attenuation of 5.6 to 5.8 dB.

The pressure distributions presented in figures 137(a) and (b) are interesting for illustrating the effect of turbulence on the measurement evidenced by small irregular variations in the amplitude and phase.

In figure 138(b), the (3,0) mode average attenuation is 5.7 dB and the average β is 0.511. Calculated values are on the order of 4.5 to 5.0 dB attenuation and 0.55 to 0.65 for β. Good values of impedance were not obtained on liner 1 at 150 fps due to a drastic reduction in driver output with increasing flow velocity. It was later discovered that this could be effectively remedied by approaching an overdriven condition on the source transducers, however, there was insufficient time at that stage to rerun the tests.

The pressure distributions are shown in figure 139(a) and (b). These are relatively unexciting, since there appears to be no major effect of flow, as predicted.

Finally, data complementary to figures 131(a)-(d) are shown in figures 140(a)-(d) for 50 fps and 141(a)-(d) for 150 fps. In this case, the effect of turbulence on the measurements is quite obvious at station 24. The pertinent data from the two-dimensional 'Fourier-Bessel' analysis are given in the following table for both flow velocities.

TABLE XIII

TWO-DIMENSIONAL ANALYSIS SHOWING EFFECT
OF AIR FLOW VELOCITY ON (3,0) MODE

CONFIGURATION: LINER 3
FREQUENCY: 1000 HERTZ

AXIAL STATION INCHES	FLOW VELOCITY					
	NO FLOW		50 FPS		150 FPS	
	Amp dB	Phase Deg.	Amp dB	Phase Deg.	Amp dB	Phase Deg.
36	122.7	118.1	127.0	73.5	126.5	49.7
32	116.1	186.8	121.3	127.6	120.9	97.4
28	110.6	255.9	115.3	215.5	116.6	137.0
24	101.6	6.9	108.4	305.6	109.3	218.1

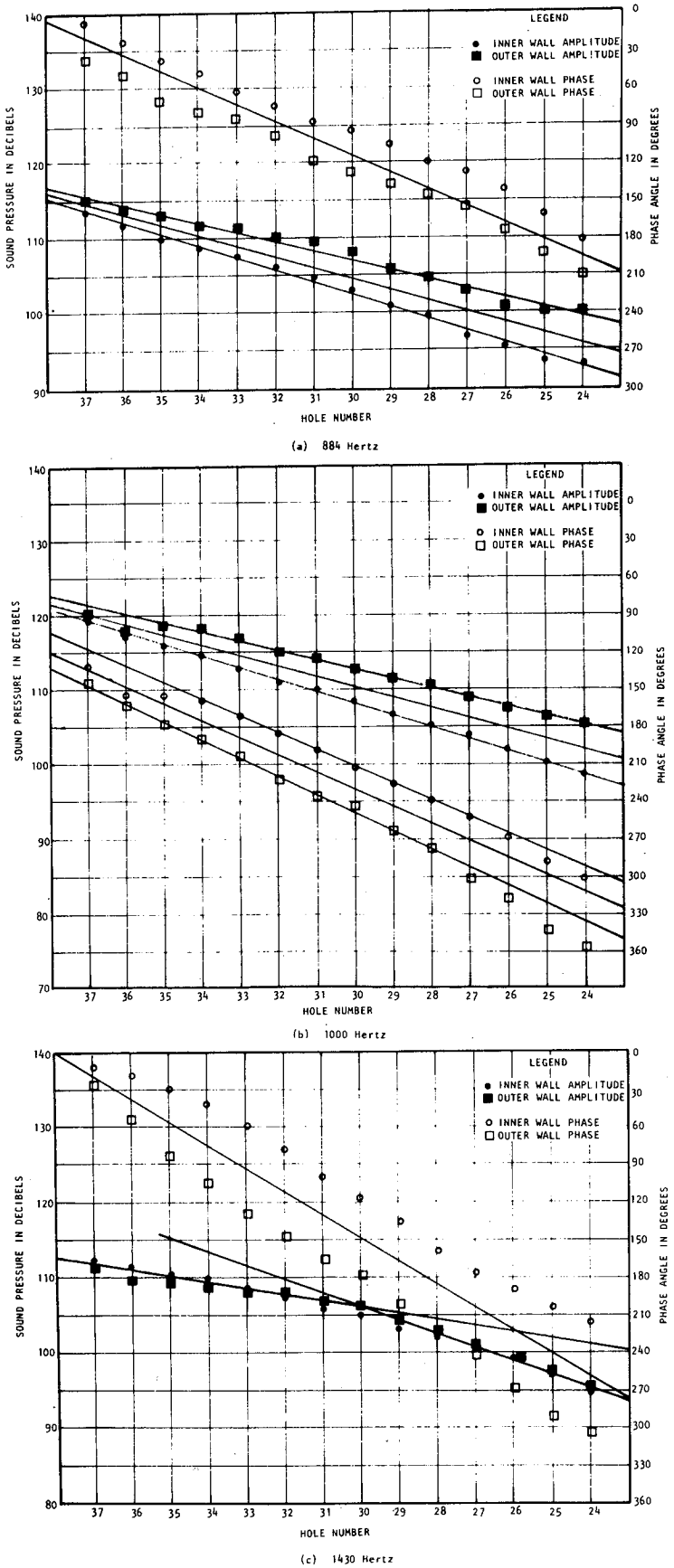
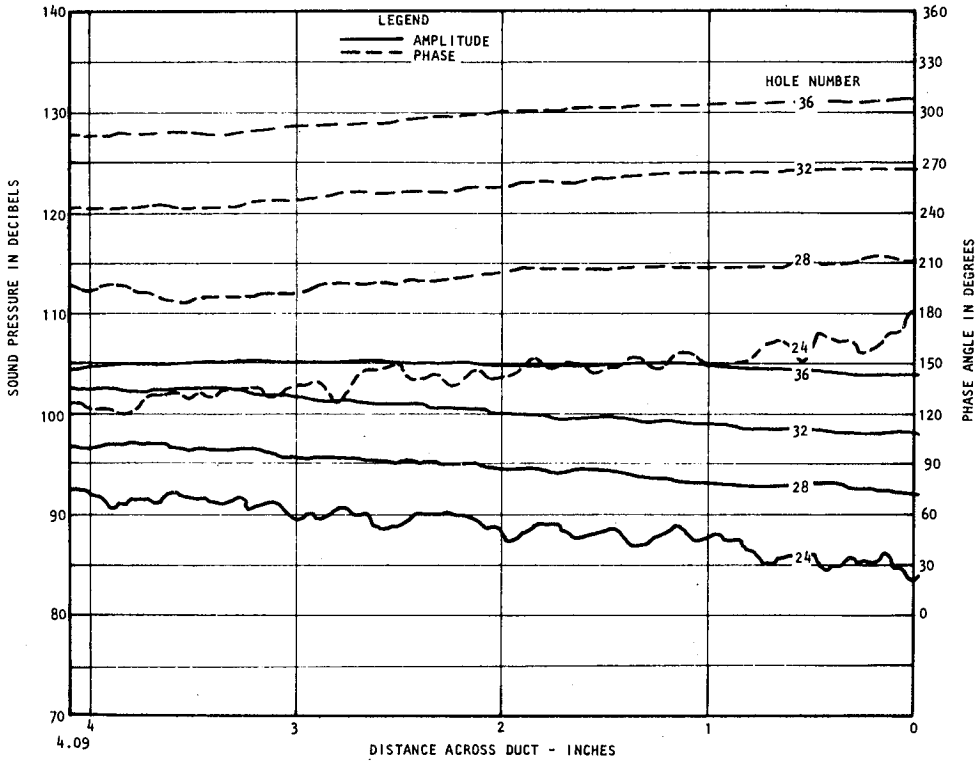
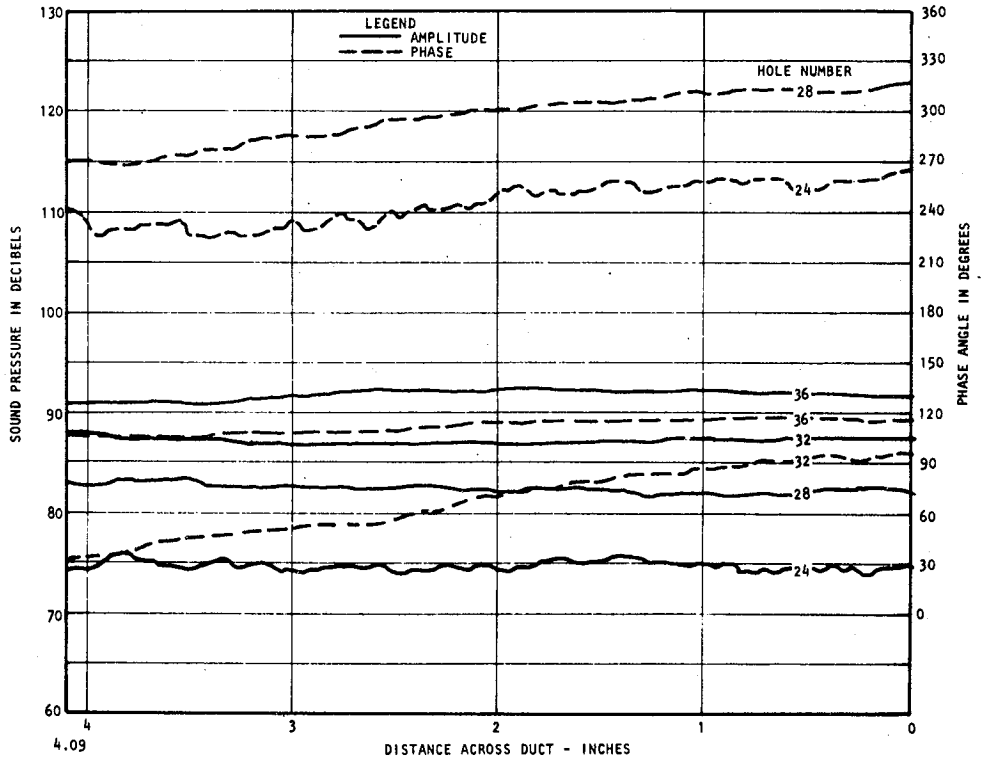


Figure 138. Sound Pressure Level Decay and Phase Angle Change for the (3,0) Mode in Liner 1 for Various Frequencies at 150 fps Flow Velocity



(a) 884 Hertz



(b) 1430 Hertz

Figure 139. Radial SPL and Phase Angle Contours for the (3,0) Mode in Liner 1 at 884 and 1430 Hertz with 150 fps Flow Velocity

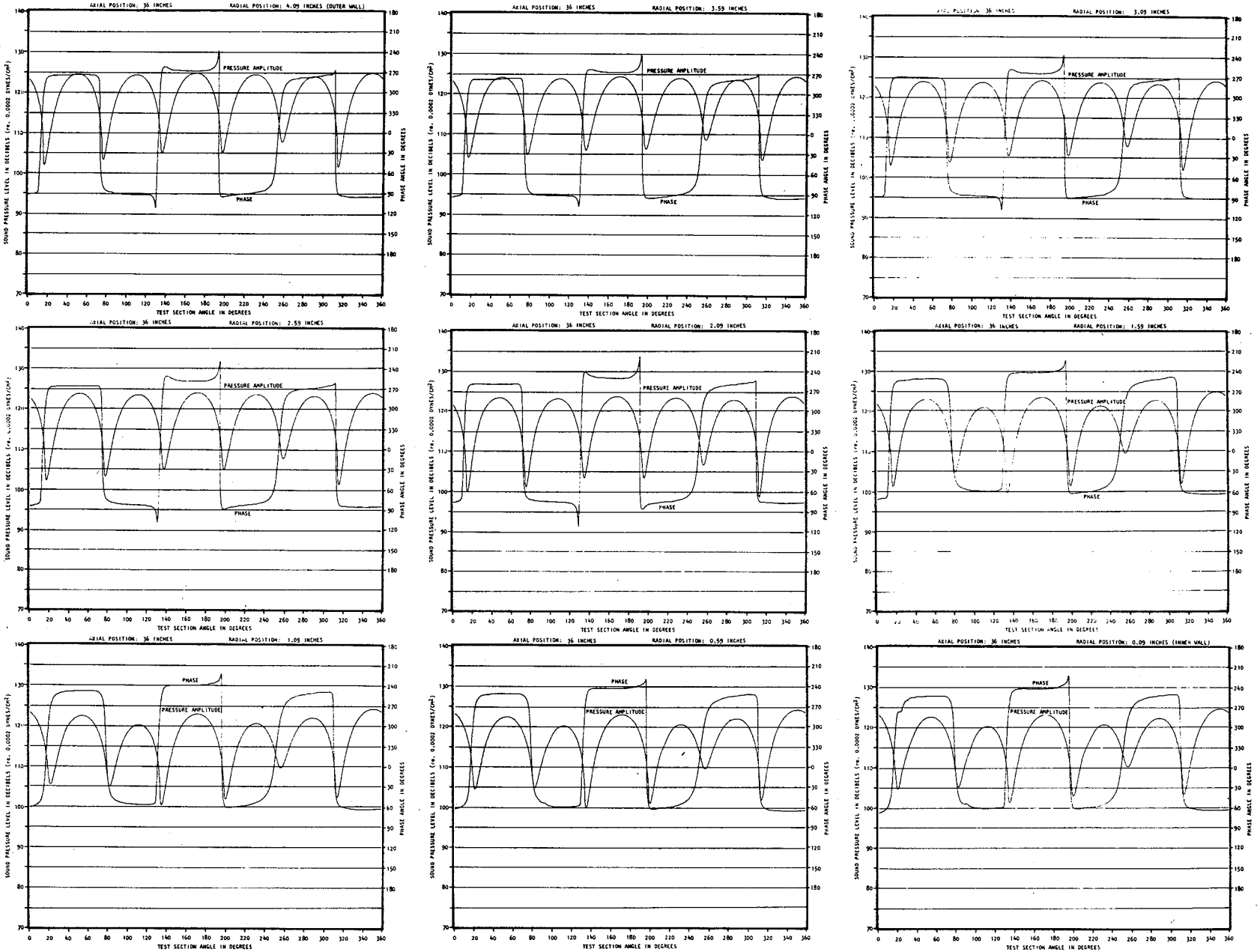


Figure 140. Angular SPL and Phase Angle Distributions in Liner 1 at 1000 Hertz with 50 fps Flow Velocity for Two-Dimensional 'Fourier-Bessel' Analysis - (a) Axial Position: 36 Inches

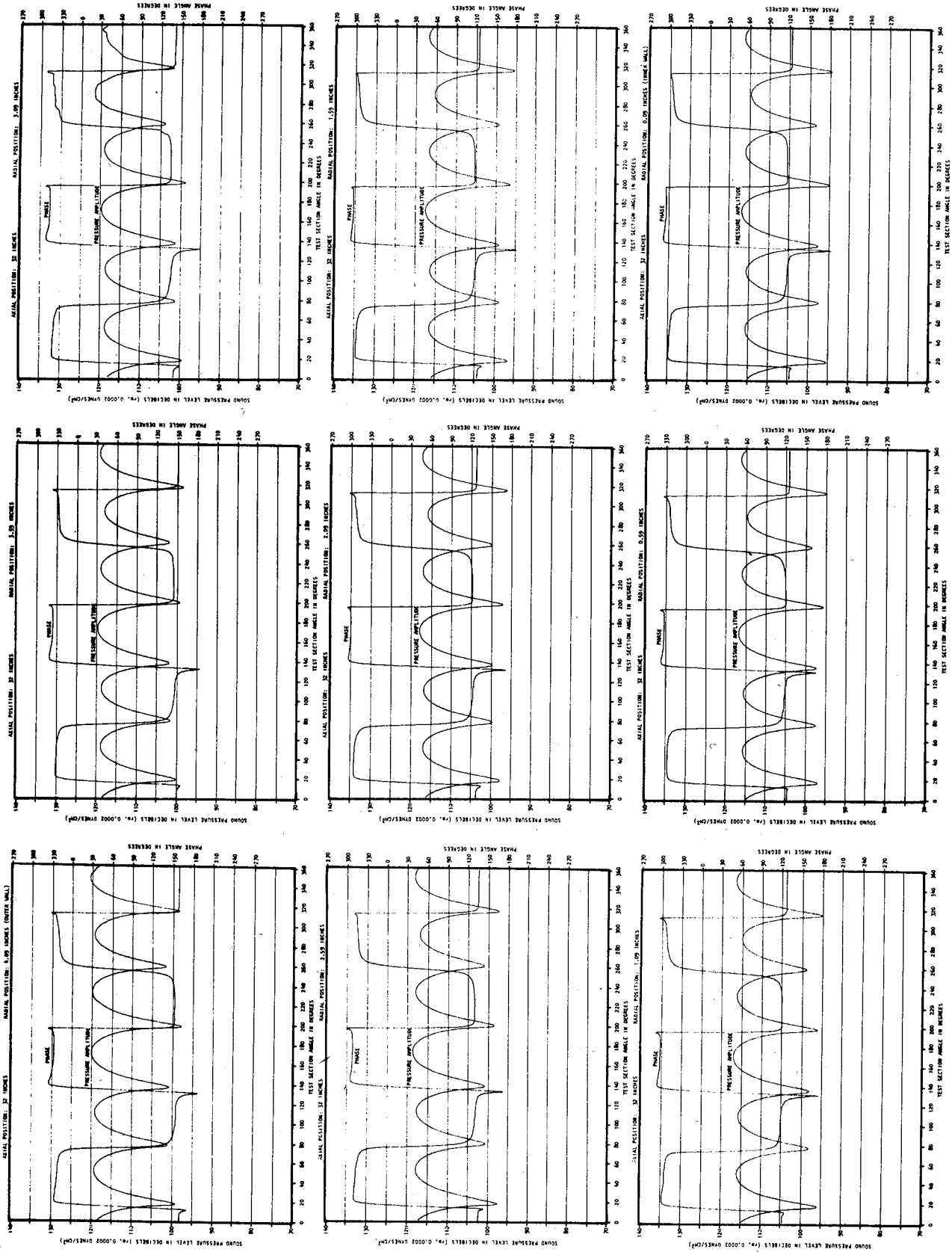


Figure 140. Cont. (b) Axial Position: 32 Inches

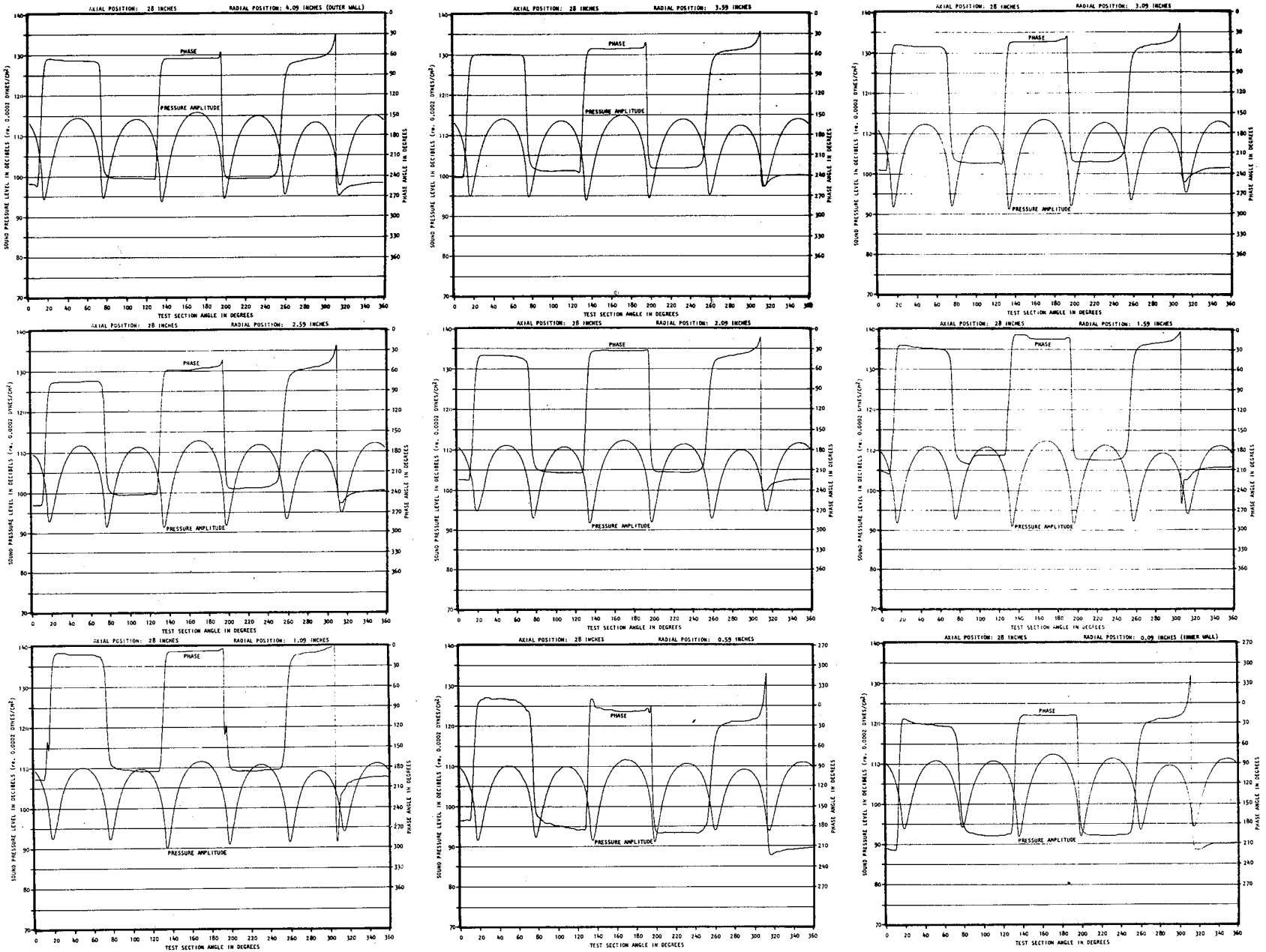


Figure 140. Cont. (c) Axial Position: 28 Inches

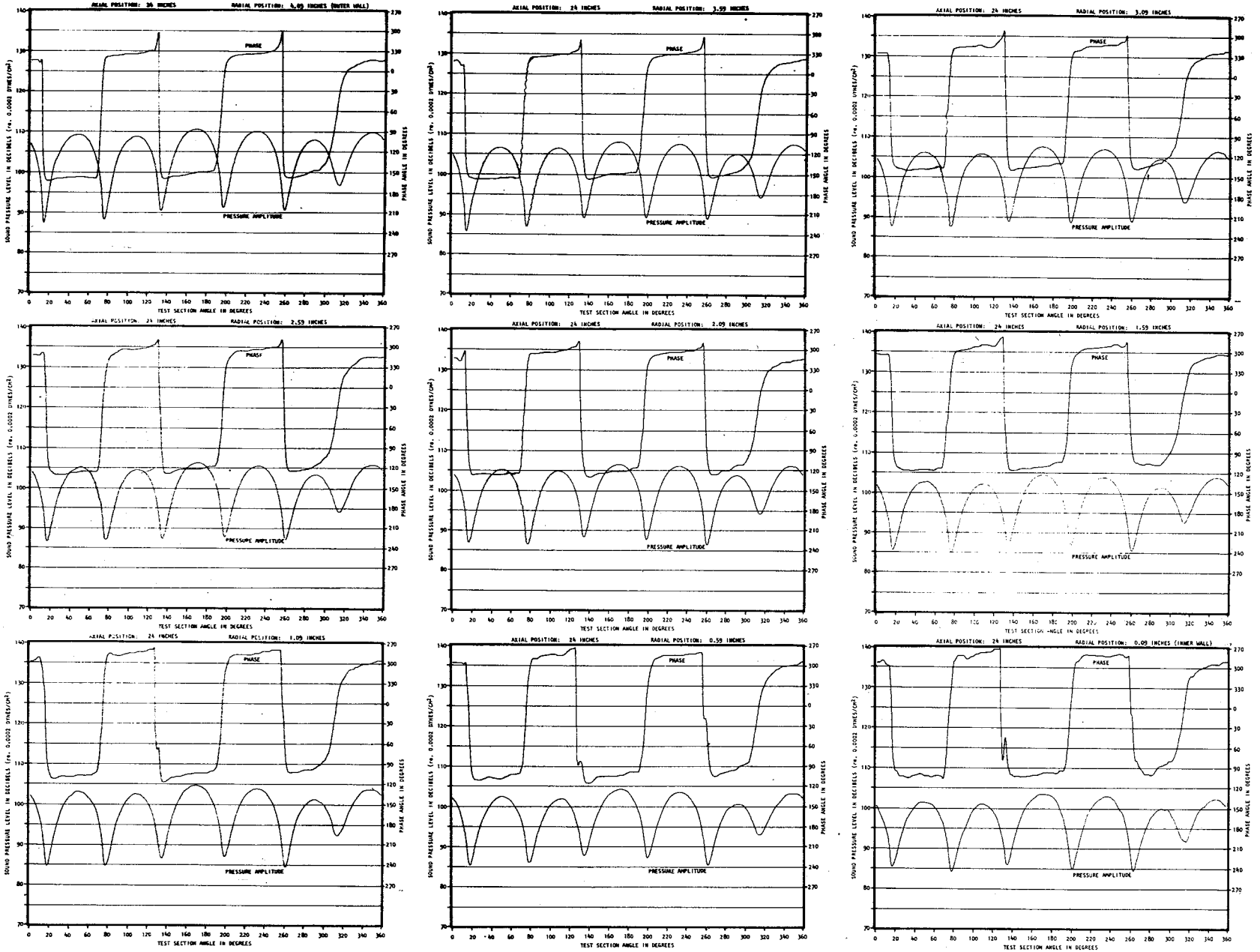


Figure 140. Cont. (d) Axial Position: 24 Inches

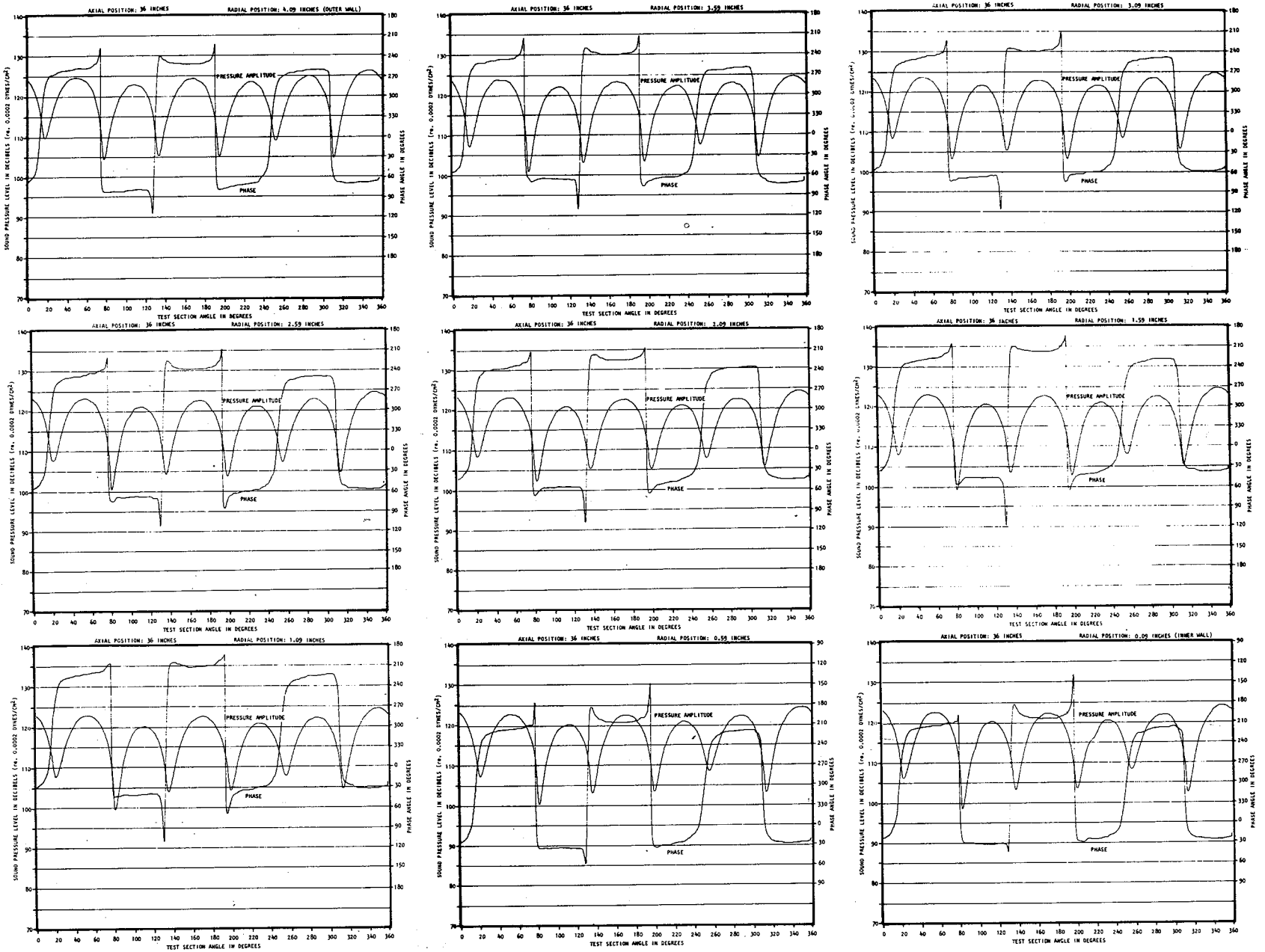


Figure 141. Angular SPL and Phase Angle Distributions in Liner 1 at 1000 Hertz with 150 fps Flow Velocity for Two-Dimensional 'Fourier-Bessel' Analysis -(a) Axial Position: 36 Inches

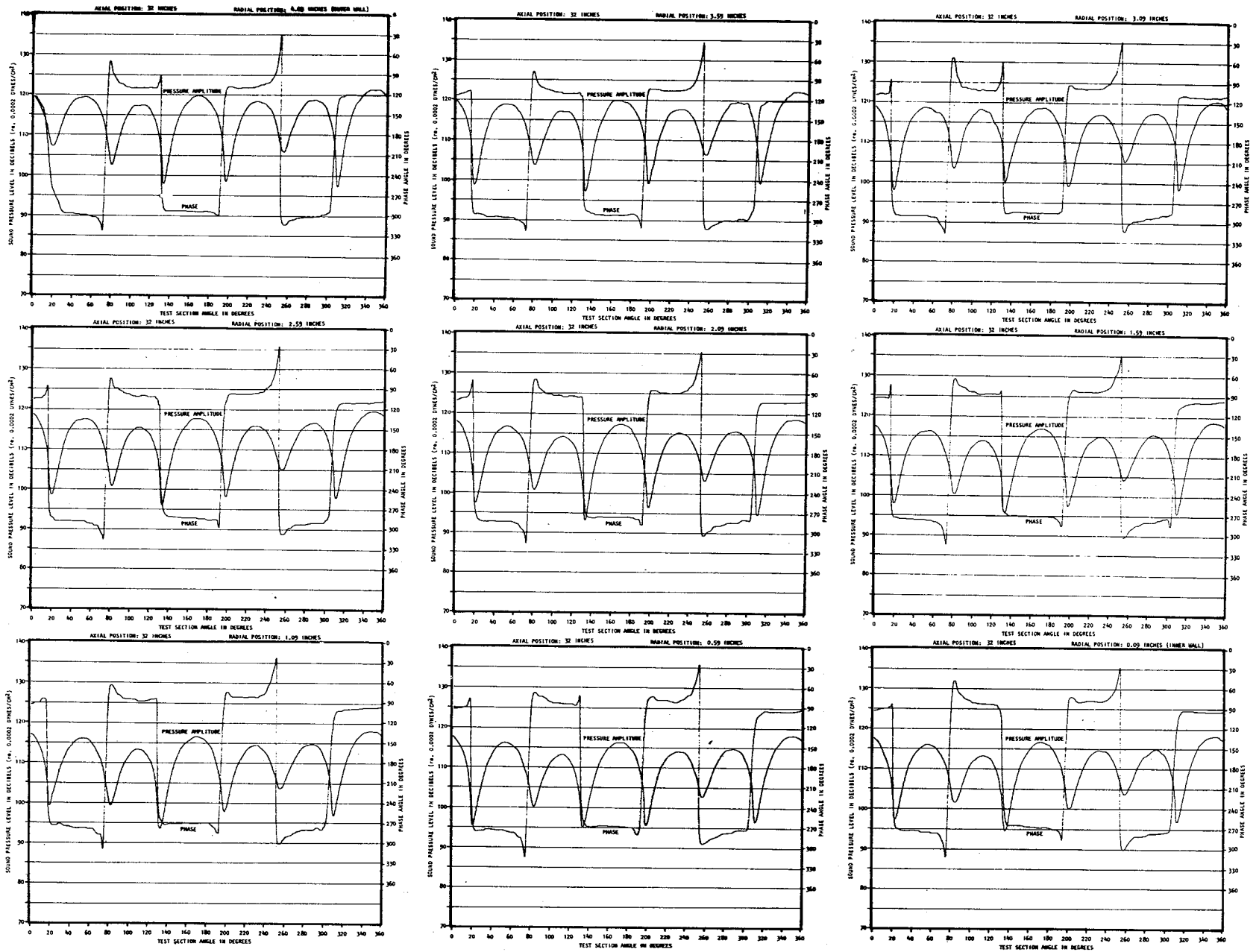


Figure 141. Cont. (b) Axial Position: 32 Inches

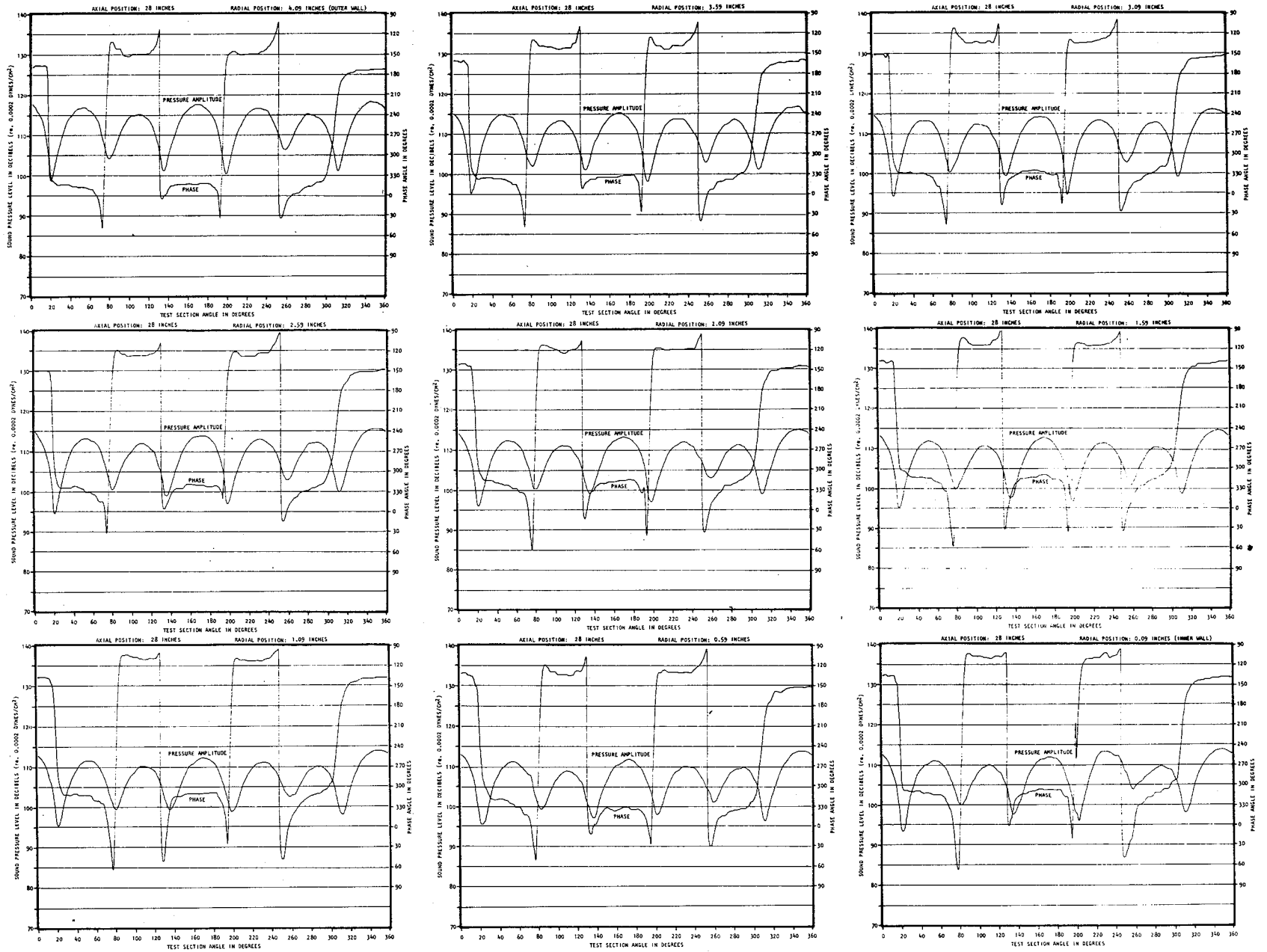


Figure 141. Cont. (c) Axial Position: 28 Inches

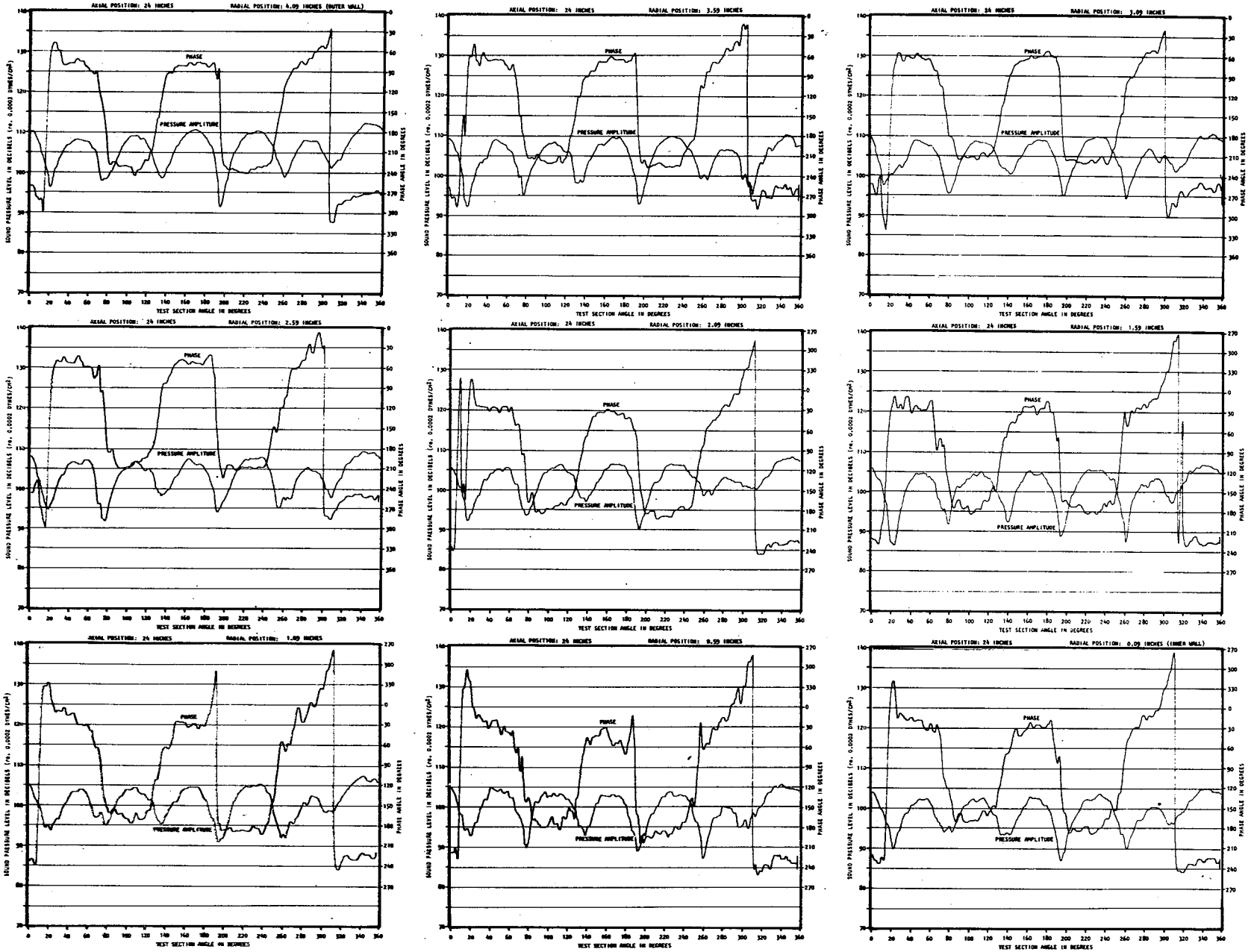


Figure 141. Cont. (d) Axial Position: 24 Inches

An analysis of the data in table XIII using a least-squares linear regression gives the following average values of attenuation and β for each of the velocity conditions.

TABLE XIV

EFFECT OF AIR FLOW VELOCITY ON COMPLEX PROPAGATION CONSTANT

VELOCITY FPS	USING DATA FROM PREVIOUS TABLE		USING DATA FROM FIGURES 127(b), 152(a), and 154(b)	
	Attenuation dB	Propagation Constant β	Attenuation dB	Propagation Constant β
0	7.10	.768	6.2	.719
50	6.37	.735	5.4	.551
150	5.76	.508	5.7	.511

Included in the last two columns of this tabulation are the attenuation and β values determined from the average values between inner and outer wall SPL levels from figures 111(b), 136(a) and 138(b). The comparison between these two sets of data is reasonable, but not good. Both sets of data do, however, show a decrease in both attenuation and β. The β decrease is to be expected, but the attenuation decrease is dependent on many factors and an increase could also occur, provided the physical characteristics such as impedance and frequency satisfy the conditions for an increase.

VII. THE MEASUREMENT OF HIGHER ORDER CIRCUMFERENTIAL MODE RADIATION IMPEDANCE FOR AN ANNULAR DUCT WITH FLOW

VII.1. Introduction

The theoretical treatment of the generation of sound in, transmission through, and radiation from bypass air ducts of the fan-jet engine family can be separated into three distinct but partially coupled problems, as discussed. The problem of sound radiation from an engine duct has not been considered in detail in the literature using this superposition approach, but approximate treatments have discussed the radiated field for simplified geometry, without the presence of the duct air flow (e.g. Morfey, ref. 8, Sofrin and Tyler, ref. 7). If the superposition approach is to be utilized in predicting sound radiation from a fan-jet engine, it is necessary to know the acoustic radiation impedance at the duct termination, since this impedance serves as the coupling link between the duct and the radiated field.

There have been basic calculations of the radiation impedance (for the plane and higher order modes) of a flanged annulus by Morfey (ref. 26), Doak (ref. 24), and Haddle (ref. 25), but the effects of axial flow through the duct and a realistic termination were not included in these studies. One other study by Lansing, Drischler and Pusey (ref. 14) implicitly calculated the radiation impedance in determining the radiated field with a realistic termination. This work, which extended the Wiener-Hopf type solutions of Levine and Schwinger (ref. 11) and Carrier (ref. 12), proceeds directly from a source distribution to the radiated field. The radiation impedance can be calculated using this procedure.

There have been few reports on measurements of radiation impedance to serve as verification of the theoretical predictions. Plane mode radiation impedance was measured by Mechel, Mertens and Schilz (refs. 54 and 55). They demonstrated that for frequencies below the first higher order mode cut-on frequency the measured plane mode radiation impedance for a circular piston compares favorably with calculated values. They also measured the effect of axial velocity on the plane mode radiation impedance for a circular aperture. The effect of velocity was to reduce radiation resistance up to a frequency of ka = 1.7, which was the frequency limit of the tests. The velocity effect on reactance is more difficult to characterize, but in general, at very low frequencies (below ka = 1) the reactance was reduced; conversely the peak value in the reactance curve increased with flow velocity.

The major shortcoming with the available data on radiation impedance is the complete lack of measurements for higher order modes. Further, no known data exists for annular ducts (or flanged annular pistons) in any frequency range. However, utilizing the facility described previously in this report, a technique for measuring higher order mode radiation impedance has been developed and it has been possible to check the predictions for no-flow radiation impedance. The technique requires rather lengthy data reduction methods, which are outlined in the following section. Data for higher order mode radiation impedance are discussed and compared with available theoretical predictions. Also, effects of flow on the radiation impedance are discussed.

VII.2. Experimental Technique for Determining Modal Radiation Impedance

The measurement of modal radiation impedance necessitated the development of several new data analysis methods because of

- o restrictions on microphone degrees-of-freedom in the test section,
- o complexity of the sound pressure field in the duct, and
- o the added complexity of measurement due to flow.

VII.2.1. Sound field mapping

The philosophy behind measuring only the axial distribution of sound pressure in a plane wave impedance tube is that the sound pressure distribution in the plane normal to the tube axis is known. Once the sound field becomes complicated enough that the sound field in the plane of the tube or duct is unknown, more detailed measurements are required to characterize the wave components. It is certainly valid to assume that radiation impedance of a higher order mode field can be calculated from the axial sound pressure distribution of that field, provided enough is known about the wave field to properly separate the components of all modes present. The measurements necessary to complete this separation are in essence a three-dimensional mapping of the duct sound field. Obviously, a continuous volume mapping of the sound field is not necessary as the boundary conditions remain uniform along the tube axis. Thus, only measurements at properly spaced points are required.

As discussed earlier, it was not feasible to mount a probe microphone projecting into the test section from the end to permit a continuous axial survey; therefore, on the outer wall of the test section, microphone mounting holes were located on a one-inch spacing down the axis of the duct. With this system, it is possible to obtain a fairly complete mapping of sound pressure in a plane normal to the axis of the annulus at the one inch spacing locations. The system does not, however, provide the usual continuous standing wave plots down the duct, with the required resolution for direct measurement of the standing wave ratio and location of the first minimum.

VII.2.2. Duct sound field

A first impression is that it is particularly expedient in the determination of radiation impedance to excite a single higher order duct mode in isolation. It has previously been shown that this capability exists for angular modes at frequencies below the first higher order radial mode cut-on frequency. It is not always possible, however, to achieve the degree of isolation required for a particular mode and in some instances mode isolation is less than 10 dB. In this instance, it is impossible to determine the radiation impedance of a single mode, because of the multiple mode axial standing wave patterns present in the duct; thus, the effects of the other modes which are spuriously excited must be analytically removed. To accomplish this, a complex Fourier analysis technique similar to one described in section III was developed. One of the interesting facets of this analysis technique is that several modes could be excited simultaneously and the data, after Fourier analysis, could be used to determine the radiation impedance of each mode. This method was ultimately incorporated, because of the significant time savings in conducting the tests. It was verified, however, that this method does degrade the accuracy of the results to a minor extent.

VII.2.3. Measurements in flow

Two major difficulties were encountered in making measurements in flow. The first involved reducing the random noise component. This was accomplished with two-stage filtering. First, the microphone signal was filtered through a 1/3 octave filter set. The output of this stage was then amplified and filtered through a 2 Hertz narrow-band tracking filter. The resultant filtered signal was very stable and had a signal to noise ratio of greater than 20 dB at 150 fps based on a source sound level of 120 dB.

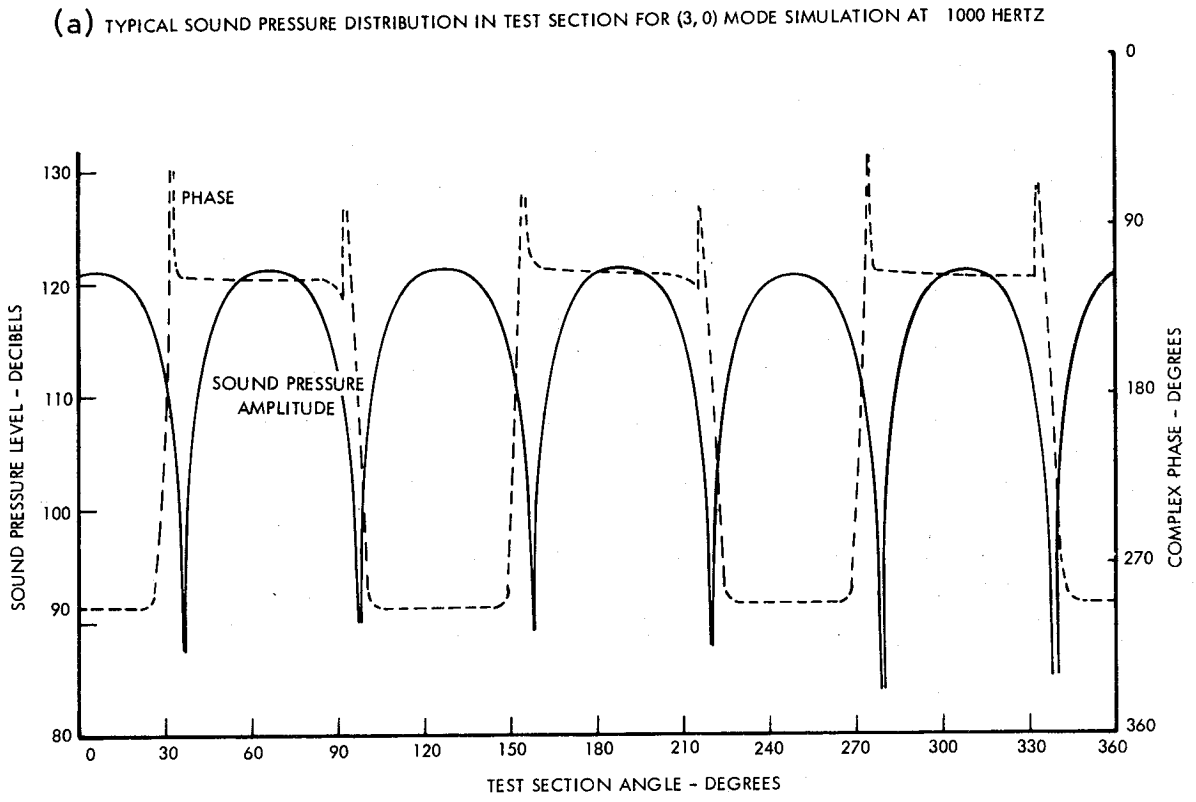
The second difficulty was evidenced when trying to maintain a constant value of wave number, $k = 2\pi f/c$, during the testing, with the inherent temperature changes associated with delivering air from the compressor and storage tanks. To overcome this difficulty, as briefly discussed previously, an analog servo control was developed using temperature as the control signal. This servo control maintained a constant value of frequency-to-sound speed ratio for temperature variations of ±20°F. The accuracy was better than four decimal places in impressed wave number, k.

VII.3. Data Analysis Methods for Determining Radiation Impedance

The problems of measuring the necessary data for calculation of radiation impedance have been outlined. The technique chosen for determining radiation impedance used the axial standing wave pattern in the duct to determine the reflection coefficient at the duct termination. The impedance was directly determined from the reflection coefficient and the propagation constant, as will be subsequently shown. However, to obtain the appropriate SPL amplitude and phase for a particular mode at each axial measuring station it was necessary to Fourier analyze the data in the circumferential direction. Figures 142(a) and 142(b) are typical of the angular (circumferential) SPL distributions where single mode setups were attempted. In figure 142(a) for a (3,0) mode at 1000 Hertz, from a cursory examination, isolation from the lower order cut-on modes has been achieved. But in figure 142(b) for the (1,0) mode, the distortion in shape and phase is evident. Use of the peak amplitude of the measured angular pressure pattern would not be sufficient to determine the (1,0) mode standing wave ratio. Therefore, the data must be reduced to its Fourier spatial components.

VII.3.1. Fourier analysis of angular pressure distribution

For a pure standing wave, the phase must change by 180 degrees on passing through a nodal point. Any deviation from the 180° phase change is indicative of either a spinning wave component of the same mode shape or other mode contributions. In either case, the pressure wave must be treated as a complex number.



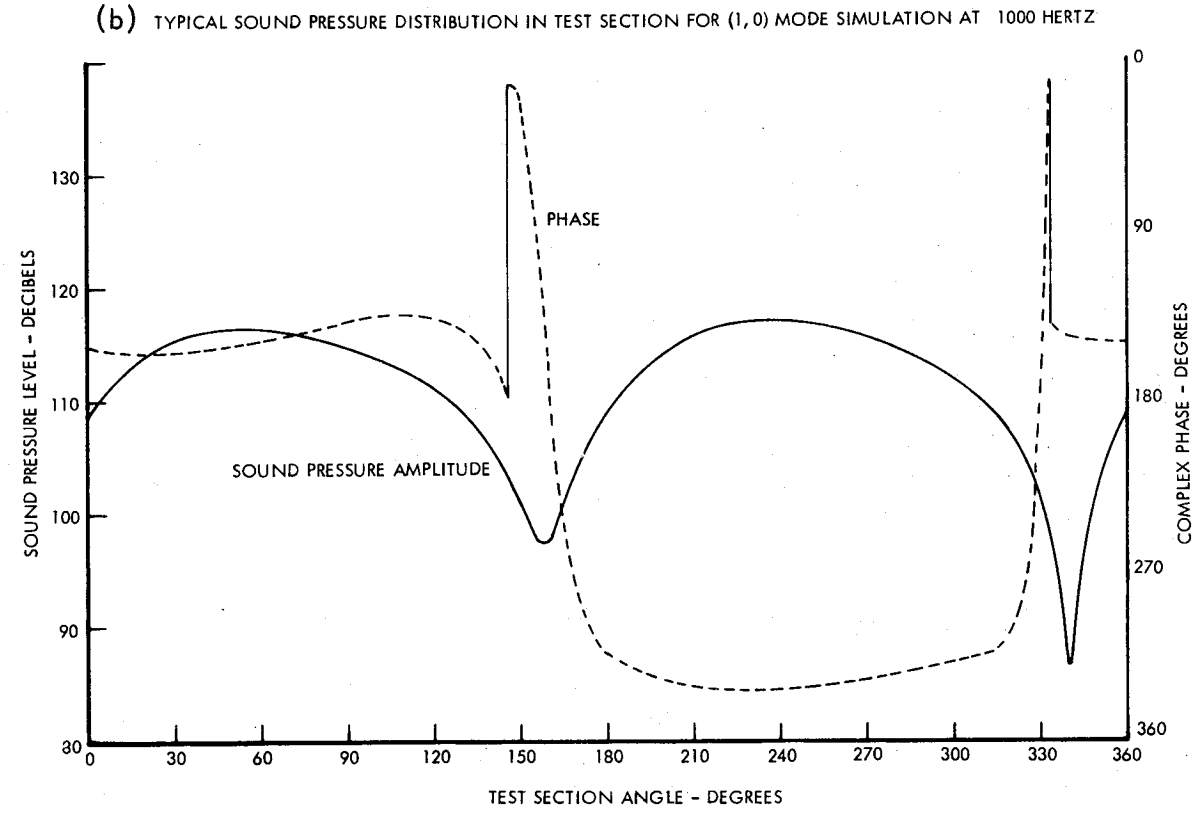


Figure 142. Examples of Angular SPL and Phase Distributions in Hard Wall Test Section

measured plane mode axial standing wave characteristics. The central idea in the higher order impedance technique is to use the peak value of the modal pressure pattern at each axial station to determine the axial pressure wave. Then using an analogy to the plane mode impedance tube methods, the impedance is calculated from the reflection coefficient and an additional factor relating to the propagation constant, β. Also, if the duct contains soft walls, the modal attenuation constant must be included in the duct analysis.

The modal standing wave in the axial direction is determined from the usual assumption of a forward and backward traveling wave set and uses a complex least-square curve fit to find the amplitude of each component. The assumed form of amplitude of the n^{th} mode pressure wave is

$$p_n(z) = A_n e^{k(\alpha_n^f + i\beta_n^f)z} + B_n e^{-k(\alpha_n^b + i\beta_n^b)z} \tag{91}$$

where α_n^f is the modal attenuation in the forward direction

β_n^f is the modal propagation constant in the forward direction

α_n^b is the reflected wave modal attenuation

β_n^b is the reflected wave modal propagation constant

A_n is the amplitude of the incident wave

B_n is the amplitude of the reflected wave.

The least square curve fit criteria were applied, minimizing with respect to the real and imaginary parts of both A_n and B_n, as was done in the spinning/standing wave analysis. In the general case, it would be very difficult to determine the correct values of the set (α_n^f, β_n^f, α_n^b, β_n^b) without some prior knowledge of the expected values. The tests to be discussed later were conducted in a hard walled annular duct and therefore the values of α_n^f and α_n^b were, for all practical purposes, negligible. The values of β_n^f and β_n^b are reasonably well approximated by assuming plug flow, using the average value of flow velocity, in the hard wall, mean flow wave equation. The exact expression for β for a plug-flow situation can be found, for instance, from Mungur and Plumblee (ref. 6). That is

$$K_n^f = \beta_n^f - i\alpha_n^f = \left[\frac{-M \pm \sqrt{M^2 + (1-M^2)\,(1-k_r^2/(kL)^2)}}{1-M^2} \right] \tag{92}$$

and

$$K_n^b = \beta_n^b - i\alpha_n^b = -\left[\frac{-M \pm \sqrt{M^2 + (1-M^2)\ (1-k_r^2/(kL)^2)}}{1-M^2}\right] \tag{93}$$

where M is the mean Mach number and k_r is the eigenvalue. The values of propagation constant determined from above, using the theoretical eigenvalue, were used in the minimization process for determining the amplitudes of the incident and reflected waves.

After determination of the wave amplitudes, the reflection coefficient is determined in the same manner as for the plane mode, i.e., the ratio of the reflected wave to the incident wave,

$$R_n = B_n/A_n \ . \tag{94}$$

VII.3.4. Acoustic impedance calculation

The calculation of radiation impedance in the presence of axial flow requires inclusion of the flow velocity effect on axial acoustic velocity. The momentum equation is, after assuming harmonic motion,

$$\frac{\partial v}{\partial z} - \frac{ikv}{M} = -\frac{1}{\rho c M}\frac{\partial p}{\partial z} \tag{95}$$

The solution yields the usual homogeneous and inhomogeneous parts. The homogeneous solution is of the form, $Ce^{ikz/M}$, which is a convected solution in the form of a frozen pattern. Because of this and its behavior at zero velocity, it is eliminated from consideration. Thus, the solution for acoustic velocity in the nth mode, is

$$v_n = \frac{1}{\rho c}\left\{\frac{A_n(\beta_n^f - i\alpha_n^f)e^{k(\alpha_n^f + i\beta_n^f)z}}{1 - M(\beta_n^f - i\alpha_n^f)} - \frac{B_n(\beta_n^b - i\alpha_n^b)e^{-k(\alpha_n^b + i\beta_n^b)z}}{1 + M(\beta_n^b - i\alpha_n^b)}\right\}. \tag{96}$$

Of course, the n^{th} pressure mode produces velocity components in all other modes, but these components have not been considered in the present analysis. In the data presentation which follows, only angular modes coupled with the zero order radial mode, have been considered. In a detailed examination of the experimental data it was not possible to detect the presence of higher order radial modes at the termination, in the frequency range considered for these tests (i.e. below 1600 Hertz).

At the end, $z = 0$, the normalized acoustic modal radiation impedance is expressed as the ratio of modal pressure to modal velocity in the n^{th} mode,

$$Z_{rad_n} = \frac{P_n}{\rho c v_n} = \frac{1 + R_n}{\dfrac{(\beta_n^f - i\alpha_n^f)}{1 - M(\beta_n^f - i\alpha_n^f)} - \dfrac{(\beta_n^b - i\alpha_n^b)R_n}{1 + M(\beta_n^b - i\alpha_n^b)}} . \tag{97}$$

If the duct walls are non-attenuating and the flow velocity is zero, the above equation reduces to the usual form,

$$Z_{rad_n} = \frac{1 + R_n}{\beta_n(1 - R_n)} . \tag{98}$$

The general expression in equation (98) was programmed for the determination of modal termination impedance, utilizing the values of reflection coefficient, R_n, determined from the least-square minimization process.

VII.3.5. Optimization of propagation constant

As discussed earlier in this section, the theoretical value of propagation constant, β, was used to determine the axial pressure pattern via the least-square curve fit. In some cases, it is evident that a longer or shorter wave-length, corresponding to different values of β, would yield a closer fit to the measured data. As a means of determining the accuracy of the curve fit, and the appropriateness of the theoretical propagation constants, the "standard error of the estimate" (the square root of the "sample variance") was computed. This computation used the sum of the square of the differences between the measured amplitude and the computed amplitude. Phase differences were not included in the estimate, but could easily be incorporated. The expression for the error is,

$$E = \sqrt{\frac{\sum_{i=1}^{I} \left[L_n(x_i) - \overline{L}_n(x_i) \right]}{I}} \tag{99}$$

where $L_n(x_i)$ is the measured SPL at the i^{th} axial station and $\overline{L}_n(x_i)$ is the 'least-square' SPL at the i^{th} axial station.

In attempting to determine the best value of β to fit the measured data, the curve-fit routine was used repetitively and values of β_n^f and β_n^b, corresponding to values computed from equation 97 for incremental values of k_r, were used. The error, E, was examined for each computation and the pair of β values which produced the minimum error was taken as the optimum set.

This procedure appears to be inherently sensitive to experimental error, since one bad data point could result in a minimized value of error at a cut-on frequency (or wavelength) significantly removed from the actual value. After examining the impedance results obtained from the optimization process, the impedance data calculated using theoretical cut-on frequency and theoretical values of β were chosen as being most representative. However, in the data presentation which follows, the computed axial standing wave pattern corresponding to both the theoretical and minimized values of β are shown. Also, the values of impedance corresponding to both values of β will be given in some cases.

VII.4. Experimental Values of Radiation Impedance and Comparison with Theory

In the experiments conducted, radiation impedance was experimentally determined at 5 frequencies. This obviously does not yield enough data for experimental verification of the detailed shape of the computed radiation impedance curves, but the data is sufficient for verifying the validity of the technique and to confirm the trends predicted by the theory.

First, it is of interest to examine the axial wave forms determined from the measured data. These are shown in figures 143(a) through (143(f). Figure 143(a) shows data measured at 1000 Hertz ($kR_0 = 4.4205$) for 32 measurement locations. In this particular case for the (1,0) mode, the standard error of the estimate, E, is only 0.25 dB, which is considered to be sufficiently accurate to determine the radiation impedance within 1-2%. Also in this instance, the β at which minimum error, E, occurs corresponds to the theoretical value of β of 0.953. In figures 143(b), 143(c) and 143(d) the measured data and calculated sound pressure patterns in the duct are shown for the plane, (2,0) and (3,0) modes for 150 fps flow velocity.

In this series of tests, fewer axial measuring points were used in order to reduce time required for the tests. This series of figures depicts the increase in wavelength with increasing mode number at constant frequency (equivalent to a decrease in β). In addition to the axial pressure pattern at the theoretical values of β, the pressure distribution calculated at the minimum error β is shown in figure 143(d) (dashed line). This difference in propagation constant results in a 25% difference in impedance magnitude. No firm conclusion was reached on whether it would be more accurate to use the impedance determined at minimum error or to use the values calculated at the theoretical propagation constant. However, all results presented will correspond to values at theoretical β, since the comparison of cut-on frequency,

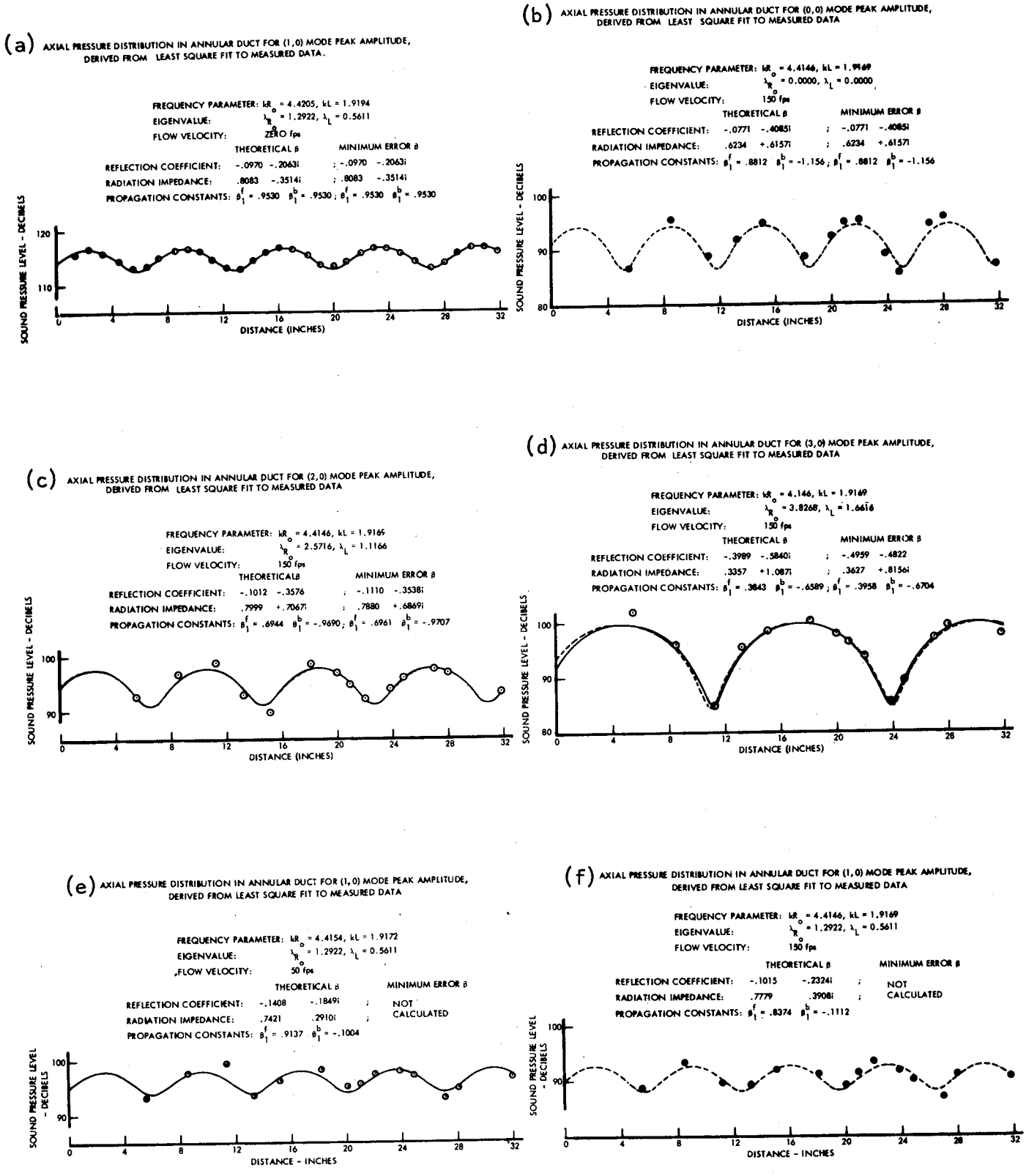


Figure 143. Examples of Axial Standing Waves in Annular Duct Showing Effects of Mode Number and Velocity

which implicitly validates the theoretical β, was so exceptionally good. It must be remembered that the amplitudes shown in the previous series of figures at each axial station were derived from the complex Fourier analysis. Thus, there are many manipulations performed on the data, before arriving at the calculated reflection coefficient and radiation impedance. It would certainly not be unusual to expect an error of the order of ± 1 dB as a result of all the data handling. Thus, the value assigned to β as a result of the minimization process is possibly dominated by the random, but small, errors introduced by the data analysis. This reasoning predominated in selecting the theoretical β as the value for use in determination of radiation impedance.

The effect of flow on the axial standing wave patterns is shown in figures 143(a), 143(e) and 143(f). The first thing to note is the calculated effect on the wavelength constants, β_1^f and β_1^b. Without flow, $\beta_1^f = 0.953$ and $\beta_1^b = -0.953$, but at 150 fps the values of wavelength constant are $\beta_1^f = .837$ and $\beta_1^b = -1.112$. Next, examination of the standing wave pattern does not reveal any significant differences, but the computed reflection coefficients and radiation impedances do reveal a trend. The change in the reactance is most significant, changing from -0.35 at zero flow to +0.39 at 150 fps. It is felt that the data at 50 fps have been significantly influenced by the data at stations 12, 18 and 27. These deviations from the standing wave curve, determined by least-squares, result in a sample variance of 1.1 dB, while at no flow the variance was 0.24 dB and at 150 fps the variance is 0.84 dB.

All the data for radiation impedance is summarized in table XV. This comprises three test series (i.e., 0, 50 fps and 150 fps flow velocity) for five modes, each at five frequencies, where possible. It was not, however, possible to determine the radiation impedance of modes below cut-on frequency. Thus the number of values decreases with increasing frequency. The data presented in the following section are plotted against a non-dimensional frequency which is referenced to the mode cut-on frequency in the nomenclature suggested by Morfey (ref. 26). Thus, this parameter is included in the tabulation for each velocity, indicating the minor change in the eigenvalue, k_r, with velocity. The most informative data in the tabulation is the sample variance, which is a good indication of the deviation of the data from the computed axial standing wave. This variance varies from a low of 0.25 dB to a high of 18.1 dB, but with the majority of data below 3 dB variance and only two error values above 5 dB.

Measured values of radiation resistance and reactance are compared with the values calculated from Haddle's (ref. 25) method, for a flanged annulus, for the (1,0), (2,0) and (3,0) modes in figure 144. The calculations, using Haddle's program were made for a hub-tip ratio of 0.566, corresponding to the experimental facility dimensions.

While the measured resistance values do not duplicate the predicted values, the agreement is close and differences are attributed (1) to differences between the physical set-up and the theoretical model and (2) to experimental error. The theoretical model assumes a flanged annulus, while the facility termination is unflanged.

TABLE XV

RADIATION IMPEDANCE CALCULATED AT THEORETICAL β BY LEAST-SQUARES METHOD

				NO FLOW				50 fps						150 fps					
APPROXIMATE FREQ, Hz	NORM FREQ, k	MODE NO.	β	$kR_o - k_r R_o$	R	X	SAMPLE VARIANCE dB	β^f	β^b	$kR_o - k_r R_o$	R	X	SAMPLE VARIANCE dB	β^f	β^b	$kR_o - k_r R_o$	R	X	SAMPLE VARIANCE dB
346.6	1.9491	0,0	±1.0	1.54	.3764	.6138	2.69	.9570	-1.047	1.54	.2877	.6193	0.28	.8096	-1.1562	1.54	.3215	.6429	1.10
566.7	3.1823	0,0	±1.0	2.51	.6334	.2864	0.98	.9572	-1.0468	2.51	.4881	.3702	0.53	.8817	-1.1550	2.51	.5005	.4529	0.57
845.8	4.7468	0,0	±1.0	3.74	.4689	.6809	2.29	.9572	-1.0469	3.74	.5035	.6066	1.97	.8814	-1.1555	3.74	.4135	.5554	1.01
1000.0	5.6144	0,0	±1.0	4.40	.5796	.6492	0.50	.9571	-1.0469	4.40	.7084	.9144	1.06	.8812	-1.1558	4.40	.6234	.6157	1.15
1350.0	7.5853	0,0	±1.0	5.94	.7349	-.0643	2.56	.9571	-1.047	5.94	1.200	.5666	3.19	.8811	-1.1560	5.94	.366	.124	8.18
346.6	1.9491	1,0	.5466	0.21	.2495	.4757	2.58	.5040	- .5940	0.21	- .1218	.4476	1.41	.4318	- .7071	.22	- .2681	.5696	1.32
566.7	3.1823	1,0	± .8584	1.18	.4471	.7296	0.36	.8157	- .9052	1.18	.4363	.8416	0.59	.7404	-1.0137	1.19	.3364	.8732	1.10
845.8	4.7468	1,0	± .9390	2.40	1.204	1.043	3.12	.8962	- .9859	2.42	.9249	.6720	1.72	.8204	-1.0946	2.43	1.1233	.6249	2.14
1004.7	5.5838	1,0	± .9530	3.08	.8083	.3514	0.24	.9168	-1.0066	3.08	.7439	.2928	1.11	.8374	-1.112	3.09	.7779	.3908	0.84
1350.0	7.5853	1,0	± .9766	4.67	.4736	.2948	2.88	.9336	-1.0236	4.67	.3559	.7080	4.75	.8777	-1.1326	4.68	.6203	-1.469	11.8
845.8	4.7468	2,0	± .7292	1.16	.5879	1.1872	2.17	.6864	- .7761	1.16	.4505	1.2978	1.67	.6114	- .8855	1.18	.5316	1.069	1.81
1000.0	5.618	2,0	± .8156	1.85	.9380	.7746	0.96	.7700	- .8599	1.85	1.071	.8390	0.91	.6944	- .9690	1.87	.7999	.7067	0.77
1350.0	7.5853	2,0	± .9037	3.40	.8846	.6073	4.27	.8607	- .9507	3.41						3.43			
1000.0	5.6441	3,0	± .4896	0.61	.3118	1.218	1.20	.4565	- .5463	0.62	.3958	1.330	0.98	.3543	- .6589	.65	.3357	1.0666	1.00
1350.0	7.5853	3,0	± .7706	2.15	1.6801	1.235	4.24	.7277	- .8177	2.15	1.383	1.085	3.16	.7927	-1.0676	2.18	.2009	.4632	16.1
1350.0	7.5853	4,0	± .5307	0.92	1.586	1.893	2.29	.4881	- .5781	0.92	1.184	2.560	2.58	.4150	- .6899	.96	.5632	3.036	3.84

Experimental Values from Unflanged Annulus with Hub-Tip Ratio of 0.566

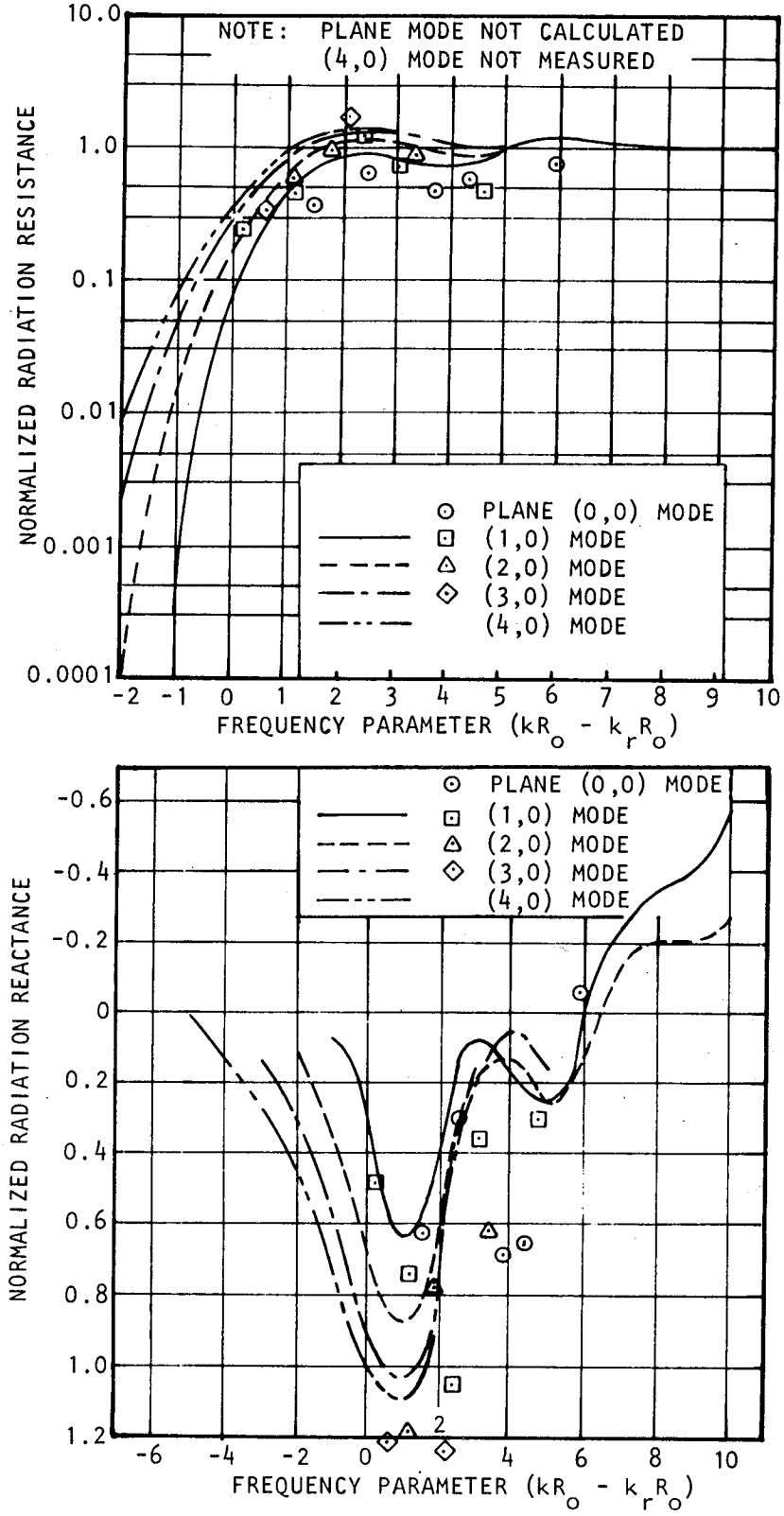


Figure 144. Comparison of Experimental and Theoretical Values of Radiation Impedance for a Flanged Annulus

The differences between measured and calculated values of reactance are much greater and in fact do not follow the calculated values. However, the trends predicted appear to be much the same and the major difference appears to be the result of a frequency shift in the peak values of reactance. There is enough experimental data to indicate that the shape of the predicted reactance behavior with frequency is similar to the measured shape. The frequency shift in the peak is believed to be due to the difference between the flanged theory and the unflanged experiment.

The measurements shown in the previous two figures were repeated at 50 and 150 fps. Figures 145(a) to 145(f) show the comparison of the data and theory. In examining the measured data, it is first noted that the measured resistance values for the (1,0) mode with flow are negative. This is to be expected for small values of kR_p as discussed by Mechel et al (ref. 54). The effect of flow is to increase the reflected pressure when the incident wave is in the direction of flow. The reflected energy is not greater than the incident energy (i.e., there is no sound source at the duct termination). However, the flow changes the phase relationship between sound pressure and acoustic velocity, thus to maintain the reflected energy, the pressure amplitude increases with the phase change. Another way of describing it would be to say that the reflected incident pressure wave is "convectively amplified," while the incident wave is "convectively attenuated." Therefore, the convective effects on pressure result in a negative radiation resistance. At higher frequencies, the effect of flow seems to result in increased peaks and dips in radiation resistance curve. The radiation reactance data are not accurate enough to attempt a qualitative assessment of the effects of flow.

VIII. RADIATED FIELD

The level and spatial distribution of the radiated field resulting from an acoustic field in a duct has been studied relatively little, especially in respect to the effects of jet velocity. There is no theoretical study known at present which allows for calculation of the radiated field from a duct mode or a complex pressure distribution as it radiates through a jet flow.

A need exists for experimental data with which to compare against theoretical predictions, as the prediction techniques emerge in the next few years. Also, comparison with the radiation theory predictions without jet flow is an equally important requirement. Thus, this section presents a series of measured radiated field patterns correlated with the in-duct conditions. In all cases presented, an attempt has been made to define the condition at the end of the duct. In some cases, where modes are excited in relative isolation, an angular SPL plot at one radial location at the duct termination provides adequate definition of the in-duct condition. In other cases, where multiple modes were excited, a complete tabulation of the individual mode amplitudes and phase, as well as the angular position of the mode in the duct (in the case of higher order stationary modes), relative to the plane of the radiated field measurement is given. Also, in this case, the reflection coefficient and the radiation impedance is tabulated for future reference.

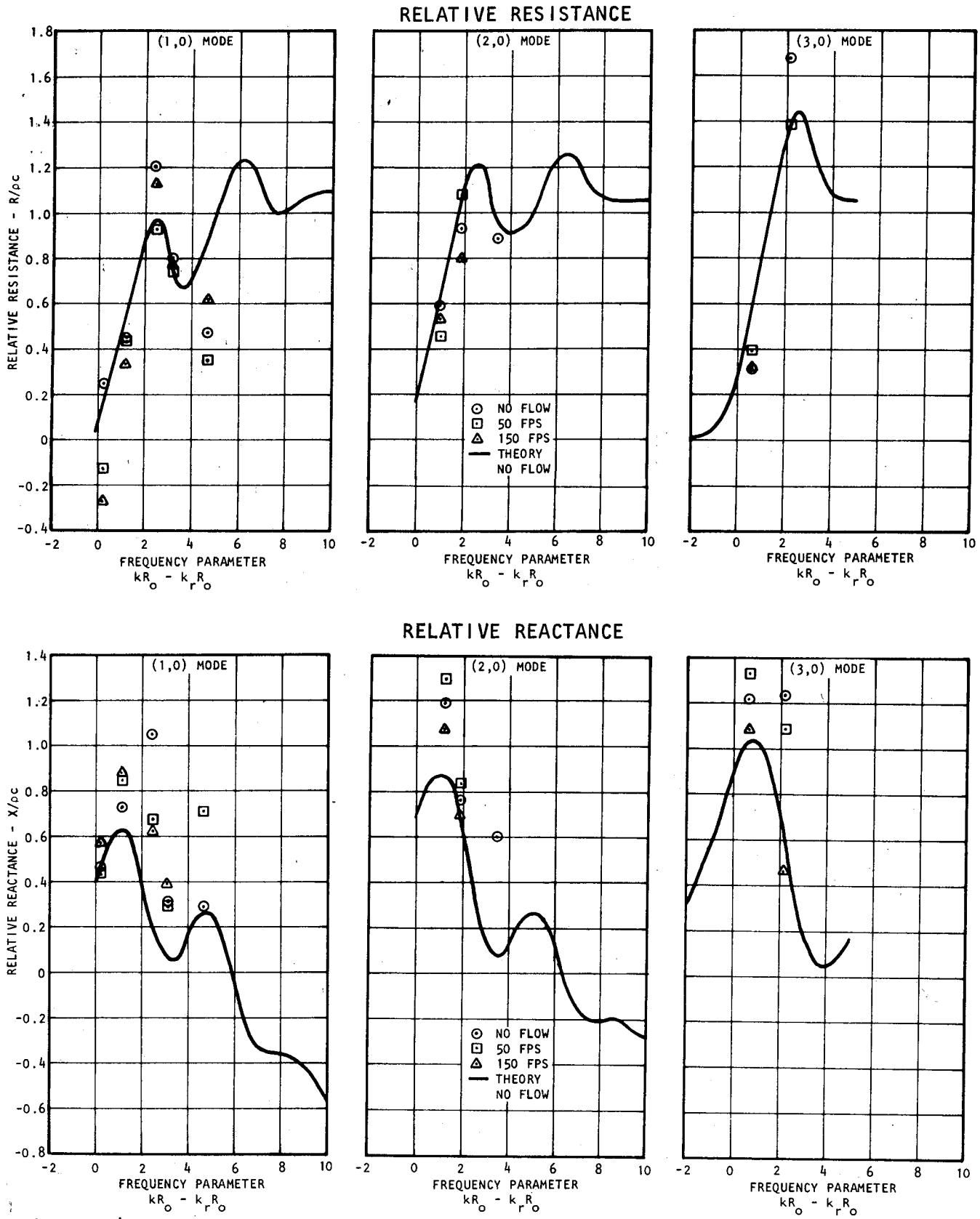


Figure 145. Effects of Flow Velocity on Radiation Impedance of an Annulus for Various Modes

The primary variables are mode order, velocity and wave number. The most complete series of tests were run with multiple mode excitation. These were restricted to the zero order radial mode, but extend through the (4,0) angular mode. Since the modes are primarily stationary angular modes, the level in the radiated field is directly related to the radiated field microphone boom plane position, relative to the angular position of the stationary mode in the duct. The radiated field solution has an $e^{im\phi}$ characteristic shape, where ϕ is the circumferential angle around the duct axis.

It is recognized that the data to follow is not complete in scope, but is hoped that enough exists to act as a guide in formulating new theoretical concepts. Certainly, enough data will be presented to serve as a check for initial analytical efforts in this field of study.

VIII.1. Description of Experiment

The noise radiated from the duct termination was measured in an anechoic room as shown in figures 1, 3, and 6. The boom on which the microphone was mounted traversed a 124 inch radius from the center of the duct termination. The configuration is shown in figure 146. The boom was driven by a variable speed electric motor and angular position was monitored by a linear potentiometer. The microphone probe was the same configuration as shown in figure 64, in order to minimize the effects of the jet flow velocity on the acoustic measurement.

The duct reference angle for the stationary angular modes is shown in figure 147. In the tabular data which is included with each figure, the position of the first node in a clockwise direction, from $\theta = 0$, is listed.

The jet flow was a rather odd flow, since it had a hole in the middle in the mixing region. This is a result of only having flow in the annular section. The mean flow characteristics of the jet were not measured. The flow velocity given is that at the exit plane of the annular duct.

Measurements below 500 Hertz are questionable, since the polyurethane foam pads on the walls were effectively anechoic only above this lower frequency limit.

VIII.2. Experimental Results

VIII.2.1. Effect of mode number and flow velocity at a fixed frequency

Figures 148-151 are a series of radiated field plots for angular stationary modes in relative isolation. The components of other modes in each case is given in part (a) of the figure, which illustrates the SPL angular distribution in the duct.

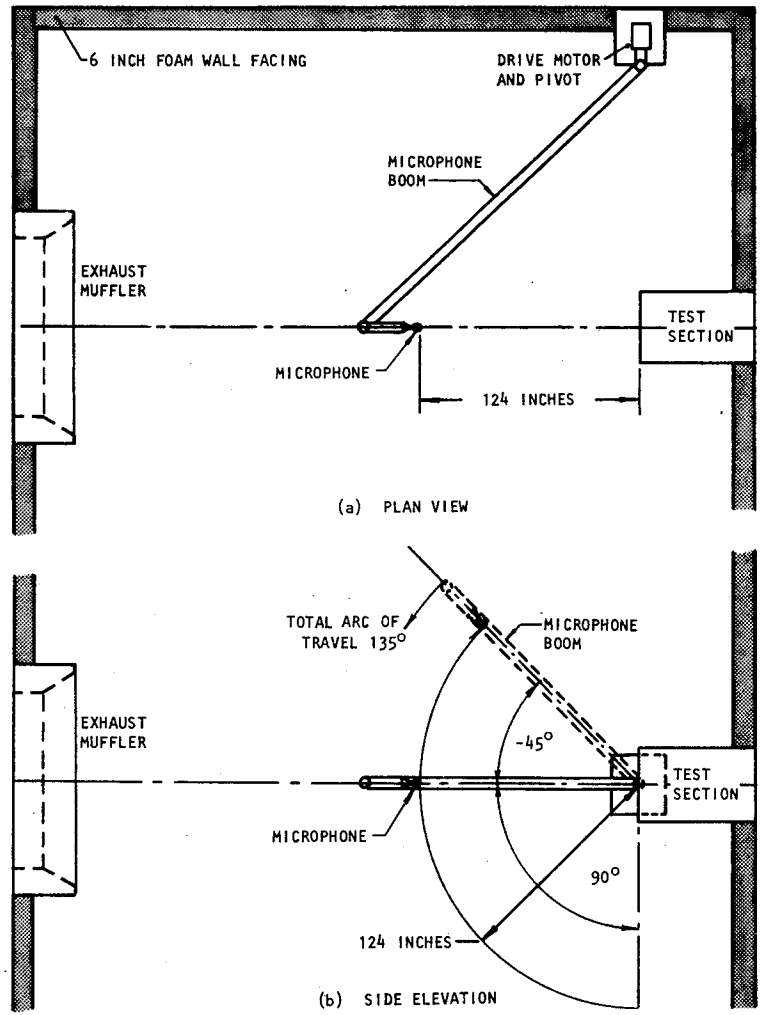
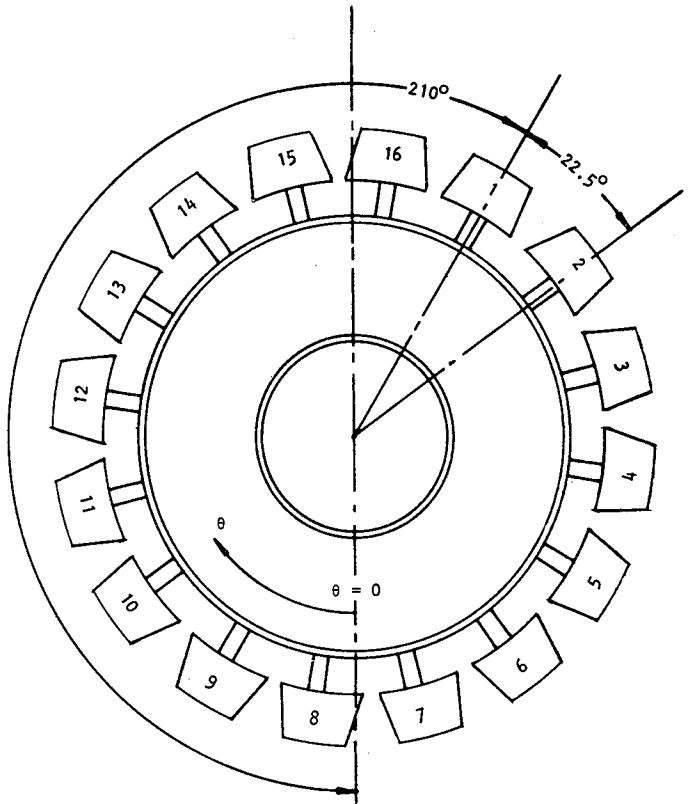
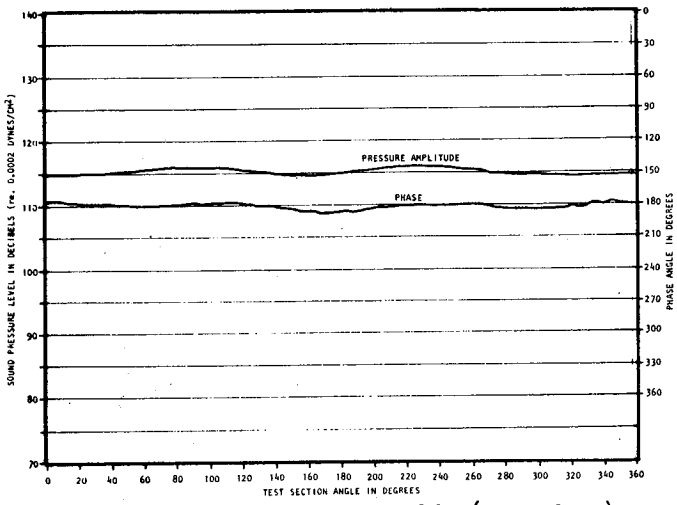


Figure 146. Schematic of Microphone Boom Arrangement for Measuring Radiated Sound Field

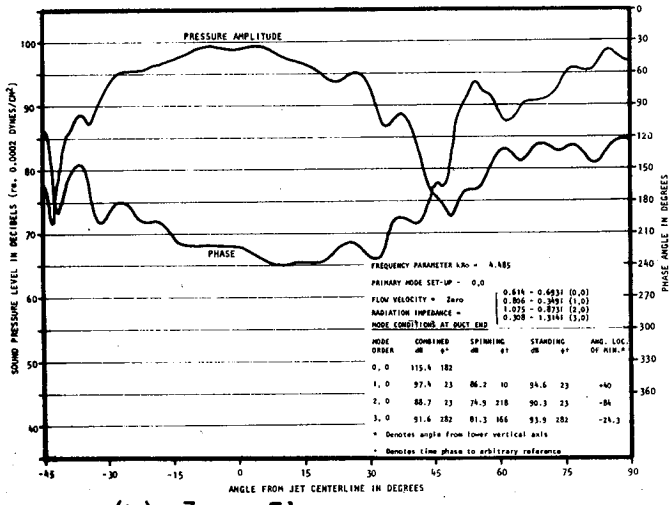


View Looking into End of Test Section from Anechoic Room

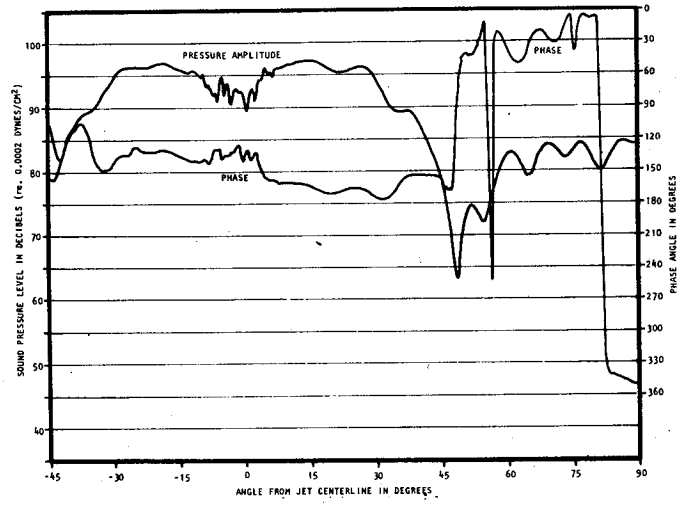
Figure 147. Duct Co-ordinates.



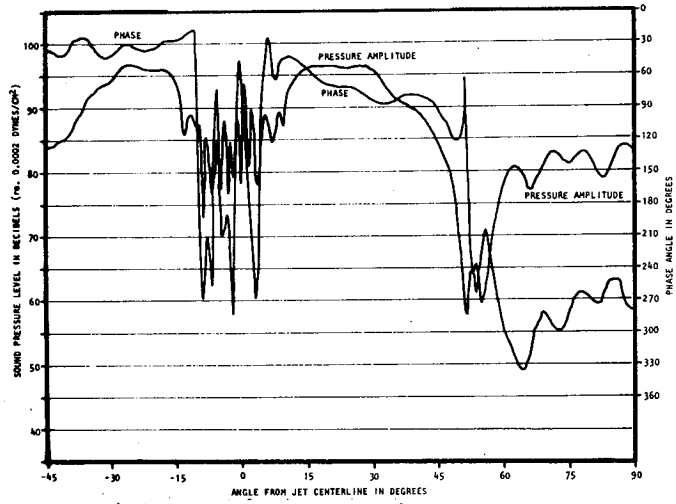
(a) Duct End at Outer Wall (No Flow)



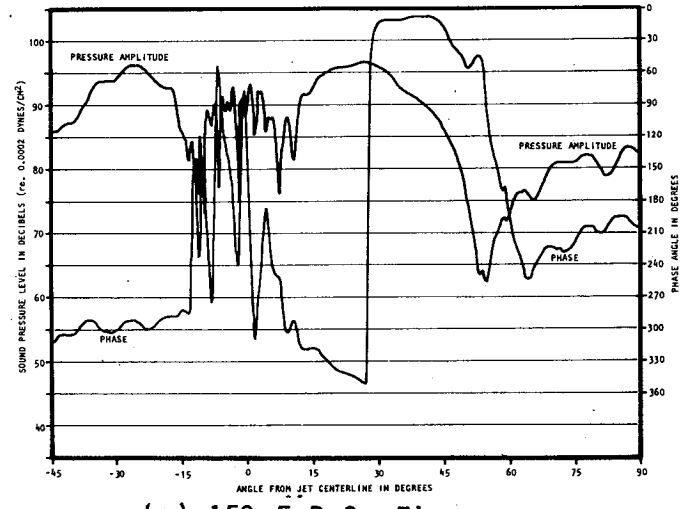
(b) Zero Flow



(c) 50 F.P.S. Flow

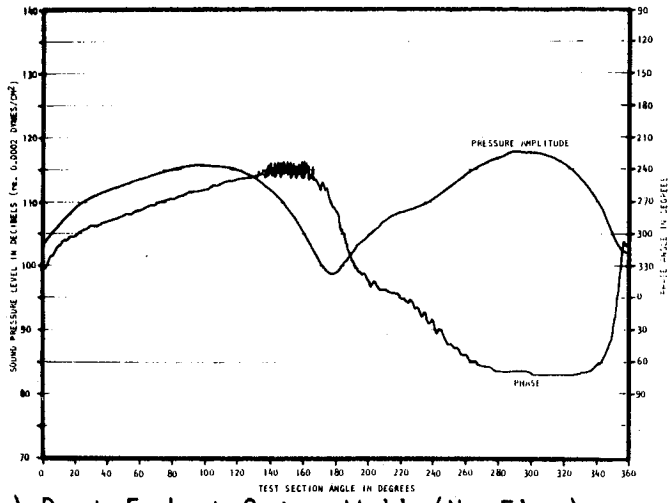


(d) 100 F.P.S. Flow

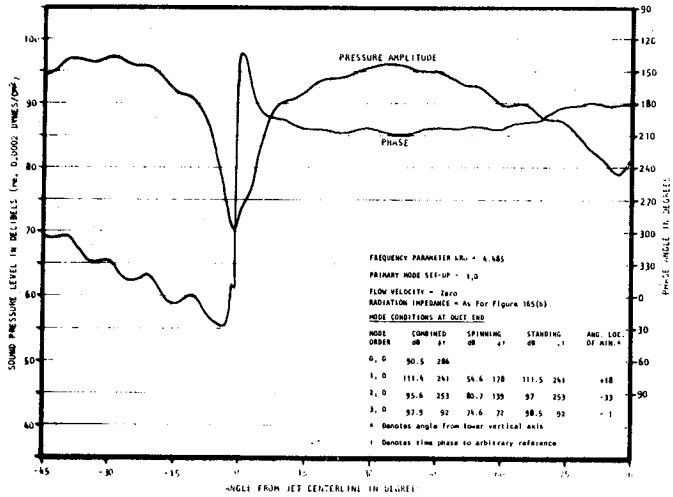


(e) 150 F.P.S. Flow

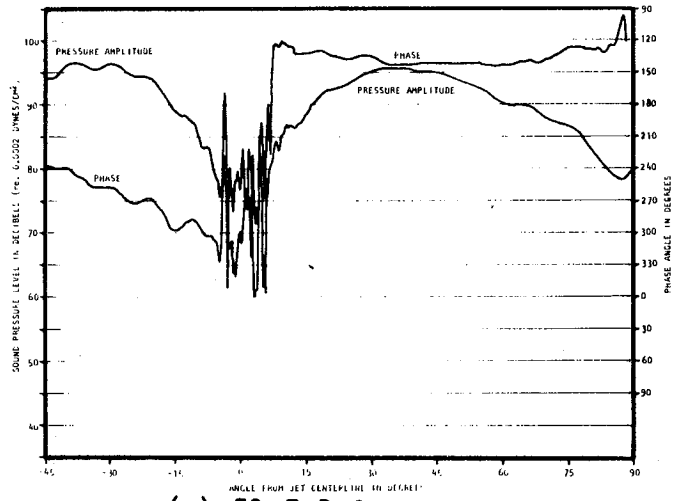
Figure 148. **Duct Exit and Radiated Field Patterns of (0,0) Mode, k Ro = 4.485**



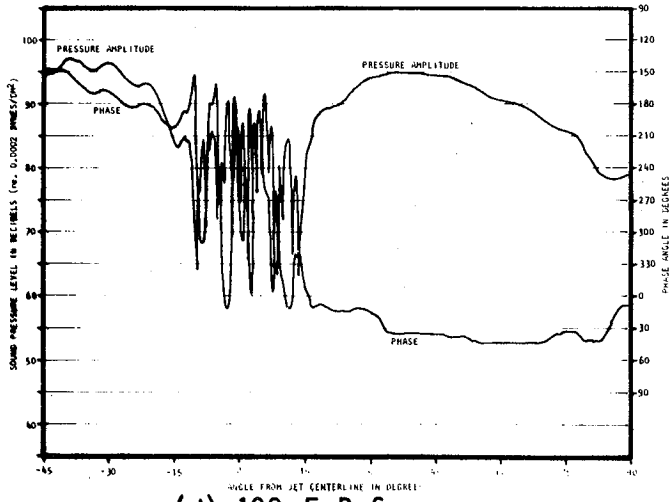
(a) Duct End at Outer Wall (No Flow)



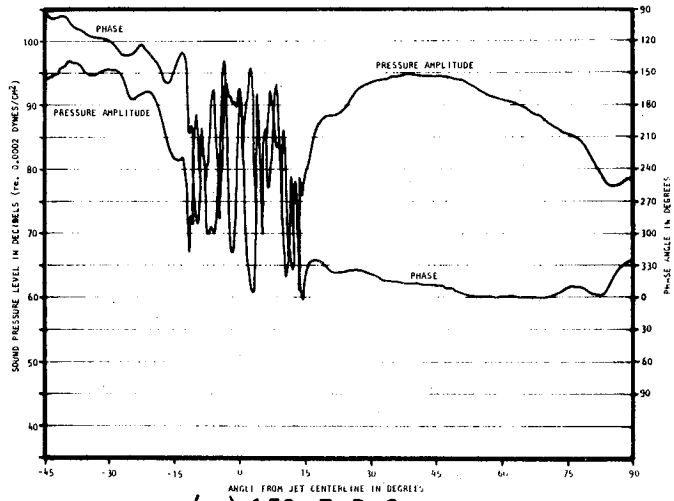
(b) Zero Flow



(c) 50 F.P.S.

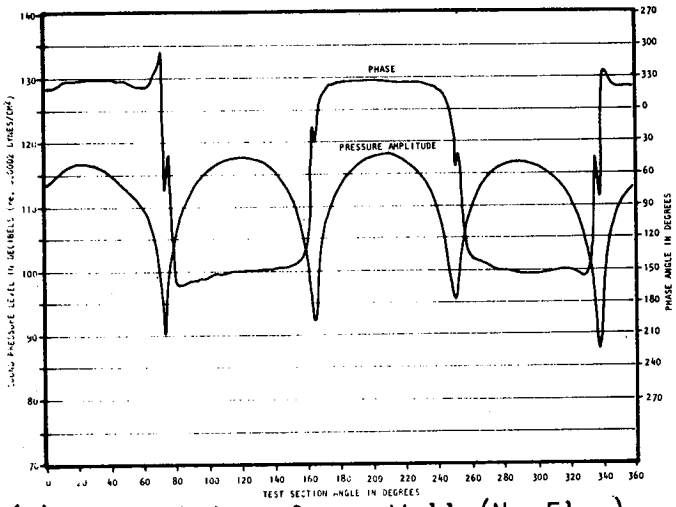


(d) 100 F.P.S

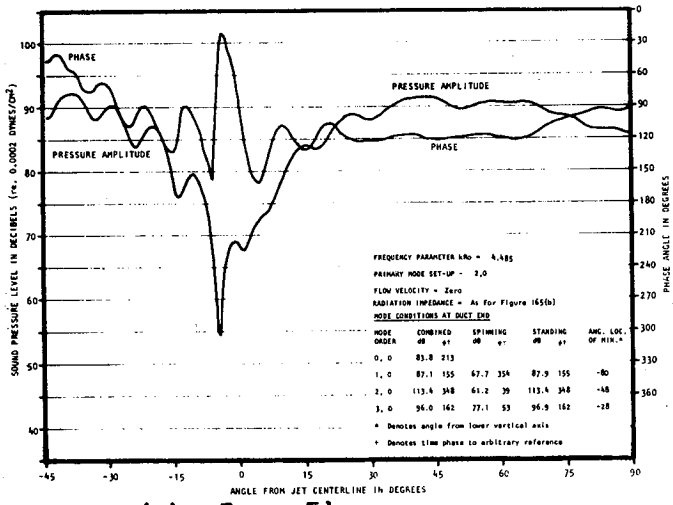


(e) 150 F.P.S.

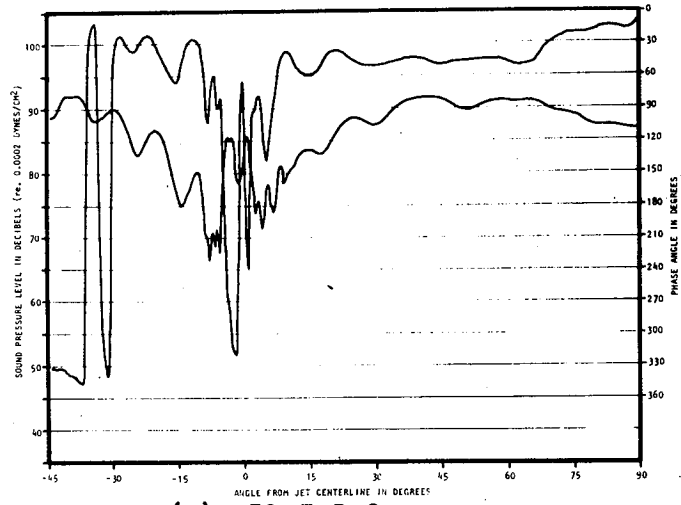
Figure 149. Duct Exit and Radiated Field Patterns of (1,0) Mode, k Ro = 4.485



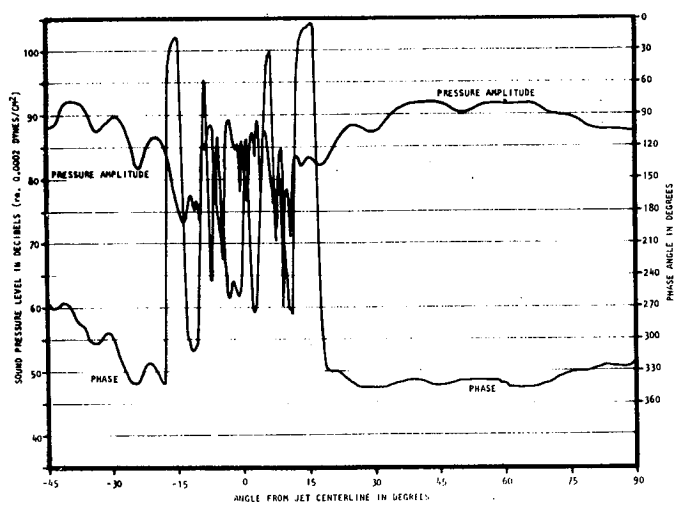
(a) Duct End at Outer Wall (No Flow)



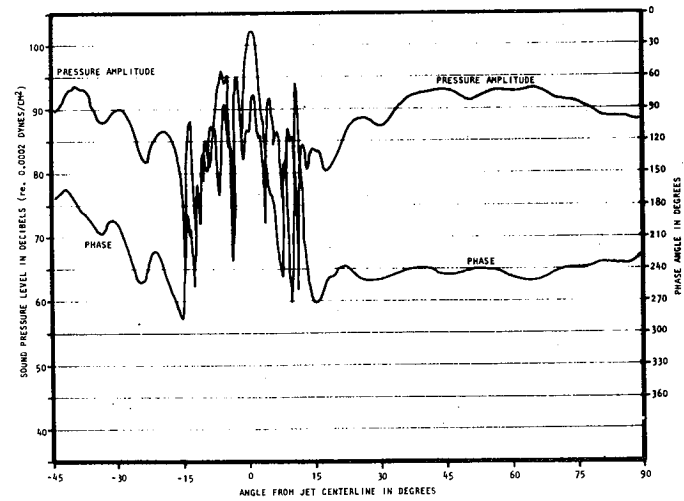
(b) Zero Flow



(c) 50 F.P.S.

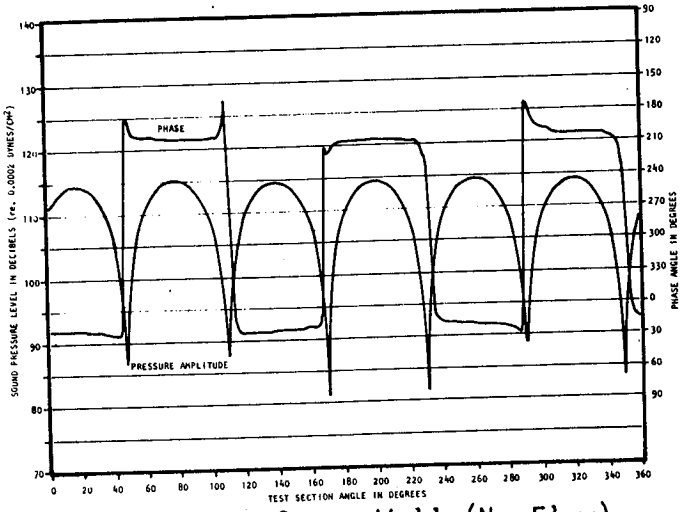


(d) 100 F.P.S.

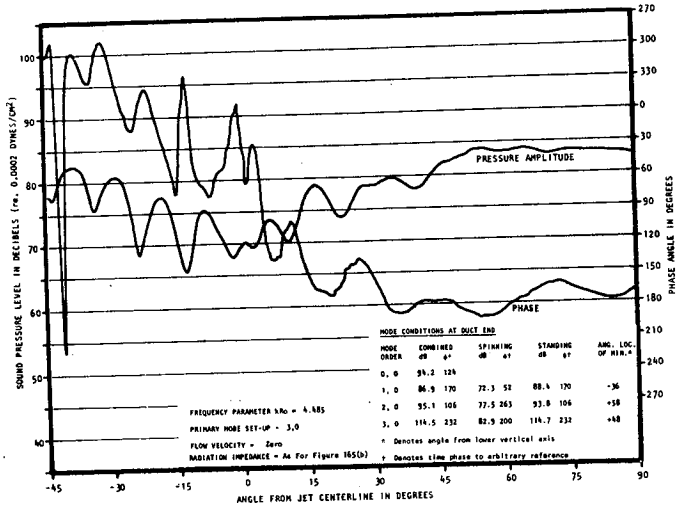


(e) 150 F.P.S.

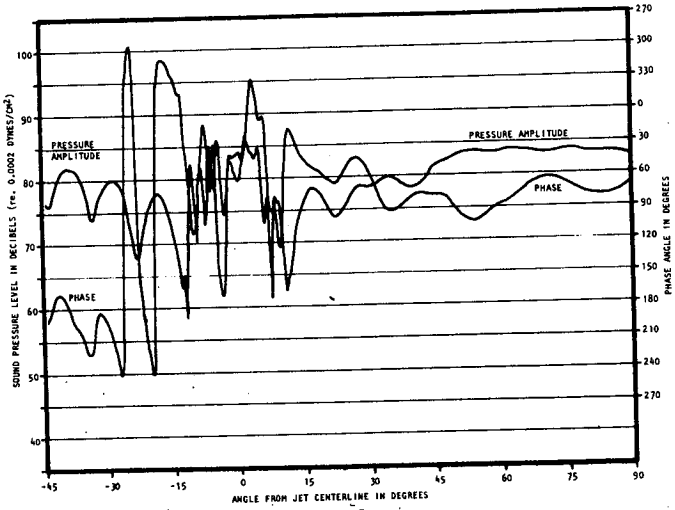
Figure 150. Duct Exit and Radiated Field Patterns of (2,0) Mode, k Ro = 4.485



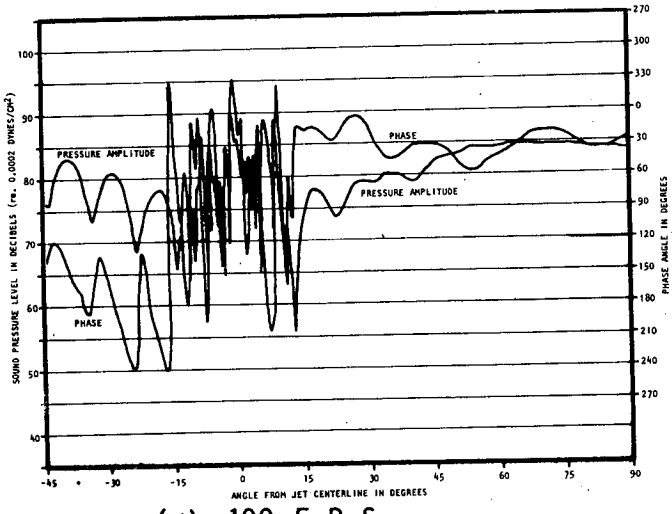
(a) Duct End at Outer Wall (No Flow)



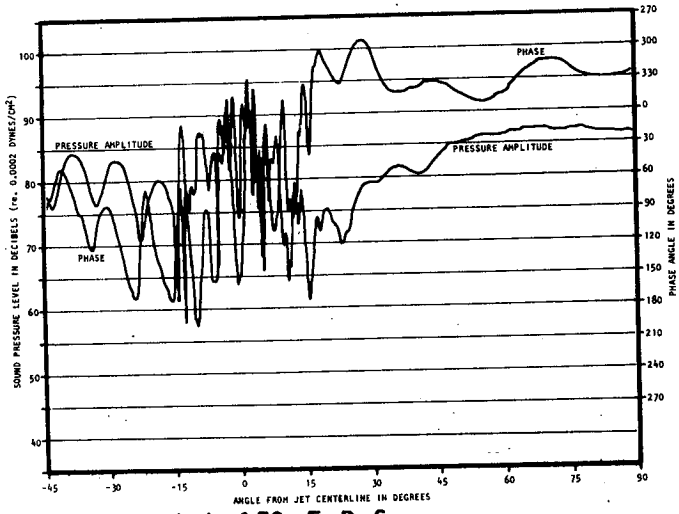
(b) Zero Flow



(c) 50 F.P.S.



(d) 100 F.P.S.



(e) 150 F.P.S.

Figure 151. Duct Exit and Radiated Field Patterns of (3,0) Mode, k Ro = 4.485

In observing the effect of mode number on the radiated field, it is seen that the plane mode is the most effective radiator; but the main plane mode power is on the axis. As the order of the mode is increased, the SPL at 90° to the axis increases significantly.

The primary effect of jet flow is to refract the sound away from the jet axis. Thus, it would be expected that jet flow would have the greatest influence on the plane mode since it is the only mode with a no-flow peak radiation angle on the jet axis. This is observed to be correct, as can be seen by careful examination of figures 148-151. A replot of the amplitude in these figures is condensed in figure 152(a)-(d) in the form of polar plots. This vividly illustrates the refractive effect of flow, particularly for the plane mode.

VIII.2.2. Effect of Frequency and Multiple Modes

Another series of tests was conducted in order to demonstrate the effect of both frequency and multiple modes on the radiated field pattern and efficiency. These data are shown in figures 153-157 from zero to 200 fps in increments of 50 fps. The results are similar to those of the previous sub-section. However, the presence of the multiple modes makes the pressure patterns non-symmetrical about the duct axis.

The effect of flow is the same as in the previous sub-section at 1000 Hertz, however, in this series of tests, the radiated sound is of less intensity (the efficiency is lower). Thus, as the flow velocity increases, the turbulent pressure in the flow controls the microphone output when it resides in the flow at the low frequencies. It is obvious, however, that as frequency is increased, the refractive action due to the jet flow becomes more pronounced. For the 1356 Hertz test in figure 157, refraction has reduced the level by some 14-15 dB at 15° off the jet axis, with a 2 dB increase observed in the region of 50-60° off the axis.

The general refractive effect of jet flow, as observed in analytical studies on point source radiation, is to redirect the acoustic energy. This is the action generally observed in the experimental data.

A final note of caution is in order concerning use of the experimental radiated field data. The pressure inside the flow region, which at 200 fps is effectively ±14 degrees about the jet axis, is not due to the sound field radiating from the duct. It is instead a pressure due to the turbulence in the flow. Thus, data in this region should be ignored, when studying the refractive effects due to flow velocity.

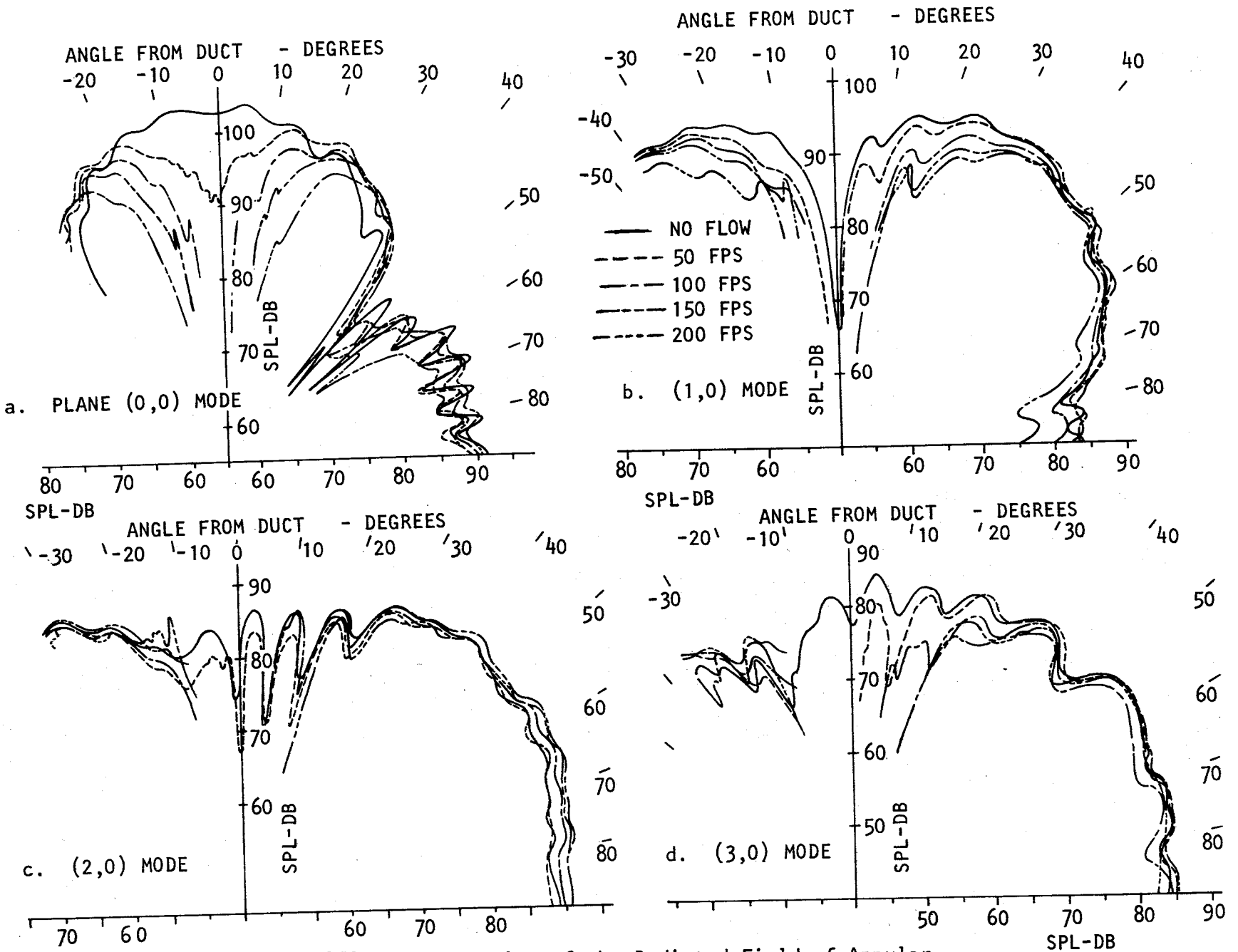
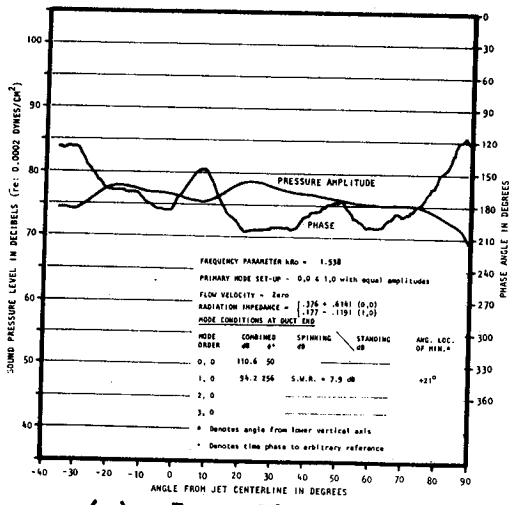
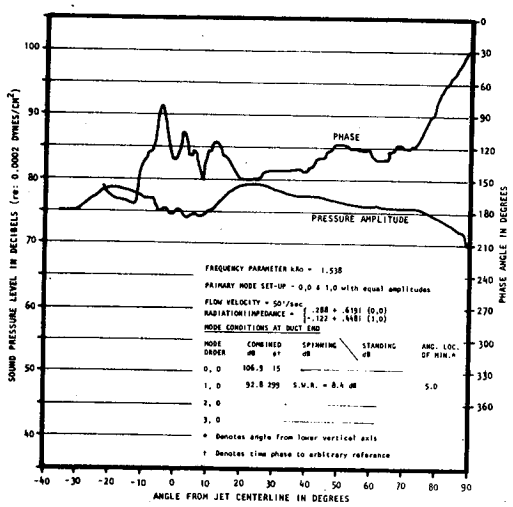


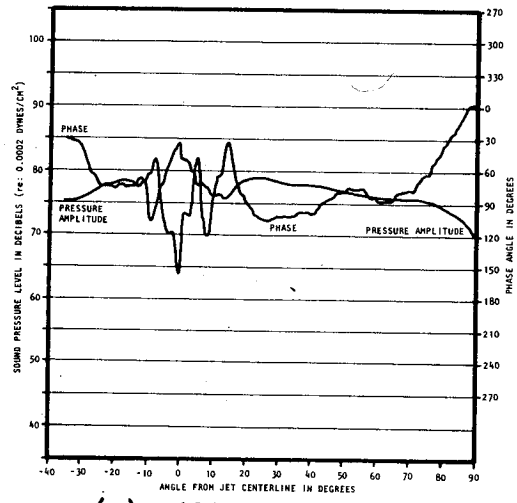
FIGURE 152. Summary plot of the Radiated Field of Annular Duct Modes Showing the Effects of Flow and Angular Mode Order at 1000 Hertz



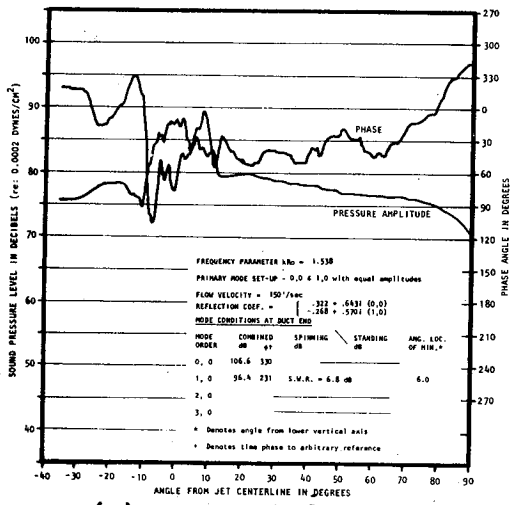
(a) Zero Flow



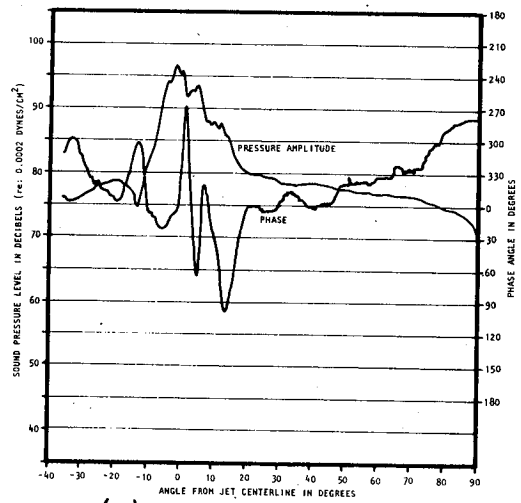
(b) 50 F.P.S.



(c) 100 F.P.S.

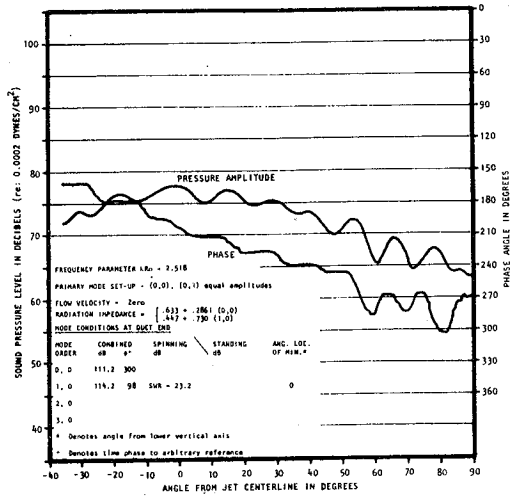


(d) 150 F.P.S.

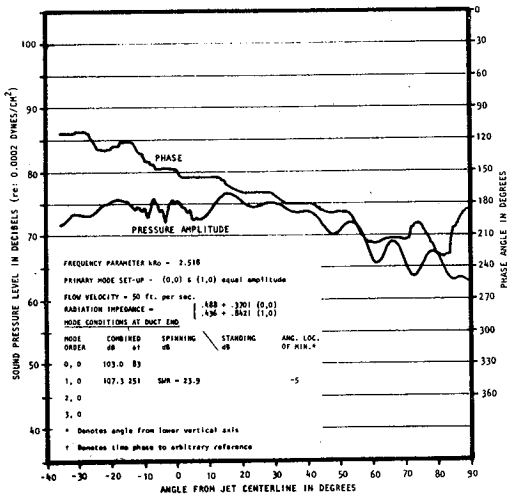


(e) 200 F.P.S.

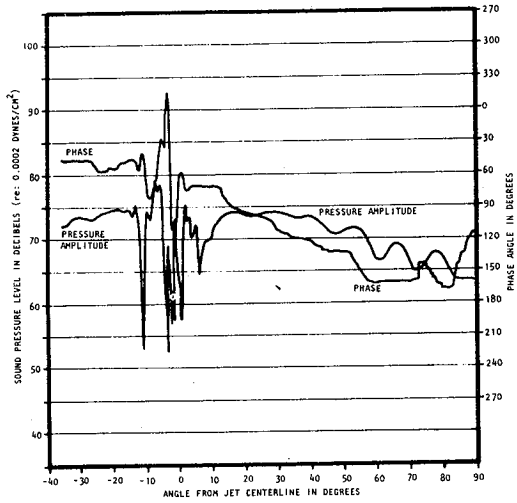
Figure 153. **Duct Exit and Radiated Field Patterns for (0,0) + (1,0) Equal Mode Combination, k Ro = 1.538**



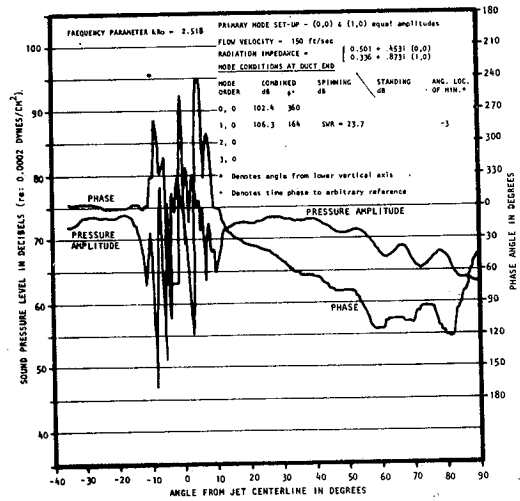
(a) Zero Flow



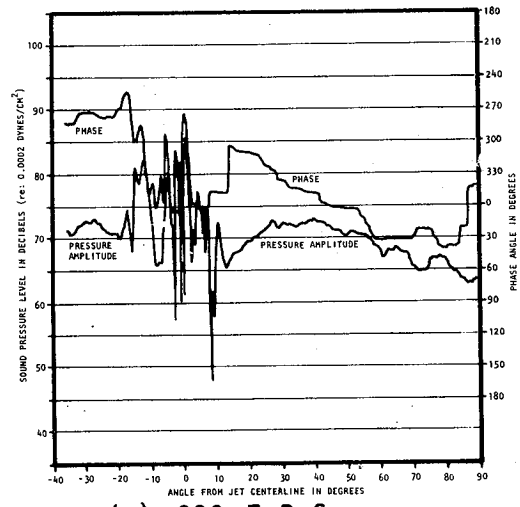
(b) 50 F.P.S.



(c) 100 F.P.S.

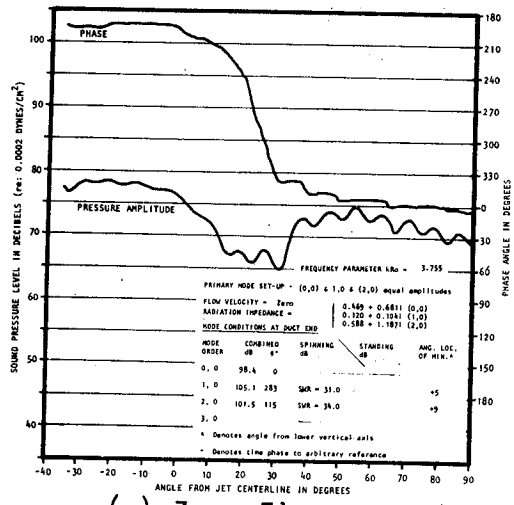


(d) 150 F.P.S.

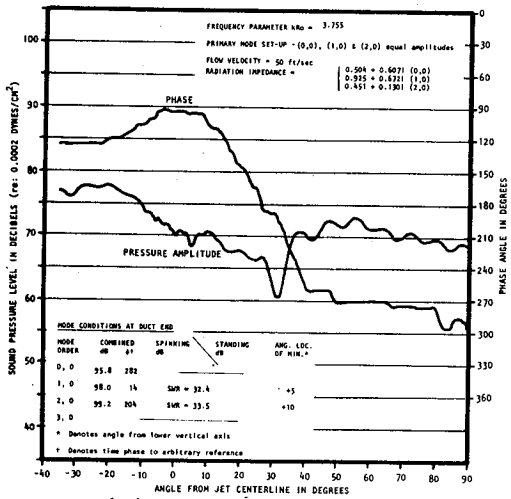


(e) 200 F.P.S.

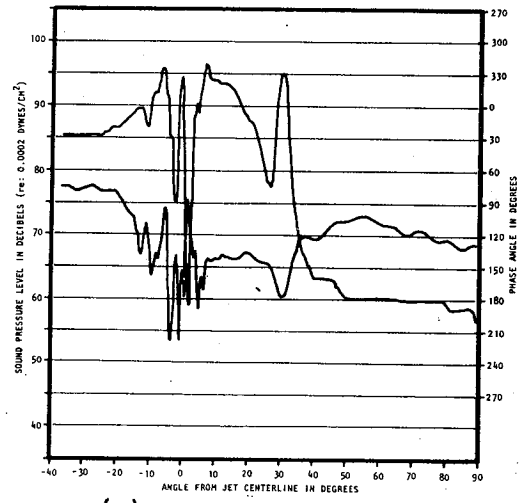
Figure 154. Duct Exit and Radiated Field Patterns for (0,0) + (1,0) Equal Mode Combination, k Ro = 2.518



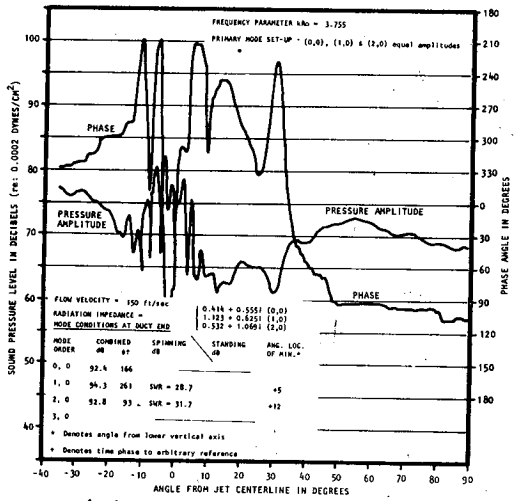
(a) Zero Flow



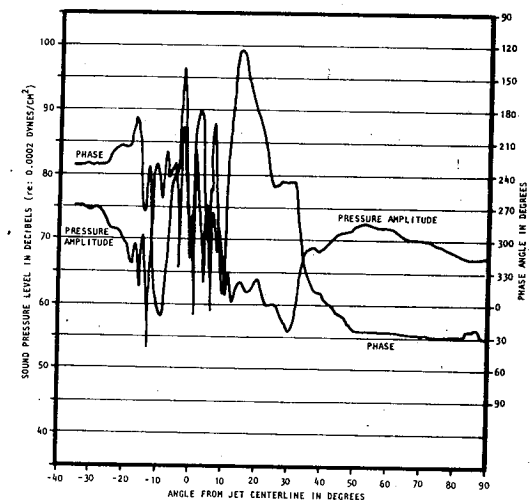
(b) 50 F.P.S.



(c) 100 F.P.S.

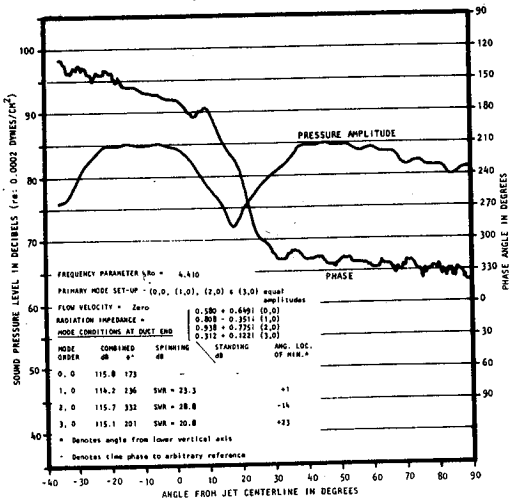


(d) 150 F.P.S.

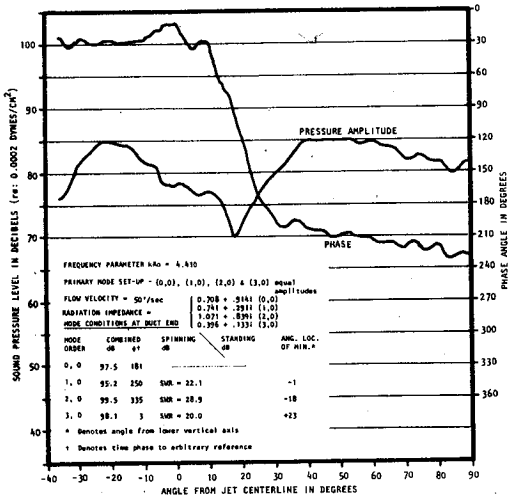


(e) 200 F.P.S.

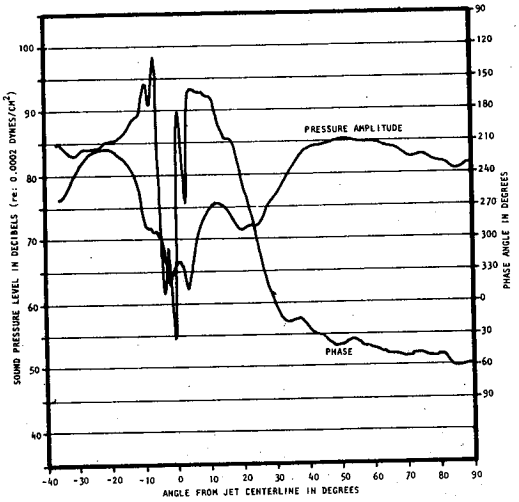
Figure 155. Duct Exit and Radiated Field Patterns for (0,0), (1,0), and (2,0) Equal Mode Combination, k Ro = 3.755



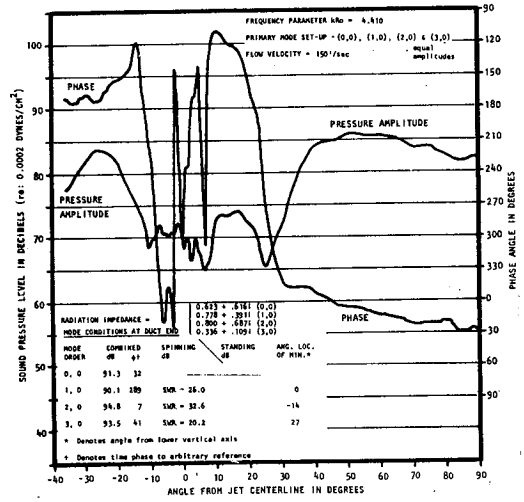
(a) Zero Flow



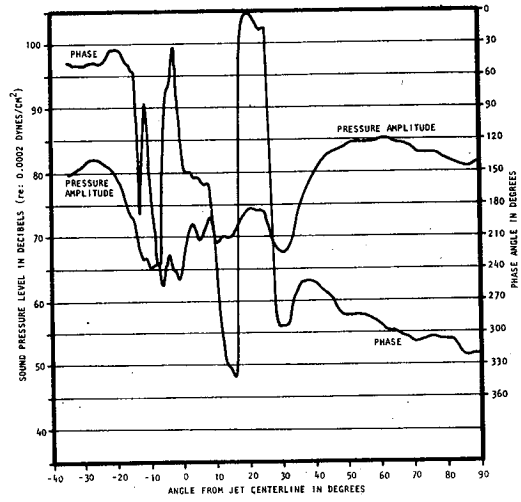
(b) 50 F.P.S.



(c) 100 F.P.S.

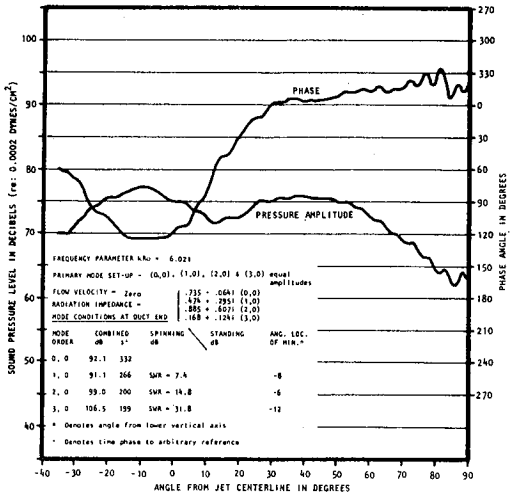


(d) 150 F.P.S.

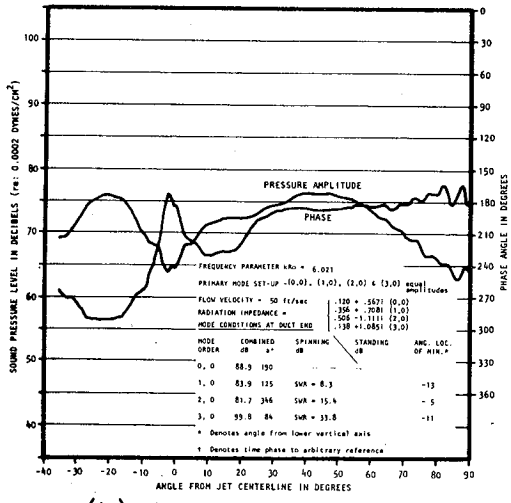


(e) 200 F.P.S.

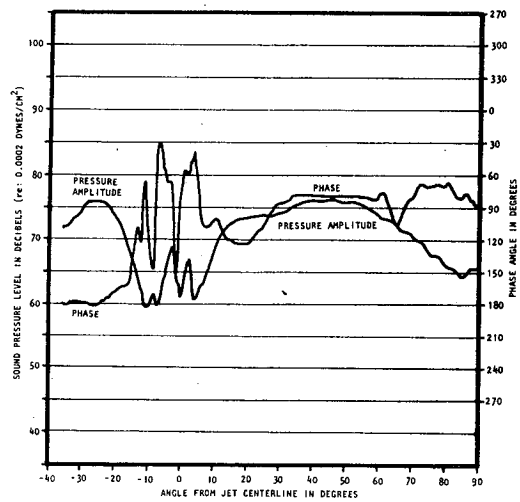
Figure 156. Duct Exit and Radiated Field Patterns for (0,0), (1,0), (2,0), and (3,0) Equal Mode Combination, k Ro = 4.410



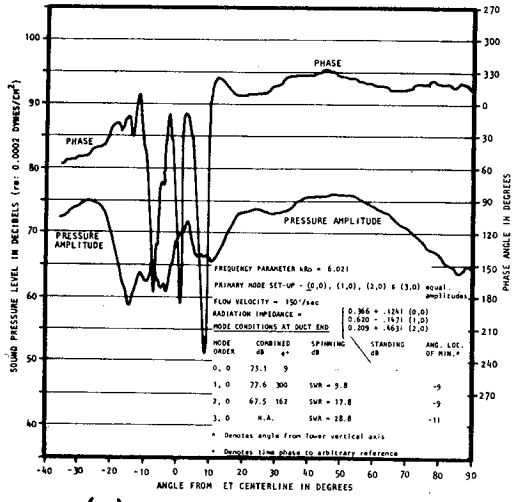
(a) Zero Flow



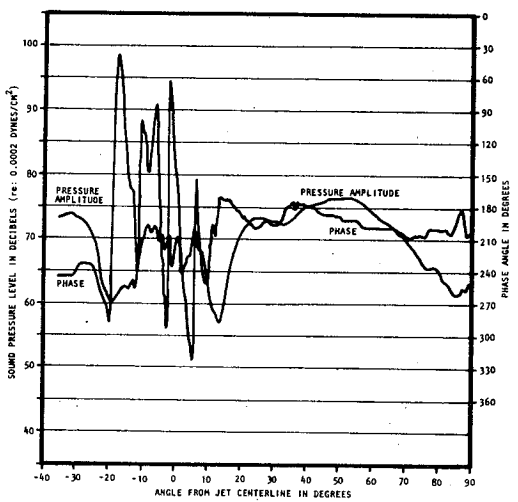
(b) 50 F.P.S.



(c) 150 F.P.S.



(d) 100 F.P.S.



(e) 200 F.P.S.

Figure 157. Duct Exit and Radiated Field Patterns for (0,0), (1,0), (2,0), and (3,0) Equal Mode Combination, k Ro = 6.021

IX. CONCLUSIONS

The primary conclusion reached from this study is that the theory describing sound propagation in an acoustically lined annular duct sustaining a mean flow, as outlined in the first section of this report, has been verified for most effects of practical interest by the experiments reported herein.

A listing of the major conclusions leading to this primary result as well as the subsidiary findings resulting from the experiments are listed below.

1. A fundamental conclusion is that audio driver units can be effectively used in the simulation of the primary characteristics of fan-generated tone noise. If the internal and mutual impedances of these sources are at sufficiently high values, then interaction effects between the sources are negligible. Subsidiary conclusions were that placement of the sources on the duct walls and design of the transducers to simulate point velocity sources were necessary for effective fan noise simulation.

2. In a series of tests in hard wall annular ducts it was shown conclusively that the fundamental results of the modal theory of sound propagation in that type of duct are valid. Mode cut-on frequencies, phase speed and radial and angular mode shapes were measured and the comparison with theoretical predictions was accurate. Effects of flow were also adequately predicted by the theory.

3. Techniques were refined for measurement of wall impedance with the two microphone method and a modification of this method was developed using one traversing microphone. These impedance measuring techniques were used to quantify the effect of flow on liner impedance.

4. The effect of flow on the impedance of locally reacting liners was to significantly increase the acoustic resistance of the liners at low frequencies. Flow effects on reactance were less significant but the trend was to change the reactance toward more positive values with increasing velocity.

5. Another series of tests conducted in five different sets of acoustically lined annular ducts verified many analytical predictions concerning sound propagation in lined annular ducts, and at the same time revealed some of the problems to be expected in liner design. Mode shapes, attenuation and phase speed generally compared quite well between measurement and prediction. However, it was found that some of the liners have drastic variations in acoustic properties across the liner surface. Variations of ±50% in acoustic resistance were detected in one of the foam liners and in one type of the locally reacting liners (porous metal over a honeycomb core). Flow predictions were qualitatively verified.

6. A method for measuring the radiation impedance of higher order modes with flow was developed. This method produced new results and in the case of zero flow, verified the theoretical predictions. It was shown that, with flow, the radiation resistance could be negative, but this result did not imply an energy source at the termination. Instead, it resulted from phase changes between sound pressure and acoustic velocity caused by the mean flow through the duct.

7. Radiated field patterns were presented for several modes and combinations of modes and the effect of jet flow on refraction of the radiated sound field was demonstrated.

REFERENCES

1. Morse, P.M.: The transmission of Sound Inside Pipes. J. Acoust. Soc. Am., Vol. 11, 1939, p. 205.

2. Rice, E. J.: Attenuation of Sound in Soft-Walled Circular Ducts. Proceedings of AFOSR-UTIAS Symposium on Aerodynamic Noise, Univ. of Toronto, May, 1968.

3. Mungur, P. and Gladwell, G. M. L.: Acoustic Wave Propagation in a Sheared Fluid Contained in a Duct. J. Sound Vib., Vol. 9, No. 1, Jan. 1969, pp. 28-48.

4. Pridmore-Brown, D. C.: Sound Propagation in a Fluid Flowing Through an Attenuating Duct. J. Fluid Mech., Vol. 4, 1958, 1393.

5. Tack, D. H. and Lambert, F.F.: Influence of Shear Flow on Sound Attenuation in Lined Ducts. J. Acoust. Soc. Am. Vol. 38, 1965, pp. 655-666.

6. Mungur, P. and Plumblee, H. E.: Propagation and Attenuation of Sound in a Soft-Walled Annular Duct Containing a Sheared Flow. Proceedings of Basic Aerodynamic Noise Research Conference, NASA Headquarters, Washington, NASA SP-207, July 1969, pp. 305-327.

7. Tyler, J. M. and Sofrin, T. G.: Axial Flow Compressor Noise Studies, SAE Trans., Vol. 70, 1962, pp. 309-332.

8. Morfey, C. L.: Rotating Pressure Patterns in Ducts. Their Generation and Transmission. J. Sound Vib., Vol. 1, No. 1, 1964, pp. 60-87.

9. Lord Rayleigh: Theory of Sound. 1945 (re-issue) New York: Dover Publications.

10. Noble, B.: Methods Based on the Wiener-Hopf Technique for the Solution of Partial Differential Equations. Pergamon Press, Inc., 1958.

11. Levine, H. and Schwinger, J.: On the Radiation of Sound from an Unflanged Circular Pipe. Phys. Rev., Vol. 73, No. 4, Second ser., Feb. 1948, pp. 383-406.

12. Carrier, G. F.: Sound Transmission from a Tube with Flow. Quart. Appl. Math., Vol. XIII, No. 4, Jan. 1956, pp. 457-561.

13. Lansing, D. L.: Exact Solution for Radiation of Sound from a Semi-Infinite Circular Duct with Application to Fan and Compressor Noise. NASA Symposium on Analytical Methods in Aircraft Aerodynamics, Ames Research Center, NASA SP-228, Oct. 1969.

14. Lansing, D. L., Drischler, J. A. and Pusey, C. G.: Radiation of Sound from an Unflanged Circular Duct with Flow. Presented at 79th Meeting of Acoust. Soc. Am. Atlantic City, 1970.

15. Zorumski, W. E. and Clark, L.: Sound Radiation from a Source in a Treated N-Section Circular Duct. Private Communication.

16. Rice, E. J.: Propagating of Waves in an Acoustically Lined Duct with a Mean Flow. Proceedings of Basic Aerodynamic Noise Research conference, NASA Headquarters, Washington, NASA SP-207, July 1969, pp. 345-355.

17. Mungur, P. M.: Boundary Conditions in Duct Acoustics. (comment), Proceedings of Basic Aerodynamic Noise Research conference, NASA Headquarters, Washington, NASA SP-207, July 1969, pp. 521-522.

18. Wynne, G. A. and Plumblee, H. E.: Calculation of Eigenvalues of the Finite Difference Equations Describing Sound Propagation in a Duct Carrying Sheared Flow. Presented at 79th Meeting of Acoust. Soc. Am. Atlantic City, 1970.

19. Morfey, C. L.: Acoustic Energy in Non-Uniform Flows. J. Sound Vib., Vol. 14, No. 2, 22 Jan. 1971, pp. 159-170.

20. Morfey, C. L.: Sound Transmission and Generation in Ducts with Flow. J. Sound Vib., Vol. 14, No. 1, 8 Jan. 1971, pp. 37-55.

21. Mohring, W.: Energy Flux in Duct Flow. J. Sound Vib., Vol. 18, No. 1, Sept. 1971, pp. 101-109.

22. Tester, B. J.: Sound Attenuation in Lined Ducts Containing Subsonic Mean Flows. Ph.D. Thesis, Univ. of Southampton, England, 1972.

23. Cantrell, R. H. and Hart, R. W.: Interaction Between Sound and Flow in Acoustic Cavities: Mass, Momentum, and Energy Considerations. J. Acoust. Soc. Am. Vol. 36, No. 4, 1964, pp. 697-706.

24. Doak, P. E.: Excitation, Transmission and Radiation of Sound from Sources in Ducts. Part III: Sound Field of a Source Distribution in a Hard-Walled Duct with Reflecting Terminations and No Mean Flow. Lockheed-Georgia Company ER-10462, February, 1970.

25. Haddle, G. P.: The Radiation Impedance of Annular Flexible Pistons in a Baffle. Lockheed-Georgia Company ER-10654, May 1970.

26. Morfey, C. L.: A note on the Radiation Efficiency of Acoustic Duct Modes. J. Sound Vib., Vol. 9, No. 3, May 1969, pp. 367-372.

27. Morse, P. M. and Ingard, U.: Theoretical Acoustics 1968 New York: McGraw Hill Publications.

28. Anon.: Study and Development of Turbofan Nacelle Modifications to Minimize Fan-Compressor Noise Radiation, Volume I - Program Summary. The Boeing Company, NASA CR-1711, January 1971.

29. Pendley, R. E. and Marsh, A. H.: Investigation of DC-8 Nacelle Modifications to Reduce Fan-Compressor Noise in Airport Communities, Part I - Summary of Program Results. McDonnell Douglas Corp., NASA CR-1705, December 1970.

30. Anon.: Progress of NASA Research Related to Noise Alleviation of Large Subsonic Jet Aircraft. NASA SP-189, Proceedings of Conference at Langley Research Center, October 1968.

31. Anon.: NASA Acoustically Treated Nacelle Program. NASA SP-220, Proceedings of Conference at Langley Research Center, October 1969.

32. Melling, T. H. and Doak, P. E.: Basic Design Considerations and Theoretical Analysis of Double-Reverberant Chamber Duct Lining Test Facilities. J. Sound Vib., vol. 14, No. 1, 8 Jan. 1971, pp. 23-35.

33. Rotta, J. C.: Turbulent Boundary Layers in Incompressible Flow. Prog. in Aero. Sci. 2, 1962.

34. Nash, J. F., Patel, V. C.: Three-Dimensional Turbulent Boundary Layers. SBC Tech. Books, 1972.

35. Clauser, F. H.: The Turbulent Boundary Layer. Adv. Appl. Mech. 4, 1956.

36. Doak, P. E.: Excitation, Transmission and Radiation of Sound from Sources in Ducts, Part II: Sound Field of a Source Distribution in a Hard-Walled Duct with Non-Reflecting Terminations and no Mean Flow. Lockheed-Georgia Co. ER-10439, January 1970.

37. Doak, P. E.: Excitation, Transmission, and Radiation of Sound from Sources in Ducts, Part I: Sound Field of a Point Source in a Hard-Walled Duct with Non-Reflecting Terminations and No Mean Flow. Lockheed Georgia Co. ER-10227, May, 1969.

38. Morse, P. M.: Vibration and Sound, Second Ed. New York, McGraw-Hill, 1948.

39. Richards, E. J. and Mead, D. J. (Eds.); Noise and Acoustic Fatigue in Aeronautics. London, Wiley Ltd., 1968.

40. Plumblee, H. E. and Dean, P. D.: Sound Measurements within and in the Radiated Field of an Annular Duct with Flow. AIAA Paper 72-197. Presented at 10th AIAA Aerospace Sciences Meeting, San Diego, Jan., 1972.

41. Scanlan, R. H. and Rosenbaum, R.: Introduction to the Study of Aircraft Vibration and Flutter. New York, the Macmillan Company, 1951.

42. Sivian, L.: Acoustical Impedance of Small Orifices. J. Acoust. Soc. Am., Vol. 7, pp. 94-101, 1935.

43. Morse, P. M., Bolt, R. H.: Sound Waves in Rooms. Rev. Mod. Physics, 16, 69-150, 1944.

44. Phillips, B.: Effects of High Wave Amplitude and Mean Flow on a Helmholtz Resonator. NASA TM X-1582, 1968.

45. Binek, J.: Behavior of Acoustic Resistance of Typical Duct Liners in the Presence of Grazing Flow Measured by a Two-Microphone Method. Msc Thesis I.S.V.R. University of Southampton, 1969.

46. Tester, B. J., Dean, P. D.: On the Measurement and Interpretation of the Acoustic Impedance of Resonant Cavity Liners in Ducts Containing Mean Flow. I.S.V.R. Memorandum 420, 1971.

47. Mechel, F., Mertens, P., Schilz, W. M.: Research on Sound Propagation in Sound-Absorbent Ducts with Superimposed Air Streams. Vol. IV, pp. 62. Univ. Gottingen, Germany (Dec. 1963). AD-431-012

48. Feder, E. and Dean, L. W.: Analytical and Experimental Studies for Predicting Noise Attenuation in Acoustically Treated Ducts for Turbo-Fan Engines. NASA CR-1373, 1969.

49. Rice, E. J.: Attenuation of Sound in Soft Walled Ducts. NASA TMX-52442, 1968.

50. Atvars, J., Mangiarotty, R. A.: Parametric Studies of the Acoustic Behavior of Duct Lining Materials. J. Acoust. Soc. Am., Vol. 48, No. 3 (Part 3), March 1970, pp. 815-825.

51. Melling, T. H.: The Acoustic Impedance of Perforates at Medium and High Sound Pressure Levels. Ph.D. Thesis Univ. of Southampton, England, 1972.

52. Dean, P. D.: On the Measurement of the Local Acoustic Impedance of the Walls of Flow Ducts and its Use in Predicting Sound Attenuation. Ph.D. Thesis, Univ. of Southampton, England, 1972.

53. Scott, R. A.: The Propagation of Sound Between Walls of Porous Materials, Proceedings of Phys. Soc. Vol. 58, 1946, pp. 358-368.

54. Mechel, F., Mertens, P. and Schilz, W.: Research on Sound Propagation in Sound Absorbent Ducts with Superimposed Air Streams. AMRL TDR-62-140, 1962.

55. Mechel, F., Mertens, P. and Schilz, W.: Research on Sound Propagation in Sound Absorbent Ducts with Superimposed Air Streams. AMRL TR-67-120, 1967.

*U.S. GOVERNMENT PRINTING OFFICE: 1973-739-153/43